Functional Organic Materials for Photocatalytic Energy Conversion

Lunjie Liu

Supervisor: Prof. Andrew I. Cooper

Thesis submitted in accordance with the requirements of the University of Liverpool for the degree of Doctor of Philosophy

July 2021

Department of Chemistry and Materials Innovation Factory

University of Liverpool

Abstract

We are living a time with rapid social development and changing scientific progress, in which energy plays a vital role in various areas of our daily life. Currently, the energy supply around the world heavily relies on burning traditional fossil fuels, which are non-renewable and have caused serious environmental issues. Therefore, it is urgent to secure alternative energy supplies. Solar energy is a promising and easily available energy source that has attracted a lot of attention because of its abundance and cleanliness. Converting solar energy to chemical energy, such as hydrogen fuel and H_2O_2 via simple photocatalytic reactions has opened a new door to meeting the huge energy demand of the future. Although various inorganic semiconductors dominated this field, organic materials also show great potential, and some of them even have comparable performance with inorganic materials. Therefore, we aim to develop more efficient organic polymer photocatalysts for solar energy conversion.

To avoid random blind trials, it is important to understand the structure-property relationships of organic photocatalysts, which requires enough samples for reliable analysis. Hence, with the assistance of high throughput workflows and theoretical computation, we rapidly investigated series of acetylenic polymer photocatalysts for H_2 evolution. Based on the best sample (TE11) of primary screening, we further modified its structure, and obtained a new polymer (TEBN11) with higher activity. However, after systematic analysis, it was found that no single property dominated the photocatalytic activity, it rather results from the interaction of multiple properties. In addition, we also investigated the effect of the linker in the organic photocatalysts on H_2 production performance. It was found that due to better visible light absorption and hydrophilicity, alkenyl linkers (-C=C-) had higher activity than alkyl (-C-C-) and alkyne (-C≡C-) linkers.

Although the process of photocatalytic H_2O_2 production is similar to that of photocatalytic H_2 evolution, we did not find strong correlations between these two photoreactions. After a large amount of screening, DE7, a pyridine-containing acetylenic polymer showed the highest performance for H_2O_2 production in pure water, that was comparable with the state-of-the-art organic photocatalysts under similar conditions. Its activity could be further improved when synthesised by microwave. However, the mechanism of photocatalytic H_2O_2 production needs to be further investigated.

Acknowledgements

Time flies. It is a bit unbelievable that my PhD study is nearly ended. Look back the last four years, everything just like happened yesterday.

Firstly, I would like to express the depth of my gratitude to my supervisor Professor Andy Cooper, not only for giving me the opportunity to study here, but also guiding me to carry out the whole PhD projects. Words cannot express how thankful I am. His rich research experience, profound knowledge, foresight, patience and amiableness, benefited me quite a lot. Actually, I failed many times during the first two years although I tried hardly, I often felt guilty about no exciting results, but he never blamed me. Instead, he gave me a lot of encouragement, especially during the time when I felt down. He is the best supervisor in my eyes. In addition, I would also like to deeply appreciate my coordinator Dr. Reiner Sebastian Sprick, he is a very outstanding researcher, and always can give me useful suggestions. I also learned a lot from him, especially admire his high work efficiency.

I would also like to thank our collaborators, Professor Martijn A. Zwijnenburg and Dr. Michał Andrzej Kochman at University College London, this thesis could not be completed without their hard work. I am also deeply impressed by their precise and careful. And I also want to thank a lot to Professor Alexander Cowan, Dr. Michael Briggs, Dr. Ben Alston at University of Liverpool, Dr. Elizabeth Gibson and Dr. John Mallows at University of Newcastle, although the PEC project was not very successful and not included in this thesis.

This work is by no means my sole achievement, I would like to gratefully thank to other people who made contributions to this work. Thank Dr. Yue Wu, Dr. Xiaobo Li and Dr. Xiaoyan Wang for helping revise the PhD thesis, thank Rob Clowes, the MIF team and technical staffs in the department of chemistry for the test support. Thank Yongjie Xu for the assistance of organic synthesis, thank Dr. Xiaobo Li, Dr. Xiaoyan Wang, Dr. Yang Bai, Haofan Yang for useful discussion. In addition, I also want to thank the China Scholarship Council for providing the PhD scholarship funding.

In addition, thanks to all AIC group members, just like the team song of the Liverpool football team, “You’ll Never Walk Alone”, I never feel alone because we are a big and loving family. In no particular order, I am truly grateful to all present and past members in our group. There

are too many on the list, but particularly Dr. Xiaofeng Wu, Dr. Ming Liu, Dr. Linjiang Chen, Professor Guohong Ning, Dr. Kewei Wang, Dr. Christian B. Meier, Dr. Peng Cui, Dr. Zhiwei Fu, Hui Gao, Ai He, Hongmei Chen, Zhongfu Pang, Wei Zhao, Xue Wang, Donglin He, Qiang Zhu, Caixin Zhao, Boyu Li, Aiting Kai, Richard Lyons. You have my enduring thanks and heartfelt appreciation.

Finally, I would like to thank my family, relatives, friends for all they have done for me during my PhD study, especially my parents and my elder sister, your endless love and continued support is always the great driving force for me to move forward. My final acknowledgement goes to my girlfriend Meiyan Gao, thank you for being a part of my life, and thank you for your extremely support and encouragement. You are everything to me.

List of Publications

● **Lunjie Liu**, Michał Andrzej Kochman, Yongjie Xu, Martijn A. Zwijnenburg*, Andrew I. Cooper* and Reiner Sebastian Sprick*. Acetylene-linked conjugated polymers for sacrificial photocatalytic hydrogen evolution from water[J]. ***Journal of Materials Chemistry A***, 2021, 9(32): 17242-17248.

● **Lunjie Liu**, Meiyan Gao, Xiaoyan Wang, Xiaobo Li* and Andrew I. Cooper*. Visible-light-driven linear conjugated polymer for highly efficient H_2O_2 production[J]. Submitted to ***Journal of the American Chemical Society.***

● **Lunjie Liu**, Michał Andrzej Kochman, Martijn A. Zwijnenburg*, Andrew I. Cooper* and Reiner Sebastian Sprick*. Linear conjugated polymer with alkenyl linker for enhanced photocatalytic hydrogen evolution[J]. Finished manuscript, plan to submit to ***Chemical Communication***.

● Zhiwei Fu, Xiaoyan Wang, Adrian M. Gardner, Xue Wang, Samantha Y. Chong, Gaia Neri, Alexander J. Cowan, **Lunjie Liu**, Xiaobo Li, Anastasia Vogel, Rob Clowes, Matthew Bilton, Linjiang Chen*, Reiner Sebastian Sprick* and Andrew I. Cooper*. A stable covalent organic framework for photocatalytic carbon dioxide reduction[J]. ***Chemical Science***, 2020, 11(2): 543-550.

● Xiaoyan Wang, Zhiwei Fu, Lirong Zheng, Chengxi Zhao, Xue Wang, Samantha Y. Chong, Fiona McBride, Rasmita Raval, Matthew Bilton, **Lunjie Liu**, Xiaofeng Wu, Linjiang Chen*, Reiner Sebastian Sprick*, and Andrew I. Cooper*. Covalent organic framework nanosheets embedding single cobalt sites for photocatalytic reduction of carbon dioxide[J]. ***Chemistry of Materials***, 2020, 32(21): 9107-9114.

● Haofan Yang, Houari Amari, **Lunjie Liu**, Chengxi Zhao, Hui Gao, Ai He, Nigel D. Browning, Marc A. Little, Reiner Sebastian Sprick* and Andrew I. Cooper*. Nano-assemblies of a soluble conjugated organic polymer and an inorganic semiconductor for sacrificial photocatalytic hydrogen production from water[J]. ***Nanoscale***, 2020, 12(48): 24488-24494.

● Hui Gao, Qiang Zhu, Alex R. Neale, Mounib Bahri, Xue Wang, Haofan Yang, **Lunjie Liu**, Rob Clowes, Nigel D. Browning, Reiner Sebastian Sprick, Marc A. Little, Laurence J. Hardwick* and Andrew I. Cooper*. Covalent Organic Framework/Carbon Nanotube Composite as Li-ion Positive Electrode with Ultra-high Rate Performance[J]. ***Advanced Energy Materials,*** 2021, Accepted.

● Xue Wang, Mounib Bahri, Zhiwei Fu, Marc A. Little, **Lunjie Liu**, Hongjun Niu, Nigel D. Browning, Samantha Y. Chong, Linjiang Chen,* John W. Ward* and Andrew I. Cooper*. Synthesis of a 3D Covalent Organic Framework with nbo Topology[J]. ***Journal of the American Chemical Society,*** 2021, Accepted.

● Yang Bai, Chao Li, **Lunjie Liu**, Yuichi Yamaguchi, Adrian Gardner, Martijn A. Zwijnenburg, Alexander J. Cowan,* Akihiko Kudo,* Andrew I. Cooper* and Reiner Sebastian Sprick*. Understanding overall water splitting under visible light using a single particulate conjugated polymer photocatalyst loaded with iridium cocatalyst[J]. Finished Manuscript.

● Wei Zhao, Peiyao Yan, Haofan Yang, Mounib Bahri, Alex James, Hongmei Chen, **Lunjie Liu**, Boyu Li, Zhongfu Pang, Rob Clowes, Nigel D. Browning, John W. Ward,* Yue Wu* and Andrew I. Cooper*. Using Sound to Synthesize Covalent Organic Frameworks in Water[J]. Submitted.

● Weiwei Zhang, Linjiang Chen, Sheng Dai, Chengxi Zhao, Cheng Ma, Lei Wei, Minghui Zhu, Samantha Y. Chong, Haofan Yang, **Lunjie Liu**, Yang Bai, Miaojie Yu, Yongjie Xu, Xiaowei Zhu, Shuhao An, Reiner Sebastian Sprick, Marc A. Little, Xiaofeng Wu, Shan Jiang, Yue-Biao Zhang, Yongzhen Wu, He Tian, Wei-Hong Zhu* and Andrew I. Cooper*. Reconstructed Covalent Organic Frameworks with Enhanced Crystallinity for Photocatalysis[J]. Submitted.

List of Abbreviations

AA	Ascorbic acid
AHQ	Anthrahydroquinone
AM1.5G	Air mass 1.5 global filter
AQ	Anthraquinone
BET	Brunauer Emmett Teller
BQ	Benzoquinone
CA	Contact angle
CB	Conduction band
CMPs	Conjugated microporous polymers
COFs	Covalent organic frameworks
CP-MAS	Cross-polarization magic angle spinning
CTFs	Covalent triazine-based frameworks
DEA	Diethylamine
DFT	Density functional theory
DMPO	5,5-Dimethyl-1-pyrroline N-oxide
DR	Disperse Red 1
EA	Electron affinity of photocatalyst's ground state
EA*	Electron affinity of photocatalyst's excited state
EIS	electrochemical impedance spectra
EPR	Electron paramagnetic resonance
EQE	External quantum efficiency
EY	Eosin Y
FT-IR	Fourier transform infrared
FTO	Fluorine-doped tin oxide
GC	Gas chromatography
GCR	Glaser cross-coupling reaction
g-C_3N_4	Graphitic carbon nitride
HEP	Hydrogen evolution photocatalyst
HER	Hydrogen evolution reaction
HOMO	Highest occupied molecular orbital
HTS	High throughput Screening
ICP-OES	Inductively coupled plasma-optical emission spectrometry
IP	Ionisation potential of photocatalyst's ground state

IP*	Ionisation potential of photocatalyst's excited state
IPA	Isopropanol
LUMO	Lowest unoccupied molecular orbital
MOFs	metal organic frameworks
MW	Microwave
NHE	Normal hydrogen electrode
NMR	Nuclear magnetic resonance
OEP	Oxygen evolution photocatalyst
PBS	Phosphate buffered saline
PDI	Perylene-3,4,9,10-tetracarboxylic dianhydride
PSA	Pressure swing adsorption
PXRD	Powder X-ray diffraction
RF	Resorcinol-formaldehyde
RP	Red phosphorus
SA	Sacrificial reagent
SCC	Solar-to-chemical conversion
SCR	Sonogashira cross-coupling reaction
SEM	Scanning electron microscopy
STH	Solar-to-hydrogen
SLS	Static light scattering
TCSPSC	Time-correlated single photon counting
TEA	Triethylamine
TEOA	Triethanolamine
TGA	Thermogravimetric analysis
UV-vis	Ultraviolet-visible
VB	Valence band
WGS	Water-gas shift reactor
XPS	X-ray photoelectron spectroscopy
λexc	Excitation wavelength
λem	Emission wavelength
e^-	Electron
h^+	Hole

Table of Contents

Abstract ..... **I**

Acknowledgements ..... **II**

List of Publications ..... **IV**

List of Abbreviations ..... **VI**

Chapter 1: Introduction ..... **- 1 -**

1.1 Research background ..... - 2 -

1.2 Solar energy conversion ..... - 3 -

1.2.1 Hydrogen (H_2) production from solar energy ..... - 3 -

1.2.2 Hydrogen peroxide (H_2O_2) production from solar energy ..... - 11 -

1.3 Organic photocatalysts for solar energy conversion ..... - 14 -

1.3.1 Organic materials for photocatalytic H_2 production ..... - 14 -

1.3.2 Organic materials for photocatalytic H_2O_2 production ..... - 20 -

1.4 Experimental techniques ..... - 25 -

1.4.1 High throughput screening workflow ..... - 25 -

1.4.2 Microwave-assisted polymer synthesis ..... - 27 -

1.5 Project aims ..... - 29 -

1.6 References ..... - 31 -

Chapter 2: Acetylene-Linked Conjugated Polymers for Sacrificial Photocatalytic Hydrogen Evolution from Water ..... **- 39 -**

2.1 Introduction ..... - 40 -

2.2 Materials design and characterization ..... - 41 -

2.2.1 Synthesis of polymers ..... - 41 -

2.2.2 Characterizations ..... - 42 -

2.3 Hydrogen evolution performance ..... - 54 -

2.3.1 Hydrogen production ..... - 54 -

2.3.2 Relationship between HER performance and polymer properties ..... - 55 -
2.4 Improved performance by changing the core ..... - 60 -
2.4.1 Synthesis of polymers ..... - 60 -
2.4.2 Characterisations ..... - 60 -
2.4.3 Hydrogen production ..... - 65 -
2.5 Summary ..... - 70 -
2.6 Experimental parts ..... - 71 -
2.6.1 Materials ..... - 71 -
2.6.2 Characterization methods ..... - 71 -
2.6.3 Synthetic procedure of polymers ..... - 72 -
2.6.4 High-throughput photocatalytic hydrogen evolution experiments ..... - 78 -
2.6.5 Kinetic photocatalytic hydrogen evolution measurements ..... - 78 -
2.6.6 Electrochemical measurements ..... - 79 -
2.6.7 Density functional theory (DFT) calculations ..... - 79 -
2.7 References ..... - 82 -
Chapter 3: Linear Conjugated Polymer with Alkenyl Linkers for Enhanced Photocatalytic Hydrogen Evolution ..... - 86 -
3.1 Introduction ..... - 87 -
3.2 Materials design and characterization ..... - 88 -
3.2.1 Synthesis of polymers ..... - 88 -
3.2.2 Characterizations ..... - 88 -
3.2.3 Hydrogen evolution ..... - 93 -
3.2.4 Stability and performance evaluation of NP2 ..... - 94 -
3.2.5 Discussion of performance and property relationship ..... - 96 -
3.3 Dye sensitization of NP2 ..... - 101 -
3.3.1 Synthesis and characterisations ..... - 101 -
3.3.2 Hydrogen evolution ..... - 104 -

3.4 NP2/TiO_2 heterojunction photocatalyst ..... - 105 -
3.4.1 Synthesis and characterisations ..... - 105 -
3.4.2 Hydrogen evolution ..... - 110 -
3.5 NP2/red phosphorus heterojunction photocatalyst ..... - 111 -
3.5.1 Synthesis and characterisations ..... - 111 -
3.5.2 Hydrogen evolution ..... - 115 -
3.6 Summary ..... - 116 -
3.7 Experimental Parts ..... - 117 -
3.7.1 Materials and methods ..... - 117 -
3.7.2 Synthetic procedures ..... - 118 -
3.7.3 Photocatalytic experiments ..... - 120 -
3.7.4 Computational details ..... - 121 -
3.8 References ..... - 123 -
Chapter 4: Organic Materials for Photocatalytic Hydrogen Peroxide Production.. - 128 -
4.1 Background ..... - 129 -
4.2 Benchmark ..... - 130 -
4.2.1 Preparation and characterization of RF523 ..... - 130 -
4.2.2 Comparation of H_2O_2 detection methods ..... - 132 -
4.3 High-throughput screen candidate materials ..... - 135 -
4.3.1 Existing polymers in previous projects ..... - 135 -
4.3.2 Design and synthesise candidate polymers ..... - 139 -
4.4 Optimization of H_2O_2 production ..... - 142 -
4.4.1 The effect of residual metal ..... - 142 -
4.4.2 Design and comparison of DE7 derivatives ..... - 145 -
4.4.3 Prepare DE7-M via microwave method ..... - 151 -
4.4.4 Further improving H_2O_2 performance of DE7-M80 ..... - 158 -
4.4.5 Stability performance evaluation of DE7-M80 ..... - 163 -

4.5 Mechanism investigation ..... - 170 -
4.5.1 Gas atmosphere ..... - 170 -
4.5.2 Radical detection ..... - 171 -
4.5.3 Half photoreaction ..... - 173 -
4.5.4 Proposed mechanism path ..... - 174 -
4.6 Summary ..... - 175 -
4.7 Experimental Parts ..... - 177 -
4.7.1 Materials and methods ..... - 177 -
4.7.2 Synthetic procedures ..... - 178 -
4.7.3 Photocatalytic experiments ..... - 186 -
4.7.4 Electrochemical analysis ..... - 187 -
4.7.5 Electron paramagnetic resonance measurements ..... - 188 -
4.7.6 Isotopic photoreaction experiments ..... - 188 -
4.8 References ..... - 189 -
Chapter 5: Summary & Outlook ..... - 195 -

Chapter 1: Introduction

1.1 Research background

Energy is the cornerstone of development. As shown in Figure 1.1, with the rapid development of our human society, the global consumption of energy has been obviously increased year by year. In the last decades, traditional fossil energy resources, such as oil, coal and natural gas still dominate the current energy pattern, but they are limited and non-renewable.[1, 2] Besides, due to the large consumption of fossil energy, the induced environment pollution and greenhouse effect issues have become serious threats to our heath and living conditions.[3, 4] Therefore, it is urgent and important to explore more clean and renewable energy for sustainable development in the future.

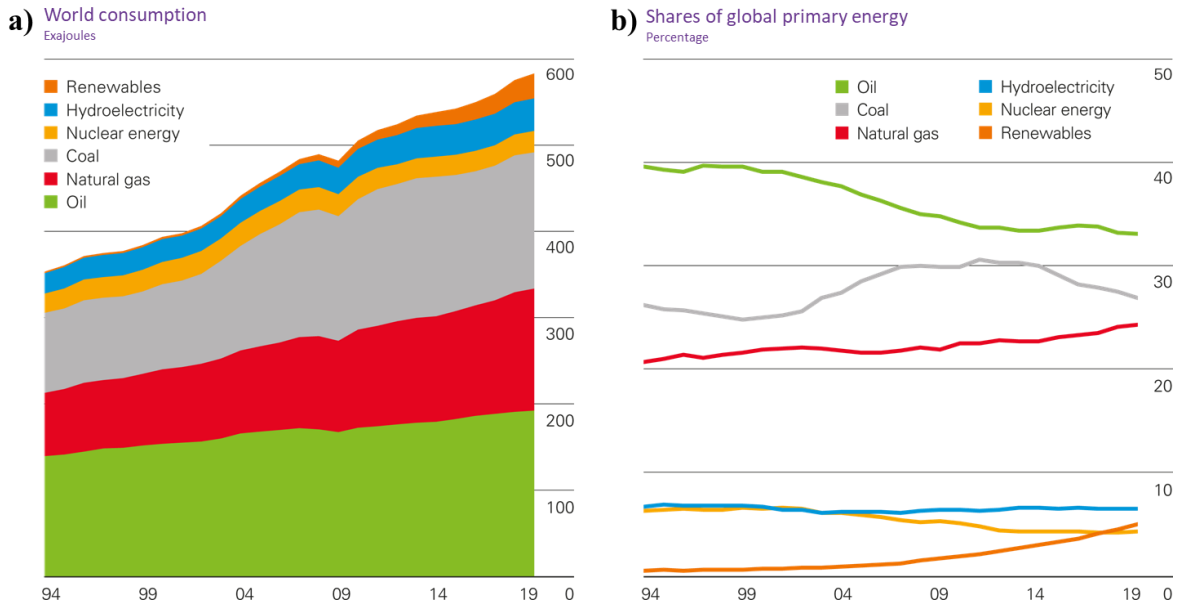

Figure 1.1 (a) Global energy consumption and (b) Shares of global primary energy from 1994 to 2019. The data are from the bp Statistical Review of World Energy 2020. Figure adapted from reference [2].

Solar energy could be the ultimate solution to meet the huge energy demand of the world. On one hand, it is abundant and non-exhaustible. The sun emits the energy at the rate of 3.8×10^{23} kW, and approximately 1.8×10^{14} kW can reach to the earth,[5] which is enough to provide 7900 times as much energy as the current usage of the world's population.[6] Although the distribution of available solar resources on the earth's surface varies in different regions (Figure 1.2),[7] there is vast scope to realize its potential. On the other hand, with appropriate technologies, solar energy could be converted to other useful chemical energy and fuels, and the process is clean and environmentally friendly,[8] which has attracted much attention. However, the main challenges lie in the high cost as well as low conversion efficiency. Hence, how to utilize the

renewable and sustainable solar energy more efficiently and economically deserves more exploration. Among various strategies, converting solar energy to H_2 or H_2O_2 via photocatalytic reactions provides a practical and feasible route, which has aroused the interest of many researchers around the world.

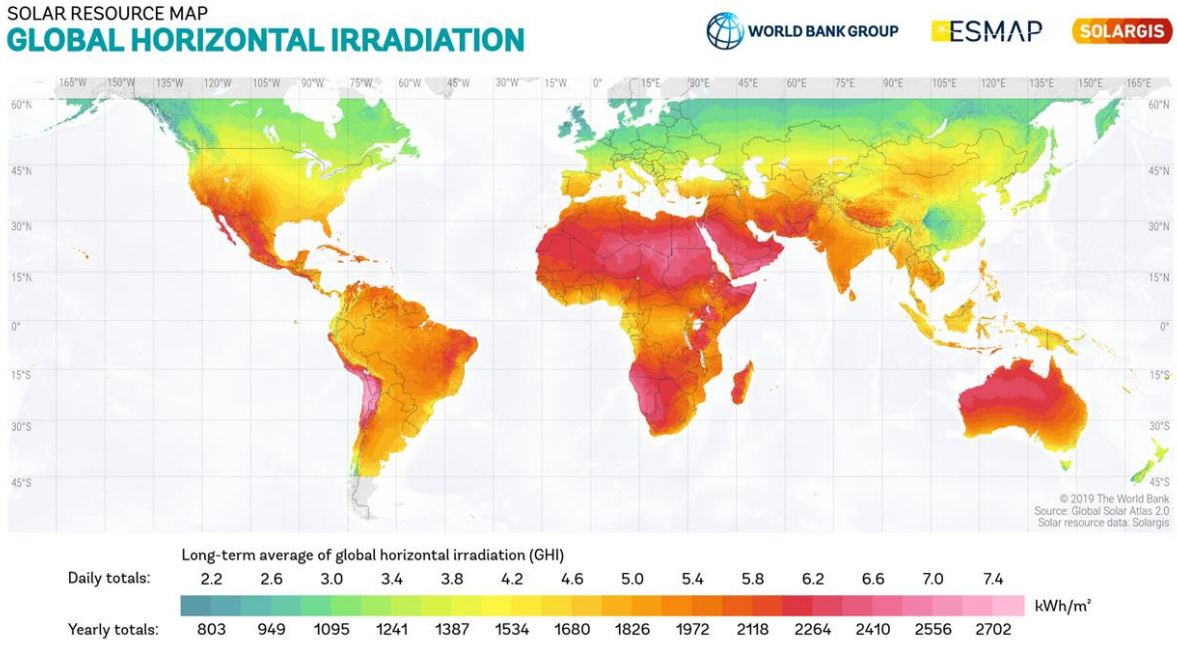

Figure 1.2 Solar resource map of global horizontal irradiation (GHI). The map is published by the World Bank Group, funded by ESMAP, and prepared by Solargis. Figure adapted from reference [7].

1.2 Solar energy conversion

1.2.1 Hydrogen (H_2) production from solar energy

Hydrogen, one of the candidates with tremendous potential to meet the future energy requirements, is an ideal sustainable future energy source. It not only can be used as fuel to provide power to fuel cells, but also can be applied as the feedstock to produce other important industry chemicals (Figure 1.3).[9] There are many advantages of H_2 compared with traditional fossil energy, for example, the consumption of H_2 will only produce water without greenhouse gases emission and environmental pollution. Besides, H_2 has very high energy density, the energy content of H_2 up to 120 MJ/kg, which is much higher than that of gasoline and other common fuels (Table 1.1).[10] What's more, H_2 can be obtained from various energy sources, including renewable solar energy.[11] Therefore, converting solar energy to H_2 provides a perfect choice for sustainable development of energy.

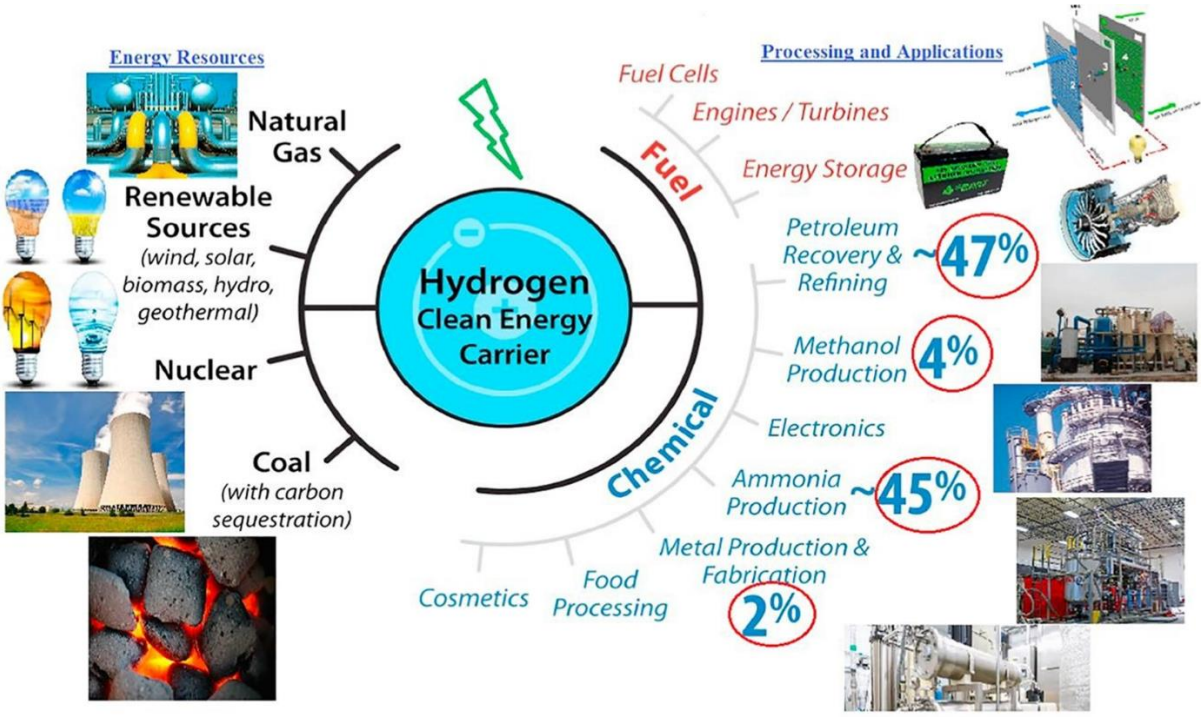

Figure 1.3 Hydrogen clean energy carrier as one of most essential clean and sustainable resource with applications in both research and industry. Figure adapted from reference [9].

Table 1.1 Energy contents of different fuels. Data adapted from reference [10].

Fuel	Energy content (MJ/kg)
Hydrogen	120
Liquefied natural gas	54.4
Propane	49.6
Aviation gasoline	46.8
Automotive gasoline	46.4
Automotive diesel	45.6
Ethanol	29.6
Methanol	19.7
Coke	27
Wood (dry)	16.2
Bagasse	9.6

1.2.1.1 Traditional methods

There are various technologies have been applied to produce H_2, of which steam reforming is the most developed and commonly used for large-scale H_2 production, mainly due to its high

conversion efficiency and low cost (Table 1.2).[9] The main chemical reactions that take place in steam reforming are as follows:

$$\text{Reformer: } C_nH_m + nH_2O \rightarrow nCO + (n + \frac{1}{2}m)H_2 \quad (1.1)$$

$$\text{WGS reactor: } CO + H_2O \rightarrow CO_2 + H_2 \quad (1.2)$$

$$\text{Methanator: } CO + 3H_2 \rightarrow CH_4 + H_2O \quad (1.3)$$

Firstly, the raw materials, such as methane and other methane containing gases are reformed to generate synthesis gas (syngas). After that, the gas mixture passes through a heat recovery step and goes into a water-gas shift reactor (WGS) where the CO reacts with steam to produce additional H_2. Finally, the mixture is further purified by methanation or pressure swing adsorption (PSA) giving H_2 with a purity of near 100%.[12, 13]

However, during this process, large amounts of CO_2 are produced at the same time, which is a serious issue as it could cause greenhouse effect.[14] In addition, it relies heavily on the fossil fuel as the energy source and feedstock (Table 1.2),[9, 12, 13] which not sustainable for future development.

Table 1.2 Representative traditional processes for H_2 production. Data adapted from reference [9, 13]

Process	Source of energy	Feedstock	Maturity	Efficiency (%)	Cost of H_2 ($US kg^{-1})
Steam reforming	Standard fossil fuels	Natural gas	Commercial	70–85	2.27
Biomass gasification	Internally generated steam	Woody biomass	Commercial	35–50	1.77–2.05

Because of the increasing interest on renewable energy, biomass has been also applied to produce H_2, because it can be obtained from vegetation and organic wastes.[15] Biomass gasification is a typical technology to convert biomass into a gaseous fuel (syngas) via the reaction with air, oxygen and/or steam. the mechanism is briefly introduced as follows:[13]

$$\text{Biomass} + \text{Air (and or Steam)} \rightarrow H_2 + CO_2 + CO + N_2 + CH_4 + \text{other CHs} + \text{tar} + H_2O + \text{char} \quad (1.4)$$

After the reaction, the gas mixture is further purified to get pure H_2. Although the efficacy is lower than steam reforming (Table 1.2),[9, 13] thanks to the abundant resources of biomass and lower cost, it still shows great potential for commercial H_2 production on a large scale.

1.2.1.2 Photocatalytic H_2 production

Compared with traditional methods, converting solar energy to H_2 via water splitting is more attractive, the possible route is illustrated in Figure 1.4. There are three main advantages: 1) both solar energy and the feedstock of water are abundant on the earth; 2) the photocatalytic conversion process is very simple and does not need complicated instruments; 3) this route is environmentally friendly as no pollution is produced. However, the main challenge is how to decrease the cost and increase the conversion efficiency. Therefore, it is important to explore highly active photocatalysts for solar-driven water splitting.

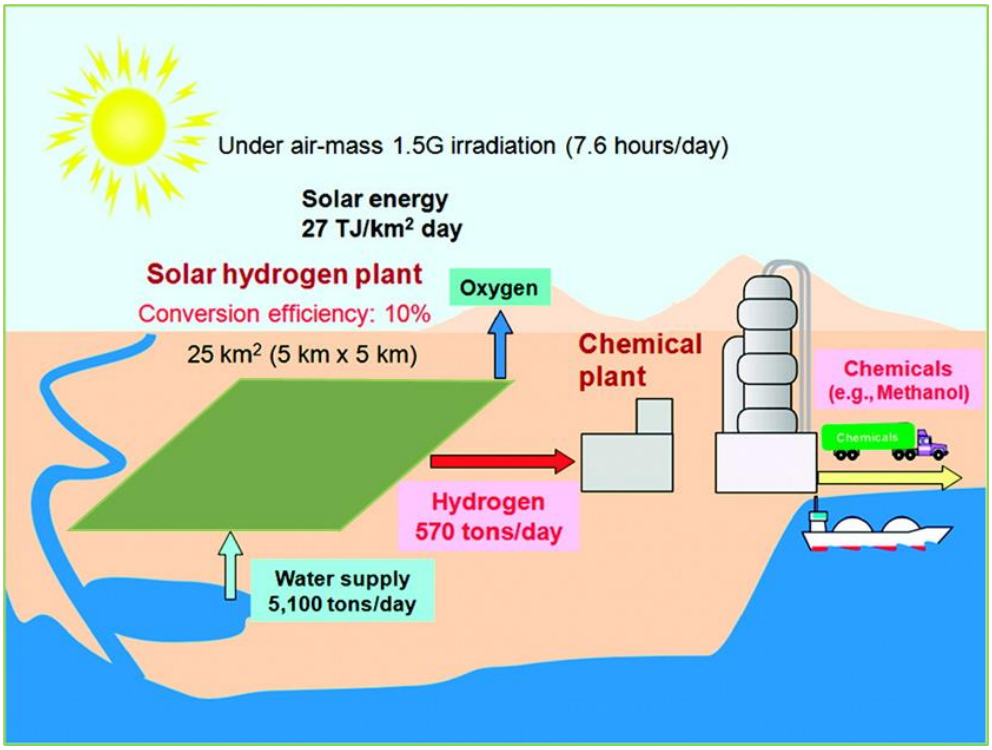

Figure 1.4 Possible route for large-scale H_2 production via solar water splitting. Figure adapted from reference [16].

The water splitting reaction is an uphill reaction with Gibbs free energy of 118.7 kJ mol^{-1}, which corresponds to a minimum energy barrier of 1.23 eV to break the water molecule into H_2 and O_2 (Figure 1.5a). The mechanism of photocatalytic water splitting for H_2 evolution is illustrated in Figure 1.5b. In detail, it involves several main steps, light absorption, charge transfer, redox reactions, and charge recombination.[17-19] When the energy of incident light is larger than the optical gap or band gap of the photocatalyst, excited electron (e^-) – hole (h^+) pairs (excitons) are generated by light absorption, which then subsequently separate into free charges in the form of polarons (radical ions).[20] In organic materials, the typical excitations are

Frenkel excitons, because their exciton binding energy values are much larger than kT at room temperature, it is difficult for them to spontaneously dissociate in the polymers.[21] In addition, excitons can also dissociate on the interface between the photocatalyst and the reaction solution, where one of the formed free charge carriers remains in polymers and the other gets transferred to takes part in the reaction in the solution. However, during separation and transformation process, the recombination of carriers may also happen at the same time. The carriers are further consumed to produce H_2 and O_2 by redox reactions as follows:

$$4H^+ + 4e^- \rightarrow 2H_2 \quad (1.5)$$

$$2H_2O + 4h^+ \rightarrow O_2 + 4H^+ \quad (1.6)$$

$$\text{Overall reaction:}\quad 2H_2O \rightarrow 2H_2 + O_2 \quad (1.7)$$

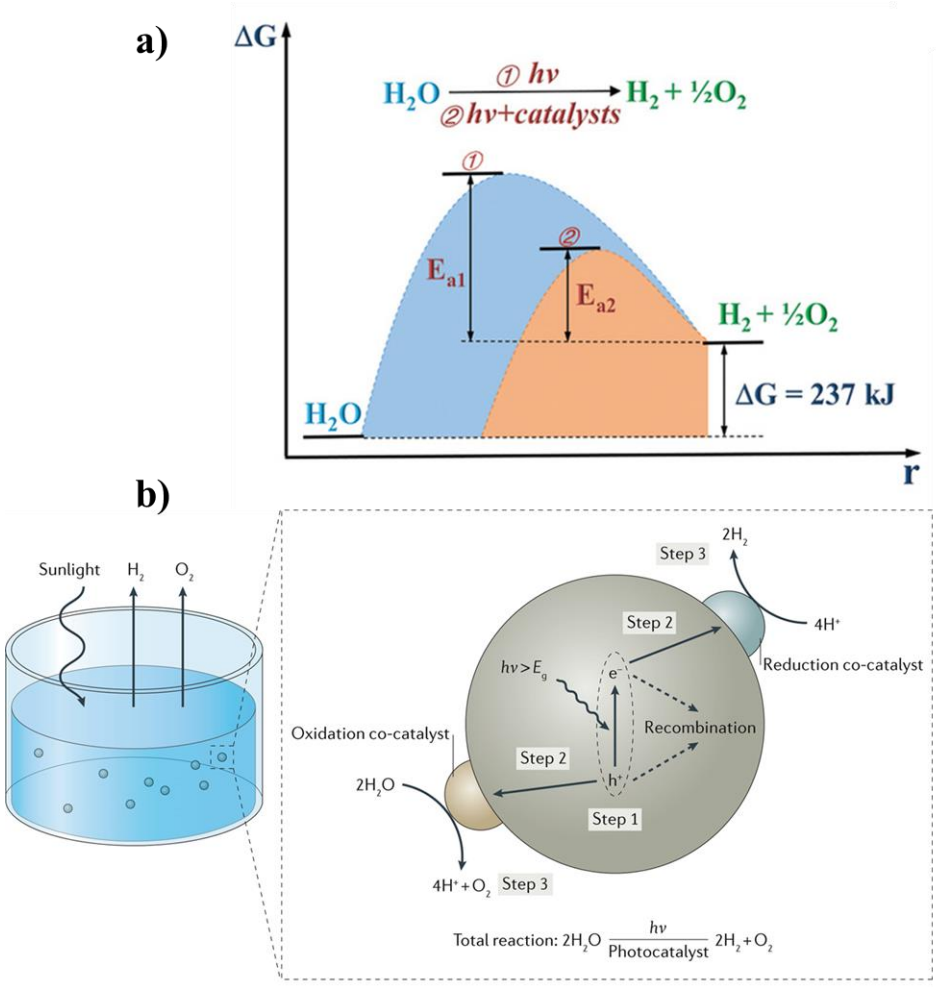

Figure 1.5 (a) Energy diagrams for photocatalytic water splitting with or without the presence of cocatalysts. Figure adapted from reference [22]. (b) Schematic illustration of the main processes within the photocatalytic water-splitting reaction. E_g, semiconductor bandgap. Figure adapted from reference [19].

The overall conversion efficiency of photocatalytic water splitting depends on the balance of thermodynamics and kinetics of the three steps altogether. In addition, with the addition of cocatalyst that has higher electron affinity, the efficiency could be further improved. Because the cocatalyst not only can lower the activation energy or overpotential for H_2/O_2 production, but also are beneficial for the electron-hole separation at the interface between cocatalyst and semiconductor.[23]

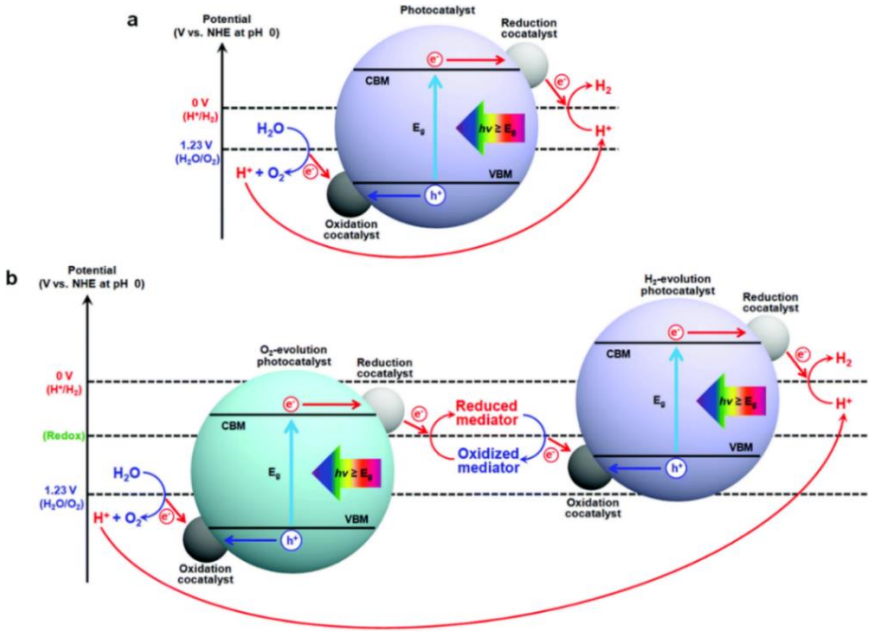

Figure 1.6 Schematic energy diagrams of (a) one-step excitation and (b) two-step Z-scheme overall water splitting on particulate photocatalysts. CBM: conduction band minimum; VBM: valence band maximum; E_g: band gap energy. Figure adapted from reference [24].

Photocatalytic water splitting can be classified into two categories: overall water splitting and sacrificial water splitting. For overall water splitting, as shown in Figure 1.6, it can be further divided into one-step and two-step overall water splitting. To achieve one-step overall water splitting (Figure 1.6a), the conduction band (CB) or highest occupied molecular orbital (HOMO) position of the photocatalyst should be more negative than the energy level of H_2 reduction. Meanwhile, its valence band (VB) or lowest unoccupied molecular orbital (LUMO) position should be more positive than the energy level of O_2 oxidation. Note that the potentials for redox reaction of H_2O are dependent on the pH value of reaction solution. In addition, although the required theoretical bandgap is 1.23 V, the energy loss is inevitable during the carrier's migration, which could be caused by the electron-transfer, charge trapping, the resulting photovoltage at the surface and the overpotentials of the reactions.[25, 26] Therefore, a

bandgap larger than 1.8 V for photocatalytic water splitting is often required. However, too large bandgap will limit the absorption of visible light and decrease the solar-energy conversion efficiency, so normally less than 2.2 V is optimal.[22, 27]

In fact, it is very difficult to fully meet the strict requirements mentioned above, as most photocatalysts either have too large bandgap or inappropriate CB/VB positions, as shown in Figure 1.7. In addition, because visible light accounts for about 43% of the solar spectrum, developing novel visible light-driven photocatalysts with narrow bandgap would be more significant in terms of practical applications. Besides, due to kinetic and energetic complexity, the oxidation reaction of H_2O to O_2 is more stringent and sluggish, which is also recognized as the bottleneck or rate-determining step for highly efficient overall water splitting.[28-32] However, inspired by the two-stage natural photosynthesis processes in green plants,[33] a Z-scheme overall water splitting route is proposed. As shown in Figure 1.6b, the valence band positions of most hydrogen evolution photocatalysts (HEP) do not match with the energy level for water oxidation. But after combining with an oxygen evolution photocatalyst (OEP) with deep valence band position, the overall water splitting could also happen to produce H_2 and O_2. The photoexcited electrons in OEP and photoexcited holes in the HEP could be recombined via an aqueous redox mediator to maintain charge neutrality and complete the cycle. In this case, it provides three advantages: 1) it can utilize visible light more efficiently with the combination of two narrow bandgap photocatalysts; 2) it can give a larger driving force for H_2 or O_2 evolution, as the CB of HEP and the VB of OEP could be located more negatively and more positively than the energy levels of H_2 evolution and O_2 evolution, respectively; 3) because the thermodynamic requirements are alleviated, it broadens the choice of more potential semiconductors.

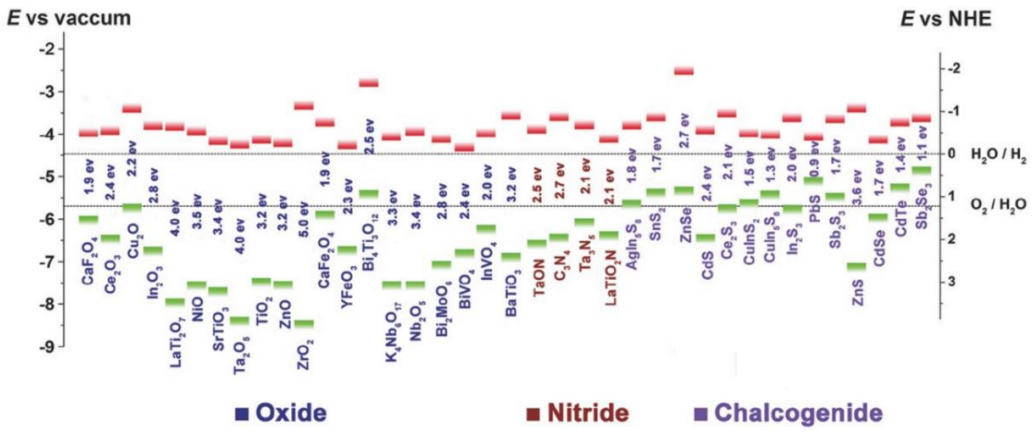

Figure 1.7 Band edge positions with respect to the vacuum level and the normal hydrogen electrode (NHE) for typical inorganic semiconductors at pH = 0. Figure adapted from reference [34].

Besides, sacrificial photocatalytic water splitting is beneficial for more efficient H_2 evolution. Typically, an electron donor sacrificial reagent (SA), such as triethylamine (TEA),[35-37] triethanolamine (TEOA),[38-40] or ascorbic acid (AA),[41-43] can be applied to quench the O_2 evolution (Figure 1.8), as the required energy for SA oxidation is normally lower than that for water oxidation,[44] which thus provides another efficient strategy to explore more promising photocatalysts. In addition, with the addition of sacrificial reagent, the recombination of photogenerated e^- and h^+ could be inhibited, which is beneficial for promoting H_2 production. In this thesis, we adapted this route and the H_2 evolution experiments were carried out in the presence of TEA as the donor sacrificial reagent. The hypothesised reactions are outlined below (Eq. 1.8-1.14).[45] TEA was excited to $TEA^{\bullet+}$ by the photogenerated holes, and then the excited electrons would take part in the proton reduction half-reaction (Eq. 1.13). It should be noted that TEA itself would decompose to diethylamine and ethanaldehyde (Eq. 1.10, 1.11 and 1.14).

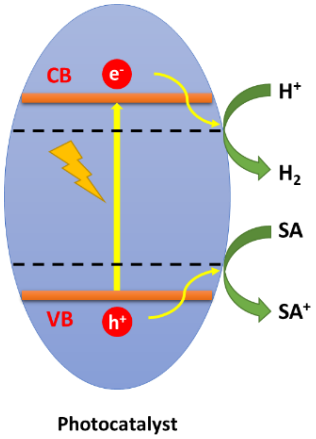

Figure 1.8 Schematic graph of photocatalytic hydrogen evolution with the addition of SA.

$$\text{Photocatalyst} \rightarrow \text{Photocatalyst}^* \quad (1.8)$$

$$\text{Photocatalyst}^* + \text{TEA} \rightarrow \text{Photocatalyst}^{\bullet-} + \text{TEA}^{\bullet+} \quad (1.9)$$

$$\text{TEA}^{\bullet+} \xrightarrow{-H^+} \text{Et}_2\text{C}^{\bullet}\text{HNCH}_3 \quad (1.10)$$

$$\text{Et}_2\text{C}^{\bullet}\text{HNCH}_3 \rightarrow \text{Et}_2\text{C}^{+}\text{HNCH}_3 + e^- \quad (1.11)$$

$$\text{Photocatalyst}^{\bullet-} \rightarrow \text{Photocatalyst} + e^- \quad (1.12)$$

$$2H_2O \xrightarrow{2e^-} H_2 + 2OH^- \quad (1.13)$$

$$\text{Et}_2\text{C}^{+}\text{HNCH}_3 \xrightarrow{OH^-} \text{Et}_2\text{NH} + \text{CH}_3\text{CHO} \quad (1.14)$$

1.2.2 Hydrogen peroxide (H_2O_2) production from solar energy

As a widely used chemical around the world,[46] H_2O_2 was first produced by Thenard in 1818 from the acidification of barium peroxide with nitric acid.[47] It is well known that H_2O_2 is a versatile and environmentally friendly oxidant and plays a critical role in a wide range applications (Figure 1.9), such as paper bleaching,[48, 49] chemical synthesis[50, 51] and the textile industry[52, 53]. Because H_2O_2 very high active oxygen content among common industrial oxidants (Table 1.3), it has more efficient oxidizing ability. In addition, it also can serve as both fuel and oxidant in a one-compartment fuel cell.[54, 55] Moreover, H_2O_2 is a kind of reducing agent, it can react with some strong oxidizers, such as $KMnO_4$ and $Ce(SO_4)_2$, which also have been used for quantitative determination of H_2O_2.[56, 57] It is reported that due to the growing global demand in the chemical and the paper & pulp industries, the H_2O_2 market size is forecast to exceed $6.2 billion by 2026.[58] Therefore, developing economical and clean H_2O_2 production methods has attracted more and more attention in recent years.

Figure 1.9 Applications of H_2O_2 in industrial manufacturing. Figure adapted from reference [59].

Table 1.3 Commonly used industrial oxidants. Date adapted from reference [60]

Oxidant	Active oxygen (wt %)	By-product
Pure O_2	100	-
Air (O_2)	23	-
O_3	100	-
H_2O_2	47.1	H_2O
***t*BuOOH**	17.8	*t*BuOH
HNO_3	25.0	NO_x, N_2O, N_2
N_2O	36.4	N_2
NaClO	21.6	NaCl
$NaClO_2$	35.6	NaCl
NaBrO	13.4	NaBr
PhIO	7.3	PhI

1.2.2.1 Traditional method

In the last decades, global H_2O_2 production has exceeded 3 million tons per annum,[61] and currently the predominant technology for industrial large-scale production of H_2O_2 is the anthraquinone (AQ) oxidation process, which accounts for more than 95% of the total production. The first commercial AQ process was applied by a German company, IG Farbenindustrie Corporation in the 1940s.[60]

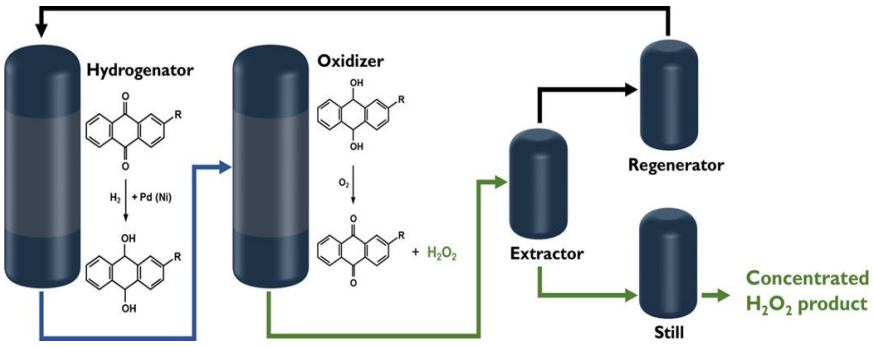

Figure 1.10 Schematic representation of the anthraquinone (AQ) oxidation process. Figure adapted from reference [62].

As shown in Figure 1.10, the AQ process consists of four main steps; 1) AQ (2-ethyl-anthraquinone or 2-amyl anthraquinone) is hydrogenated in to the corresponding anthraquinol or anthrahydroquinone (AHQ) in an organic solvent with Pd or Ni catalyst and H_2 (now Ni is rarely used because trace Ni will be not good for home products); 2) The AHQ is further oxidized to AQ in air or oxygen-enriched gas, and generates H_2O_2 at the same time; 3) The

obtained H_2O_2 is extracted from the working solution, and the AQ is recycled; 4) the crude H_2O_2 is further purified and concentrated to different concentrations (*e.g.*, 30%, 35%, 50%, 60% and 70%) for commercial applications. Although the AQ process has a high yield of H_2O_2 and is safe enough for large scale operation, the required high energy input for these multistep reactions as well as large amount of produced waste gas, solid and water cannot be ignored. Therefore, further improvements or new methods deserve to explore.

1.2.2.2 Photocatalytic H_2O_2 production

As an emerging technology, converting H_2O and O_2 into H_2O_2 via photocatalytic reaction under solar illumination has sparked a research boom in recent years.[46, 59, 63] Compared with the AQ process, the photocatalytic method is more attractive, not only because of the simple reaction process, but also it provides a more sustainable and greener pathway. As shown in Figure 1.11, the process is very similar to photocatalytic H_2 evolution. After excitation by the incident light, the generated electrons and holes separate and transfer to the surface-active sites of the photocatalyst. Meanwhile, the recombination of electrons and holes will also happen during this process. The difference is the reduction part, instead of reducing H^+ to H_2, in this step, the O_2 is reduced to H_2O_2 via an indirect two-step single-electron reduction (Eq. 1.15-1.16) or a direct one-step two-electron reduction route (Eq. 1.17). In addition, the required potential for O_2 reduction to $O_2^{\bullet-}$ and H_2O_2 is -0.33 V (*vs.* NHE) and +0.68 V (*vs.* NHE), respectively, while the reduction potential for H_2 evolution is 0 V (*vs.* NHE). Besides, the Gibbs free energy change (ΔG°) for photocatalytic H_2O_2 production from H_2O and O_2 is 117 kJ mol^{-1}, which is much less than that for photocatalytic H_2 production from H_2O (237 kJ mol^{-1}). Therefore, despite the similar mechanism, the actual reaction requirements for these two photocatalytic processes could be still quite different.

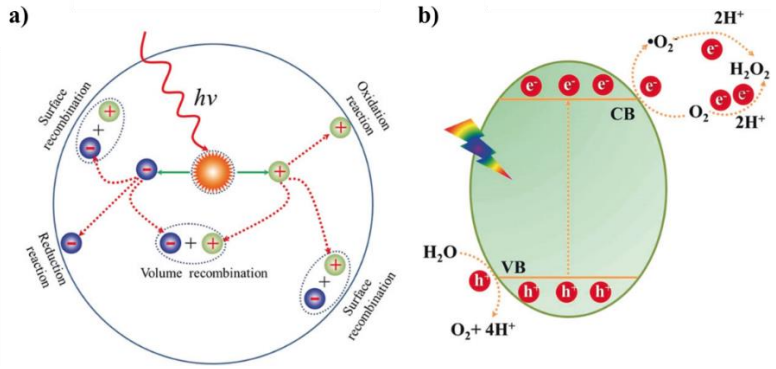

Figure 1.11 (a) Photoexcitation and charge migration pathway in a photocatalyst. (b) Schematic representation of the photocatalytic H_2O_2 production. Figure adapted from reference [46].

$$O_2 + e^- \rightarrow O_2^{\bullet -}\ (E\,^\circ = -0.33\ V\ \textit{vs.}\ NHE,\ pH = 0) \quad (1.15)$$

$$O_2^{\bullet -} + 2H^+ + e^- \rightarrow H_2O_2\ (E\,^\circ = +1.01\ V\ \textit{vs.}\ NHE,\ pH = 0) \quad (1.16)$$

$$O_2 + 2H^+ + 2e^- \rightarrow H_2O_2\ (E\,^\circ = +0.68\ V\ \textit{vs.}\ NHE,\ pH = 0) \quad (1.17)$$

$$1/2O_2 + H_2O \rightarrow H_2O_2\ (\Delta G^\circ = 117\ kJ\ mol^{-1}) \quad (1.18)$$

$$2H_2O + 2h^+ \rightarrow H_2O_2 + 2H^+\ (E\,^\circ = +1.78\ V\ \textit{vs.}\ NHE) \quad (1.19)$$

$$H_2O + h^+ \rightarrow \cdot OH + 2H^+\ (E\,^\circ = +2.73\ V\ \textit{vs.}\ NHE) \quad (1.20)$$

$$\cdot OH + \cdot OH \rightarrow H_2O_2 \quad (1.21)$$

1.3 Organic photocatalysts for solar energy conversion

1.3.1 Organic materials for photocatalytic H_2 production

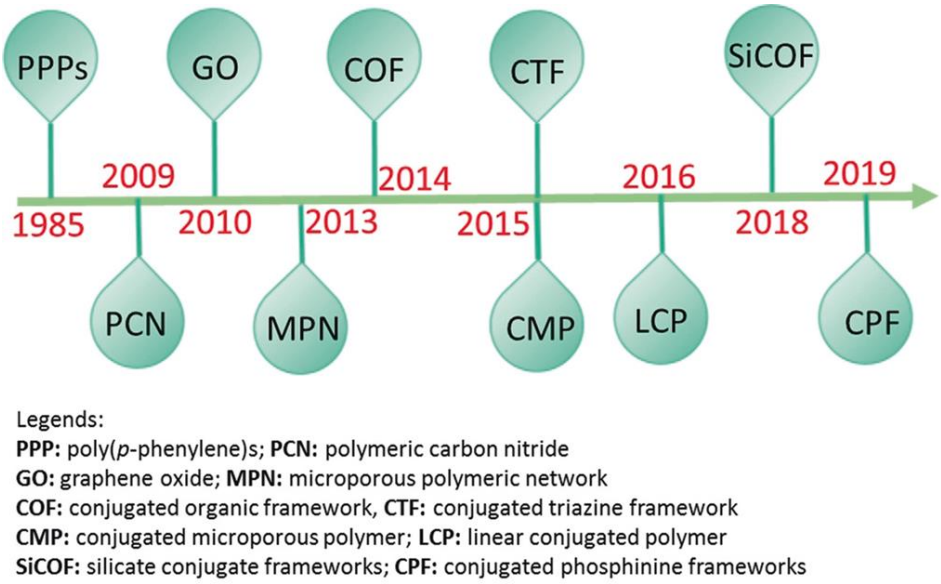

Figure 1.12 Historical development of selected organic photocatalysts for hydrogen evolution reaction. Figure adapted from reference [26].

Although inorganic photocatalysts dominated the field of photocatalytic hydrogen evolution, organic materials also show advantages due to the flexible tunability of properties and comparable performance. The first example of photocatalytic H_2 evolution using organic photocatalyst (linear poly(*p*-phenylene)s) was reported by Yanagida and co-workers in 1985.[64] However, after that the organic photocatalysts did not attract too much attention because of poor activity and conversion efficiency. Until 2009, the emergence of graphitic carbon nitride ($g\text{-}C_3N_4$)[65] as a robust metal-free organic photocatalyst for solar water splitting inspired research enthusiasm around the world, and in following year, numerous efforts have been made

to further improve its activity.[66-70] There are two typical structures of g-C_3N_4, triazine structure (Figure 1.13a) and heptazine structure (Figure 1.13b), and they can be synthesized with different cheap raw materials via various simple methods (Figure 1.13c), which also a tremendous advantage for its widespread application. To date, the best carbon nitride-based material was synthesized by simple postcalcination of polymeric carbon nitride in eutectic salts of NaCl/KCl in Wang's group.[71] After modulating the polymerization process and optimizing the structure, it achieved the highest external quantum efficiency (EQE, incident photon to hydrogen conversion yield) of 60% at 420 nm for solar hydrogen production from "sea water", indicating great improvement compared with the initial g-C_3N_4 photocatalyst in 2009 (EQE < 1%).

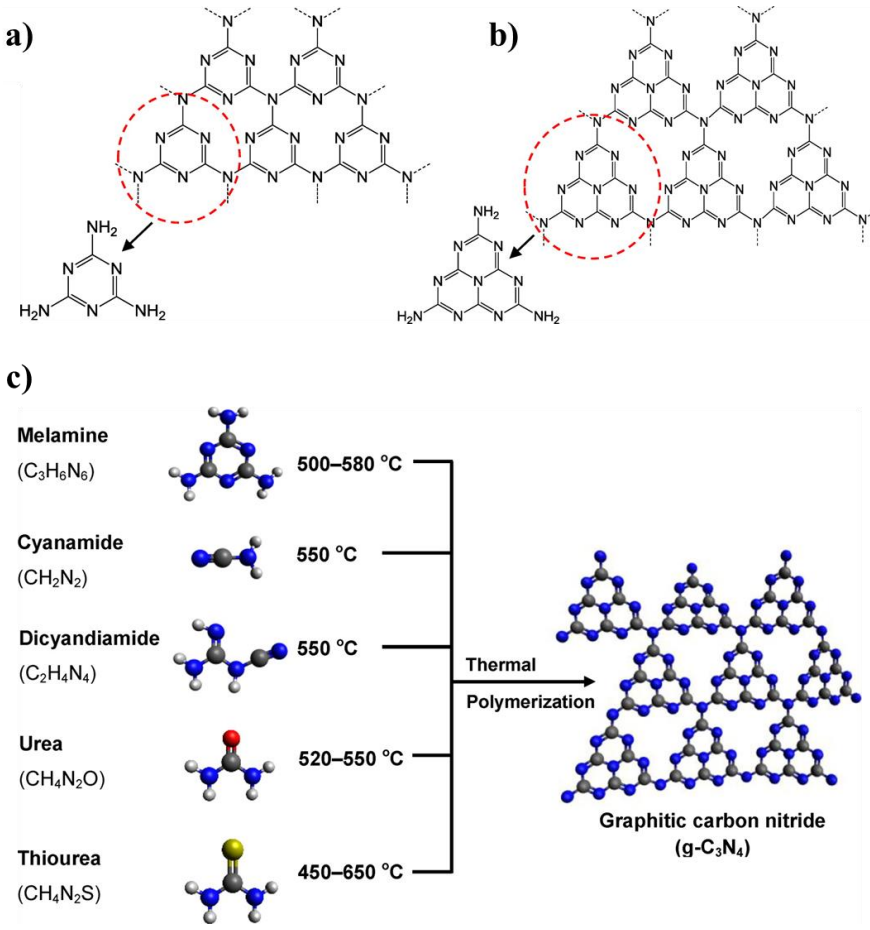

Figure 1.13 (a) Triazine and (b) tri-s-triazine (heptazine) structures of g-C_3N_4. (c) Schematic illustration of the synthesis process of g-C_3N_4 by thermal polymerization of different precursors. The black, blue, white, red, and yellow balls denote C, N, H, O, and S atoms, respectively. Figure adapted from reference [66].

In addition to g-C_3N_4 and its derivatives, series of new kinds of organic photocatalysts have also been developed and reported, such as linear polymers,[72-74] conjugated microporous polymers (CMPs),[35, 37, 75] covalent triazine-based frameworks (CTFs),[76-78] covalent organic frameworks (COFs),[40, 41, 79] and their typical structures are displayed in Figure 1.14.

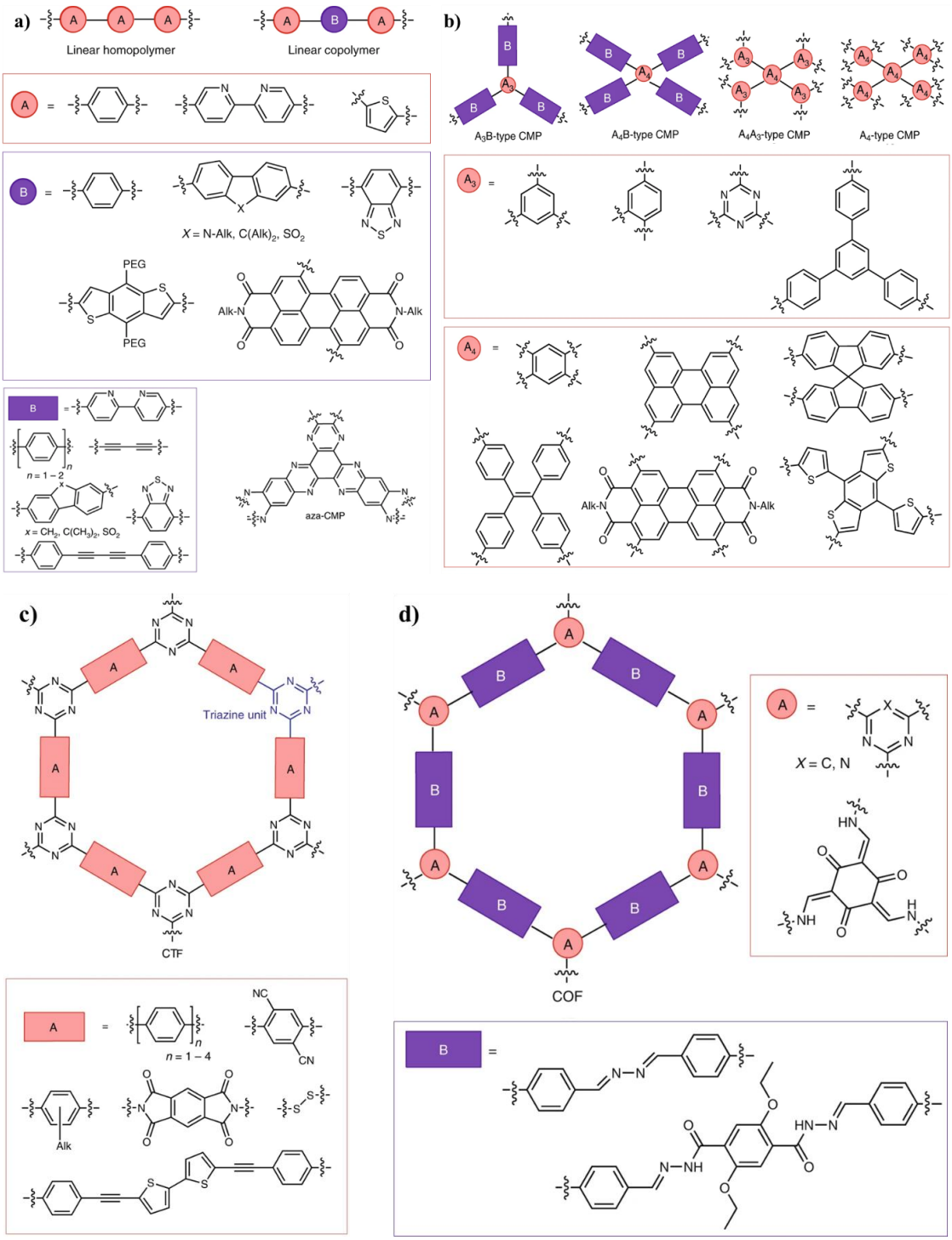

Figure 1.14 Nominal structures of organic photocatalysts: (a) linear homopolymer and copolymer; (b) CMP; (c) CTF; (d) COF. Figure adapted from reference [25].

The representative linear polymer photocatalyst of poly(dibenzo[*b*,*d*]thiophene sulfone) (P10) was reported by our group in 2018.[72] It had an EQE of 11.6% at 420 nm in the presence of a sacrificial electron donor, which was the highest EQE reported for any hydrogen-evolving polymer photocatalyst outside carbon nitrides. After that, with the assistance of robotic experimentation and high-throughput computation, we rapidly discovered other polymer photocatalysts with much better H_2 evolution performance under solar simulator irradiation. The EQE of the best sample of dibenzo[*b*,*d*]thiophene sulfone-dibenzo[*b*,*d*]thiophene co-polymer (P64) reached 20.7% at 420 nm, which was nearly as twice that of P10.

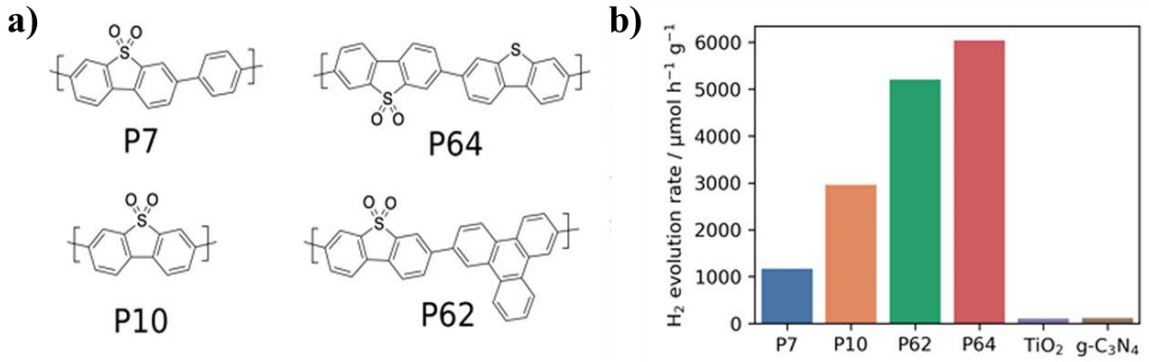

Figure 1.15 (a) Structures and (b) H_2 evolution performance of representative linear polymer photocatalysts. Each measurement was performed in water/methanol/triethylamine mixture with 25 mg of catalyst under solar simulator irradiation. Except those with platinized TiO_2 and platinized carbon nitride were performed with 25 mg in water/triethanolamine (10 vol%) mixture under solar simulator irradiation, because they were inactive in water/methanol/triethylamine mixture. Figure adapted from reference [36].

CMPs are a class of amorphous porous materials with pore sizes of less than 2 nm. due to the unique electronic properties, adjustable structures and high rigidness, these new π-conjugated frameworks have been widely investigated for photocatalytic H_2 evolution,[35, 37, 75, 80-82] since their first discovery in 2007.[83] As shown in Figure 1.16, the dibenzo[*b*,*d*]thiophene sulfone-based CMP (S-CMP3) is a representative in this kind of materials.[37] The hydrogen evolution rate (HER) of S-CMP3 was 3106.0 μmol g^{-1} h^{-1}, which is more than three times higher than the linear nonporous analogue (P35) of 826.1 μmol g^{-1} h^{-1}, and the EQE of S-CMP3 was up to 13.2% at 420 nm, which was higher than the previously reported EQE for P10, although not exceeded P64. However, it should be noted that porosity is beneficial for photocatalytic H_2 evolution, but it does not mean that porous materials are definite better than non-porous materials. Even

in the same study, linear polymers P3 and P7 exhibited much higher HER performance than the corresponding CMPs (F-CMP2 and S-CMP2). To date, the highest EQE of 29.3% at 420 nm for organic polymer photocatalysts was obtained from a donor-π-acceptor (D-π-A) CMP (PyBS-3).[84] It was prepared via statistical copolymerization strategy, and the feed molar ratio of pyrene unit (donor) to dibenzothiophene-S,S-dioxide unit (acceptor) was 25:75 for PyBS-3.

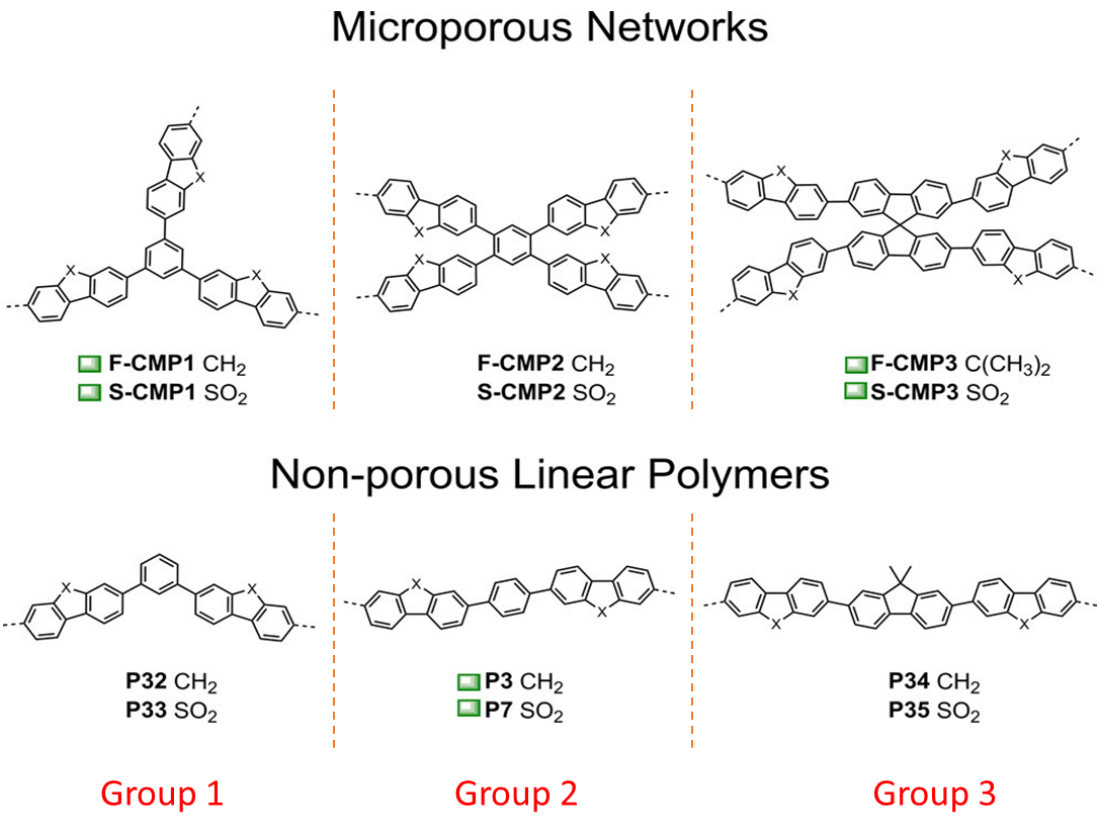

Figure 1.16 Structures of the microporous (up) and corresponding non-porous polymers (down). For each group, the photocatalyst showing higher performance under visible light is marked with a green square. Figure adapted from reference [37].

CTFs can be regarded as a subclass of CMPs. The typical characteristic of CTFs is the triazine unit in the porous structure, and they are normally predicted to show greater driving force for water oxidation.[85] The most common methods for synthesising CTFs are the trifluoromethanesulfonic acid-catalyzed trimerization of aromatic nitriles[86] and high-temperature ionothermal synthesis,[87] which are both attractive for the preparation of metal-free photocatalysts. However, these methods are restricted because of limited monomers and harsh reaction conditions. Using Pd(0)-catalyzed Suzuki-Miyaura coupling reaction, as shown in Figure 1.17, large series of CTFs could been synthesised under moderate conditions for photocatalytic H_2 production.[76, 86] Among them, CTF-15 (2,5-linked benzonitrile, marked red

box) showed the highest HER performance of 2946 μmol g^{-1} h^{-1} for sacrificial water splitting, and a high EQE of 15.9% was determined at 420 nm, which outperformed most other CTF photocatalysts, such as CTF-HUST-A1-^{t}BuOK (7.4% at 420 nm),[78] CTF-1-100W (6% at 420 nm)[77], however, it is still less than the state-of-the-art D-A_1-A_2 CTF with an EQE of 22.8% at 420 nm.[88]

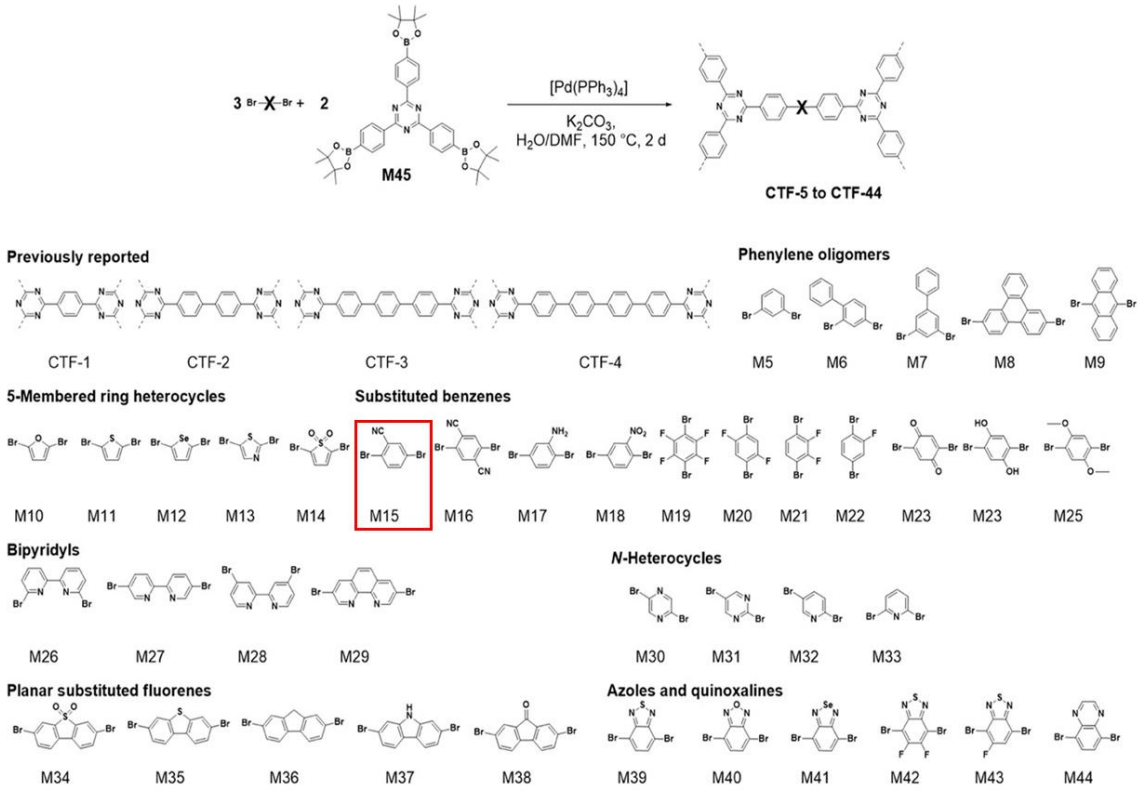

Figure 1.17 Synthesis of the CTF photocatalysts via Pd(0)-catalyzed Suzuki-Miyaura coupling reaction. Figure adapted from reference [76].

Unlike amorphous CMPs and CTFs, COFs are a class of crystalline porous polymers with highly ordered structures, besides, they are also metal-free polymers.[89-91] COFs are very attractive for photocatalytic applications due to their excellent structural regularity, permanent porosity, robust framework, and outstanding activity. The sulfone-containing COF (FS-COF, Figure 1.18) has been reorganized as a representative photocatalyst for solar H_2 evolution.[41] The HER performance of FS-COF was 10.1 mmol g^{-1} h^{-1}, and after dye sensitization, the HER could be further improved to 16.3 mmol g^{-1} h^{-1}. The EQE of 3.2% was determined at 420 nm for FS-COF, which is a leading value among COFs-based photocatalysts, although less than representative CMPs or CTFs mentioned above. The high photocatalytic performance was ascribed to crystallinity, strong visible light absorption, and hydrophilic mesopores of FS-COF.

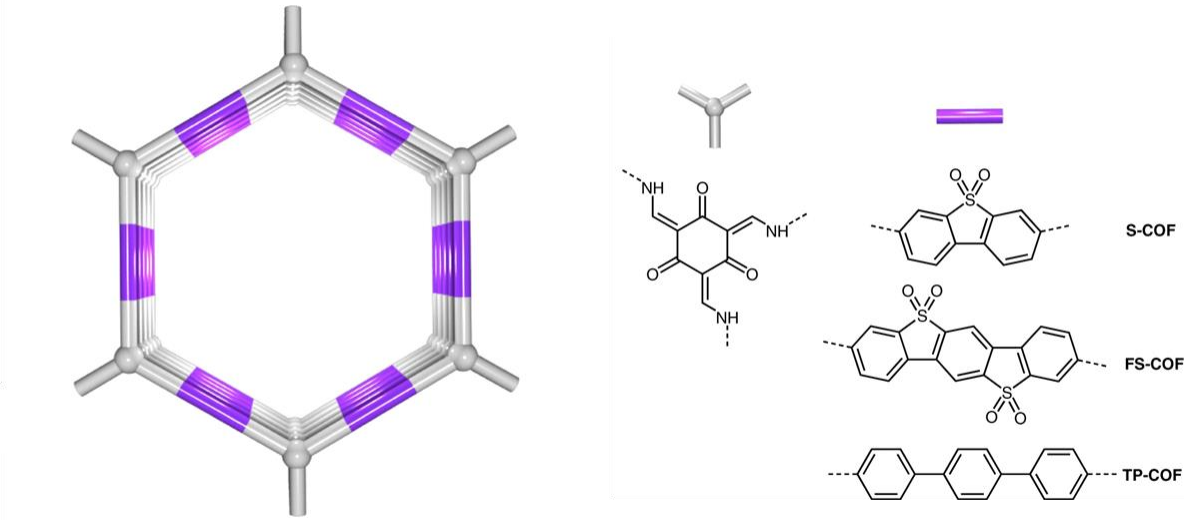

Figure 1.18 Chemical structures of S-COF, FS-COF and TP-COF. Figure adapted from reference [41].

1.3.2 Organic materials for photocatalytic H_2O_2 production

Photocatalytic H_2O_2 production is a relatively new research area compared with photocatalytic H_2 production. To date, the main photocatalysts (Figure 1.19) developed can be classified as Titanium dioxide (TiO_2)-based materials,[46, 92, 93] metal organic frameworks (MOFs)-based materials[94-96] and g‐ C_3N_4-based materials[97-99].

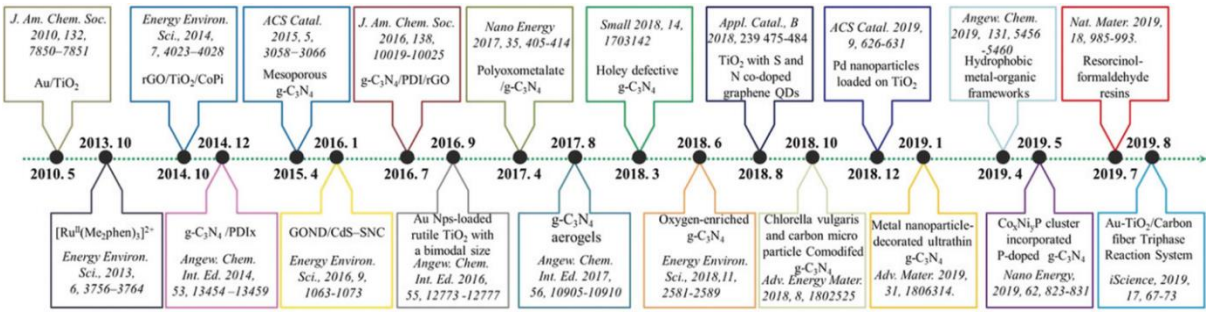

Figure 1.19 Representative photocatalysts in recent years for photocatalytic H_2O_2 production. Figure adapted from reference [46].

g-C_3N_4 is a promising photocatalyst candidate for the production of H_2O_2, because it has suitable conduction band position (-1.3 V *vs.* NHE) for the oxygen reduction in water, and its bandgap (~2.7 V) is tuneable for more efficient visible light absoption.[98] Teruhisa *et al.* reported the single Sb atom doped carbon nitride photocatalyst (Sb-SAPC) for H_2O_2 production in a pure water and oxygen mixture under visible light irradiation (Figure 1.20a).[99] Due to the

collaborative effect between the single Sb atom active sites for selective two-electron ORR and the support shell of highly concentrated holes at the neighbouring N atoms, Sb-SAPC can produce super high amount (470.5 μmol) of H_2O_2 in 8 hours. It also achieved a solar-to-chemical conversion (SCC) efficiency of 0.61%, and the EQE at 420 nm was 17.6%, which is the highest value among organic photocatalysts for H_2O_2 production so far. A Similar novel metal doping strategy was also adopted by Kim's group, they simultaneously introduced two redox cocatalysts, atomically dispersed cobalt for improving oxidation activity and anthraquinone for improving reduction selectivity, onto C_3N_4 nanosheets (Figure 1.20b), and achieved more efficient photocatalytic H_2O_2 activity than the bulk C_3N_4 and ultrathin C_3N_4.[97]

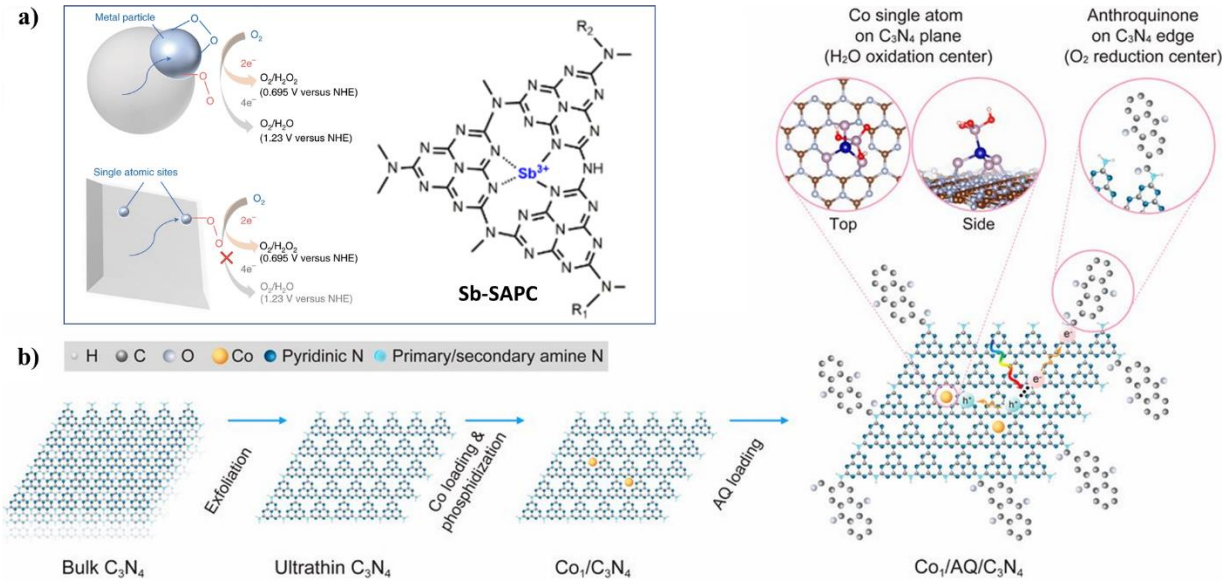

Figure 1.20 (a) Oxygen reduction reaction on a metal particle (top) and an isolated atomic site (bottom) and structure of Sb-SAPC photocatalyst (single Sb atoms dispersed on carbon nitride). Figure adapted from reference [99]. (b) Spatial separation of Co single atom (as oxidation center) and anthraquinone (AQ, as reduction center) cocatalysts by anchoring them in the center (*i.e.*, pyridinic N) and on the edge (*i.e.*, primary/secondary amine N) of 2D ultrathin C_3N_4, respectively. Figure adapted from reference [97].

CTFs also have been applied for photocatalytic H_2O_2 production. For example, Xu *et al.* incorporated acetylene (-C≡C-) or diacetylene (-C≡C-C≡C-) moieties into CTFs (Figure 1.21),[56] and found that H_2O_2 production increased remarkably under visible light illumination, which was attributed to the promotion of charge separation in conjugated structures, and the formation of suitable intermediates for H_2O_2 formation. In addition, they also proposed a new two-electron oxidation pathway (Eq. 1.19) toward H_2O_2 production for CTF-EDDBN

(acetylene incorporated-CTF) and CTF-BDDBN (diacetylene incorporated-CTF). Instead of four-electron water oxidation to form O_2, the H_2O was oxidized to H_2O_2 via the two-electron route. Similar situation could be a found in the metal-free carbon nanodot-carbon nitride (C_3N_4) nanocomposite for visible water splitting.[100] However, in this case, the produced H_2O_2 via two-electron water oxidation from C_3N_4 was further decomposed to O_2 by carbon nanodot.

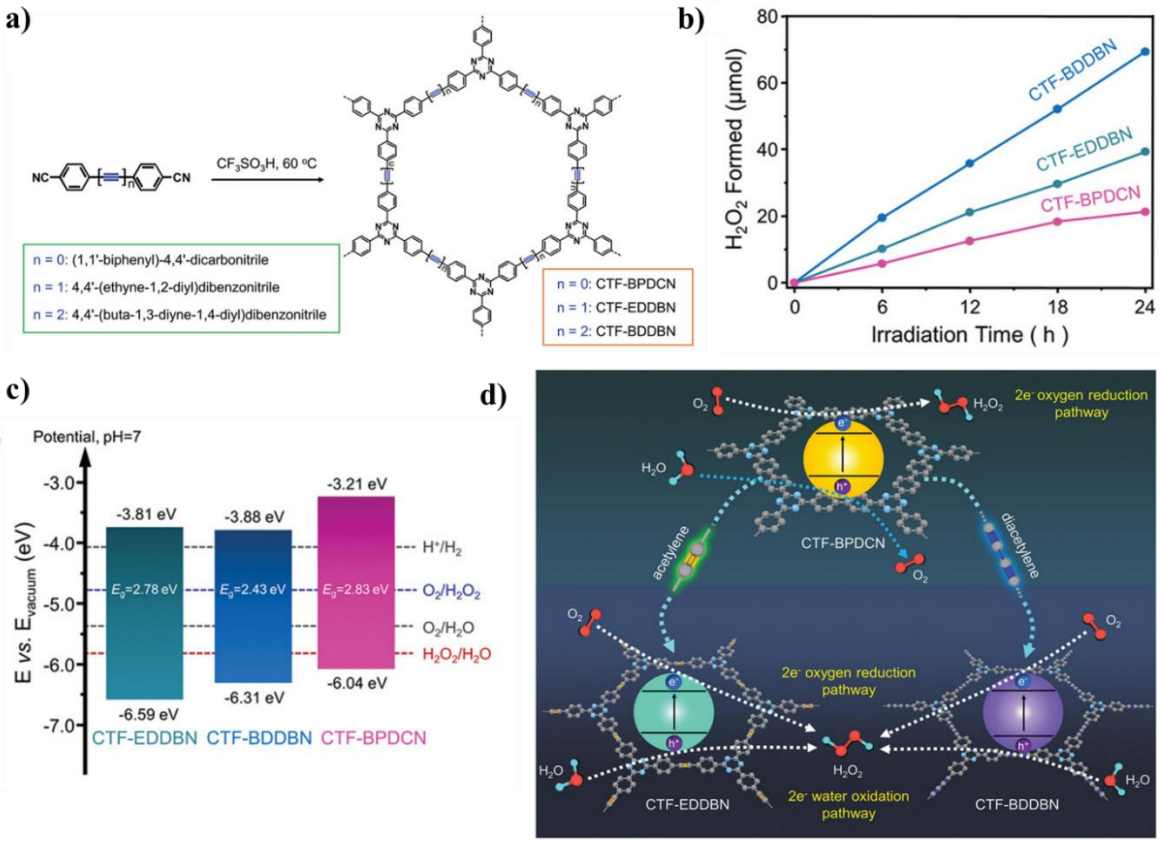

Figure 1.21 Scheme of the synthesis (a), typical time course of H_2O_2 production in pure water saturated with O_2 under visible light irradiation (b), the electronic band structures (c), and schematic illustration of different reaction pathways toward H_2O_2 production of CTF - BPDCN, CTF - EDDBN, and CTF - BDDBN. Figure adapted from reference [56].

Few COF materials have been reported for photocatalytic H_2O_2 production. The first COF photocatalysts in this area was proposed by Arne Thomas and co-workers in 2020.[101] It was found that enediamine units can react with molecular O_2 to generate superoxide radicals and Wurster salts in erythrocytes, which can further react to form hydrogen peroxide (Figure 1.22a and 1.22b).[102] Inspired by the strong reducing agent of the diarylamine (donor) moiety, they designed two-dimensional COFs based on a (diarylamino)benzene linker (Figure 1.22c) that forms a Kagome (kgm) lattice and showed strong visible light absorption. The H_2O_2 production

rate for TAPD-$(Me)_2$ COF and TAPD-$(OMe)_2$ COF was 97 μmol h^{-1} g^{-1} and 91 μmol h^{-1} g^{-1}, respectively. Given that the photoreaction was carried out in a sacrificial solution with 10 vol. % ethanol as the electron donor reagent, it is not desirable for practical H_2O_2 production, which would increase the difficulty for further separation.

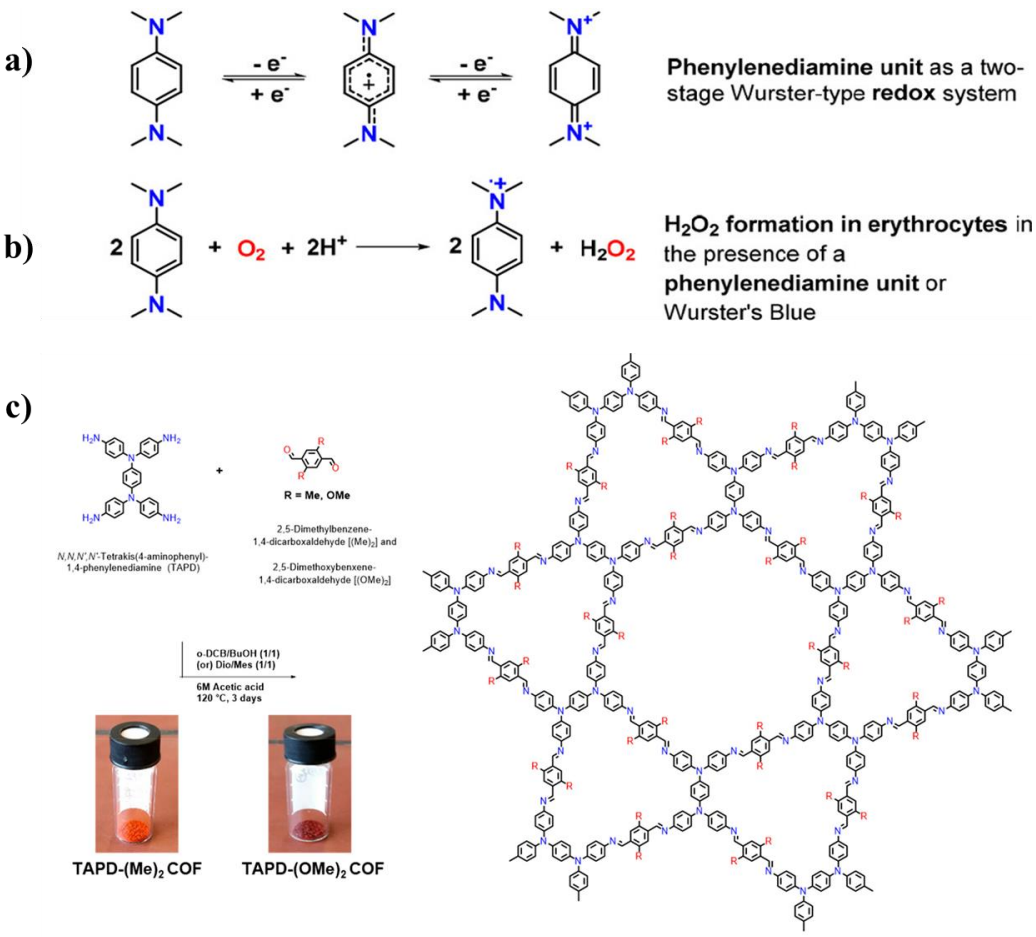

Figure 1.22 (a) *N*,*N*,*N*′,*N*′-Tetramethyl-*p*-phenylenediamine (TMPD) as a two-stage Wurster-type redox system. (b) Generation of hydrogen peroxide in erythrocytes in the presence of TMPD. (c) Synthesis of TAPD-$(Me)_2$ and TAPD-$(OMe)_2$ COFs forming a dual pore Kagome lattice. Figure adapted from reference [101].

Different from commonly used metal-free organic polymers (*e.g.*, CTFs, COFs) for photocatalysis, Shiraishi *et al*. reported that another kind of inexpensive metal-free polymer, resorcinol-formaldehyde (RF) resins, act as efficient semiconductor photocatalysts to produce H_2O_2 (Figure 1.23).[103] The best sample of RF523 in this study achieved a SCC efficiency of around 0.5% under simulated sunlight irradiation in pure water, which was higher than any other reported powder catalysts used in artificial photosynthesis at that time. The excellent photocatalytic activity could be attributed to the unique π-stacking of the donor-accepter

(benzenoid-quinoid) couples and the low bandgap (~2.0 eV) for broad-wavelength light absorption up to 700 nm. In their follow-up work, they optimized the synthesis methods,[104] the RF523 prepared by the acid-catalysed high-temperature hydrothermal method exhibited enhanced photocatalytic activity and higher SCC efficiency of 0.7%, which is the highest efficiency so far for photocatalytic H_2O_2 production.

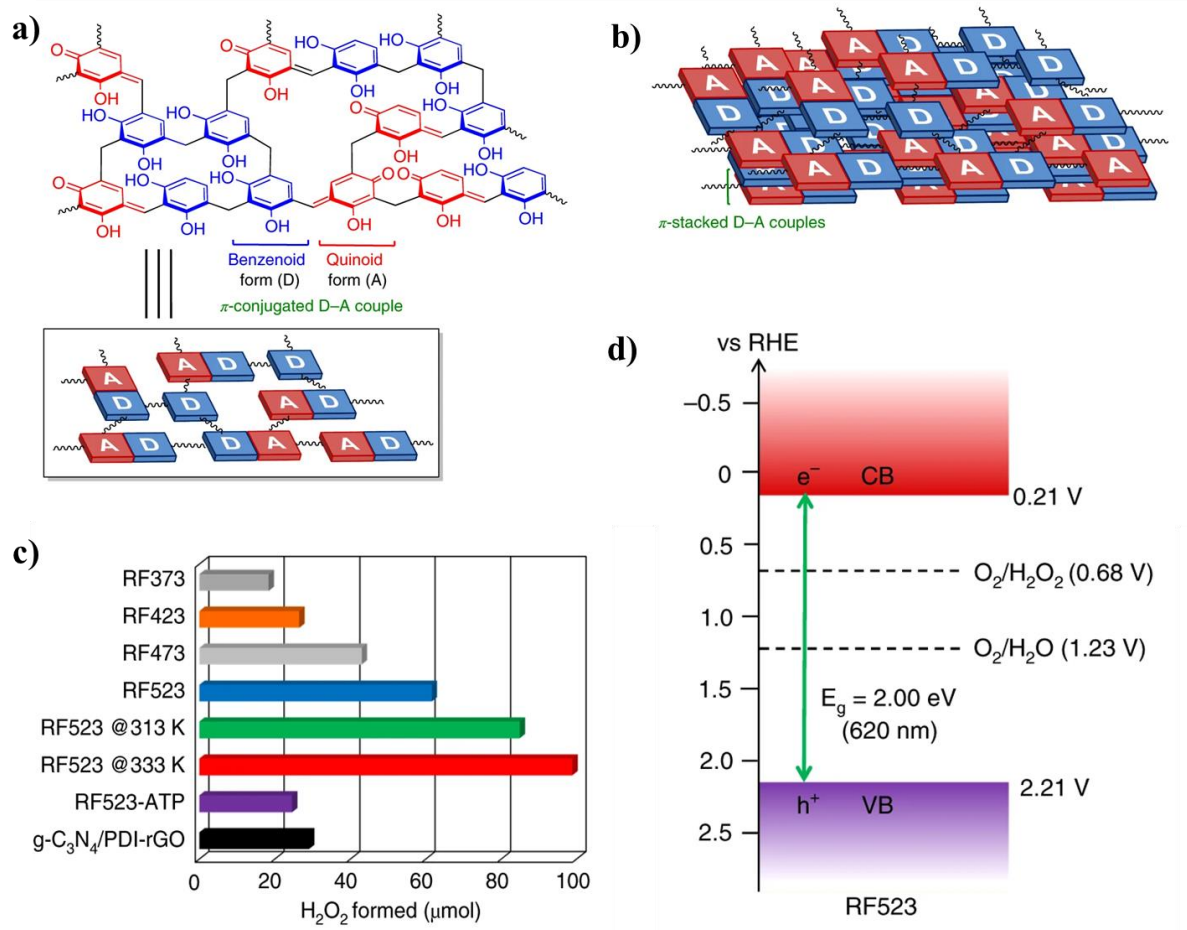

Figure 1.23 Fundamental structure (a) and π-conjugated and π-stacked D-A structure (b) of RF resins. (c) Amounts of H_2O_2 generated by 24 h of photoirradiation on the respective catalysts at 298 K. (d) Electronic band structure of RF523. Figure adapted from reference [103].

1.4 Experimental techniques

Basic characterisations of materials in this thesis were carried out with standard techniques, including scanning electron microscopy (SEM), Fourier-transform infrared spectroscopy (FT-IR), powder X-ray diffraction (PXRD), thermogravimetric analysis (TGA), UV-vis absorption spectroscopy, photoluminescence (PL) spectroscopy, time-correlated single photon counting (TCSPC), static light scattering (SLS), inductively coupled plasma optical emission spectrometer (ICP-OES), X-ray photoelectron spectroscopy (XPS), solid-state nuclear magnetic resonance (NMR), Raman, particle size measurement, surface area measurement, elemental analysis. Because they are commonly used in the field, they will not be introduced in great detail.

1.4.1 High throughput screening workflow

High-throughput screening (HTS) is a well-established and powerful technology for accelerated research. Its first advent could be traced back to the mid-1990s for compounds screening.[105] Nowadays, due to the advantages of high efficiency and systematization, HTS has been widely applied in various fields, such as bioresearch,[106] drug discovery,[107] organic solar cells,[108] gas separation,[109] electrochemical water splitting,[110] and photoelectrochemical water splitting.[111] In our group, we established a high throughput screening workflow for accelerating exploration of candidate polymer photocatalysts for H_2 evolution from water splitting.[36, 76] Moreover, with the integration of a mobile robotic chemist and high-throughput computation, an automation platform was created, which provided a blueprint and made a big step for building artificial intelligence driven chemistry laboratories in the future.[112, 113] In this thesis, we only applied the part for photocatalytic H_2 evolution performance test.

As shown in Figure 1.24, the synthesised polymers were charged in the reaction vials, and then with the assistance of the Swing instrument, the mixture of water/methanol/triethylamine (1:1:1) could be added automatically and precisely with the auto arm in N_2 atmosphere. After that, the capper moved to the top of the vials and capped them one by one. All vials were subsequently transferred to an ultrasonic bath for 10 min before placed on the roller. After illuminating for a certain time under AM1.5 solar simulated light, the reaction vials were all put in the sample rack (99 positions) connected with the GC instrument. The produced H_2 was measured by the GC automatically.

Figure 1.24 Workflow for high-throughput screening: (a) Swing by Chemspeed Technologies; (b) Solar simulator (AM1.5G, Class AAA, IEC/JIS/ASTM, 1440 W xenon, 12 × 12 in., MODEL: 94123A) with rocker/roller device; c) HS-20 GC System.

1.4.2 Microwave-assisted polymer synthesis

Microwave (MW) is a form of electromagnetic radiation with wavelengths ranging from 1 mm to 1 m with corresponding frequencies from 300 to 0.3 GHz, it locates between infrared (IR) and radio waves, as shown in Figure 1.25a.

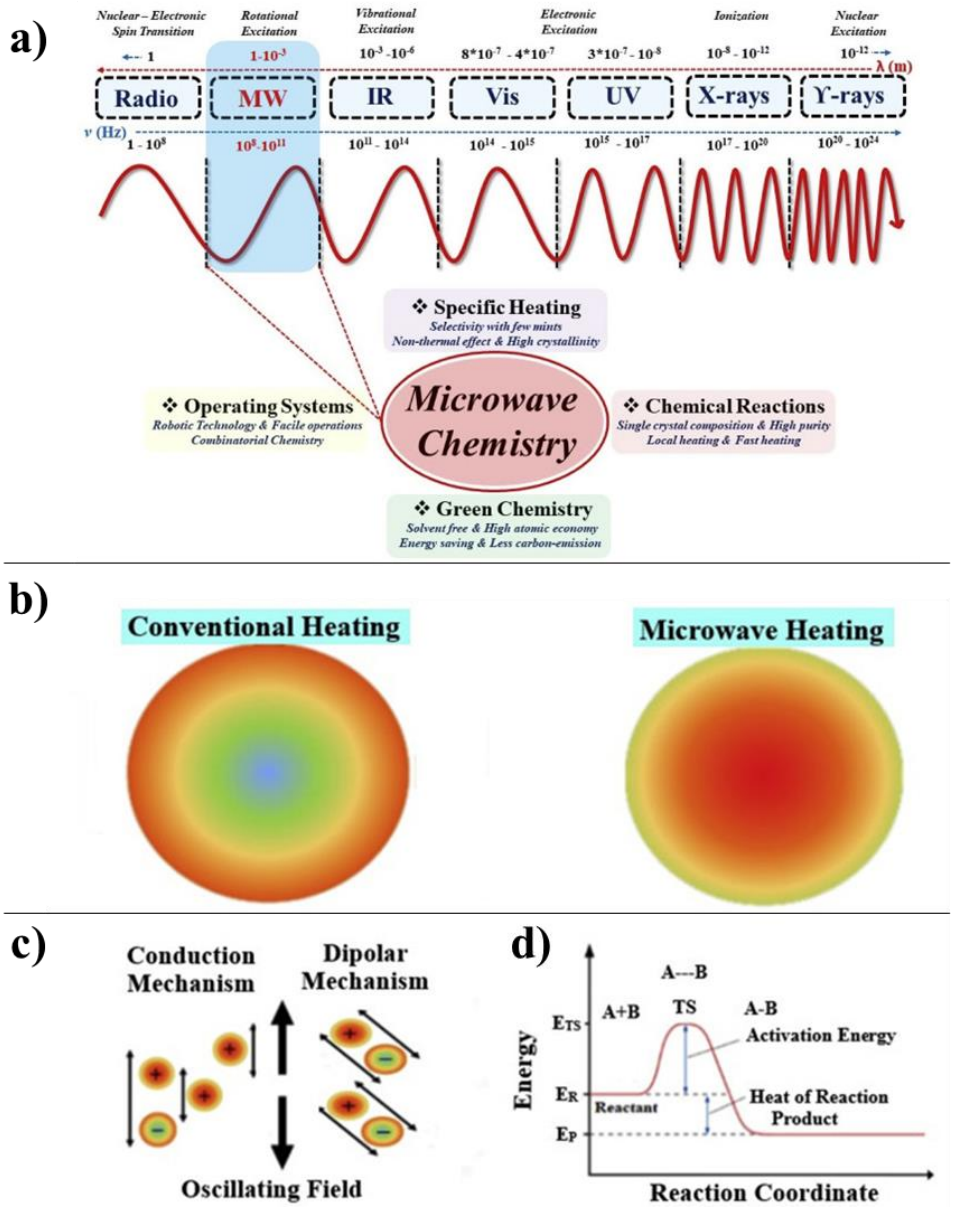

Figure 1.25 (a) The representation of multiple advantages of microwave chemistry with an appropriate combination of operating systems, green chemistry approach, specific heating, and chemical reactions. IR-infrared; MW-microwave; UV-ultraviolet. (b) Temperature profile of reaction mixture after t min as alerted by the treatment in traditional oil bath and microwaves. (c) Representation of oscillating field in conduction and dipolar mechanisms. (d) Activation energy diagram for the chemical reaction under microwave conditions. Figure adapted from reference [114].

MW chemistry is an emerging new technology for green chemistry. The MW method was first reported for rapid organic synthesis in 1986,[115, 116] before that, it was mainly applied for food processing. In comparison to conventional heating method on a hot plate or in an oil/sand bath, MW heating model has advantages such as uniform heating (Figure 1.25b), fast reaction rate, low cost, good product yield and good reproducibility. There are two recognized mechanism of MW heating.[114] In the ionic conduction mechanism, it states that the heat generated from the ion collision in the reaction solution. While in the dipolar polarization mechanism, the thermal energy comes from the energy loss during the alternation of polar units of reactants or solvents, and based on this mechanism, the accessible frequency of 2.45 GHz is used for most commercial microwave systems in order to avoid interference with telecommunication devices.[114, 117] In MW synthetic reactions, the activation energy required for initiating the reaction and heating energy for the final product is provided by MW energy exchange in a short time (Figure 1.25d), which is the main reason for enhanced reaction rate.

In **Chapter 4**, given that the traditional Sonogashira coupling relations normally take 2-3 days, we then applied the Biotage microwave system (Figure 1.26) to rapidly synthesize polymers (2 hours) for photocatalytic H_2O_2 production.

Figure 1.26 Automation for microwave assisted organic synthesis, Biotage Initator$^+$ microwave system.

1.5 Project aims

The core aim of this thesis is to develop more promising organic polymers with high performance for efficient solar energy conversion, including photocatalytic H_2 evolution and H_2O_2 production.

As explained in 1.2, the photocatalytic conversion process mainly consists of three steps: light absorption, separation and migration of photoexited carries, and redox reaction on the active sites. Therefore, to achieve high activity, the polymer photocatalysts should be rationally designed and optimized to make the three main steps more efficient. For example, catalysts with low bandgap are beneficial to absorb more visible light, decreasing the recombination probability of photogenerated electrons and holes and loading cocatalysts[23] can also promote the photocatalytic performance. However, it should be noted that the photocatalytic reaction is a complex process, and based on previous work,[36, 76] normally no single property can dominate the performance. Even though, it is still important to explore the structure-property-performance relationship, which can provide great guiding significance for exploring high-active photocatalysts and avoiding blind attempts. According to the reported organic materials for photocatalytic hydrogen evolution or hydrogen peroxide production, the common features are worthy of consideration: 1) appropriate optical gap and band level (HOMO or LUMO) position; 2) good hydrophilicity and dispersibility; 3) good stability with robust structure. For polymer catalysts synthesized via metal-catalyst polymerization, the residual metals in the final polymers should be paid attention since they could be possible to serve as cocatalyst for photocatalytic reactions.[118, 119]

Due to their unique optical-electrical and mechanical properties, acetylenic conjugated polymers have shown great potential as photocatalysts. For instance, it was found that after incorporation of an acetylene group, the visible light absorption and H_2 production performance of linear conjugated polymer (P7) could be enhanced obviously.[120] Moreover, acetylenic polymers also show excellent activity in overall water splitting,[121] photoelectrochemical water splitting,[122] photocatalytic radical polymerization[123] and photocatalytic oxidative coupling[124]. Based on these studies, it reveals that the C≡C bonds can not only improve the photoelectric property as active sites, but also facilitate gas adsorption, which inspired us to explore more candidate acetylenic polymers for photocatalytic solar energy conversion. However, in our previous studies,[35-37, 76, 86] most polymer photocatalysts were synthesized via Pd(0)-catalysed

Suzuki-Miyaura coupling reactions (*e.g.*, P10 and P64), which would limit the selection of monomers as the acetylene group needs to be introduced into a bromo- or boric acid ester-monomer first. Therefore, we used another typical coupling reaction, Sonogashira coupling, which is the Pd-Cu catalyzed cross-coupling of a terminal alkyne and an aryl or vinyl halide.[125] Because of the diversity of commercial dibromo monomers, we could establish a small library of candidate materials. Moreover, with the assistance of the high throughput workflow as well as theoretical calculations, it is helpful to systematically investigate the relationship between the structure and property. Relevant work will be detailed in **Chapter 2**.

Based on previous work,[36, 37, 41, 74, 126] the dibenzo[*b,d*]thiophene sulfone was proved to be an efficient building block for constructing high-performance organic polymer photocatalysts, which was mainly attributed to its strong electron-withdrawing ability and good hydrophilicity. Combined with the interest in the linker's effect on photoactivity,[40, 86, 127] we designed six new polymers with three different linkers (*e.g.*, alkyl linker (-C-C-), alkenyl linker (-C=C-) and alkyne linker (-C≡C-)) and investigated their photocatalytic H_2 evolution performance. This work will be detailed in **Chapter 3**.

In addition, due to the simple and clean procedure, photocatalytic H_2O_2 production has become an attractive research topic in recent years. It also aroused our great interest, especially for organic materials in this field. We have large number of polymers in the lab, and we can also synthesis more organic photocatalysts with the assistance of high throughput workflow and microwave instrument. However, we are still not very familiar with this area. Therefore, the main target is to rapidly screen out active candidate materials, and them more attention will be paid on the mechanism investigation. More detail will be discussed in **Chapter 4**.

1.6 References

1. Balat, M., Status of Fossil Energy Resources: A Global Perspective. *Energy Sources Part B* **2007,** *2* (1), 31-47.
2. BP, Statistical Review of World Energy 2020. **2020**.
3. Hassan, A.; Ilyas, S. Z.; Jalil, A.; Ullah, Z., Monetization of the environmental damage caused by fossil fuels. *Environ. Sci. Pollut. Res.* **2021,** *28* (17), 21204-21211.
4. Perera, F., Pollution from Fossil-Fuel Combustion is the Leading Environmental Threat to Global Pediatric Health and Equity: Solutions Exist. *Int. J. Env. Res. Public Health* **2018,** *15* (1).
5. Kannan, N.; Vakeesan, D., Solar energy for future world: - A review. *Renew. Sustain. Energy Rev.* **2016,** *62*, 1092-1105.
6. Shahsavari, A.; Akbari, M., Potential of solar energy in developing countries for reducing energy-related emissions. *Renew. Sustain. Energy Rev.* **2018,** *90*, 275-291.
7. TheWorldBank; ESMAP; Solargis, Solar resource maps of world: Global Horizontal Irradiation. **2019**.
8. Gong, J.; Li, C.; Wasielewski, M. R., Advances in solar energy conversion. *Chem. Soc. Rev.* **2019,** *48* (7), 1862-1864.
9. Abdalla, A. M.; Hossain, S.; Nisfindy, O. B.; Azad, A. T.; Dawood, M.; Azad, A. K., Hydrogen production, storage, transportation and key challenges with applications: A review. *Energy Convers. Manage.* **2018,** *165*, 602-627.
10. Ni, M.; Leung, M. K. H.; Sumathy, K.; Leung, D. Y. C., Potential of renewable hydrogen production for energy supply in Hong Kong. *Int. J. Hydrogen Energy* **2006,** *31* (10), 1401-1412.
11. Midilli, A.; Ay, M.; Dincer, I.; Rosen, M. A., On hydrogen and hydrogen energy strategies: I: current status and needs. *Renew. Sustain. Energy Rev.* **2005,** *9* (3), 255-271.
12. Steinberg, M.; Cheng, H. C., Modern and prospective technologies for hydrogen production from fossil fuels. *Int. J. Hydrogen Energy* **1989,** *14* (11), 797-820.
13. Nikolaidis, P.; Poullikkas, A., A comparative overview of hydrogen production processes. *Renew. Sustain. Energy Rev.* **2017,** *67*, 597-611.
14. Gangadharan, P.; Kanchi, K. C.; Lou, H. H., Evaluation of the economic and environmental impact of combining dry reforming with steam reforming of methane. *Chem. Eng. Res. Des.* **2012,** *90* (11), 1956-1968.
15. McKendry, P., Energy production from biomass (part 1): overview of biomass. *Bioresour. Technol.* **2002,** *83* (1), 37-46.
16. Maeda, K.; Domen, K., Photocatalytic Water Splitting: Recent Progress and Future Challenges. *The Journal of Physical Chemistry Letters* **2010,** *1* (18), 2655-2661.
17. Hisatomi, T.; Kubota, J.; Domen, K., Recent advances in semiconductors for photocatalytic and photoelectrochemical water splitting. *Chem. Soc. Rev.* **2014,** *43* (22), 7520-7535.
18. Hisatomi, T.; Minegishi, T.; Domen, K., Kinetic Assessment and Numerical Modeling of Photocatalytic Water Splitting toward Efficient Solar Hydrogen Production. *Bull. Chem. Soc. Jpn.* **2012,** *85* (6), 647-655.
19. Chen, S.; Takata, T.; Domen, K., Particulate photocatalysts for overall water splitting. *Nat. Rev. Mater.* **2017,** *2* (10), 17050.
20. Le, T.-H.; Kim, Y.; Yoon, H., Electrical and Electrochemical Properties of Conducting Polymers. *Polymers* **2017,** *9* (4).
21. Guiglion, P.; Butchosa, C.; Zwijnenburg, M. A., Polymer Photocatalysts for Water Splitting: Insights from Computational Modeling. *Macromol. Chem. Phys.* **2016,** *217* (3), 344-353.

22. Zhao, C.; Chen, Z.; Shi, R.; Yang, X.; Zhang, T., Recent Advances in Conjugated Polymers for Visible-Light-Driven Water Splitting. *Adv. Mater.* **2020,** *32* (28), 1907296.
23. Ran, J.; Zhang, J.; Yu, J.; Jaroniec, M.; Qiao, S. Z., Earth-abundant cocatalysts for semiconductor-based photocatalytic water splitting. *Chem. Soc. Rev.* **2014,** *43* (22), 7787-7812.
24. Wang, Z.; Li, C.; Domen, K., Recent developments in heterogeneous photocatalysts for solar-driven overall water splitting. *Chem. Soc. Rev.* **2019,** *48* (7), 2109-2125.
25. Wang, Y.; Vogel, A.; Sachs, M.; Sprick, R. S.; Wilbraham, L.; Moniz, S. J. A.; Godin, R.; Zwijnenburg, M. A.; Durrant, J. R.; Cooper, A. I.; Tang, J., Current understanding and challenges of solar-driven hydrogen generation using polymeric photocatalysts. *Nat. Energy* **2019,** *4* (9), 746-760.
26. Rahman, M.; Tian, H.; Edvinsson, T., Revisiting the Limiting Factors for Overall Water-Splitting on Organic Photocatalysts. *Angew. Chem. Int. Ed.* **2020,** *59*, 2-18.
27. Le Bahers, T.; Rérat, M.; Sautet, P., Semiconductors Used in Photovoltaic and Photocatalytic Devices: Assessing Fundamental Properties from DFT. *J. Phys. Chem. C* **2014,** *118* (12), 5997-6008.
28. Kubacka, A.; Fernández-García, M.; Colón, G., Advanced Nanoarchitectures for Solar Photocatalytic Applications. *Chem. Rev.* **2012,** *112* (3), 1555-1614.
29. Kong, D.; Zheng, Y.; Kobielusz, M.; Wang, Y.; Bai, Z.; Macyk, W.; Wang, X.; Tang, J., Recent advances in visible light-driven water oxidation and reduction in suspension systems. *Mater. Today* **2018,** *21* (8), 897-924.
30. Fukuzumi, S.; Hong, D., Homogeneous versus Heterogeneous Catalysts in Water Oxidation. *Eur. J. Inorg. Chem.* **2014,** *2014* (4), 645-659.
31. Yang, L.; Zhou, H.; Fan, T.; Zhang, D., Semiconductor photocatalysts for water oxidation: current status and challenges. *Phys. Chem. Chem. Phys.* **2014,** *16* (15), 6810-6826.
32. Kamdar, J. M.; Grotjahn, D. B., An Overview of Significant Achievements in Ruthenium-Based Molecular Water Oxidation Catalysis. *Molecules* **2019,** *24* (3).
33. Wang, Y.; Suzuki, H.; Xie, J.; Tomita, O.; Martin, D. J.; Higashi, M.; Kong, D.; Abe, R.; Tang, J., Mimicking Natural Photosynthesis: Solar to Renewable H2 Fuel Synthesis by Z-Scheme Water Splitting Systems. *Chem. Rev.* **2018,** *118* (10), 5201-5241.
34. Lu, Q.; Yu, Y.; Ma, Q.; Chen, B.; Zhang, H., 2D Transition-Metal-Dichalcogenide-Nanosheet-Based Composites for Photocatalytic and Electrocatalytic Hydrogen Evolution Reactions. *Adv. Mater.* **2016,** *28* (10), 1917-1933.
35. Sprick, R. S.; Jiang, J.-X.; Bonillo, B.; Ren, S.; Ratvijitvech, T.; Guiglion, P.; Zwijnenburg, M. A.; Adams, D. J.; Cooper, A. I., Tunable Organic Photocatalysts for Visible-Light-Driven Hydrogen Evolution. *J. Am. Chem. Soc.* **2015,** *137* (9), 3265-3270.
36. Bai, Y.; Wilbraham, L.; Slater, B. J.; Zwijnenburg, M. A.; Sprick, R. S.; Cooper, A. I., Accelerated Discovery of Organic Polymer Photocatalysts for Hydrogen Evolution from Water through the Integration of Experiment and Theory. *J. Am. Chem. Soc.* **2019,** *141* (22), 9063-9071.
37. Sprick, R. S.; Bai, Y.; Guilbert, A. A. Y.; Zbiri, M.; Aitchison, C. M.; Wilbraham, L.; Yan, Y.; Woods, D. J.; Zwijnenburg, M. A.; Cooper, A. I., Photocatalytic Hydrogen Evolution from Water Using Fluorene and Dibenzothiophene Sulfone-Conjugated Microporous and Linear Polymers. *Chem. Mater.* **2019,** *31* (2), 305-313.
38. Wang, X.; Chen, B.; Dong, W.; Zhang, X.; Li, Z.; Xiang, Y.; Chen, H., Hydrophilicity-Controlled Conjugated Microporous Polymers for Enhanced Visible-Light-Driven Photocatalytic H2 Evolution. *Macromol. Rapid Commun.* **2019,** *40* (6), 1800494.
39. Yu, F.; Wang, Z.; Zhang, S.; Ye, H.; Kong, K.; Gong, X.; Hua, J.; Tian, H., Molecular Engineering of Donor–Acceptor Conjugated Polymer/g-C3N4 Heterostructures for Significantly Enhanced Hydrogen Evolution Under Visible-Light Irradiation. *Adv. Funct. Mater.* **2018,** *28* (47), 1804512.

40. Pachfule, P.; Acharjya, A.; Roeser, J.; Langenhahn, T.; Schwarze, M.; Schomäcker, R.; Thomas, A.; Schmidt, J., Diacetylene Functionalized Covalent Organic Framework (COF) for Photocatalytic Hydrogen Generation. *J. Am. Chem. Soc.* **2018,** *140* (4), 1423-1427.
41. Wang, X.; Chen, L.; Chong, S. Y.; Little, M. A.; Wu, Y.; Zhu, W.-H.; Clowes, R.; Yan, Y.; Zwijnenburg, M. A.; Sprick, R. S.; Cooper, A. I., Sulfone-containing covalent organic frameworks for photocatalytic hydrogen evolution from water. *Nat. Chem.* **2018,** *10* (12), 1180-1189.
42. Zhang, X.; Peng, B.; Zhang, S.; Peng, T., Robust Wide Visible-Light-Responsive Photoactivity for H2 Production over a Polymer/Polymer Heterojunction Photocatalyst: The Significance of Sacrificial Reagent. *ACS Sustainable Chem. Eng.* **2015,** *3* (7), 1501-1509.
43. Cao, W.-N.; Wang, F.; Wang, H.-Y.; Chen, B.; Feng, K.; Tung, C.-H.; Wu, L.-Z., Photocatalytic hydrogen production from a simple water-soluble [FeFe]-hydrogenase model system. *Chem. Commun.* **2012,** *48* (65), 8081-8083.
44. Wang, M.; Shen, S.; Li, L.; Tang, Z.; Yang, J., Effects of sacrificial reagents on photocatalytic hydrogen evolution over different photocatalysts. *J. Mater. Sci.* **2017,** *52* (9), 5155-5164.
45. Matsuoka, S.; Fujii, H.; Yamada, T.; Pac, C.; Ishida, A.; Takamuku, S.; Kusaba, M.; Nakashima, N.; Yanagida, S., Photocatalysis of oligo(p-phenylenes): photoreductive production of hydrogen and ethanol in aqueous triethylamine. *J. Phys. Chem.* **1991,** *95* (15), 5802-5808.
46. Hou, H.; Zeng, X.; Zhang, X., Production of Hydrogen Peroxide by Photocatalytic Processes. *Angew. Chem. Int. Ed.* **2020,** *59* (40), 17356-17376.
47. Lindström, B.; Pettersson, L. J., A Brief History of Catalysis. *CATTECH* **2003,** *7* (4), 130-138.
48. Mamaye, M.; Kiflie, Z.; Feleke, S.; Yimam, A., Evaluation of Soda Delignification and Single-Stage Hydrogen Peroxide Bleaching for the Ethiopian Sugarcane Bagasse for Paper Production. *Sugar Tech* **2020,** *22* (4), 706-717.
49. Henniges, U.; Krämer, M.; Gille, L.; Brückle, I., Calcium Phytate as a Pretreatment for Iron-contaminated Papers Prior to Hydrogen Peroxide Bleaching. *Stud. Conserv.* **2021,** *66* (4), 244-251.
50. Walker, K. L.; Dornan, L. M.; Zare, R. N.; Waymouth, R. M.; Muldoon, M. J., Mechanism of Catalytic Oxidation of Styrenes with Hydrogen Peroxide in the Presence of Cationic Palladium(II) Complexes. *J. Am. Chem. Soc.* **2017,** *139* (36), 12495-12503.
51. Muhammad, Y.; Shoukat, A.; Rahman, A. U.; Rashid, H. U.; Ahmad, W., Oxidative desulfurization of dibenzothiophene over Fe promoted Co–Mo/Al2O3 and Ni–Mo/Al2O3 catalysts using hydrogen peroxide and formic acid as oxidants. *Chin. J. Chem. Eng.* **2018,** *26* (3), 593-600.
52. Khaliq, A. D.; Chafidz, A.; Maddun, F. R.; Herimawan, H. R.; Yusuf, G. M.; Rahmillah, F. I., The use of hydrogen peroxide and sky stabilizer agent in bleaching process of textile fabrics. *AIP Conf. Proc.* **2019,** *2138* (1), 050011.
53. Ambaye, T. G.; Hagos, K., Photocatalytic and biological oxidation treatment of real textile wastewater. *Nanotechnol. Environ. Eng.* **2020,** *5* (3), 28.
54. Yamada, Y.; Yoneda, M.; Fukuzumi, S., A Robust One-Compartment Fuel Cell with a Polynuclear Cyanide Complex as a Cathode for Utilizing H2O2 as a Sustainable Fuel at Ambient Conditions. *Chem. Eur. J.* **2013,** *19* (35), 11733-11741.
55. Mousavi Shaegh, S. A.; Nguyen, N.-T.; Mousavi Ehteshami, S. M.; Chan, S. H., A membraneless hydrogen peroxide fuel cell using Prussian Blue as cathode material. *Energy & Environmental Science* **2012,** *5* (8), 8225-8228.
56. Chen, L.; Wang, L.; Wan, Y.; Zhang, Y.; Qi, Z.; Wu, X.; Xu, H., Acetylene and Diacetylene Functionalized Covalent Triazine Frameworks as Metal-Free Photocatalysts for

Hydrogen Peroxide Production: A New Two-Electron Water Oxidation Pathway. *Adv. Mater.* **2020,** *32* (2), 1904433.
57. Zheng, Y.; Yu, Z.; Ou, H.; Asiri, A. M.; Chen, Y.; Wang, X., Black Phosphorus and Polymeric Carbon Nitride Heterostructure for Photoinduced Molecular Oxygen Activation. *Adv. Funct. Mater.* **2018,** *28* (10), 1705407.
58. Kiran Pulidindi, H. P., Hydrogen Peroxide Market Size Worth Over $6.2 billion by 2026. **2020**.
59. Liu, J.; Zou, Y.; Jin, B.; Zhang, K.; Park, J. H., Hydrogen Peroxide Production from Solar Water Oxidation. *ACS Energy Lett.* **2019,** *4* (12), 3018-3027.
60. Campos-Martin, J. M.; Blanco-Brieva, G.; Fierro, J. L. G., Hydrogen Peroxide Synthesis: An Outlook beyond the Anthraquinone Process. *Angew. Chem. Int. Ed.* **2006,** *45* (42), 6962-6984.
61. Yi, Y.; Wang, L.; Li, G.; Guo, H., A review on research progress in the direct synthesis of hydrogen peroxide from hydrogen and oxygen: noble-metal catalytic method, fuel-cell method and plasma method. *Catal. Sci. Technol.* **2016,** *6* (6), 1593-1610.
62. Yang, S.; Verdaguer-Casadevall, A.; Arnarson, L.; Silvioli, L.; Čolić, V.; Frydendal, R.; Rossmeisl, J.; Chorkendorff, I.; Stephens, I. E. L., Toward the Decentralized Electrochemical Production of H2O2: A Focus on the Catalysis. *ACS Catal.* **2018,** *8* (5), 4064-4081.
63. Zeng, X.; Liu, Y.; Hu, X.; Zhang, X., Photoredox catalysis over semiconductors for light-driven hydrogen peroxide production. *Green Chem.* **2021,** *23* (4), 1466-1494.
64. Yanagida, S.; Kabumoto, A.; Mizumoto, K.; Pac, C.; Yoshino, K., Poly(p-phenylene)-catalysed photoreduction of water to hydrogen. *J. Chem. Soc., Chem. Commun.* **1985,** *8* ( ), 474-475.
65. Wang, X.; Maeda, K.; Thomas, A.; Takanabe, K.; Xin, G.; Carlsson, J. M.; Domen, K.; Antonietti, M., A metal-free polymeric photocatalyst for hydrogen production from water under visible light. *Nat. Mater.* **2009,** *8* (1), 76-80.
66. Ong, W.-J.; Tan, L.-L.; Ng, Y. H.; Yong, S.-T.; Chai, S.-P., Graphitic Carbon Nitride (g-C3N4)-Based Photocatalysts for Artificial Photosynthesis and Environmental Remediation: Are We a Step Closer To Achieving Sustainability? *Chem. Rev.* **2016,** *116* (12), 7159-7329.
67. Mishra, A.; Mehta, A.; Basu, S.; Shetti, N. P.; Reddy, K. R.; Aminabhavi, T. M., Graphitic carbon nitride (g–C3N4)–based metal-free photocatalysts for water splitting: A review. *Carbon* **2019,** *149*, 693-721.
68. Jourshabani, M.; Lee, B.-K.; Shariatinia, Z., From Traditional Strategies to Z-scheme Configuration in Graphitic Carbon Nitride Photocatalysts: Recent Progress and Future Challenges. *Appl. Catal. B-Environ.* **2020,** *276*, 119157.
69. Liang, Q.; Shao, B.; Tong, S.; Liu, Z.; Tang, L.; Liu, Y.; Cheng, M.; He, Q.; Wu, T.; Pan, Y.; Huang, J.; Peng, Z., Recent advances of melamine self-assembled graphitic carbon nitride-based materials: Design, synthesis and application in energy and environment. *Chem. Eng. J.* **2021,** *405*, 126951.
70. Malik, R.; Tomer, V. K., State-of-the-art review of morphological advancements in graphitic carbon nitride (g-CN) for sustainable hydrogen production. *Renew. Sustain. Energy Rev.* **2021,** *135*, 110235.
71. Zhang, G.; Lin, L.; Li, G.; Zhang, Y.; Savateev, A.; Zafeiratos, S.; Wang, X.; Antonietti, M., Ionothermal Synthesis of Triazine–Heptazine-Based Copolymers with Apparent Quantum Yields of 60 % at 420 nm for Solar Hydrogen Production from "Sea Water". *Angew. Chem. Int. Ed.* **2018,** *57* (30), 9372-9376.
72. Sachs, M.; Sprick, R. S.; Pearce, D.; Hillman, S. A. J.; Monti, A.; Guilbert, A. A. Y.; Brownbill, N. J.; Dimitrov, S.; Shi, X.; Blanc, F.; Zwijnenburg, M. A.; Nelson, J.;

Durrant, J. R.; Cooper, A. I., Understanding structure-activity relationships in linear polymer photocatalysts for hydrogen evolution. *Nat. Commun.* **2018,** *9* (1), 4968.
73. Sprick, R. S.; Bonillo, B.; Clowes, R.; Guiglion, P.; Brownbill, N. J.; Slater, B. J.; Blanc, F.; Zwijnenburg, M. A.; Adams, D. J.; Cooper, A. I., Visible-Light-Driven Hydrogen Evolution Using Planarized Conjugated Polymer Photocatalysts. *Angew. Chem. Int. Ed.* **2016,** *55* (5), 1792-1796.
74. Woods, D. J.; Hillman, S. A. J.; Pearce, D.; Wilbraham, L.; Flagg, L. Q.; Duffy, W.; McCulloch, I.; Durrant, J. R.; Guilbert, A. A. Y.; Zwijnenburg, M. A.; Sprick, R. S.; Nelson, J.; Cooper, A. I., Side-chain tuning in conjugated polymer photocatalysts for improved hydrogen production from water. *Energy & Environmental Science* **2020,** *13* (6), 1843-1855.
75. Wang, L.; Wan, Y.; Ding, Y.; Wu, S.; Zhang, Y.; Zhang, X.; Zhang, G.; Xiong, Y.; Wu, X.; Yang, J.; Xu, H., Conjugated Microporous Polymer Nanosheets for Overall Water Splitting Using Visible Light. *Adv. Mater.* **2017,** *29* (38).
76. Meier, C. B.; Clowes, R.; Berardo, E.; Jelfs, K. E.; Zwijnenburg, M. A.; Sprick, R. S.; Cooper, A. I., Structurally Diverse Covalent Triazine-Based Framework Materials for Photocatalytic Hydrogen Evolution from Water. *Chem. Mater.* **2019,** *31* (21), 8830-8838.
77. Xie, J.; Shevlin, S. A.; Ruan, Q.; Moniz, S. J. A.; Liu, Y.; Liu, X.; Li, Y.; Lau, C. C.; Guo, Z. X.; Tang, J., Efficient visible light-driven water oxidation and proton reduction by an ordered covalent triazine-based framework. *Energy & Environmental Science* **2018,** *11* (6), 1617-1624.
78. Zhang, S.; Cheng, G.; Guo, L.; Wang, N.; Tan, B.; Jin, S., Strong-Base-Assisted Synthesis of a Crystalline Covalent Triazine Framework with High Hydrophilicity via Benzylamine Monomer for Photocatalytic Water Splitting. *Angew. Chem. Int. Ed.* **2020,** *59* (15), 6007-6014.
79. Vyas, V. S.; Haase, F.; Stegbauer, L.; Savasci, G.; Podjaski, F.; Ochsenfeld, C.; Lotsch, B. V., A tunable azine covalent organic framework platform for visible light-induced hydrogen generation. *Nat. Commun.* **2015,** *6* (1), 8508.
80. Rahman, M. Z.; Kibria, M. G.; Mullins, C. B., Metal-free photocatalysts for hydrogen evolution. *Chem. Soc. Rev.* **2020,** *49* (6), 1887-1931.
81. Xu, Y.; Jin, S.; Xu, H.; Nagai, A.; Jiang, D., Conjugated microporous polymers: design, synthesis and application. *Chem. Soc. Rev.* **2013,** *42* (20), 8012-8031.
82. Zhang, G.; Lan, Z.-A.; Wang, X., Conjugated Polymers: Catalysts for Photocatalytic Hydrogen Evolution. *Angew. Chem. Int. Ed.* **2016,** *55* (51), 15712-15727.
83. Jiang, J.-X.; Su, F.; Trewin, A.; Wood, C. D.; Campbell, N. L.; Niu, H.; Dickinson, C.; Ganin, A. Y.; Rosseinsky, M. J.; Khimyak, Y. Z.; Cooper, A. I., Conjugated Microporous Poly(aryleneethynylene) Networks. *Angew. Chem. Int. Ed.* **2007,** *46* (45), 8574-8578.
84. Shu, C.; Han, C.; Yang, X.; Zhang, C.; Chen, Y.; Ren, S.; Wang, F.; Huang, F.; Jiang, J.-X., Boosting the Photocatalytic Hydrogen Evolution Activity for D–π–A Conjugated Microporous Polymers by Statistical Copolymerization. *Adv. Mater.* **2021,** *33* (26), 2008498.
85. Kong, D.; Han, X.; Xie, J.; Ruan, Q.; Windle, C. D.; Gadipelli, S.; Shen, K.; Bai, Z.; Guo, Z.; Tang, J., Tunable Covalent Triazine-Based Frameworks (CTF-0) for Visible-Light-Driven Hydrogen and Oxygen Generation from Water Splitting. *ACS Catal.* **2019,** *9* (9), 7697-7707.
86. Meier, C. B.; Sprick, R. S.; Monti, A.; Guiglion, P.; Lee, J.-S. M.; Zwijnenburg, M. A.; Cooper, A. I., Structure-property relationships for covalent triazine-based frameworks: The effect of spacer length on photocatalytic hydrogen evolution from water. *Polymer* **2017,** *126*, 283-290.
87. Kuhn, P.; Antonietti, M.; Thomas, A., Porous, Covalent Triazine-Based Frameworks Prepared by Ionothermal Synthesis. *Angew. Chem. Int. Ed.* **2008,** *47* (18), 3450-3453.

88. Guo, L.; Niu, Y.; Razzaque, S.; Tan, B.; Jin, S., Design of D–A1–A2 Covalent Triazine Frameworks via Copolymerization for Photocatalytic Hydrogen Evolution. *ACS Catal.* **2019,** *9* (10), 9438-9445.
89. Banerjee, T.; Gottschling, K.; Savasci, G.; Ochsenfeld, C.; Lotsch, B. V., H2 Evolution with Covalent Organic Framework Photocatalysts. *ACS Energy Lett.* **2018,** *3* (2), 400-409.
90. Geng, K.; He, T.; Liu, R.; Tan, K. T.; Li, Z.; Tao, S.; Gong, Y.; Jiang, Q.; Jiang, D., Covalent Organic Frameworks: Design, Synthesis, and Functions. *Chem. Rev.* **2020**.
91. Wang, H.; Wang, H.; Wang, Z.; Tang, L.; Zeng, G.; Xu, P.; Chen, M.; Xiong, T.; Zhou, C.; Li, X.; Huang, D.; Zhu, Y.; Wang, Z.; Tang, J., Covalent organic framework photocatalysts: structures and applications. *Chem. Soc. Rev.* **2020,** *49* (12), 4135-4165.
92. Baran, T.; Wojtyła, S.; Minguzzi, A.; Rondinini, S.; Vertova, A., Achieving efficient H2O2 production by a visible-light absorbing, highly stable photosensitized TiO2. *Appl. Catal. B-Environ.* **2019,** *244*, 303-312.
93. Song, H.; Wei, L.; Chen, L.; Zhang, H.; Su, J., Photocatalytic Production of Hydrogen Peroxide over Modified Semiconductor Materials: A Minireview. *Top. Catal.* **2020,** *63* (9), 895-912.
94. Chen, X.; Kondo, Y.; Kuwahara, Y.; Mori, K.; Louis, C.; Yamashita, H., Metal–organic framework-based nanomaterials for photocatalytic hydrogen peroxide production. *Phys. Chem. Chem. Phys.* **2020,** *22* (26), 14404-14414.
95. Isaka, Y.; Kawase, Y.; Kuwahara, Y.; Mori, K.; Yamashita, H., Two-Phase System Utilizing Hydrophobic Metal–Organic Frameworks (MOFs) for Photocatalytic Synthesis of Hydrogen Peroxide. *Angew. Chem. Int. Ed.* **2019,** *58* (16), 5402-5406.
96. Kholdeeva, O.; Maksimchuk, N., Metal-Organic Frameworks in Oxidation Catalysis with Hydrogen Peroxide. *Catalysts* **2021,** *11* (2).
97. Chu, C.; Zhu, Q.; Pan, Z.; Gupta, S.; Huang, D.; Du, Y.; Weon, S.; Wu, Y.; Muhich, C.; Stavitski, E.; Domen, K.; Kim, J.-H., Spatially separating redox centers on 2D carbon nitride with cobalt single atom for photocatalytic H2O2 production. *Proc. Natl. Acad. Sci.* **2020,** *117* (12), 6376.
98. Haider, Z.; Cho, H.-i.; Moon, G.-h.; Kim, H.-i., Minireview: Selective production of hydrogen peroxide as a clean oxidant over structurally tailored carbon nitride photocatalysts. *Catal. Today* **2019,** *335*, 55-64.
99. Teng, Z.; Zhang, Q.; Yang, H.; Kato, K.; Yang, W.; Lu, Y.-R.; Liu, S.; Wang, C.; Yamakata, A.; Su, C.; Liu, B.; Ohno, T., Atomically dispersed antimony on carbon nitride for the artificial photosynthesis of hydrogen peroxide. *Nat. Catal.* **2021,** *4* (5), 374-384.
100. Liu, J.; Liu, Y.; Liu, N.; Han, Y.; Zhang, X.; Huang, H.; Lifshitz, Y.; Lee, S.-T.; Zhong, J.; Kang, Z., Metal-free efficient photocatalyst for stable visible water splitting via a two-electron pathway. *Science* **2015,** *347* (6225), 970.
101. Krishnaraj, C.; Sekhar Jena, H.; Bourda, L.; Laemont, A.; Pachfule, P.; Roeser, J.; Chandran, C. V.; Borgmans, S.; Rogge, S. M. J.; Leus, K.; Stevens, C. V.; Martens, J. A.; Van Speybroeck, V.; Breynaert, E.; Thomas, A.; Van Der Voort, P., Strongly Reducing (Diarylamino)benzene-Based Covalent Organic Framework for Metal-Free Visible Light Photocatalytic H2O2 Generation. *J. Am. Chem. Soc.* **2020,** *142* (47), 20107–20116.
102. Munday, R., Generation of superoxide radical, hydrogen peroxide and hydroxyl radical during the autoxidation of N,N,N′,N′-tetramethyl-p-phenylenediamine. *Chemico-Biological Interactions* **1988,** *65* (2), 133-143.
103. Shiraishi, Y.; Takii, T.; Hagi, T.; Mori, S.; Kofuji, Y.; Kitagawa, Y.; Tanaka, S.; Ichikawa, S.; Hirai, T., Resorcinol–formaldehyde resins as metal-free semiconductor photocatalysts for solar-to-hydrogen peroxide energy conversion. *Nat. Mater.* **2019,** *18* (9), 985-993.

104. Shiraishi, Y.; Hagi, T.; Matsumoto, M.; Tanaka, S.; Ichikawa, S.; Hirai, T., Solar-to-hydrogen peroxide energy conversion on resorcinol–formaldehyde resin photocatalysts prepared by acid-catalysed polycondensation. *Commun. Chem.* **2020,** *3* (1), 169.
105. Hertzberg, R. P.; Pope, A. J., High-throughput screening: new technology for the 21st century. *Curr. Opin. Chem. Biol.* **2000,** *4* (4), 445-451.
106. Zeng, W.; Guo, L.; Xu, S.; Chen, J.; Zhou, J., High-Throughput Screening Technology in Industrial Biotechnology. *Trends Biotechnol.* **2020,** *38* (8), 888-906.
107. Macarron, R.; Banks, M. N.; Bojanic, D.; Burns, D. J.; Cirovic, D. A.; Garyantes, T.; Green, D. V. S.; Hertzberg, R. P.; Janzen, W. P.; Paslay, J. W.; Schopfer, U.; Sittampalam, G. S., Impact of high-throughput screening in biomedical research. *Nat Rev. Drug. Discov.* **2011,** *10* (3), 188-195.
108. Rodr ́guez-Mart ́nez, X.; Pascual-San-Jos é, E.; Campoy-Quiles, M., Accelerating organic solar cell material's discovery: high-throughput screening and big data. *Energy & Environmental Science* **2021,** *14* (6), 3301-3322.
109. Rogacka, J.; Seremak, A.; Luna-Triguero, A.; Formalik, F.; Matito-Martos, I.; Firlej, L.; Calero, S.; Kuchta, B., High-throughput screening of metal – Organic frameworks for CO2 and CH4 separation in the presence of water. *Chem. Eng. J.* **2021,** *403*, 126392.
110. Xiang, C.; Suram, S. K.; Haber, J. A.; Guevarra, D. W.; Soedarmadji, E.; Jin, J.; Gregoire, J. M., High-Throughput Bubble Screening Method for Combinatorial Discovery of Electrocatalysts for Water Splitting. *ACS Comb. Sci.* **2014,** *16* (2), 47-52.
111. Katz, J. E.; Gingrich, T. R.; Santori, E. A.; Lewis, N. S., Combinatorial synthesis and high-throughput photopotential and photocurrent screening of mixed-metal oxides for photoelectrochemical water splitting. *Energy & Environmental Science* **2009,** *2* (1), 103-112.
112. Burger, B.; Maffettone, P. M.; Gusev, V. V.; Aitchison, C. M.; Bai, Y.; Wang, X.; Li, X.; Alston, B. M.; Li, B.; Clowes, R.; Rankin, N.; Harris, B.; Sprick, R. S.; Cooper, A. I., A mobile robotic chemist. *Nature* **2020,** *583* (7815), 237-241.
113. Cooper, A. I., Boxing Clever: Robotic Screening of Catalysts Using an Adapted Gas Chromatograph. *Matter* **2020,** *3* (3), 611-612.
114. Kumar, A.; Kuang, Y.; Liang, Z.; Sun, X., Microwave chemistry, recent advancements, and eco-friendly microwave-assisted synthesis of nanoarchitectures and their applications: a review. *Materials Today Nano* **2020,** *11*, 100076.
115. Gedye, R.; Smith, F.; Westaway, K.; Ali, H.; Baldisera, L.; Laberge, L.; Rousell, J., The use of microwave ovens for rapid organic synthesis. *Tetrahedron Lett.* **1986,** *27* (3), 279-282.
116. Giguere, R. J.; Bray, T. L.; Duncan, S. M.; Majetich, G., Application of commercial microwave ovens to organic synthesis. *Tetrahedron Lett.* **1986,** *27* (41), 4945-4948.
117. Wiesbrock, F.; Hoogenboom, R.; Schubert, U. S., Microwave-Assisted Polymer Synthesis: State-of-the-Art and Future Perspectives. *Macromol. Rapid Commun.* **2004,** *25* (20), 1739-1764.
118. Kosco, J.; Sachs, M.; Godin, R.; Kirkus, M.; Francas, L.; Bidwell, M.; Qureshi, M.; Anjum, D.; Durrant, J. R.; McCulloch, I., The Effect of Residual Palladium Catalyst Contamination on the Photocatalytic Hydrogen Evolution Activity of Conjugated Polymers. *Adv. Energy Mater.* **2018,** *8* (34), 1802181.
119. Li, L.; Cai, Z.; Wu, Q.; Lo, W.-Y.; Zhang, N.; Chen, L. X.; Yu, L., Rational Design of Porous Conjugated Polymers and Roles of Residual Palladium for Photocatalytic Hydrogen Production. *J. Am. Chem. Soc.* **2016,** *138* (24), 7681-7686.
120. Zhang, X.-H.; Wang, X.-P.; Xiao, J.; Wang, S.-Y.; Huang, D.-K.; Ding, X.; Xiang, Y.-G.; Chen, H., Synthesis of 1,4-diethynylbenzene-based conjugated polymer photocatalysts and their enhanced visible/near-infrared-light-driven hydrogen production activity. *J. Catal.* **2017,** *350*, 64-71.

121. Wang, L.; Wan, Y.; Ding, Y.; Wu, S.; Zhang, Y.; Zhang, X.; Zhang, G.; Xiong, Y.; Wu, X.; Yang, J.; Xu, H., Conjugated Microporous Polymer Nanosheets for Overall Water Splitting Using Visible Light. *Adv. Mater.* **2017,** *29* (38), 1702428.
122. Sun, H. J.; Oner, I. H.; Wang, T.; Zhang, T.; Selyshchev, O.; Neumann, C.; Fu, Y. B.; Liao, Z. Q.; Xu, S. Q.; Hou, Y.; Turchanin, A.; Zahn, D. R. T.; Zschech, E.; Weidinger, I. M.; Zhang, J.; Feng, X. L., Molecular Engineering of Conjugated Acetylenic Polymers for Efficient Cocatalyst-free Photoelectrochemical Water Reduction. *Angew. Chem. Int. Ed.* **2019,** *58* (30), 10368-10374.
123. Li, X.; Zhang, Y. C.; Zhao, Y.; Zhao, H. P.; Zhang, B.; Cai, T., Xanthene Dye-Functionalized Conjugated Porous Polymers as Robust and Reusable Photocatalysts for Controlled Radical Polymerization. *Macromolecules* **2020,** *53* (5), 1550-1556.
124. Lan, X.; Liu, X.; Zhang, Y.; Li, Q.; Wang, J.; Zhang, Q.; Bai, G., Unveiling Charge Dynamics in Acetylene-Bridged Donor−π–Acceptor Covalent Triazine Framework for Enhanced Photoredox Catalysis. *ACS Catal.* **2021**, 7429-7441.
125. Sonogashira, K., Development of Pd–Cu catalyzed cross-coupling of terminal acetylenes with sp2-carbon halides. *J. Organomet. Chem.* **2002,** *653* (1), 46-49.
126. Lan, Z.-A.; Zhang, G.; Chen, X.; Zhang, Y.; Zhang, K. A. I.; Wang, X., Reducing the Exciton Binding Energy of Donor–Acceptor-Based Conjugated Polymers to Promote Charge-Induced Reactions. *Angew. Chem. Int. Ed.* **2019,** *58* (30), 10236-10240.
127. Mo, C.; Yang, M.; Sun, F.; Jian, J.; Zhong, L.; Fang, Z.; Feng, J.; Yu, D., Alkene-Linked Covalent Organic Frameworks Boosting Photocatalytic Hydrogen Evolution by Efficient Charge Separation and Transfer in the Presence of Sacrificial Electron Donors. *Adv. Sci.* **2020,** *7* (12), 1902988.

Chapter 2: Acetylene-Linked Conjugated Polymers for Sacrificial Photocatalytic Hydrogen Evolution from Water

Author contributions:

All the experimental work were performed by the thesis author in this chapter, except for ICP, element analysis, solid state NMR and XPS, which were measured by the technical staffs in the test centre. Yongjie Xu guided the thesis author to synthesise the monomers. Dr. Michał Andrzej Kochman carried out the computational work in this chapter. Professor Martijn A. Zwijnenburg supervised the computational work and reviewed the whole work. Dr. Reiner Sebastian Sprick and Professor Andrew I. Cooper supervised and reviewed the whole work.

2.1 Introduction

In previous work of our group, a large series of conjugated polymers was synthesized by Suzuki-Miyaura polycondensation and tested as hydrogen production photocatalysts using a high-throughput workflow, showing that the screening allows for the accelerated discovery of high performance photocatalysts.[1-4] Acetylene-linked polymer photocatalysts and photoelectrode materials have been used for water splitting or pollutants degradation under visible light illumination with good results.[5-9] For example, acetylene-linked thiophene polymers on Cu foam supports exhibited high cathodic photocurrents, demonstrating the potential of acetylene-bridged materials.[5] Similarly, 1,4-diethynylbenzene-based linear conjugated polymers were found to be more photocatalytically active compared with 1,4-benzene-based linear conjugated polymers, and introducing the alkynyl group into their backbones can enhance visible light absorption, photocurrent intensity, and hydrogen production activity.[6] Motivated by these studies mentioned above and other reported work using acetylene–based photocatalysts[8, 10, 11], it was found that the introduction of acetylene-moieties (C≡C) not only can low the band gap to absorb more visible light, but also can promote charge separations in conjugated structures, minimize exciton binding energy and increase charge career mobility, which facilitate the migration of photogenerated excitons to the surface of the photocatalyst and enhance the photocatalytic activity.

To synthesise acetylenic polymers with alkynyl monomers, there are two kinds of widely applied reactions, the Glaser cross-coupling reaction (GCR)[12] and the Sonogashira cross-coupling reaction (SCR)[13], as illustrated in Figure 2.1. The GCR is more facile, however, normally the alkynyl monomer is expensive and unstable, besides, it is complex and time-

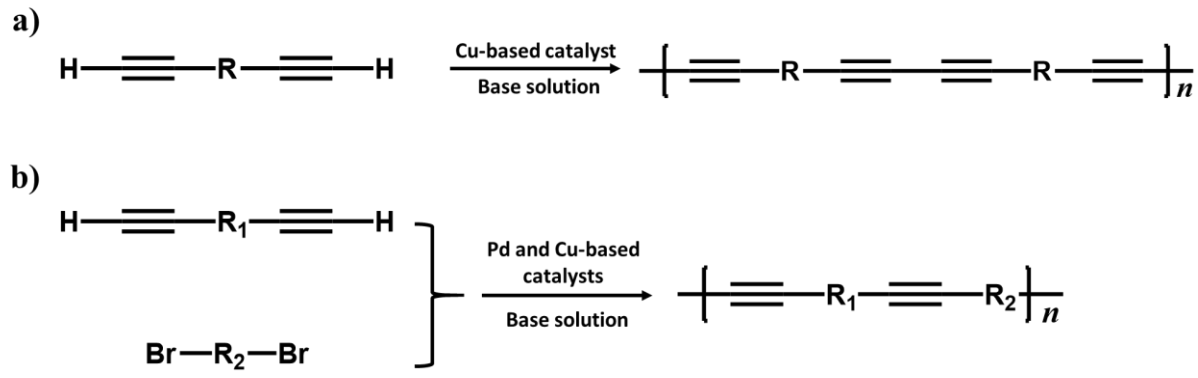

Figure 2.1 Simplified mechanism of (a) Glaser cross-coupling reaction and (b) Sonogashira cross-coupling reaction.

consuming to synthesise an alkynyl monomer if it is not commercially available. On the other hand, SCR provides more choices to synthesise various structures of polymers due to the diversity of dibromo monomers.

In this study, we synthesized a new library of acetylene-linked conjugated polymers based on commercial 1,3,5-triethynylbenzene (TE) and 1,4-diethynylbenzene (DE) via the SCR. The photocatalytic hydrogen evolution activities of these polymers in the presence of triethylamine (TEA) as a hole scavenger and platinum as a co-catalyst were tested using our high-throughput workflow.

2.2 Materials design and characterization

2.2.1 Synthesis of polymers

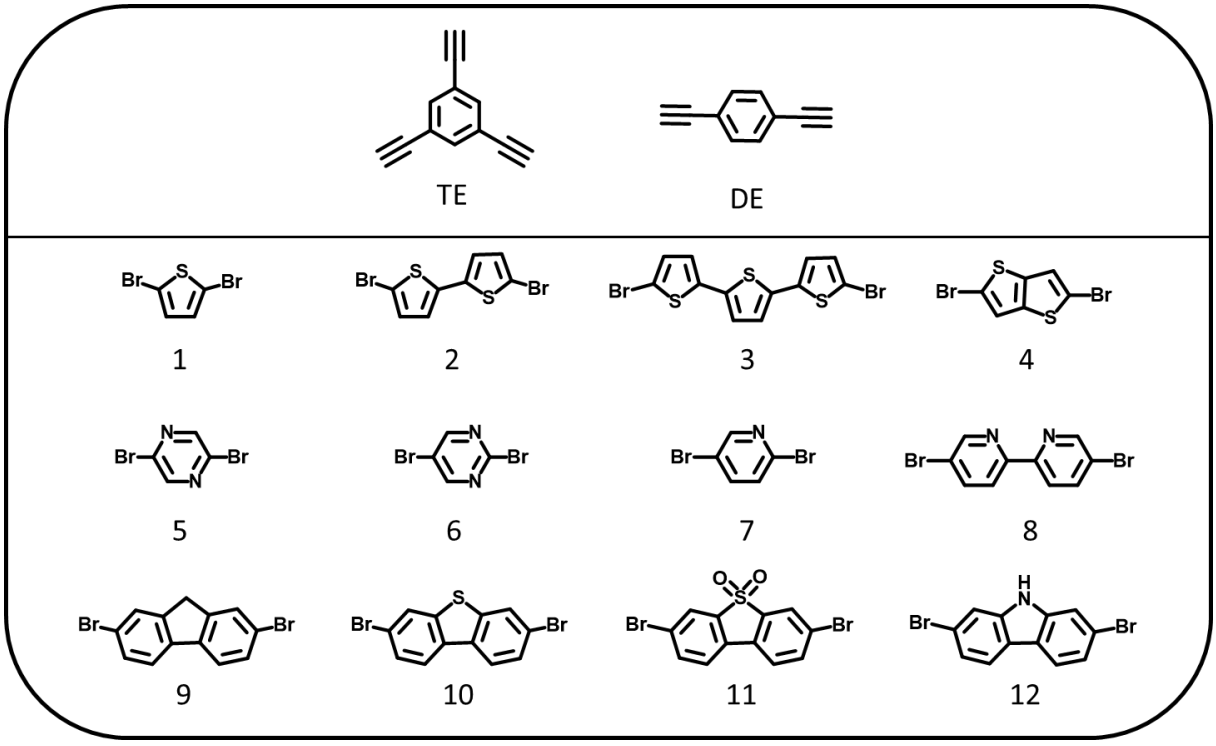

Figure 2.2 Structures of the 1,3,5-triethynylbenzene (TE), 1,4-diethynylbenzene (DE) and dibromo monomers (1–12) used to synthesize the polymer photocatalysts.

All polymers were synthesized by Pd-catalyzed Sonogashira polycondensation of 1,3,5-triethynylbenzene or 1,4-diethynylbenzene with a range of dibromo-functionalized monomer linkers (1-12; Figure 2.2) to give the corresponding TE-n or DE-n polymer photocatalysts (whereby n is the corresponding dibromo monomer linker). The polymers were classified into

three subsets: sulfur heterocycles (1-4), nitrogen heterocycles (5-8), and planar heterofluorenes (9-12). Heteroatom doping could change the crystallinity, morphology, distribution of electrons, optical property and the position of redox energy level, which further effect the photocatalytic performance.[14-16] Therefore, the group consists of sulfur is selected to narrow down the optical gap and improve the visible light absorption,[17, 18] while nitrogen-doping is also considered to modulate the optoelectronic properties and thus improve the photocatalytic performance.[19, 20] Moreover, duo to the unique π-conjugated structure and optical property, fluorene-based polymers have shown good activity for hydrogen evolution form photocatalytic water splitting in our previous work.[3, 4, 21] Therefore, four typical fluorene-based polymers were synthesized with Sonogashira coupling instead of previous Suzuki coupling.

2.2.2 Characterizations

All materials were characterized by microanalysis and FT-IR (Figure 2.3). After cross coupling, the typical peaks of C≡C-H at around 3300 cm^{-1} in the TE and DE monomer disappeared, and the peak at around 2190 cm^{-1} can be assigned to the C≡C stretching modes of the acetylene linker,[22] which means the success of the polymerization. In addition, we found that the crosslinked TE polymer networks were amorphous while the linear DE polymers were semi-crystalline, as evidenced by their powder X-ray diffraction patterns (Figure 2.4). Normally, crystalline photocatalysts tend to have better performance because of less defects.[23, 24] However, it is not absolute, as the amorphous photocatalysts were even superior in some cases.[25, 26] Scanning electron microscopy images (Figure 2.5) showed variable morphologies for the polymers; most TE polymers tended to form spherical nano aggregates, while the linear DE polymers consisted mainly of flakes or blocks. Thermogravimetric measurements under N_2 showed that all polymers were thermally stable to around 250 ℃ under N_2 (Figure 2.6). The apparent Brunauer-Emmett-Teller surface areas (SA_{BET}) were estimated using nitrogen adsorption isotherms at 77 K and up to 1 bar (Figure 2.7 and Table 2.1). Porosity is a beneficial factor for photocatalytic reactions as it could enlarge the surface area of photocatalysts and make more active sites exposed.[3, 27] The BET surface areas of all linear DE polymers fell below 60 $m^2\ g^{-1}$, while the TE polymers showed variable surface areas: 5 polymers had surface areas ranging from 150-600 $m^2\ g^{-1}$ that denoted a degree of porosity, with other samples being essentially non-porous (SA_{BET} < 30 $m^2\ g^{-1}$), which could be caused by the collapse of the structure during the polymerization.

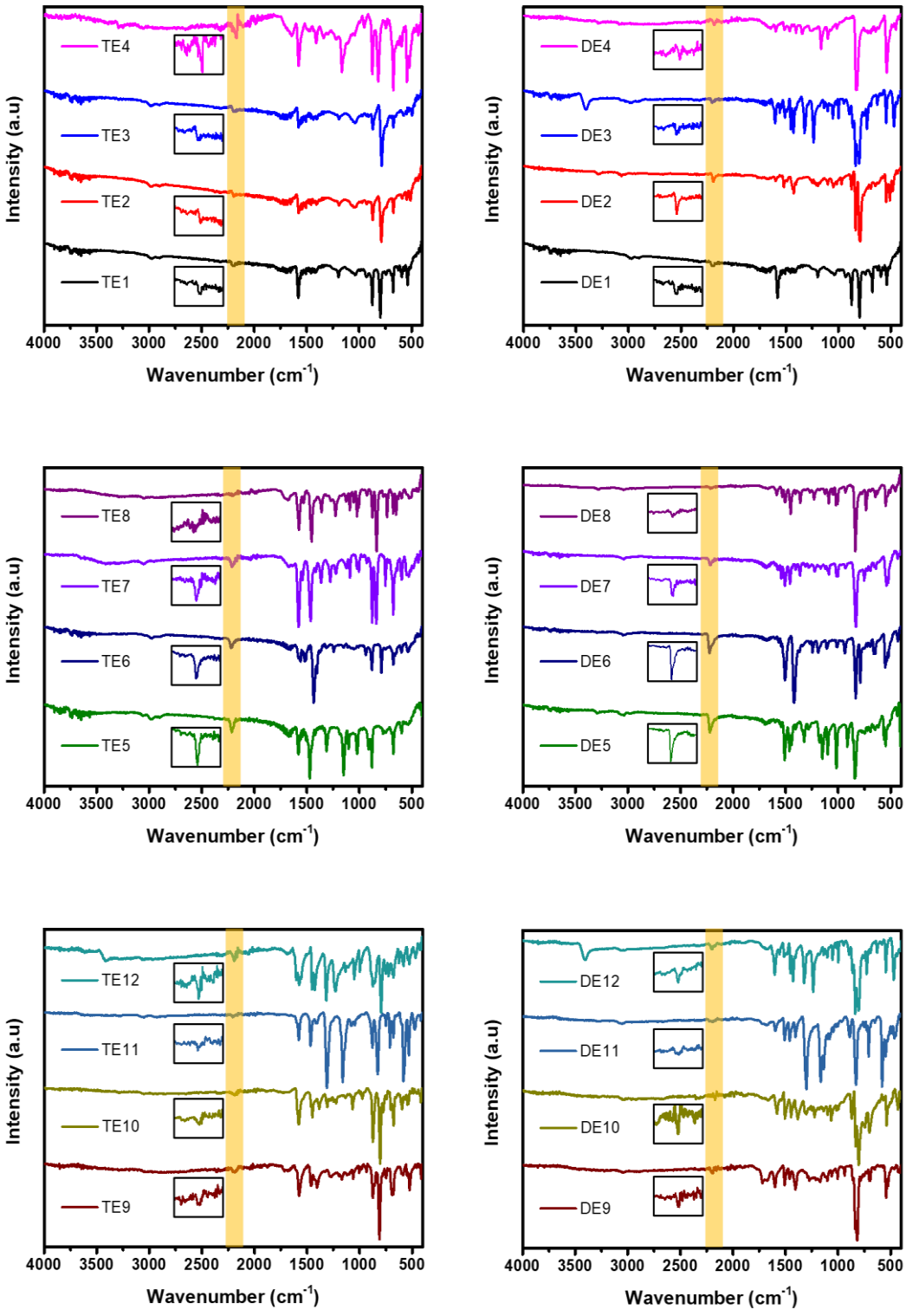

Figure 2.3 Fourier-transform infrared spectroscopy of TE1-12 and DE1-12.

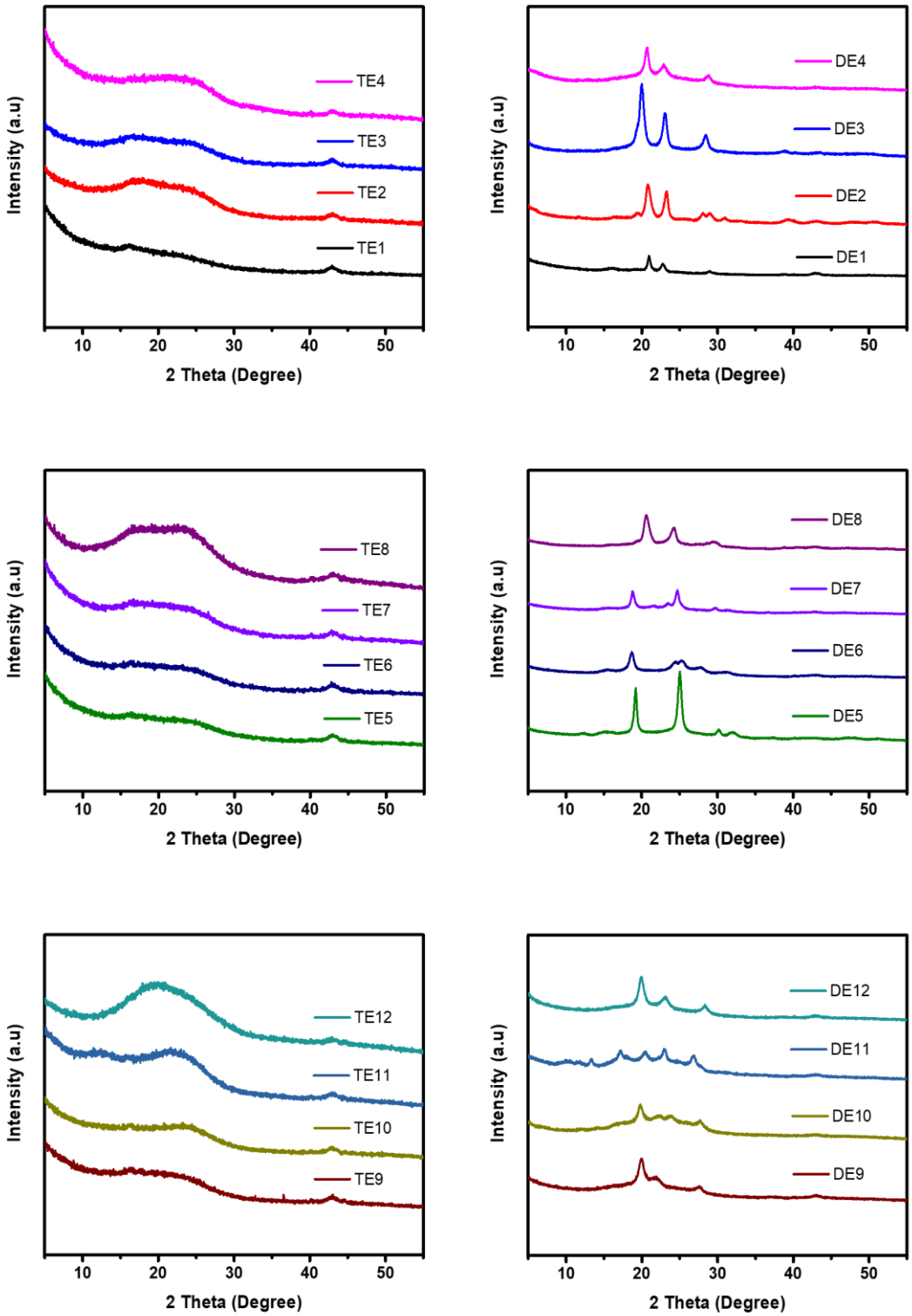

Figure 2.4 PXRD patterns of TE1-12 and DE1-12.

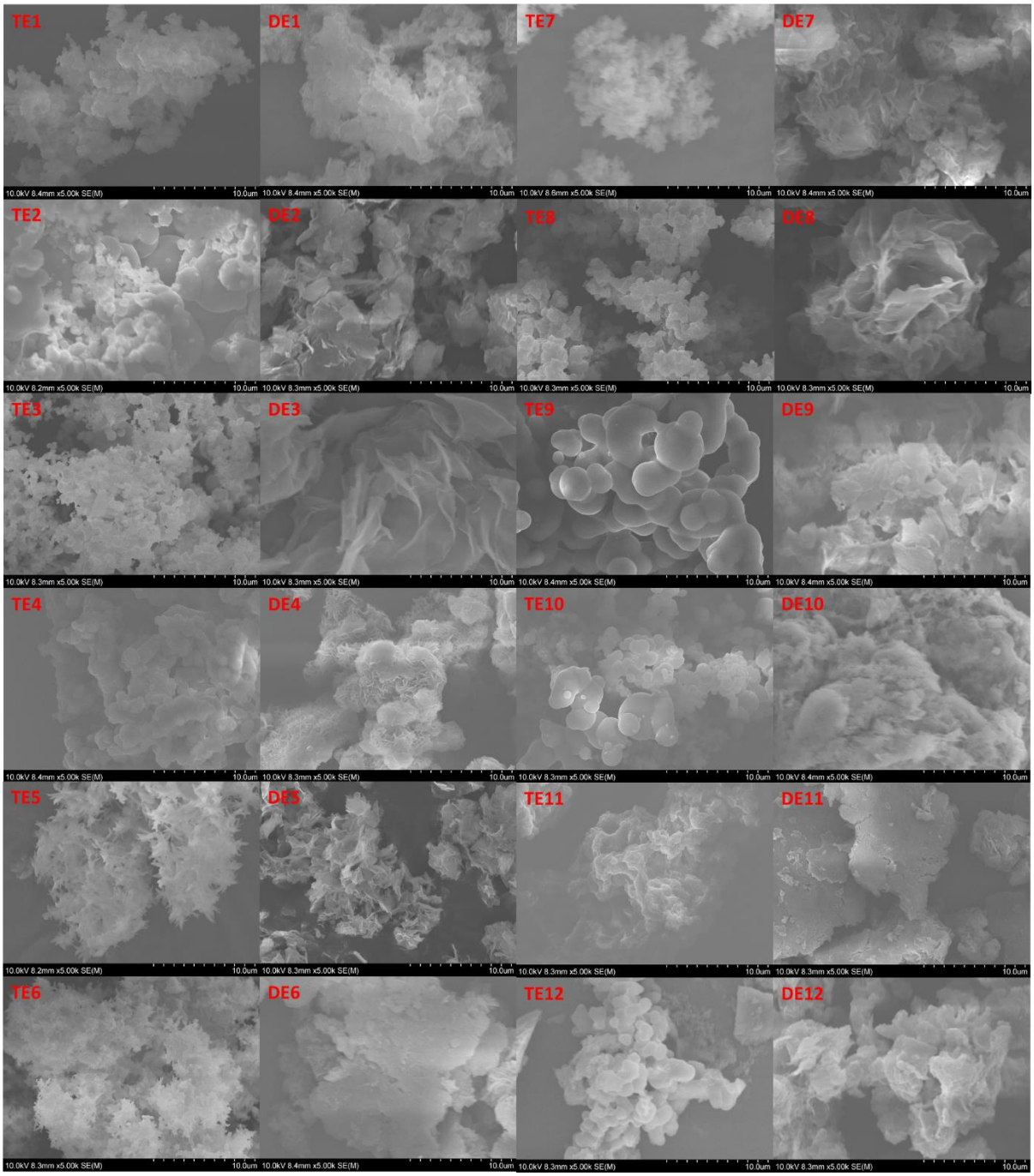

Figure 2.5 SEM images of TE1-12 and DE1-12.

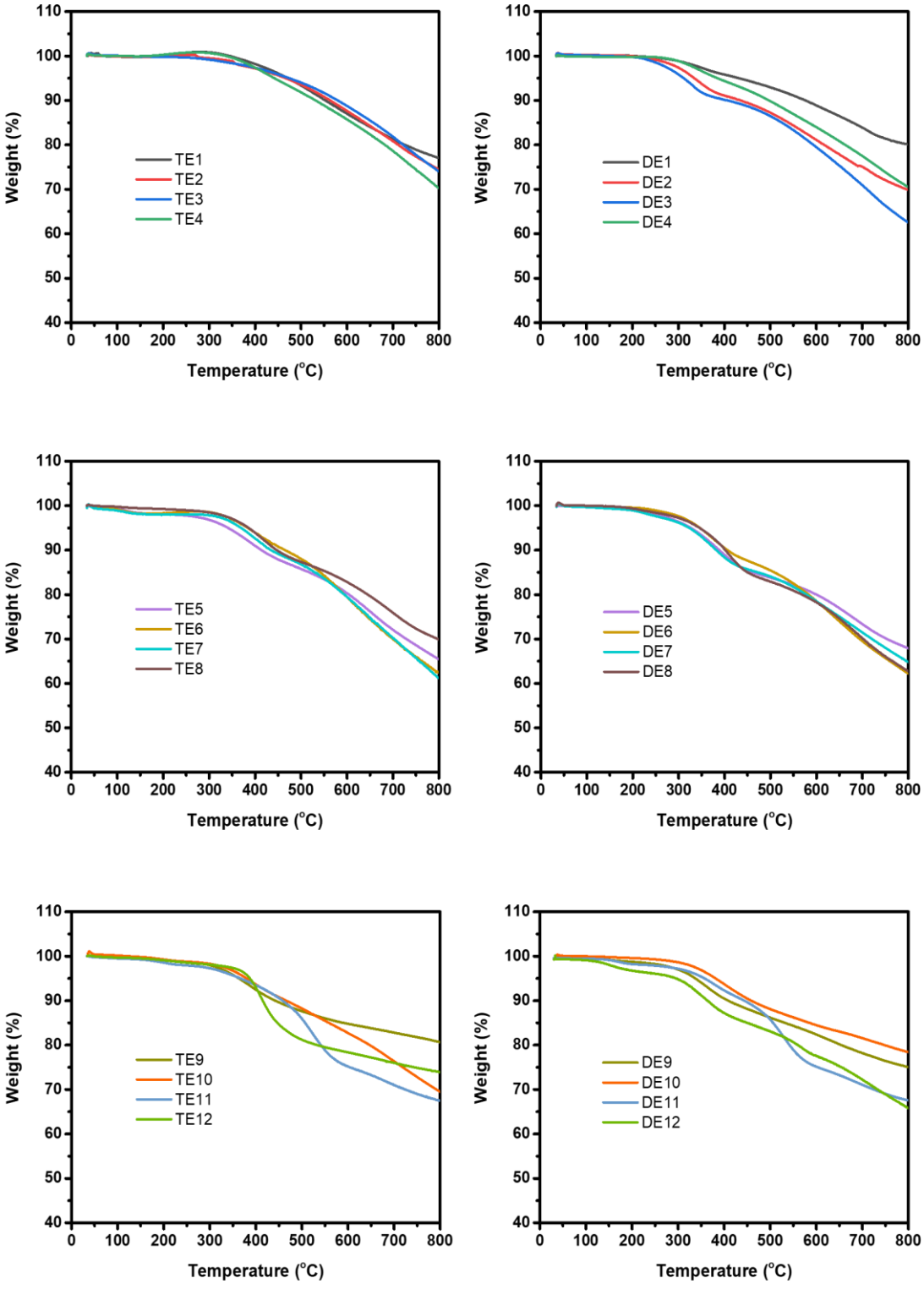

Figure 2.6 Thermogravimetric data of TE1-12 and DE1-12.

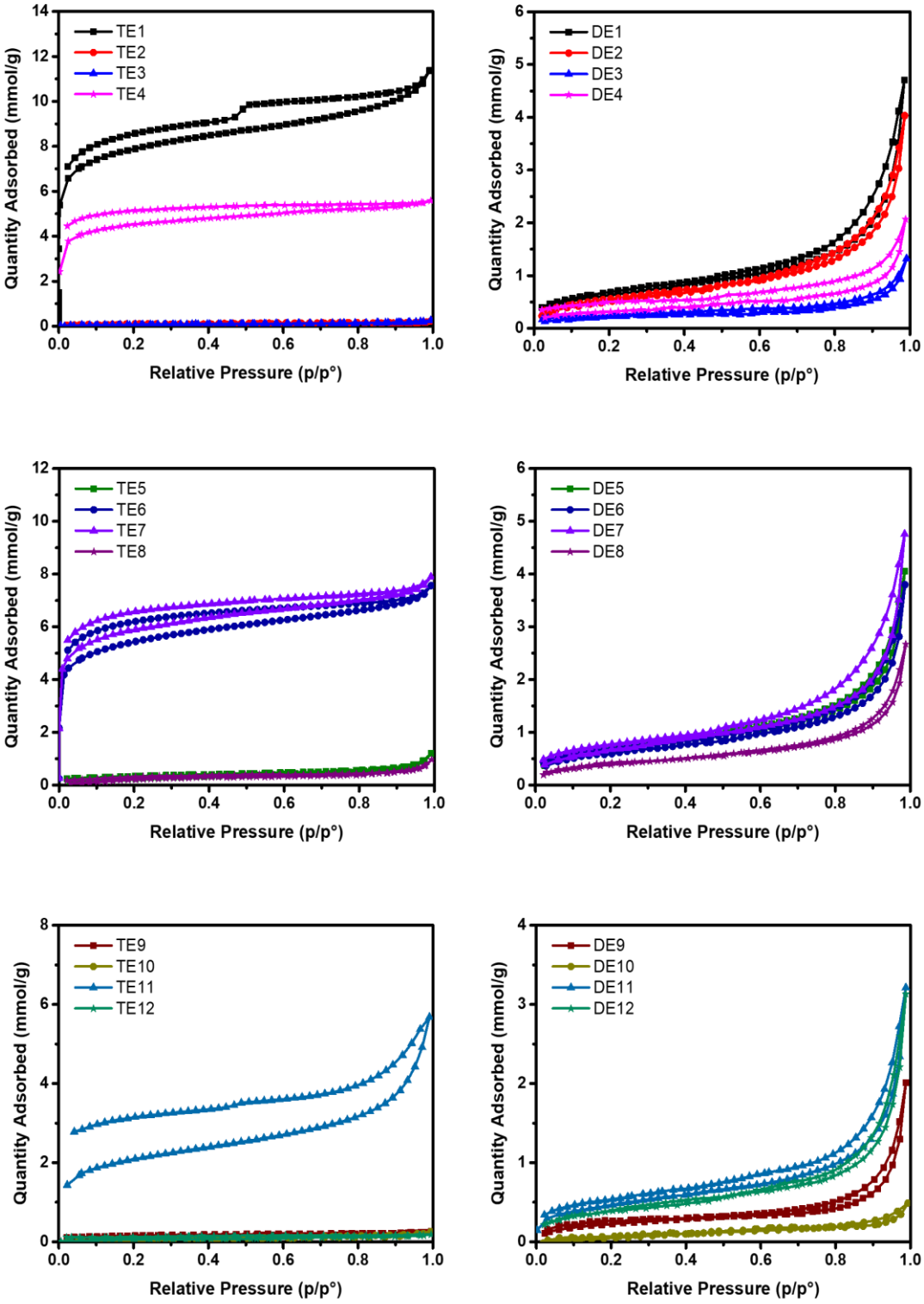

Figure 2.7 Nitrogen sorption isotherm of TE1-12 and DE1-12.

Table 2.1 BET surface areas and Experimental optical gaps of TE1-12 and DE1-12.

TE-n polymer	Surface area[a] / $m^2 g^{-1}$	Optical gap[b] / eV	Optical gap[c] / eV	DE-n polymer	Surface area[a] / $m^2 g^{-1}$	Optical gap[b] / eV	Optical gap[c] / eV
TE1	550	1.93	2.06	**DE1**	51	2.11	2.24
TE2	3	1.81	1.94	**DE2**	46	1.93	2.07
TE3	6	1.78	1.92	**DE3**	17	1.82	1.95
TE4	311	1.65	1.85	**DE4**	25	1.79	1.93
TE5	22	1.99	2.43	**DE5**	56	2.19	2.37
TE6	388	2.11	2.38	**DE6**	48	2.23	2.42
TE7	424	2.17	2.44	**DE7**	54	2.25	2.44
TE8	19	2.34	2.52	**DE8**	29	2.13	2.28
TE9	7	1.92	2.15	**DE9**	19	2.15	2.31
TE10	3	2.17	2.35	**DE10**	7	2.02	2.18
TE11	155	2.11	2.31	**DE11**	38	2.21	2.34
TE12	4	1.67	2.01	**DE12**	34	2.19	2.33

[a] BET surface area determined from the absorption branch of the absorption isotherm measured at 77 K. [b] Calculated from the absorption on-set in the UV-vis spectrum. [c] Calculated from Kubelka-Munk formula based on the spectrum of $(\alpha h\nu)^{\wedge 1/2} \propto E_g$.

UV-visible absorption spectra were measured in the solid state to study optical properties of the materials (Figure 2.8). All polymers had absorption onsets in the visible part of the solar spectrum and most TE polymers had a small red shift in their onset compared to their corresponding DE polymers. Based on the absorption spectra, the optical gaps of the polymers can be calculated. As shown in Table 2.1, they range from 1.85 eV for TE4 to 2.52 eV for TE8.

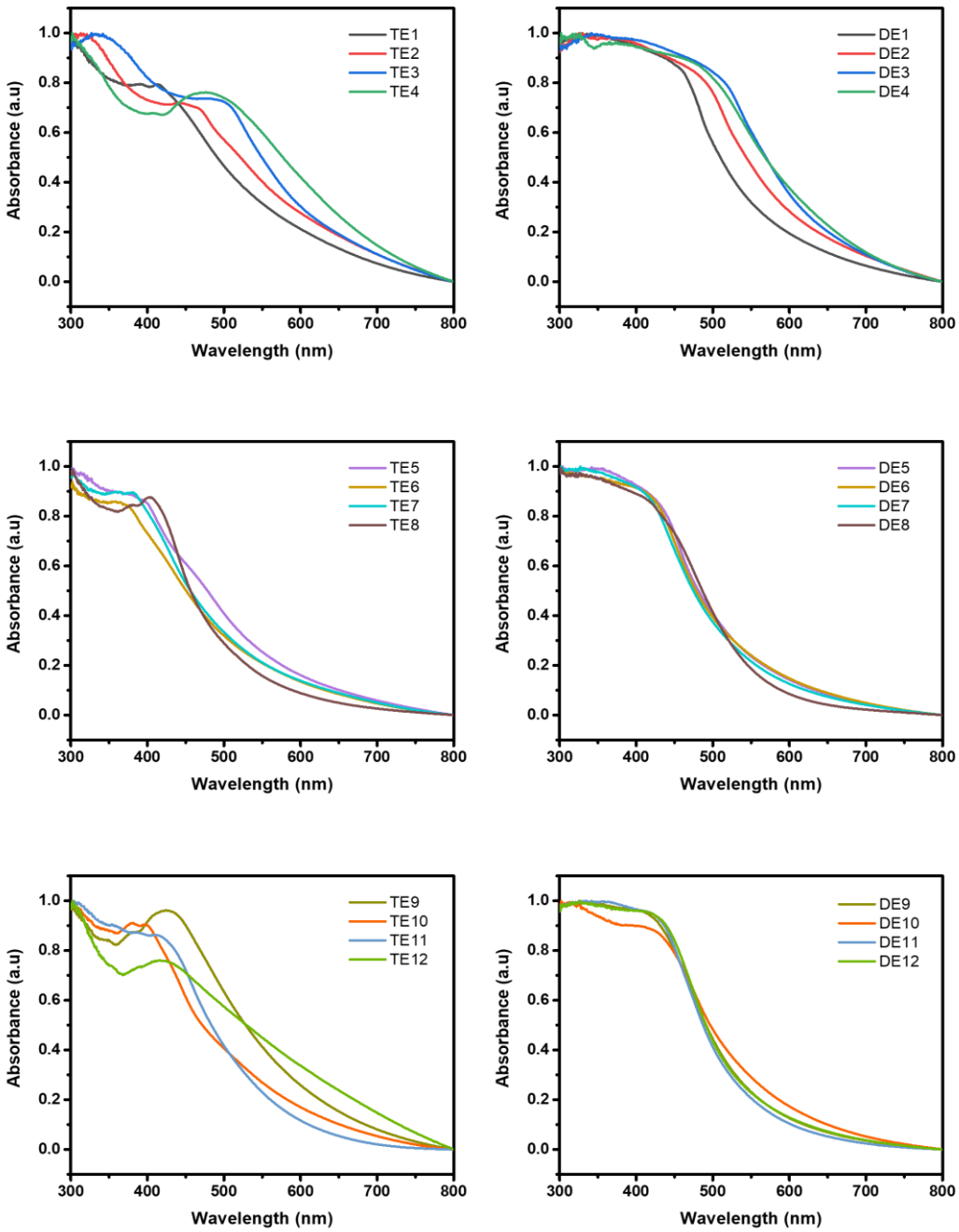

Figure 2.8 Reflectance UV-visible spectra of TE1-12 and DE1-12 measured in the solid-state.

In addition, the electron affinity (EA) and ionization potential (IP) were predicted based on density functional theory (Table 2.2 and Figure 2.9). EA governs the driving force for proton reduction, while IP governs the driving force for water oxidation (or TEA oxidation in this case), which are often approximated in the literature (though not here) by the energy of the LUMO (lowest unoccupied molecular orbital) and HOMO (highest occupied molecular orbital), respectively.[2, 28, 29] The EA values of all polymers are more negative than the required energy level in theory for hydrogen evolution, which means they all should be able to reduce protons

when illuminated. All polymers should also be able drive the overall oxidation of TEA to diethylamine and acetaldehyde. However, for a number of the polymers, *e.g.*, TE3/4 and DE3/4, the one-hole oxidation of TEA, the first step in the overall oxidation, is predicted to be endergonic, suggesting that this step might give rise to a thermodynamic barrier.

Table 2.2 DFT Calculations of IP, EA and fundamental gap of TE1-12 and DE1-12.

TE-n Polymer	IP / V	EA / V	Fundamental gap[a] / V	DE-n Polymer	IP / V	EA / V	Fundamental gap[a] / V
TE1	0.92	-1.88	2.80	**DE1**	0.67	-1.59	2.26
TE2	0.67	-1.78	2.45	**DE2**	0.52	-1.59	2.11
TE3	0.50	-1.72	2.23	**DE3**	0.41	-1.60	2.01
TE4	0.81	-1.85	2.65	**DE4**	0.60	-1.59	2.19
TE5	1.45	-1.57	3.02	**DE5**	1.22	-1.27	2.49
TE6	1.49	-1.66	3.15	**DE6**	1.26	-1.33	2.59
TE7	1.30	-1.84	3.14	**DE7**	1.05	-1.53	2.59
TE8	1.24	-1.75	2.99	**DE8**	1.05	-1.58	2.63
TE9	0.91	-2.09	3.00	**DE9**	0.74	-1.89	2.63
TE10	1.06	-1.99	3.05	**DE10**	0.88	-1.79	2.67
TE11	1.28	-1.62	2.90	**DE11**	1.10	-1.46	2.56
TE12	0.89	-2.15	3.04	**DE12**	0.72	-1.94	2.66

[a] The fundamental gap (E_f) was obtained via the formula: E_f = IP-EA.

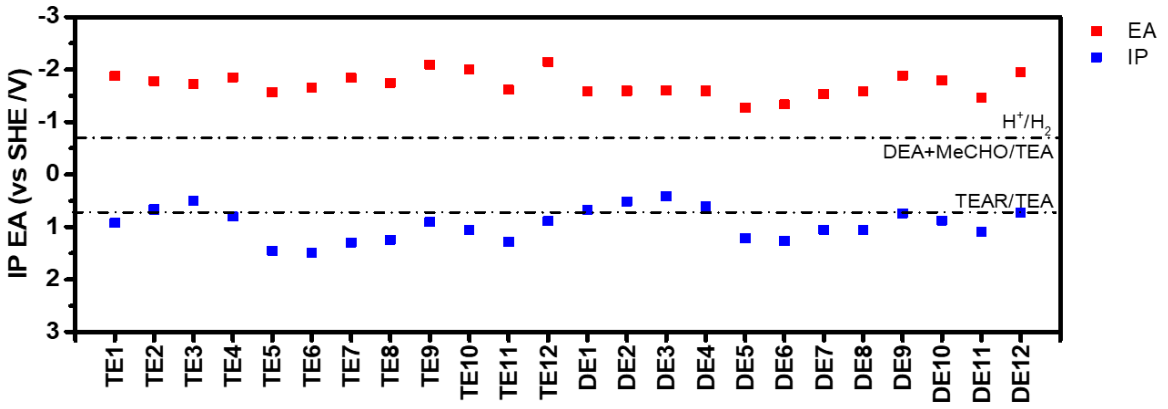

Figure 2.9 Predicted IP and EA potentials of the different polymers. Solution half reactions are shown as calculated for pH 12.3, the measured pH of the TEA/MeOH/water mixture (MeCHO-acetaldehyde; TEAR-deprotonated TEA radical).

Accordingly, time-resolved single photon counting experiments were performed to study the lifetime of the excited state (Table 2.3). The weighted average fluorescence lifetimes of TE and DE polymers were varied from 0.3 ns to 2.6 ns, with most materials having lifetimes shorter than 1 ns. Given that the differences of them were very small, the lifetimes may not be statistically significant.

Table 2.3 Estimated fluorescence lifetimes of TE1-12 and DE1-12.

Polymer	λ_{em} / nm	τ_1 / ns	B_1 / %	τ_2 / ns	B_2 / %	τ_3 / ns	B_3 / %	χ^2	τ_{avg} / ns
TE1	407	0.15	67.06	0.80	26.53	4.85	6.40	1.443	0.63
TE2	416	0.07	83.95	0.59	13.58	6.28	2.47	1.195	0.29
TE3	455	0.14	59.86	1.05	26.44	2.89	13.70	1.604	0.76
TE4	404	0.08	73.29	0.54	20.90	2.93	5.81	1.495	0.34
TE5	475	0.23	53.51	1.05	37.10	4.98	9.40	1.530	0.98
TE6	415	0.21	61.39	1.04	29.63	5.55	8.98	1.387	0.94
TE7	460	0.16	66.01	0.84	27.53	4.32	6.46	1.475	0.62
TE8	486	0.15	68.48	0.78	23.68	4.86	7.83	1.570	0.67
TE9	524	0.32	49.89	1.47	34.27	7.55	15.84	1.324	1.86
TE10	486	0.20	56.76	0.90	34.46	4.16	8.78	1.577	0.79
TE11	500	0.20	53.21	0.78	40.51	3.68	6.28	1.531	0.66
TE12	407	1.16	46.54	2.32	36.19	7.00	17.27	1.147	2.59
DE1	530	0.16	36.91	0.52	60.86	2.69	2.23	1.128	0.43
DE2	456	0.13	63.56	0.64	32.49	2.91	3.95	1.462	0.41
DE3	630	0.09	73.56	0.58	22.89	2.71	3.55	1.442	0.30
DE4	430	0.20	42.23	0.53	56.32	5.26	1.46	1.090	0.46
DE5	420	0.26	18.65	0.83	79.66	2.83	1.69	1.028	0.76
DE6	530	0.29	45.77	1.06	43.33	4.20	10.90	1.370	1.05
DE7	465	0.26	27.72	0.76	66.86	3.18	5.42	1.228	0.75
DE8	403	0.35	46.72	0.68	50.40	5.85	2.88	1.108	0.67
DE9	574	0.32	30.45	1.20	53.43	3.66	16.13	1.336	1.33
DE10	525	0.18	55.54	0.82	35.27	3.56	9.19	1.369	0.72
DE11	525	0.27	42.07	1.09	45.92	3.97	12.00	1.541	1.09
DE12	409	0.16	60.26	0.72	33.91	4.64	5.84	1.255	0.61

[a] Fluorescence lifetimes for all polymers obtained from fitting time-correlated single photon counting decays to a sum of three exponentials, which yield τ_1, τ_2, and τ_3 according $\sum_{i=1}^{n}(A + B_i exp(-t/\tau_i))$. τ_{avg} is the weighted average lifetime calculated as $\sum_{i=1}^{n}(B_i\tau_i)$.

To study the wetting behaviour of the polymers, contact angle against water measurements were performed (Figure 2.10 and Table 2.4). Polymers TE4, TE6, TE7 and TE11 absorbed water and swelled, while the TE8 polymer showed the highest water contact angle (115.7 °). TE5 had the lowest contact angle of 59.5 °, the contact angles of the DE polymers ranged from 75.9 ° to 94.0 °. However, using mixture solvent could more direct information, which should consider in the future since not investigated in this work.

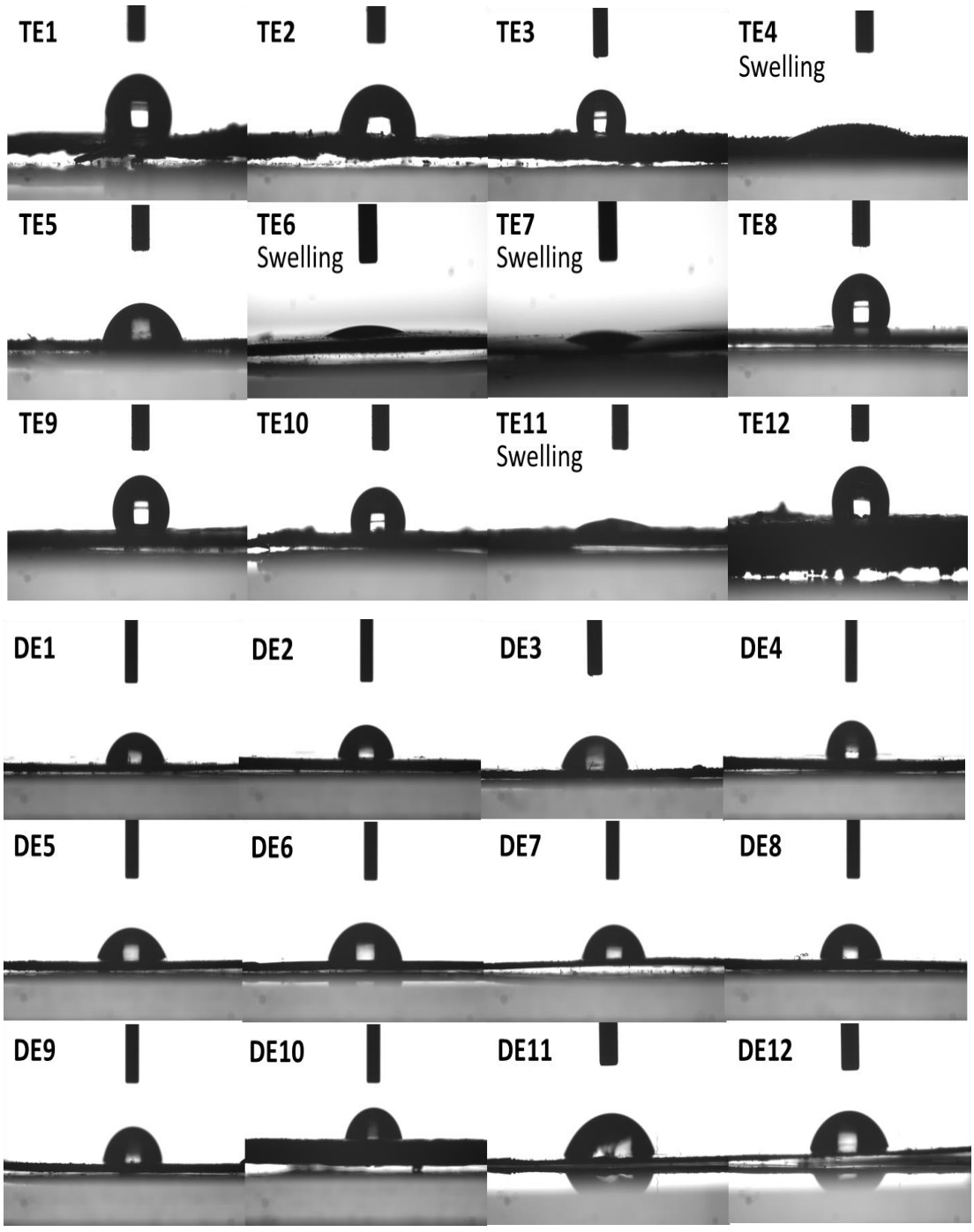

Figure 2.10 Contact angle images against water of TE1-12 and DE1-12. For materials that swell, the image was taken immediately after the water droplet was deposited onto the polymer pallet.

Table 2.4 Contact angles against water of TE1-12 and DE1-12 pallets.

TE-n Polymer	Contact angle against water / °	DE-n Polymer	Contact angle against water / °
TE1	100.1 (±2.1)	**DE1**	80.9 (±2.3)
TE2	84.9 (±1.4)	**DE2**	86.9 (±2.1)
TE3	101.9 (±1.1)	**DE3**	76.0 (±0.7)
TE4	Swelling	**DE4**	94.0 (±5.1)
TE5	59.5 (±1.3)	**DE5**	80.2 (±2.1)
TE6	Swelling	**DE6**	75.9 (±2.0)
TE7	Swelling	**DE7**	80.8 (±2.0)
TE8	115.7 (±0.7)	**DE8**	84.9 (±1.8)
TE9	113.3 (±1.8)	**DE9**	87.5 (±0.8)
TE10	104.8 (±0.9)	**DE10**	77.6 (±2.1)
TE11	Swelling	**DE11**	76.7 (±2.7)
TE12	103.7 (±4.4)	**DE12**	84.1 (±2.1)

Table 2.5 Average transmission values of TE1-12 and DE1-12.

TE-n Polymer	Transmission TEA/MeOH/H_2O / %	Particle size[a] / µm	DE-n Polymer	Transmission TEA/MeOH/H_2O / %	Particle size[a] / µm
TE1	5.8	35.5	**DE1**	2.3	18.5
TE2	50.5	48.8	**DE2**	1.7	10.3
TE3	71.5	40.4	**DE3**	28.3	16.3
TE4	40.0	27.0	**DE4**	21.7	15.5
TE5	0.5	18.1	**DE5**	15.0	8.9
TE6	4.3	25.0	**DE6**	2.4	10.1
TE7	4.6	20.6	**DE7**	16.3	12.5
TE8	12.8	21.0	**DE8**	4.6	13.1
TE9	71.2	86.1	**DE9**	3.3	12.5
TE10	12.2	68.5	**DE10**	78.8	18.5
TE11	28.8	25.5	**DE11**	6.6	11.7
TE12	84.6	51.9	**DE12**	18.9	16.9

[a] 50^{th} Percentile of particle size volume distribution.

The dispersibility of all polymers in TEA/methanol (MeOH)/water mixtures was determined by measuring the transmittance of the resulting photocatalyst dispersions (Table 2.5), where lower transmission means better dispersibility (that is, less particle settling). The dispersibility of TE5 polymers was the highest with a transmittance value of just 0.5%, while the transmittance of TE12 and DE10 were approximately 80%, indicating poor dispersibility in the reaction mixture, which could also be observed by eye. Particle size distributions of polymers were measured by static light scattering experiments (Table 2.4). The DE polymers were found to have smaller average particle sizes (8.9-18.5 μm) compared to the respective TE polymers (20.6-86.1 μm).

2.3 Hydrogen evolution performance

2.3.1 Hydrogen production

To rapidly screen the photocatalytic activity of all polymers, we used the same high-throughput workflow reported that we reported previously.[2, 28] TEA was used as a hole scavenger and 3 wt.% Pt was added by photodeposition from H_2PtCl_6 as a cocatalyst for promoting hydrogen evolution. After 2-hour illumination under simulated solar light (1 sun), the TE11 photocatalyst showed the highest hydrogen production rate (Figure 2.11 and Table 2.6) of 1811.0 μmol g^{-1} h^{-1}.

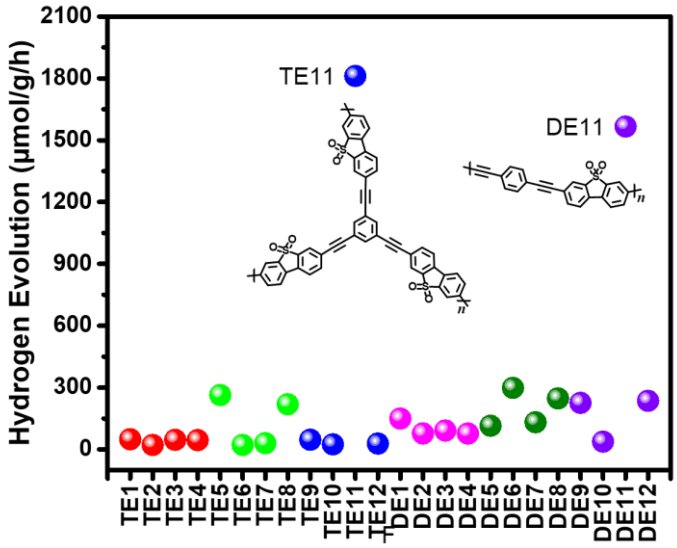

Figure 2.11 Hydrogen evolution rate of TE1-12 and DE1-12. Conditions: 5 mg polymer with 3 wt.% Pt were dispersed in 5 mL TEA/MeOH/water (1:1:1) mixture, irradiated by a solar simulator (AM1.5G, Class AAA, IEC/JIS/ASTM, 1440 W Xe, 12 × 12 in., MODEL: 94123A, illumination time: 2 hours).

Table 2.6 High-throughput hydrogen evolution performance of TE1-12 and DE1-12.

TE-n Polymer	Hydrogen evolution[a] / μmol g^{-1} h^{-1}	DE-n Polymer	Hydrogen evolution[a] / μmol g^{-1} h^{-1}
TE1	49.7	**DE1**	149.5
TE2	21.3	**DE2**	77.4
TE3	46.4	**DE3**	90.9
TE4	45.2	**DE4**	77.0
TE5	263.4	**DE5**	115.0
TE6	21.2	**DE6**	298.7
TE7	29.9	**DE7**	131.8
TE8	219.1	**DE8**	247.5
TE9	47.1	**DE9**	225.6
TE10	24.3	**DE10**	37.9
TE11	1811.0	**DE11**	1565.7
TE12	28.4	**DE12**	235.7

[a] 5 mg polymer with 3 wt.% Pt were dispersed in 5 mL triethylamine/methanol/water (1:1:1) mixture, irradiated by a solar simulator (AM1.5G, Class AAA, IEC/JIS/ASTM, 1440 W Xe, 12 × 12 in., MODEL: 94123A, illumination time: 2 hours).

2.3.2 Relationship between HER performance and polymer properties

The optical gap is an important factor that will affect the light absorption for these polymer catalysts. For the purposes of the subsequent analysis, we assume that the onset of light absorption of the polymer corresponds to excitations into charge-separated states. Although smaller optical gaps are beneficial for broader visible spectral absorption one must also consider the thermodynamic driving force, and we found that most polymers with high HER have relatively large optical gaps (2.5-3.1 eV) with DE11 and TE11 in particular having much higher rates (Figure 2.12). Similarly, correlation of EA and IP with hydrogen evolution rates shows no clear trend (Figure 2.13-2.14) with the most active materials again clustering in a relatively narrow window.

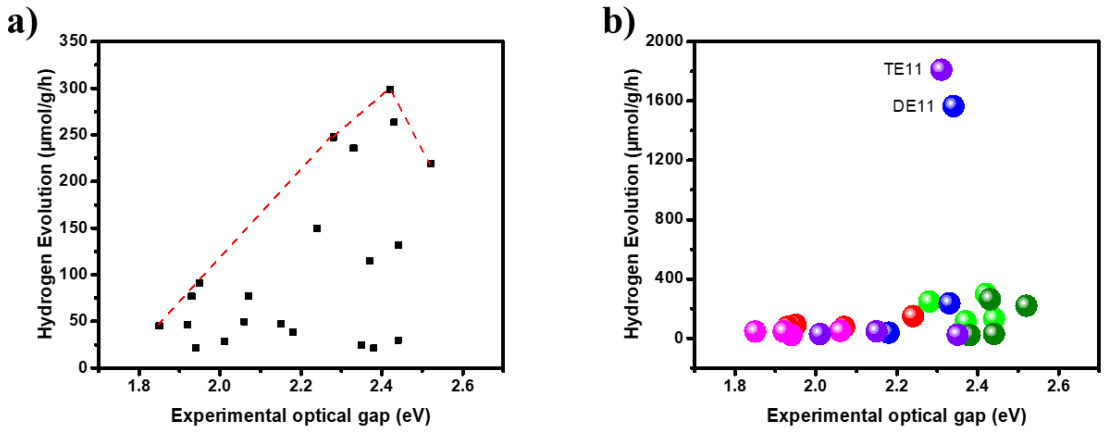

Figure 2.12 Comparison of the experimental optical gap to the hydrogen evolution rates of a) except for TE11 and DE11, b) all TE and DE polymers.

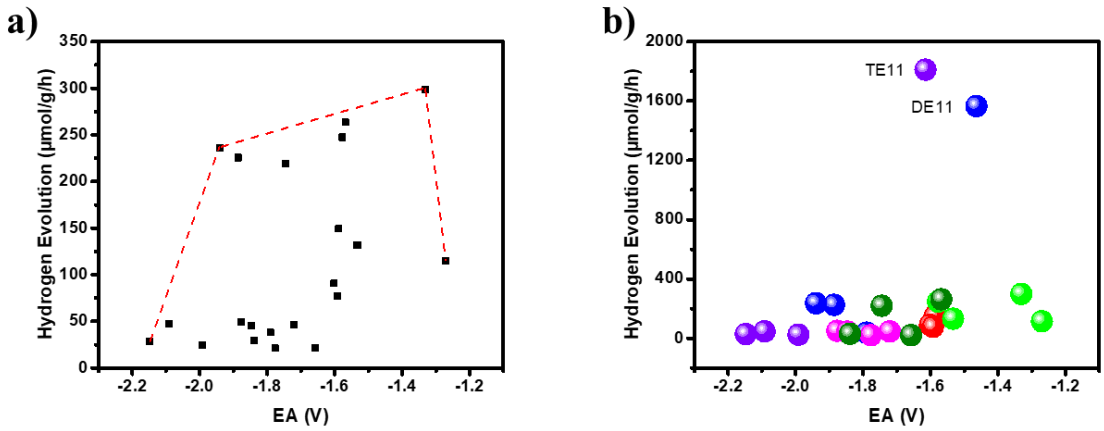

Figure 2.13 Predicted Comparison of the predicted EA to the hydrogen evolution rates of a) except for TE11 and DE11, b) all TE and DE polymers.

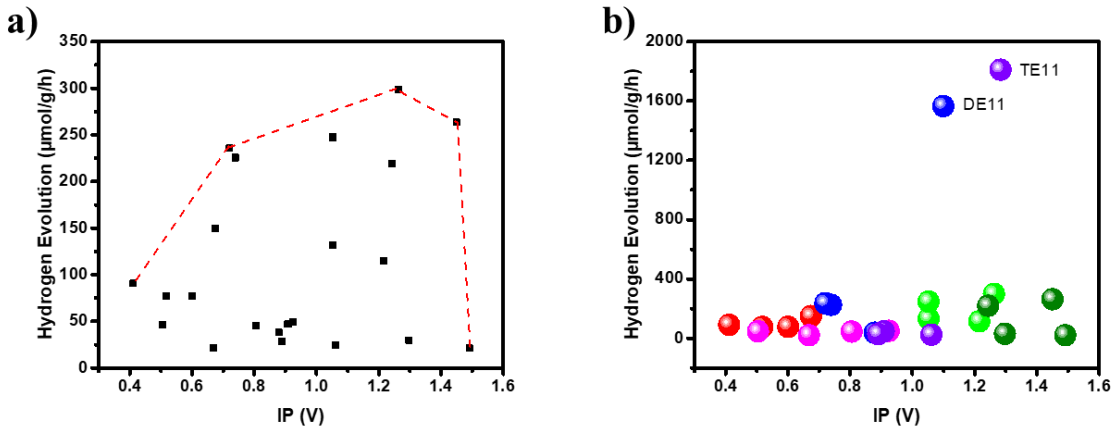

Figure 2.14 Predicted Comparison of the predicted EA to the hydrogen evolution rates of a) except for TE11 and DE11, b) all TE and DE polymers.

The dispersibility of the polymer catalysts in the TEA/MeOH/H_2O mixture also has a significant impact on the HER; this in turn is influenced by the density, the particle size and the wettability of the polymers. Light transmittance was measured and plotted vs HER (Figure 2.15). The results show that most active materials have low light transmittance of less than 50%, which means that they are well dispersed in the reaction medium. No polymers with transmission values (> 40%) have high HERs. These trends are consistent with a negative correlation found between average particle size and photocatalytic H_2 evolution activity of polymer catalysts (Figure 2.16). By contrast, contact angle shows no obvious correlation with the hydrogen evolution rate (Figure 2.17), though we note that these values refer to pure water, rather than the TEA/MeOH/H_2O reaction medium.

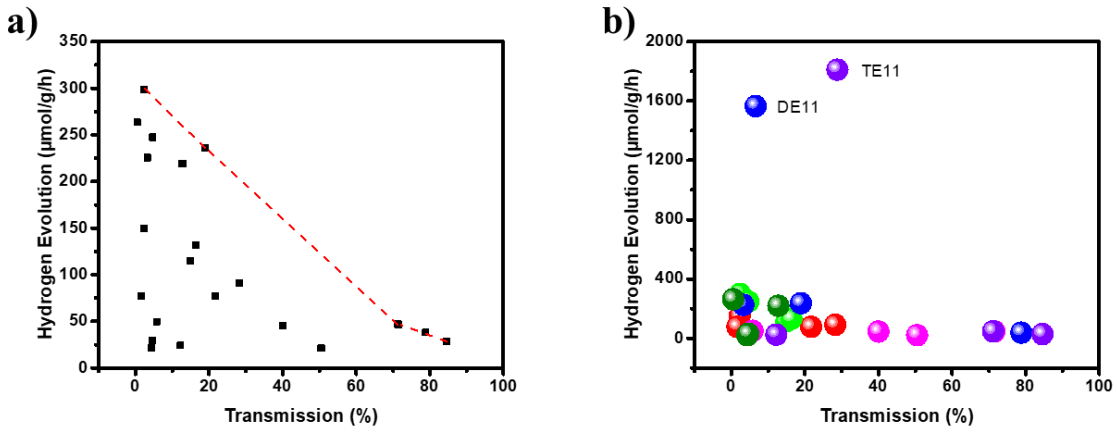

Figure 2.15 Comparison of the light transmittance to the hydrogen evolution rates of a) except for TE11 and DE11, b) all TE and DE polymers.

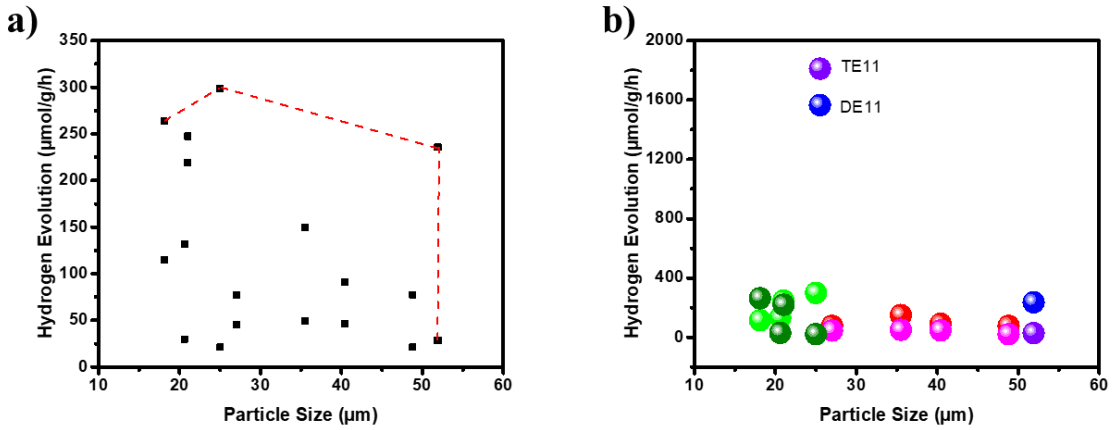

Figure 2.16 Comparison of the particle size (measured in static light scattering experiments) to the hydrogen evolution rates of a) except for TE11 and DE11, b) all TE and DE polymers.

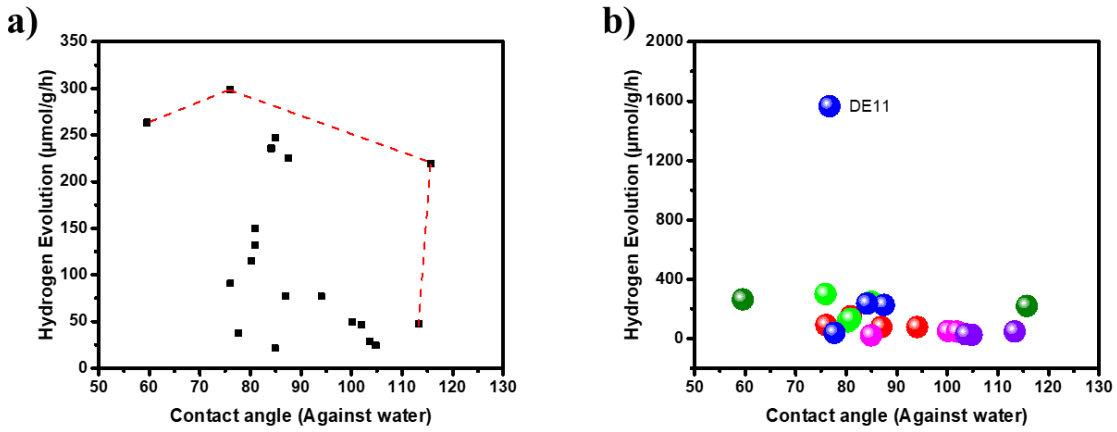

Figure 2.17 Comparison of the contact angle to the hydrogen evolution rates of a) except for swelling samples and DE11, b) except for swelling samples (TE4, TE6, TE7 and TE11).

Taking surface area into account (Figure 2.18), we found that all of the materials with the highest photocatalytic activity had BET surface areas smaller than 200 m^2 g^{-1}, perhaps because factors such as dispersibility and (conceivably) semicrystallinity are dominant. Finally, the average fluorescence lifetime (Figure 2.19) of the materials showed no clear correlation with photocatalytic performance, although all materials with very short lifetimes (< 0.5 ns) were also found to have low photocatalytic performances.

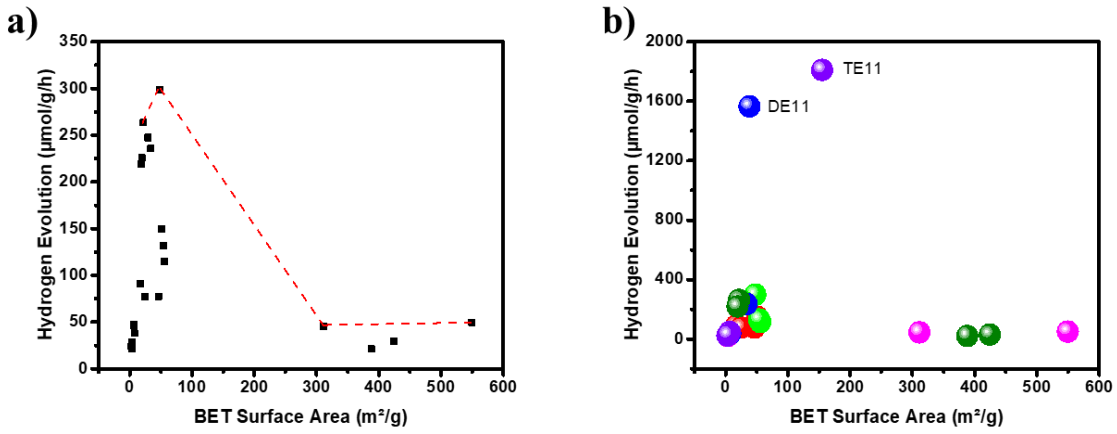

Figure 2.18 Comparison of the surface area (SA_{BET}, in N_2) to the hydrogen evolution rates of a) except for TE11 and DE11, b) all TE and DE polymers.

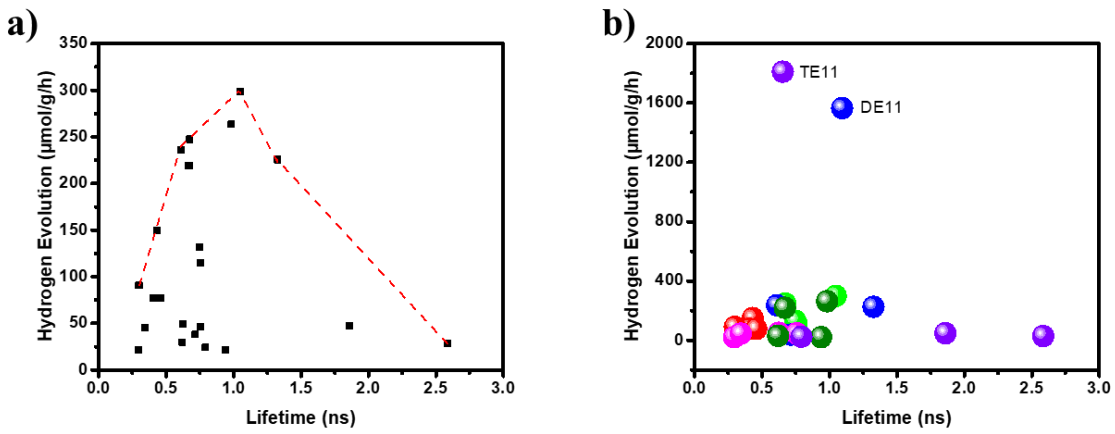

Figure 2.19 Comparison of the averaged fluorescence lifetime to the hydrogen evolution rates of a) except for TE11 and DE11, b) all TE and DE polymers.

Taken together, it seems once more that there is no single property that dominates the photocatalytic activity, as found in previous studies.[2, 28] However, for these materials, it seems that optical gap and dispersibility of the polymers in the suspension seem to have the largest overall effect on photocatalytic performance.

2.4 Improved performance by changing the core

2.4.1 Synthesis of polymers

According to the high-throughput screening results, TE11 exhibited the best performance for photocatalytic hydrogen evolution. The moiety of dibenzo[*b*,*d*]thiophene sulfone could play a leading role[1, 3] since DE11 also shown high activity although was second to TE11. In an attempt to find better catalysts than TE11, we modified the linker by using TEB instead of TE, which bears additional phenylenes and therefore extends the conjugation length of the linker. We also explored TEBN with N-doping, which is the triazine analogue of TEB (Figure 2.20).

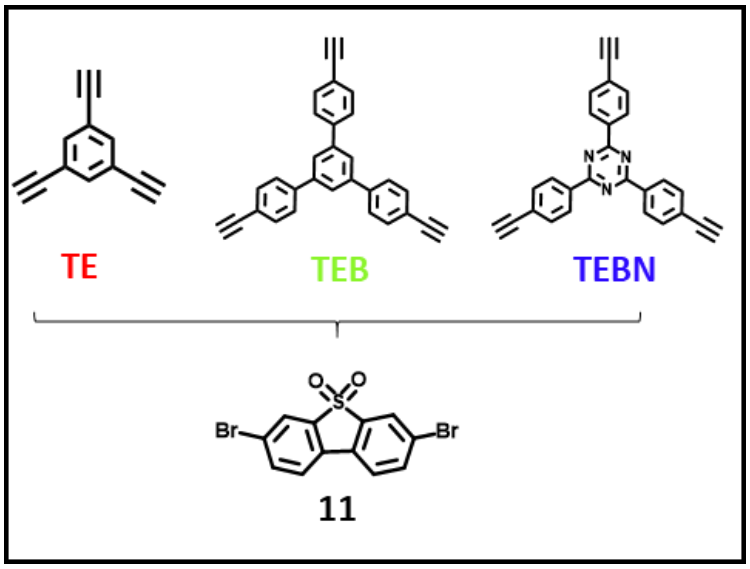

Figure 2.20 Chemical structures of expanded TE analogues.

2.4.2 Characterisations

TEB11 and TEBN11 were characterised by FT-IR (Figure 2.21a), and characteristic bands at 1160 cm^{-1} and 2190 cm^{-1} were attributed to the S=O stretching vibration and C≡C stretching modes, respectively.[30] The presence of alkyne bonds was furthermore confirmed by solid-state ^{13}C cross-polarization magic angle spinning (CP-MAS) NMR spectra (Figure 2.21b) showing a characteristic peak at approximately 90 ppm, and Raman spectra also showed a feature at 2210 cm^{-1} indicative of carbon-carbon triple bonds (Figure 2.21c),[22] which implicated the success of the polymerization. PXRD patterns of all three materials showed that these materials were amorphous (Figure 2.21d). Their morphologies varied: TE11 comprised porous flake-like structures while TEB11 was composed of non-uniform nanospheres; TEBN11 consisted mainly of large, fused aggregates (Figure 2.22). The absorption onset of TEB11 was found

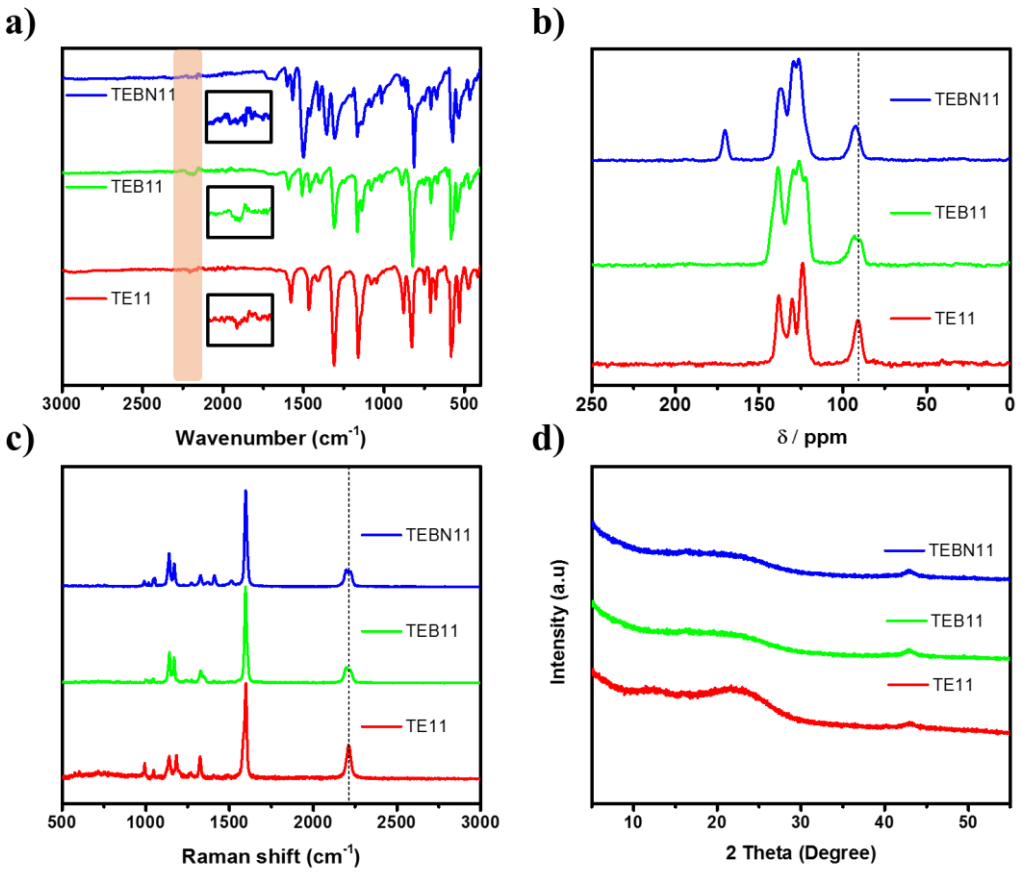

Figure 2.21 (a) Fourier-transform infrared spectra; (b) Solid-state ^{13}C NMR spectra; (c) Raman spectra; (d) PXRD patterns of TE11, TEB11 and TEBN11.

to be similar to TE11, while TEBN11 showed a slight bathochromic shift (Figure 2.23a). In line with this observation, TEBN11 was also predicted to have a narrower fundamental gap than TE11 (Figure 2.23b). Compared with TE11, the photoluminescence emission spectra of TEB11 and TEBN11 showed a red shift (Figure 2.24a), which was consistent with the absorption spectrum. The O=S=O can be confirmed by the X-ray photoelectron spectra and they also showed a shift in the high-resolution peaks of C 1s, O 1s and S 2p after modification of TE11 (Figure 2.25), which could be attributed to the changes of electronic properties induced by extending the linker length and introduction of nitrogen into the benzene-ring.[31] TEB11 and TEBN11 also showed increased fluorescence lifetime (Figure 2.24b and Table 2.7) and improved thermal stability compared with TE11 (Figure 2.26); by contrast, the materials were found to be more hydrophobic against water (Figure 2.27 and Table 2.8), but in the mixture of TEA/MeOH/H_2O, thanks to the organic solvent, the wettability and dispersibility was improved (Table 2.8). Finally, average particle sizes were found to be similar for TE11, TEB11 and TEBN11 (Table 2.9).

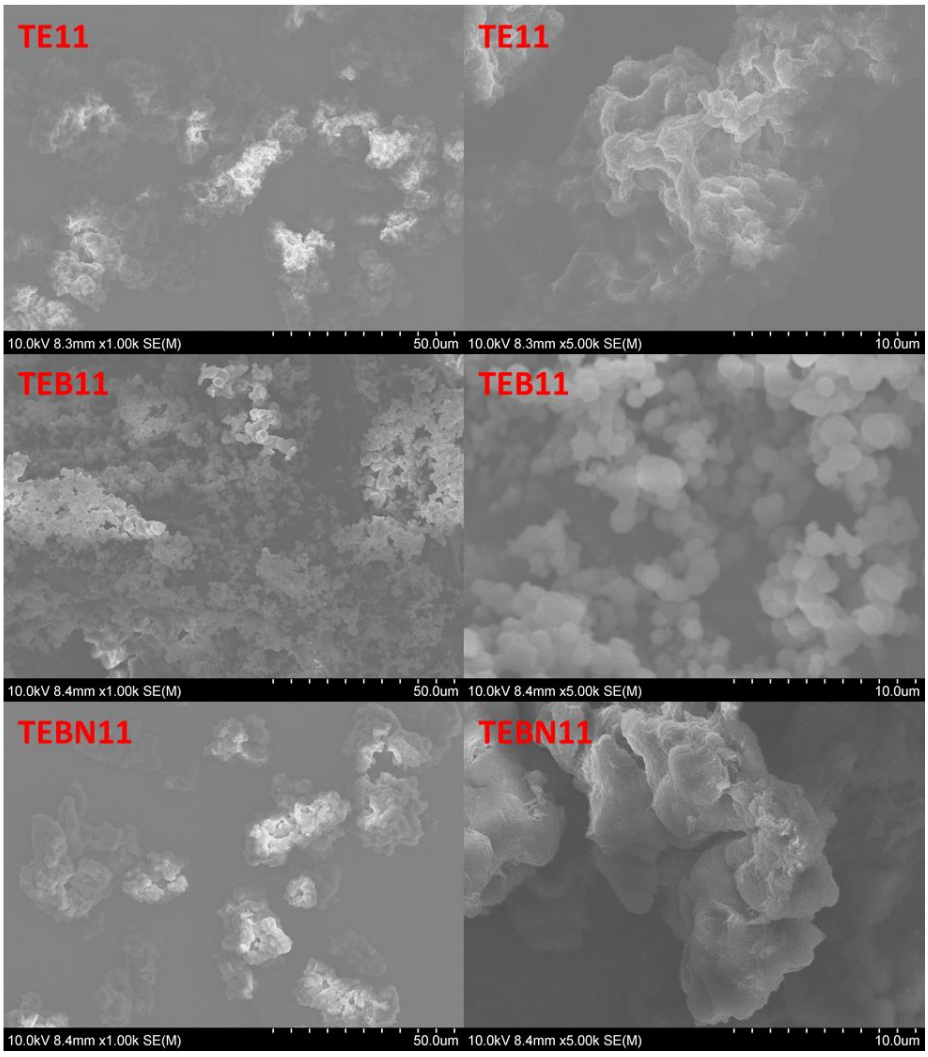

Figure 2.22 SEM images of TE11, TEB11 and TEBN11.

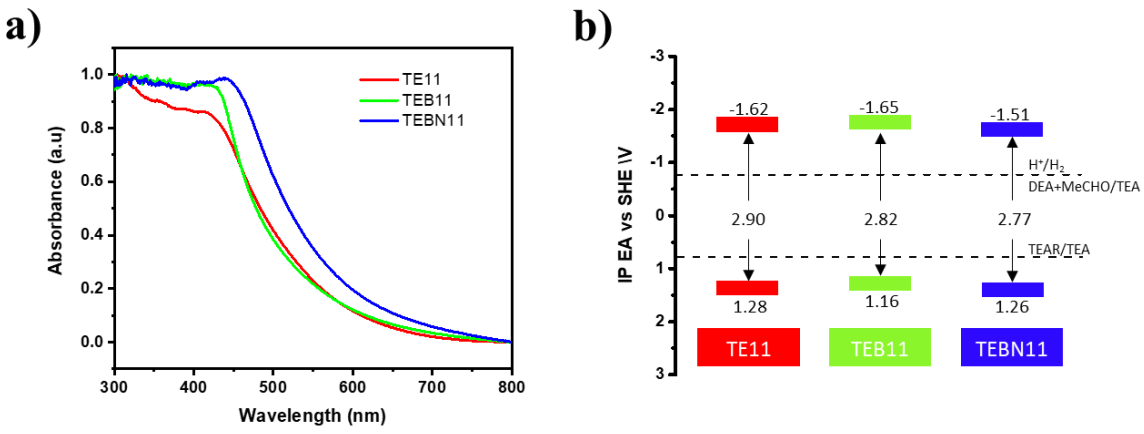

Figure 2.23 a) Solid state UV-vis spectra for copolymers. b) Calculated EA and IP positions for resulting copolymers. Solution half reactions are shown as calculated for pH 12.5 (MeCHO-acetaldehyde; TEAR-deprotonated TEA radical) of TE11, TEB11, and TEBN11.

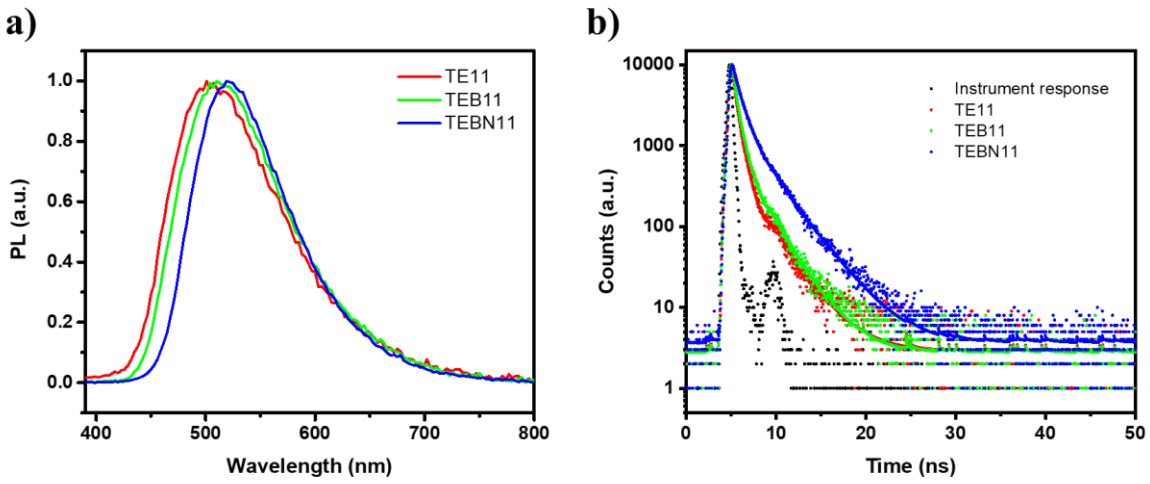

Figure 2.24 a) Photoluminescence emission spectra (λ_{exc} = 371 nm) and b) Fluorescence lifetime of TE11, TEB11 and TEBN11.

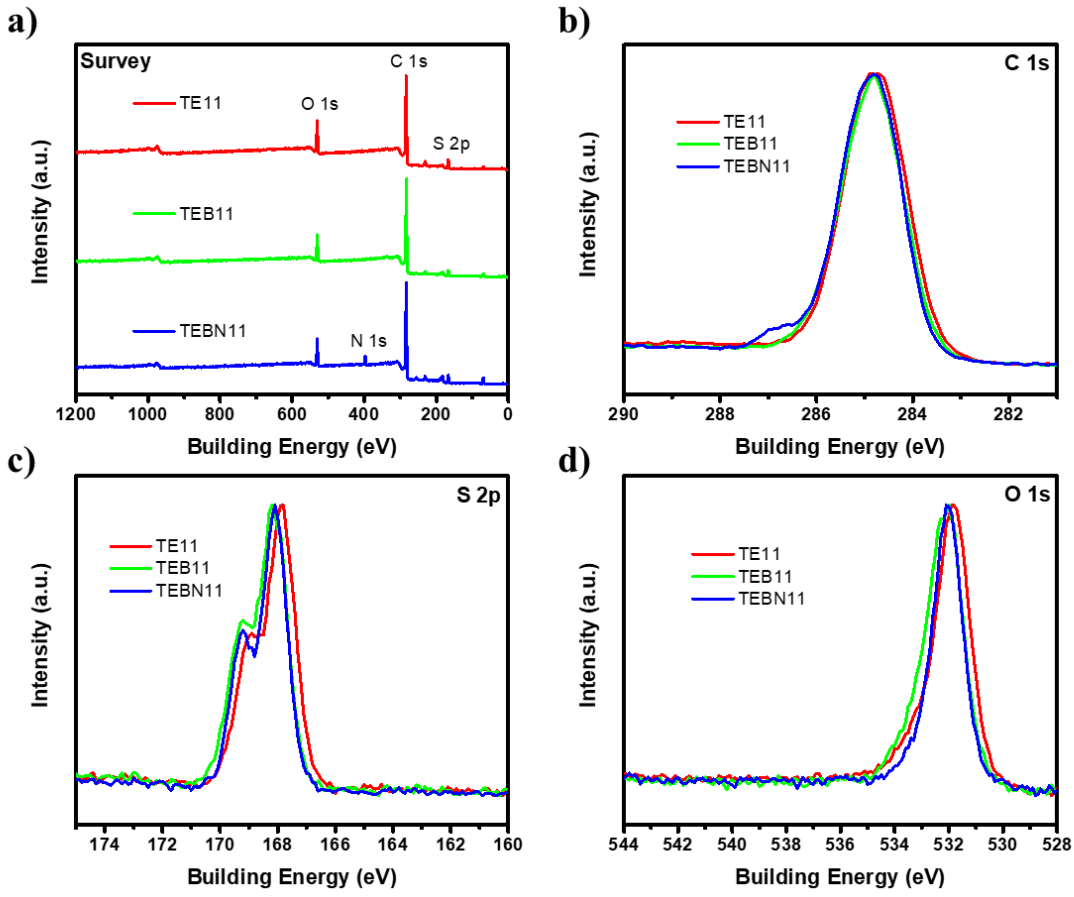

Figure 2.25 XPS spectra of TE11, TEB11 and TEBN11: a) survey spectra, high resolution spectra of b) C 1s, c) S 2p and d) O 1s.

Table 2.7 Estimated fluorescence lifetimes of TE11, TEB11 and TEBN11.

Polymer	λem / nm	τ_1 / ns	B_1 / %	τ_2 / ns	B_2 / %	τ_3 / ns	B_3 / %	χ^2	τ_{avg}[a] / ns
TE11	500	0.20	53.21	0.78	40.51	3.68	6.28	1.531	0.66
TEB11	510	0.28	52.72	0.99	40.50	3.81	6.78	1.281	0.80
TEBN11	520	0.53	34.56	1.40	44.08	3.52	21.36	1.487	1.55

[a] Fluorescence lifetimes for all polymers obtained from fitting time-correlated single photon counting decays to a sum of three exponentials, which yield τ_1, τ_2, and τ_3 according $\sum_{i=1}^{n}(A + B_i exp(-t/\tau_i))$. τ_{avg} is the weighted average lifetime calculated as $\sum_{i=1}^{n}(B_i\tau_i)$.

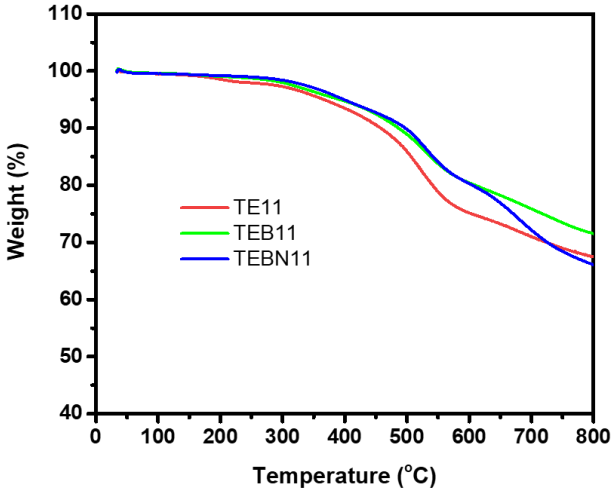

Figure 2.26 Thermogravimetric data of TE11, TEB11 and TEBN11.

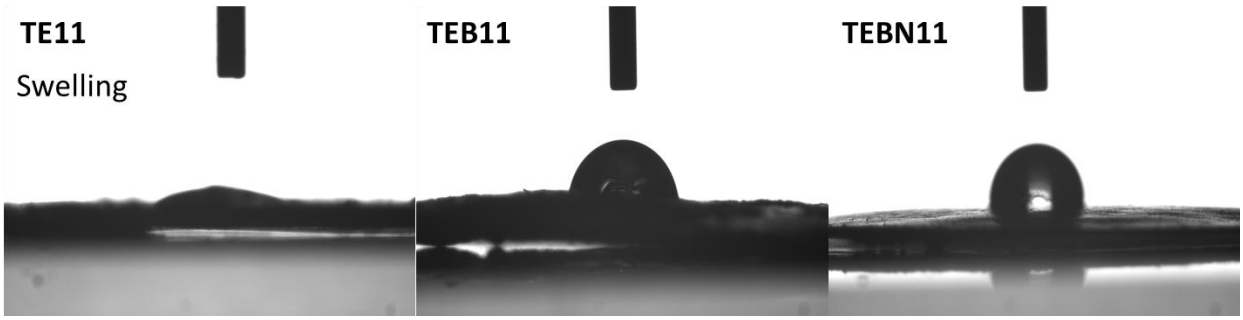

Figure 2.27 Contact angle images against water of TE11, TEB11 and TEBN11. For swelling polymer TE11, the image is taken several seconds after the drop is deposited onto the polymer surface.

Table 2.8 Transmission, BET and contact angle of TE11, TEB11 and TEBN11.

Polymer	Transmission TEA/MeOH/H_2O / %	Surface Area[a] / $m^2 g^{-1}$	Contact angle against water / °
TE11	22.7	154.9	Swelling
TEB11	7.3	12.8	81.3 (±2.0)
TEBN11	17.9	13.6	94.8 (±2.0)

[a] BET surface area determined from the absorption branch of the absorption isotherm measured at 77 K.

Table 2.9 Particle sizes by static light scattering of TE11, TEB11 and TEBN11.

Polymer	*D*x50[a] / µm	*D*[4,3][b] / µm	*D*[3,2][c] / µm	Relative external surface area[d] / $m^2 kg^{-1}$
TE11	25.5	26.7	23.9	251.5
TEB11	39.5	42.2	22.3	268.8
TEBN11	27.7	29.2	22.8	262.8

[a] 50th Percentile of particle size volume distribution; [b] Volume mean diameter; [c] Surface area mean diameter (Sauter mean diameter);[32] [d] Relative extrinsic surface area calculated by dividing the total surface area of the particles by the total mass, assuming a density of 1 g cm^{-3}.

2.4.3 Hydrogen production

To further investigate the photocatalytic performance, the scale-up kinetic hydrogen evolution experiments were carried out under visible light irradiation (300 W Xe light source, $\lambda > 420$ nm filter). A sacrificial hydrogen production rate of 1894 µmol g^{-1} h^{-1} was determined for TEBN11 in TEA/MeOH/H_2O mixtures loaded with platinum, which was nearly twice as high as for TE11 (1080 µmol g^{-1} h^{-1}), while the HER rate of TEB11 (1186 µmol g^{-1} h^{-1}) was only slightly increased compare with TE11 (Figure 2.28a and Table 2.10). The materials were found to contain similar amounts of platinum of approximately 1 wt. % (Table 2.10). All three materials are also active without additional platinum, in this case residual palladium from the synthesis facilitate the proton reduction reaction (Table 2.10).[3, 33]

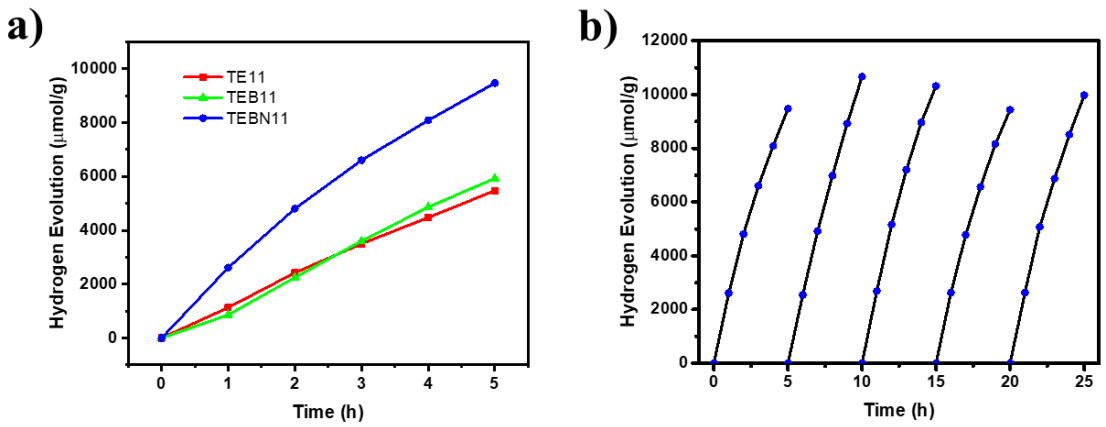

Figure 2.28 a) Photocatalytic HER performance of TE11, TEB11 and TEBN11. b) Repeat photocatalysis runs for TEBN11under visible light (300 W Xe light source with λ > 420 nm filter) in TEA/MeOH/H2O mixture with 3 wt. % Pt, the TEBN11 was recovered, and the reaction solution was replaced between runs.

Table 2.10 Transmission, BET, contact angle and HER of TE11, TEB11 and TEBN11.

Polymer	Added Pt before photoreaction[a] / wt. %	Detected Pt after photoreaction[b] / wt. %	HER[c] / μmol g^{-1} h^{-1}	HER[d] / μmol g^{-1} h^{-1}	HER[e] / μmol g^{-1} h^{-1}
TE11	3.0	1.2	1714.8	1811.0	1080 ±41
TEB11	3.0	0.8	1983.8	2103.2	1186 ±131
TEBN11	3.0	1.1	2664.1	3288.5	1894 ±258

[a] The amount was calculated based on the assumption that full deposition of the H_2PtCl_6 precursor occurs.
[b] The amount was determined vis ICP-OES measurements.
[c] 5 mg polymer without Pt in 5 mL TEA/MeOH/H_2O mixture under a solar simulator (AM1.5G, Class AAA, IEC/JIS/ASTM, 1440 W Xe, 12 ×12 in., MODEL: 94123A, illumination time: 2 hours).
[d] 5 mg polymer with 3 wt. % Pt in 5 mL TEA/MeOH/H_2O mixture under a solar simulator (AM1.5G, Class AAA, IEC/JIS/ASTM, 1440 W Xe, 12 ×12 in., MODEL: 94123A, illumination time: 2 hours).
[e] 25 mg polymer with 3 wt. % Pt in 25 mL TEA/MeOH/H_2O mixture under visible light illumination (300 W Xe light with a λ > 420 nm filter).

The higher photocatalytic performance of TEBN11 compared to TEB11 and TE11 seems to originate from its deeper IP and red-shifted absorption onset allowing for enhanced light absorption. This seems to be much more important than the accessible surface area in this case, which is different to what was observed in a previous study.[3]

Photocurrent measurements (Figure 2.29) also showed that TEBN11 had a larger photo-response current. In addition, the photocatalytic activity had no obvious decrease over 25 hours

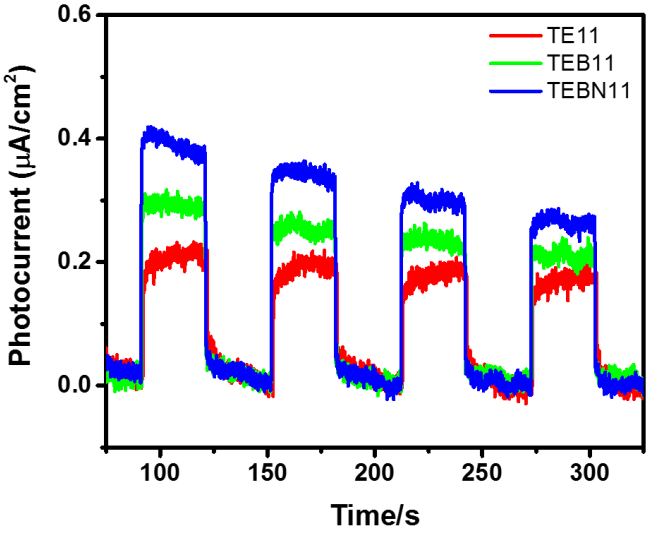

Figure 2.29 Photocurrent densities vs. time for TE11, TEB11 and TEBN11 with applied potentials at 0.6 V vs. Ag/AgCl under intermittent irradiation.

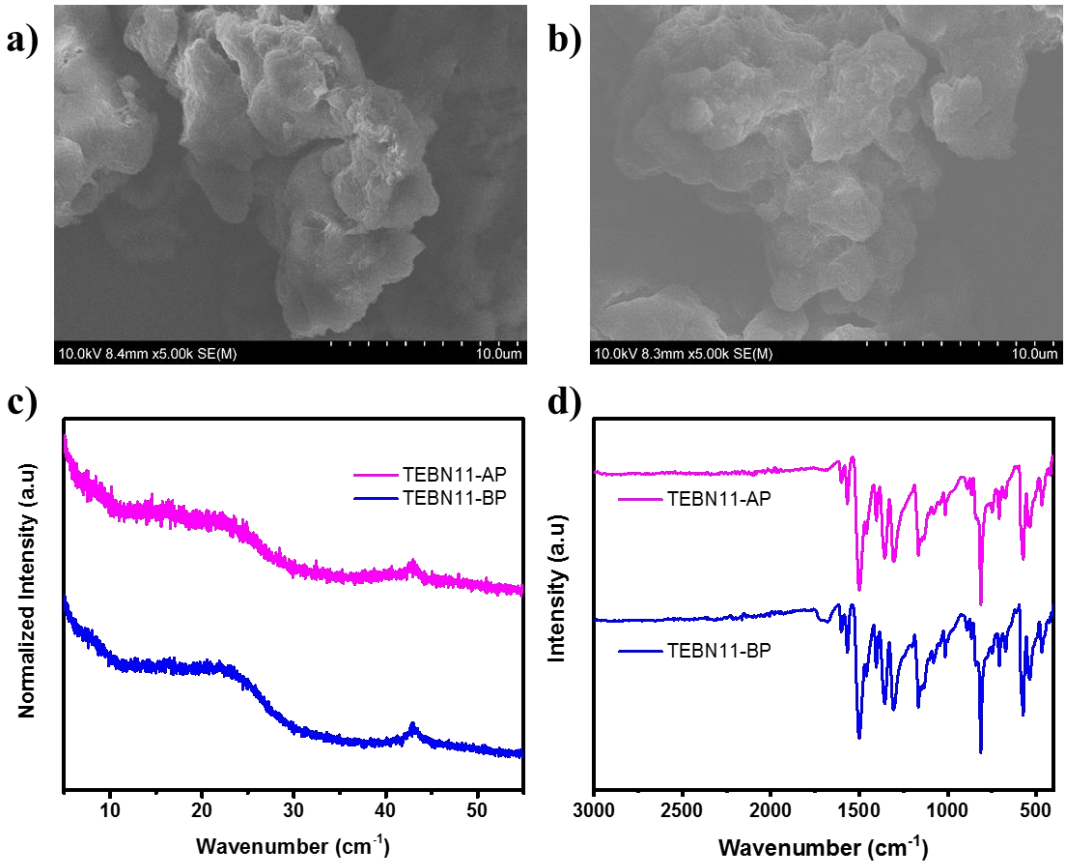

Figure 2.30 SEM images of TEBN11 a) before and b) after photocatalytic H_2 evolution reaction. c) PXRD patterns and d) IR-IR spectra of TEBN11 before (BP) and after (AP) photocatalytic H_2 evolution reaction.

(Figure 2.28b) and the morphology also did not change (Figure 2.30a and 2.30b). PXRD patterns (Figure 2.30c) and FT-IR results (Figure 2.30d) before and after the photocatalytic experiments were nearly the same, which indicating that TEBN11 has good photocatalytic stability. The external quantum efficiency (EQE) was measured at different wavelength to evaluate the HER performance, the EQE value of TEBN11 was 2.7% at 420 nm, which is higher than TEB11 (1.6% at 420 nm) and TE11 (1.6% at 420 nm), and also relatively high compared to some organic polymer catalysts reported, such as covalent triazine-based framework (CTF-2, 1.6% at 420 nm)[34], cyano - substituted carbon-linked framework (OB-POP-3, 2.0% at 420 nm)[35], diacetylene functionalized COF (TP-BDDA, 1.3% at 420 nm),[8] although lower than other dibenzo[*b,d*]thiophene sulfone co-polymers (P7, 7.2% at 420 nm,[36] P10, 11.6% at 420 nm[37] and P64, 20.7% at 420 nm[2]) (Table 2.11). The EQEs at different wavelengths of TEBN11 broadly follow the absorption profile (Figure 2.31), in line with a photocatalytic process.[3]

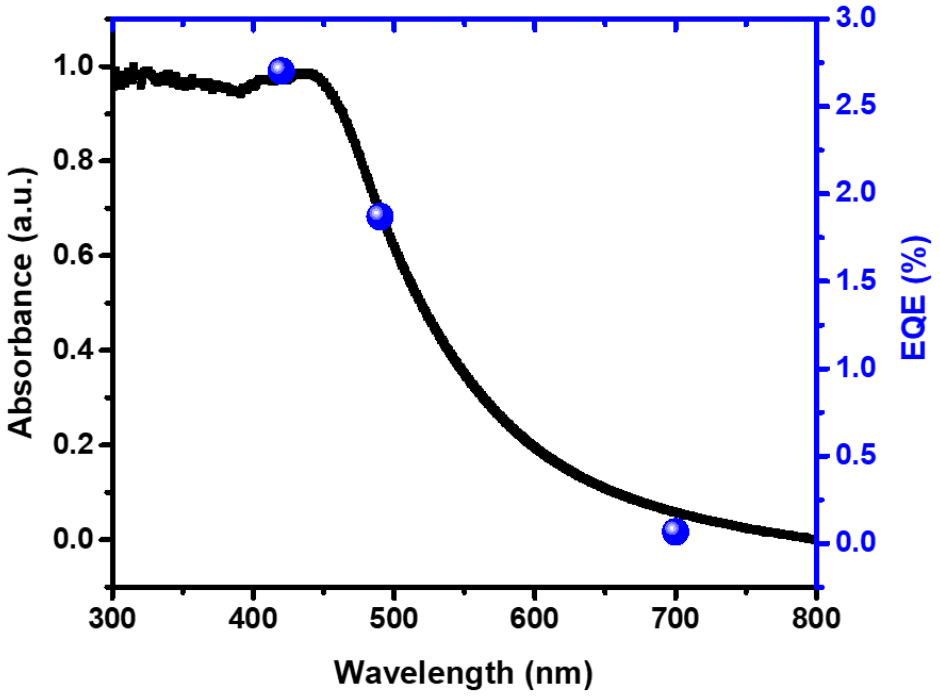

Figure 2.31 Wavelength dependent external quantum efficiency (EQE) values and solid UV-vis spectrum of TEBN11, λ = 420, 490, 700 nm.

Table 2.11 Comparation of TEBN11 with recent representative organic polymer photocatalysts for photocatalytic H_2 evolution.

Sample	Co-catalyst	Reaction solution[a]	λ / nm	EQE / %	Ref.
TEBN11	3 wt.% Pt	TEA/MeOH/H_2O	420	2.7	**This work**
TEBN11	3 wt.% Pt	TEA/MeOH/H_2O	490	1.9	**This work**
TEBN11	3 wt.% Pt	TEA/MeOH/H_2O	700	0.1	**This work**
TEB11	3 wt.% Pt	TEA/MeOH/H_2O	420	1.6	**This work**
TE11	3 wt.% Pt	TEA/MeOH/H_2O	420	1.6	**This work**
P7	Pd residue	TEA/MeOH/H_2O	420	7.2	[36]
P10	Pd residue	TEA/MeOH/H_2O	420	11.6	[37]
P64	Pd residue	TEA/MeOH/H_2O	420	20.7	[2]
CTF-2	3 wt.% Pt	TEA/MeOH/H_2O	420	1.6	[34]
OB-POP-3	3 wt.% Pt	TEOA/H_2O	420	2.0	[35]
N_3-COF	0.68 wt.% Pt	TEOA/PBS buffer	450	0.44	[38]
PCP_{4e}	2 wt.% Pt	TEA/H_2O	350	1.8	[39]
2DPCN	3 wt.% Pt	TEOA/H_2O	490	1.3	[40]
TFPT-OCH_3	3 wt.% Pt	TEOA/H_2O	405	1.03	[41]
NCQDs/PFTBTA Pdot	-	DEA/H_2O	420	0.56	[42]
TP-BDDA	3 wt.% Pt	TEOA/H_2O	420	1.3	[8]

[a] TEA: triethylamine, DEA: diethylamine, MeOH: methanol, TEOA: triethanolamine, PBS: phosphate buffered saline.

2.5 Summary

In summary, 24 acetylene-linked organic polymers were synthesized via Sonogashira poly-condensation and used as photocatalysts for sacrificial hydrogen production from water under visible illumination. Using a high-throughput workflow, photocatalyst TE11, a co-polymer of 1,3,5-triethynylbenzene and dibenzo[*b*,*d*]thiophene sulfone, was identified as the best-performing material with a sacrificial hydrogen evolution rate of 1811.0 μmol g^{-1} h^{-1}. Among these two series of materials, it seems that the sulfone group have large effect on the photocatalytic activity, which can not only improve the hydrophilicity, but also facilitate thermodynamic driving force for hole transfer ability, therefore enhance the photocatalytic activity as reported before.[1, 3, 4] When correlating material properties with the observed hydrogen evolution rates, we found that no single factor is responsible for the high activity of the best performing polymer photocatalysts, it is rather a result of the interaction of multiple properties. We further optimized the structure of polymer of TE11 by increasing the size of the core and adding a triazine ring. This resulted in a further increase in hydrogen production rate under visible light illumination from 1080 μmol g^{-1} h^{-1} for TE11 to 1894 μmol g^{-1} h^{-1} for TEBN11 with an EQE of 2.7% at 420 nm. The material was found to be stable under irradiation for 25 hours, which demonstrates their potential as robust organic photocatalysts for hydrogen production.

It should be noted that in the sacrificial system, methanol was used for wetting and mixing the TEA into the water. When NP2 was added in the H_2O/methanol mixture for photocatalytic reaction, no H_2 was detected, and similar result can be found in reported work,[37] which suggests that the methanol cannot be serve as sacrificial reagent in this case. We did not do the isotopic labelling experiment to confirm the H_2 source in this study, because in previous study, we have done it with D_2O,[21, 43] and found that, among the final gas product, only negligible H_2 can be detected, and the predominant proportion was D_2, which confirmed that this is a photocatalytic process of water splitting.

2.6 Experimental parts

2.6.1 Materials

All reagents were obtained from Sigma-Aldrich, Fluorochem, TCI or Alfa Aesar and used as received, except for 1,3,5-tris-(4-ethynyl-phenyl)-benzene,[44] 2,4,6-tris(4-ethynyl)phenyl]-1,3,5-triazine,[45] which were synthesized using reported literature procedures.

2.6.2 Characterization methods

The absorption spectra of the polymers were recorded on a Cary 5000 UV-visible-NIR spectrophotometer as powders. Transmission FT-IR spectra were obtained with an attenuated total reflectance (ATR) method on a Bruker Tensor-27 spectrometer at room temperature. Photoluminescence spectra were performed on a Shimadzu RF-5301PC fluorescence spectrometer. Time-correlated single photon counting (TCSPC) experiments were measured on an Edinburgh Instruments LS980-D2S2-STM spectrometer (EPL-375 diode, $\lambda = 371$ nm). The instrument response of the TCSPC spectrometer was measured with colloidal silica (LUDOX® HS-40, Sigma-Aldrich) at the excitation wavelength. Decay times were fitted in the FAST software using three decay exponents. Thermogravimetric analysis was performed by heating samples under N_2 in open platinum pans from 25 to 800 °C at 10 °C min^{-1} on an EXSTAR6000 instrument. PXRD measurements were performed on a Panalytical Empyrean diffractometer with a Cu X-ray source. Static light scattering measurements were performed on a Malvern Mastersizer 3000 Particle Sizer at a laser obscuration of 5-10%. Particle sizes were fitted according to the Mie theory with the Malvern 'General Purpose' analysis model. Transmittance of high-throughput samples was measured on a Formulaction S.A.S. Turbiscan AGS system with an 880 nm NIR diode and a detector at 180 ° (relative to the light source) in a cylindrical glass cell. Surface areas were tested on Micromeritics 2420 instrument at a temperature of 77 K. Before analysis, polymer samples were degassed offline at 110 °C for 15 hours under dynamic vacuum (10^{-5} bar). CHNS-O Analyzer was measured using standard microanalytical procedures. Palladium and copper contents were determined using ICP-OES Agilent 5110 equipped with a collision/reaction cell after a microwave digest of the materials in nitric acid (67-69%, trace metal analysis grade) in a microwave. Water contact angles were measured using pressed pellets and a drop-shape analysis apparatus (Krüss DSA100) with the Young-Laplace fitting method. The morphology of the polymer particles was studied using a Hitachi S4800 SEM. X-Ray photoelectron spectroscopy (XPS) measurement were performed on a Thermo Fisher ESCALAB 250Xi instrument. The Raman measurements were performed

on an inVia Reflex Qontor Confocal Raman microscope upon excitation of 785 nm laser. ^{13}C magic-angle spinning measurements were carried out at 100.63 MHz using a Bruker Avance III HD spectrometer and 4 mm (rotor o.d.) probe. Spectra were acquired at a spin rate of 10 kHz. Cross-polarisation (CP) spectra were recorded with TOSS spinning sideband suppression, 4 ms contact time and with a recycle delay of 4 s. Carbon spectral referencing is relative to neat tetramethylsilane, carried out by setting the high frequency signal from an external sample of adamantane to 38.5 ppm.

2.6.3 Synthetic procedure of polymers

General procedure for the Sonogashira polycondensation: in a glovebox, a glass vial was charged with the monomers, $Pd(PPh_3)_2Cl_2$, CuI, triphenylphosphine, anhydrous *N*,*N*-dimethylformamide and triethylamine, and then sealed with a silicone septum. The sealed vials were taken out of the glovebox, inserted in a sand bath preheated to 100 ℃ and kept at this temperature for 2 days. After cooling to room temperature, the mixture was quenched by addition of methanol, and the solids were filtered off. Further purification was carried out by Soxhlet extraction with methanol and chloroform. The final product was dried in the vacuum oven at 80 ℃ overnight. See the supplementary data for detail results of all polymers.

TE1: 2,5-Dibromothiophene (242 mg, 1 mmol), 1,3,5-triethynylbenzene (100 mg, 0.68 mmol), $Pd(PPh_3)_2Cl_2$ (18 mg, 0.03 mmol), CuI (10 mg, 0.05 mmol), triphenylphosphine (13 mg, 0.05 mmol), *N*,*N*-dimethylformamide (9 mL) and triethylamine (9 mL) were used in this polycondensation reaction described in the general procedure. After work-up and Soxhlet the product was obtained as a red solid (149.6 mg, 83%). Anal. Calcd for $(C_{12}H_4S)_n$: C, 79.97; H, 2.24; S, 17.79%; Found C, 75.50; H, 3.00; S, 15.50%. Pd content: 1.27%, Cu content: 0.04%.

TE2: 5,5'-Dibromo-2,2'-bithiophene (324 mg, 1 mmol), 1,3,5-triethynylbenzene (100 mg, 0.68 mmol), $Pd(PPh_3)_2Cl_2$ (18 mg, 0.03 mmol), CuI (10 mg, 0.05 mmol), triphenylphosphine (13 mg, 0.05 mmol), *N*,*N*-dimethylformamide (9 mL) and triethylamine (9 mL) were used in this polycondensation reaction described in the general procedure. After work-up and Soxhlet the product was obtained as a red solid (239.8 mg, 91%). Anal. Calcd for $(C_{16}H_6S_2)_n$: C, 73.25; H, 2.31; S, 24.44%; Found C, 71.00; H, 3.00;S, 23.00%. Pd content: 0.31%, Cu content: 0.02%.

TE3: 5,5''-Dibromo-2,2':5',2''-terthiophene (406 mg, 1 mmol), 1,3,5-triethynylbenzene (100 mg, 0.68 mmol), $Pd(PPh_3)_2Cl_2$ (18 mg, 0.03 mmol), CuI (10 mg, 0.05 mmol), triphenylphosphine (13 mg, 0.05 mmol), *N*,*N*-dimethylformamide (9 mL) and triethylamine (9mL) were used in this polycondensation reaction described in the general procedure. After work-up and Soxhlet the product was obtained as a red solid (319.7 mg, 93%). Anal. Calcd for $(C_{20}H_8S_3)_n$: C, 69.74; H, 2.34; S, 27.92%; Found C, 68.00; H, 3.00; S, 26.00%. Pd content: 0.40%, Cu content: 0.00%.

TE4: 2,5-Dibromothieno[3,2-*b*]thiophene (298 mg, 1 mmol), 1,3,5-triethynylbenzene (100 mg, 0.68 mmol), $Pd(PPh_3)_2Cl_2$ (18 mg, 0.03 mmol), CuI (10 mg, 0.05 mmol), triphenylphosphine (13 mg, 0.05 mmol), *N*,*N*-dimethylformamide (9 mL) and triethylamine (9 mL) were used in this polycondensation reaction described in the general procedure. After work-up and Soxhlet the product was obtained as a red solid (163.4 mg, 69%). Anal. Calcd for $(C_{14}H_4S_2)_n$: C, 71.16; H, 1.71;S, 27.13%; Found C, 65.50; H, 2.00;S, 22.50%. Pd content: 0.99%, Cu content: 0.08%.

TE5: 2,5-Dibromopyrazine (238 mg, 1 mmol), 1,3,5-triethynylbenzene (100 mg, 0.68 mmol), $Pd(PPh_3)_2Cl_2$ (18 mg, 0.03 mmol), CuI (10 mg, 0.05 mmol), triphenylphosphine (13 mg, 0.05 mmol), *N*,*N*-dimethylformamide (9 mL) and triethylamine (9 mL) were used in this polycondensation reaction described in the general procedure. After work-up and Soxhlet the product was obtained as a yellow solid (146.6 mg, 83%). Anal. Calcd for $(C_{12}H_4N_2)_n$: C, 81.81; H, 2.29; N, 15.90%; Found C, 69.34; H, 2.48; N, 13.20%. Pd content: 1.50%, Cu content: 0.19%.

TE6: 2,5-Dibromopyrimidine (238 mg, 1 mmol), 1,3,5-triethynylbenzene (100 mg, 0.68 mmol), $Pd(PPh_3)_2Cl_2$ (18 mg, 0.03 mmol), CuI (10 mg, 0.05 mmol), triphenylphosphine (13 mg, 0.05 mmol), *N*,*N*-dimethylformamide (9 mL) and triethylamine (9 mL) were used in this polycondensation reaction described in the general procedure. After work-up and Soxhlet the product was obtained as a yellow solid (168.4 mg, 96%). Anal. Calcd for $(C_{12}H_4N_2)_n$: C, 81.81; H, 2.29; N, 15.90%; Found C, 69.35; H, 2.51; N, 12.69%. Pd content: 1.10%, Cu content: 0.21%.

TE7: 2,5-Dibromopyridine (237 mg, 1 mmol), 1,3,5-triethynylbenzene (100 mg, 0.68 mmol), $Pd(PPh_3)_2Cl_2$ (18 mg, 0.03 mmol), CuI (10 mg, 0.05 mmol), triphenylphosphine (13 mg, 0.05 mmol), *N*,*N*-dimethylformamide (9 mL) and triethylamine (9 mL) were used in this

polycondensation reaction described in the general procedure. After work-up and Soxhlet the product was obtained as a yellow solid (154.3 mg, 88%). Anal. Calcd for $(C_{13}H_5N)_n$: C, 89.13; H, 2.88; N, 8.00%; Found C, 74.98; H, 2.77; N, 6.54%. Pd content: 0.11%, Cu content: 0.13%.

TE8: 5,5'-Dibromo-2,2'-bipyridine (314 mg, 1 mmol), 1,3,5-triethynylbenzene (100 mg, 0.68 mmol), $Pd(PPh_3)_2Cl_2$ (18 mg, 0.03 mmol), CuI (10 mg, 0.05 mmol), triphenylphosphine (13 mg, 0.05 mmol), *N*,*N*-dimethylformamide (9 mL) and triethylamine (9 mL) were used in this polycondensation reaction described in the general procedure. After work-up and Soxhlet the product was obtained as a yellow solid (116.0 mg, 46%). Anal. Calcd for $(C_{18}H_8N_2)_n$: C, 85.70; H, 3.20; N, 11.10%; Found C, 73.01; H, 2.91; N, 9.33%. Pd content: 0.88%, Cu content: 0.40%.

TE9: 2,7-Dibromofluorene (324 mg, 1 mmol), 1,3,5-triethynylbenzene (100 mg, 0.68 mmol), $Pd(PPh_3)_2Cl_2$ (18 mg, 0.03 mmol), CuI (10 mg, 0.05 mmol), triphenylphosphine (13 mg, 0.05 mmol), *N*,*N*-dimethylformamide (9 mL) and triethylamine (9 mL) were used in this polycondensation reaction described in the general procedure. After work-up and Soxhlet the product was obtained as a yellow solid (251.5 mg, 96%). Anal. Calcd for $(C_{21}H_{10})_n$: C, 96.16; H, 3.84%; Found C, 80.63; H, 3.53%. Pd content: 0.94%, Cu content: 0.11%.

TE10: 3,7-Dibromodibenzo[*b*,*d*]thiophene (342 mg, 1 mmol), 1,3,5-triethynylbenzene (100 mg, 0.68 mmol), $Pd(PPh_3)_2Cl_2$ (18 mg, 0.03 mmol), CuI (10 mg, 0.05 mmol), triphenylphosphine (13 mg, 0.05 mmol), *N*,*N*-dimethylformamide (9 mL) and triethylamine (9 mL) were used in this polycondensation reaction described in the general procedure. After work-up and Soxhlet the product was obtained as a yellow solid (262.5 mg, 94%). Anal. Calcd for $(C_{20}H_8S)_n$: C, 85.69; H, 2.88; S, 11.44%; Found C, 73.50; H, 3.00; S, 9.50%. Pd content: 0.59%, Cu content: 0.04%.

TE11: 3,7-Dibromodibenzo[*b*,*d*]thiophene sulfone (374 mg, 1 mmol), 1,3,5-triethynylbenzene (100 mg, 0.68 mmol), $Pd(PPh_3)_2Cl_2$ (18 mg, 0.03 mmol), CuI (10 mg, 0.05 mmol), triphenylphosphine (13 mg, 0.05 mmol), *N*,*N*-dimethylformamide (9 mL) and triethylamine (9 mL) were used in this polycondensation reaction described in the general procedure. After work-up and Soxhlet the product was obtained as a yellow solid (291.7 mg, 94%). Anal. Calcd for $(C_{20}H_8O_2S)_n$: C, 76.91; H, 2.58; S, 10.26%; Found C, 69.50; H, 3.00; S, 9.00%. Pd content: 0.64%, Cu content: 0.10%.

TE12: 2,7-Dibromo-9*H*-carbazole (325 mg, 1 mmol), 1,3,5-triethynylbenzene (100 mg, 0.68 mmol), $Pd(PPh_3)_2Cl_2$ (18 mg, 0.03 mmol), CuI (10 mg, 0.05 mmol), triphenylphosphine (13 mg, 0.05 mmol), *N*,*N*-dimethylformamide (9 mL) and triethylamine (9 mL) were used in this polycondensation reaction described in the general procedure. After work-up and Soxhlet the product was obtained as a black solid (236.1 mg, 90%). Anal. Calcd for $(C_{20}H_9N)_n$: C, 91.23; H, 3.45; N, 5.32%; Found C, 73.64; H, 3.23; N, 3.40%. Pd content: 0.42%, Cu content: 0.20%.

DE1: 2,5-Dibromothiophene (242 mg, 1 mmol), 1,4-diethynylbenzene (126 mg, 1 mmol), $Pd(PPh_3)_2Cl_2$ (18 mg, 0.03 mmol), CuI (10 mg, 0.05 mmol), triphenylphosphine (13 mg, 0.05 mmol), *N*,*N*-dimethylformamide (9 mL) and triethylamine (9 mL) were used in this polycondensation reaction described in the general procedure. After work-up and Soxhlet the product was obtained as a red solid (195.7 mg, 95%). Anal. Calcd for $(C_{14}H_6S)_n$: C, 81.52; H, 2.93; S, 15.54%; Found C, 76.00; H, 3.00; S, 14.00%. Pd content: 0.27%, Cu content: 0.01%.

DE2: 5,5'-Dibromo-2,2'-bithiophene (324 mg, 1 mmol), 1,4-diethynylbenzene (126 mg, 1 mmol), $Pd(PPh_3)_2Cl_2$ (18 mg, 0.03 mmol), CuI (10 mg, 0.05 mmol), triphenylphosphine (13 mg, 0.05 mmol), *N*,*N*-dimethylformamide (9 mL) and triethylamine (9 mL) were used in this polycondensation reaction described in the general procedure. After work-up and Soxhlet the product was obtained as a red solid (268.4 mg, 93%). Anal. Calcd for $(C_{18}H_8S_2)_n$: C, 74.97; H, 2.80; S, 22.23%; Found C, 67.00; H, 3.00; S, 20.00%. Pd content: 0.40%, Cu content: 0.02%.

DE3: 5,5''-Dibromo-2,2':5',2''-terthiophene (406 mg, 1 mmol), 1,4-diethynylbenzene (126 mg, 1 mmol), $Pd(PPh_3)_2Cl_2$ (18 mg, 0.03 mmol), CuI (10 mg, 0.05 mmol), triphenylphosphine (13 mg, 0.05 mmol), *N*,*N*-dimethylformamide (9 mL) and triethylamine (9 mL) were used in this polycondensation reaction described in the general procedure. After work-up and Soxhlet the product was obtained as a red solid (364.2 mg, 98%). Anal. Calcd for $(C_{22}H_{10}S_3)_n$: C, 71.32; H, 2.72; S, 25.96%; Found C, 64.00; H, 3.50; S, 23.50%. Pd content: 0.45%, Cu content: 0.04%.

DE4: 2,5-Dibromothieno[3,2-*b*]thiophene (298 mg, 1 mmol), 1,4-diethynylbenzene (126 mg, 1 mmol), $Pd(PPh_3)_2Cl_2$ (18 mg, 0.03 mmol), CuI (10 mg, 0.05 mmol), triphenylphosphine (13 mg, 0.05 mmol), *N*,*N*-dimethylformamide (9 mL) and triethylamine (9 mL) were used in this polycondensation reaction described in the general procedure. After work-up and Soxhlet the product was obtained as a red solid (250.0 mg, 95%). Anal. Calcd for $(C_{14}H_4S_2)_n$: C, 73.25; H, 2.31; S, 24.44%; Found C, 67.00; H, 3.00; S, 22.50%. Pd content: 0.86%, Cu content: 0.05%.

DE5: 2,5-Dibromopyrazine (238 mg, 1 mmol), 1,4-diethynylbenzene (126 mg, 1 mmol), $Pd(PPh_3)_2Cl_2$ (18 mg, 0.03 mmol), CuI (10 mg, 0.05 mmol), triphenylphosphine (13 mg, 0.05 mmol), *N*,*N*-dimethylformamide (9 mL) and triethylamine (9 mL) were used in this polycondensation reaction described in the general procedure. After work-up and Soxhlet the product was obtained as a yellow solid (190.9 mg, 94%). Anal. Calcd for $(C_{14}H_6N_2)_n$: C, 83.16; H, 2.99; N, 13.85%; Found C, 70.87; H, 2.89; N, 11.39%. Pd content: 1.00%, Cu content: 0.09%.

DE6: 2,5-Dibromopyrimidine (238 mg, 1 mmol), 1,4-diethynylbenzene (126 mg, 1 mmol), $Pd(PPh_3)_2Cl_2$ (18 mg, 0.03 mmol), CuI (10 mg, 0.05 mmol), triphenylphosphine (13 mg, 0.05 mmol), *N*,*N*-dimethylformamide (9 mL) and triethylamine (9 mL) were used in this polycondensation reaction described in the general procedure. After work-up and Soxhlet the product was obtained as a yellow solid (197.9 mg, 98%). Anal. Calcd for $(C_{14}H_6N_2)_n$: C, 83.16; H, 2.99; N, 13.85%; Found C, 72.07; H, 2.90;N, 11.67%. Pd content: 1.07%, Cu content: 0.05%.

DE7: 2,5-Dibromopyridine (237 mg, 1 mmol), 1,4-diethynylbenzene (126 mg, 1 mmol), $Pd(PPh_3)_2Cl_2$ (18 mg, 0.03 mmol), CuI (10 mg, 0.05 mmol), triphenylphosphine (13 mg, 0.05 mmol), *N*,*N*-dimethylformamide (9 mL) and triethylamine (9 mL) were used in this polycondensation reaction described in the general procedure. After work-up and Soxhlet the product was obtained as a yellow solid (194.0 mg, 96%). Anal. Calcd for $(C_{15}H_7N)_n$: C, 89.53; H, 3.51; N, 6.96%; Found C, 76.27; H, 3.23; N, 5.77%. Pd content: 0.43%, Cu content: 0.05%.

DE8: 5,5'-Dibromo-2,2'-bipyridine (314 mg, 1 mmol), 1,4-diethynylbenzene (126 mg, 1 mmol), $Pd(PPh_3)_2Cl_2$ (18 mg, 0.03 mmol), CuI (10 mg, 0.05 mmol), triphenylphosphine (13 mg, 0.05 mmol), *N*,*N*-dimethylformamide (9 mL) and triethylamine (9 mL) were used in this polycondensation reaction described in the general procedure. After work-up and Soxhlet the product was obtained as a yellow solid (268.8 mg, 97%). Anal. Calcd for $(C_{20}H_{10}N_2)_n$: C, 86.31; H, 3.62; N, 10.07%; Found C, 71.54; H, 3.18; N, 8.43%. Pd content: 0.58%, Cu content: 0.64%.

DE9: 2,7-Dibromofluorene (324 mg, 1 mmol), 1,4-diethynylbenzene (126 mg, 1 mmol), $Pd(PPh_3)_2Cl_2$ (18 mg, 0.03 mmol), CuI (10 mg, 0.05 mmol), triphenylphosphine (13 mg, 0.05 mmol), *N*,*N*-dimethylformamide (9 mL) and triethylamine (9 mL) were used in this polycondensation reaction described in the general procedure. After work-up and Soxhlet the

product was obtained as a yellow solid (185.0 mg, 64%). Anal. Calcd for $(C_{23}H_{12})_n$: C, 95.81; H, 4.19%; Found C, 82.23; H, 3.81%. Pd content: 0.46%, Cu content: 0.07%.

DE10: 3,7-Dibromodibenzo[*b*,*d*]thiophene (342 mg, 1 mmol), 1,4-diethynylbenzene (126 mg, 1 mmol), $Pd(PPh_3)_2Cl_2$ (18 mg, 0.03 mmol), CuI (10 mg, 0.05 mmol), triphenylphosphine (13 mg, 0.05 mmol), *N*,*N*-dimethylformamide (9 mL) and triethylamine (9 mL) were used in this polycondensation reaction described in the general procedure. After work-up and Soxhlet the product was obtained as a yellow solid (299.0 mg, 98%). Anal. Calcd for $(C_{22}H_{10}S)_n$: C, 86.25; H, 3.29; S, 10.46%; Found C, 73.50; H, 3.00; S, 9.00%. Pd content: 0.50%, Cu content: 0.06%.

DE11: 3,7-Dibromodibenzo[*b*,*d*]thiophene sulfone (374 mg, 1 mmol), 1,4-diethynylbenzene (126 mg, 1 mmol), $Pd(PPh_3)_2Cl_2$ (18 mg, 0.03 mmol), CuI (10 mg, 0.05 mmol), triphenylphosphine (13 mg, 0.05 mmol), *N*,*N*-dimethylformamide (9 mL) and triethylamine (9 mL) were used in this polycondensation reaction described in the general procedure. After work-up and Soxhlet the product was obtained as a yellow solid (306.6 mg, 91%). Anal. Calcd for $(C_{22}H_{10}O_2S)_n$: C, 78.09; H, 2.98; S, 9.47%; Found C, 70.00; H, 3.00; S, 9.00%. Pd content: 0.61%, Cu content: 0.04%.

DE12: 2,7-Dibromo-9*H*-carbazole (325 mg, 1 mmol), 1,4-diethynylbenzene (126 mg, 1 mmol), $Pd(PPh_3)_2Cl_2$ (18 mg, 0.03 mmol), CuI (10 mg, 0.05 mmol), triphenylphosphine (13 mg, 0.05 mmol), *N*,*N*-dimethylformamide (9 mL) and triethylamine (9 mL) were used in this polycondensation reaction described in the general procedure. After work-up and Soxhlet the product was obtained as a yellow solid (139.1 mg, 48%). Anal. Calcd for $(C_{22}H_{11}N)_n$: C, 91.33; H, 3.83; N, 4.84%; Found C, 77.16; H, 3.58; N, 3.61%. Pd content: 0.43%, Cu content: 0.29%.

TEB11: 3,7-Dibromodibenzo[*b*,*d*]thiophene sulfone (374 mg, 1 mmol), 1,3,5-tris(4-ethynyl-phenyl) benzene (252 mg, 0.68 mmol), $Pd(PPh_3)_2Cl_2$ (18 mg, 0.03 mmol), CuI (10 mg, 0.05 mmol), triphenylphosphine (13 mg, 0.05 mmol), *N*,*N*-dimethylformamide (9 mL) and triethylamine (9 mL) were used in this polycondensation reaction described in the general procedure. After work-up and Soxhlet the product was obtained as a yellow solid (392.7 mg, 73%). Anal. Calcd for $(C_{38}H_{20}O_2S)_n$: C, 84.42; H, 3.73; S, 5.93%; Found C, 75.50; H, 4.00; S, 6.50%. Pd content: 0.48%, Cu content: 0.05%.

TEBN11: 3,7-Dibromodibenzo[*b*,*d*]thiophene sulfone (374 mg, 1 mmol), 2,4,6-tris(4-ethynyl)phenyl]-1,3,5-triazine (254 mg, 0.68 mmol), $Pd(PPh_3)_2Cl_2$ (18 mg, 0.03 mmol), CuI (10 mg, 0.05 mmol), triphenylphosphine (13 mg, 0.05 mmol), *N*,*N*-dimethylformamide (9 mL) and triethylamine (9 mL) were used in this polycondensation reaction described in the general procedure. After work-up and Soxhlet the product was obtained as a yellow solid (353.0 mg, 65%). Anal. Calcd for $(C_{22}H_{10}O_2N_3S)_n$: C, 77.33; H, 3.15; N, 7.73; S, 5.90%; Found C, 70.50; H, 3.00; N, 5.00; S, 6.50%. Pd content: 0.54%, Cu content: 0.12%.

2.6.4 High-throughput photocatalytic hydrogen evolution experiments

High-throughput screening experiments were carried out using an automatic platform. For this, a sample vial (10 mL) was charged with 5 mg of polymer powders and H_2PtCl_6 solution (0.01 mL, 3 wt. % in H_2O), then all vials along with degassed jars of triethylamine, methanol, and H_2O were transferred to the Chemspeed Accelerator SWING and purged with nitrogen for 6 hours. After that, the liquid transfer head was used to transfer liquids (trimethylamine/methanol/water = 1:1:1; total volume = 5 mL) form the jars to the vials automatically under inert conditions, then the vials were capped with the capper/crimper tool. The sealed vials were subsequently taken out and transferred to an ultrasonic bath to finely disperse polymers by ultrasonication for 10 minutes. Photocatalytic hydrogen evolution experiments were performed on an Oriel Solar Simulator 94123A with an output of 1.0 Sun (Class AAA, 1440 W Xe lamp, 12 × 12 in.). After 2 hours, the amount of hydrogen evolved was determined on an Agilent HS-GC (7890B). Control experiments of mixtures of trimethylamine/methanol/water or trimethylamine/methanol/water/H_2PtCl_6 showed that no hydrogen was produced in the absence of a photocatalyst.

2.6.5 Kinetic photocatalytic hydrogen evolution measurements

A quartz reaction flask was charge with 25 mg polymer and 25 mL mixtures of water/triethylamine/methanol=1:1:1 and 0.02 mL H_2PtCl_6 solution (8 wt. % in H_2O), the flask was sealed with a rubber stopper. After ultrasonication for 10 minutes, the well-dispersed suspension was degassed by bubbling with N_2 for 30 minutes before illuminating with a 300 W Newport Xe light source with a filter ($\lambda > 420$ nm). The concentration of hydrogen was determined by a Bruker 450-GC gas chromatograph equipped with TCD detector. For longer-term stability experiments, after illumination for 5 hours, the polymer was recovered through filtration, and after drying, 25 mL mixtures of water/triethylamine/methanol=1:1:1 were added

again for the next run. For external quantum efficiency (EQE) measurements, experiments were performed under a light-emitting diode irradiation (λ = 420, 490, 700 nm), and the EQE was estimated using the following formula:

$$\mathrm{EQE\%} = \frac{2 \times \text{Number of evolved } H_2 \text{ molecules}}{\text{Number of incident photons}} \times 100\%$$

2.6.6 Electrochemical measurements

Electrochemical experiments were performed on the BioLogic SP200 workstation. The transient photocurrent responses (*I*–t) and electrochemical impedance spectra (EIS) of samples were investigated in a three-electrode system (FTO, Pt plate, and Ag/AgCl as working, counter, and reference electrode, respectively) using a 300 W Xe light source (Newport). The electrolyte was 0.5 M Na_2SO_4 aqueous solution and was degassed for 30 minutes by N_2 at room temperature before the measurement. The working electrode was prepared as follows: 2 mg of the photocatalyst was ultrasonicated with 10 μL Nafion (5 wt. %) aqueous solution and 100 μL ethanol giving a slurry. The slurry was then coated onto FTO glass electrodes with an active area of 1 cm^2. The applied bias for intermittent photocurrent intensity measurement was 0.6 V vs. Ag/AgCl. The EIS spectra were determined by applying a 10 mV AC signal over the frequency range of 100 kHz to 10 mHz at a DC bias of 0.6 V vs. Ag/AgCl.

2.6.7 Density functional theory (DFT) calculations

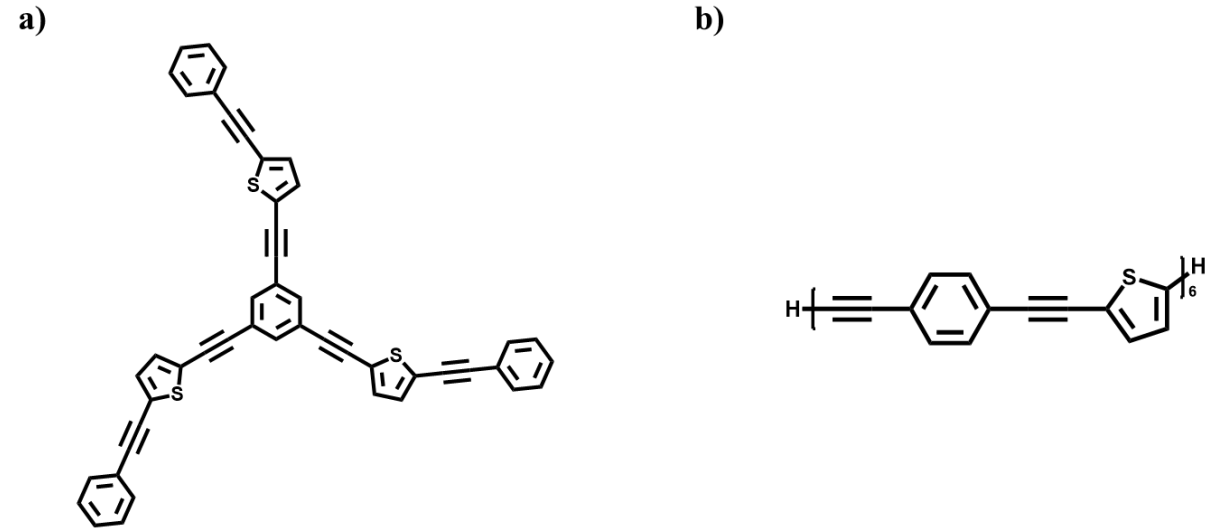

Figure 2.32 Simulation models of polymers (a) TE1 and (b) DE1.

For each of the TE polymers, the simulation model consisted of a single unit of monomer 1 substituted with three units of monomer 2. The latter were capped by phenylacetylene (–C≡C–C_6H_5) groups. In Figure 2.32a, the resulting model is shown on the example of polymer TE1. The DE polymers, in turn, were each represented by an oligomer which consists of six repeat units (see Figure 2.32b). The termini of the oligomer chain were capped with hydrogen atoms. The structures of the oligomers were constructed with the program STK.[46] Afterwards, for each oligomer, we generated a set of 500 trial structures to serve as the starting points for the conformation search. These were sampled from molecular dynamics (MD) trajectories in which the electronic structure of the oligomer was treated with the use of the extended semiempirical tight-binding[47] (xTB) model. In order to allow the oligomer to sample a broad volume of the conformation space, during the MD simulations the temperature of the system was maintained at 600 K. Afterwards, the trial structures were optimized at the xTB level of theory.

The resulting equilibrium geometries were ranked according to energy. It was assumed that the lowest-energy conformer of each oligomer is representative of the properties of the given polymer. Accordingly, this conformer was selected for the calculation of the electronic and optical properties.

The xTB calculations were performed with the Semiempirical Extended Tight-Binding Program Package (xtb2019), version 5.6.4SE, and used the GFN2 parameterization of the xTB model.[48] Aqueous solvation was represented via the generalized Born model augmented with the hydrophobic solvent accessible surface area term (GBSA). At the stage of the conformation search, all oligomers were considered to exist in the charge-neutral forms.

DFT calculations are helpful for computationally screening of candidate polymer photocatalysts and to gain a deep understanding of the structure and property relationships. For the DFT calculations, the TE and DE polymers were represented by finite (i.e., nonperiodic) oligomeric models; linear oligomers of composition $(L(DE))_6$ in the case of DE polymers and a TE centered $(TE)(L(TE))_3$ oligomers in the case of the TE polymers (Figure 2.32). The starting structures of the oligomers were constructed with the program STK.[46] Having identified the representative conformer of each oligomer, we proceeded to optimize its geometry using density functional theory (DFT). To calculate the adiabatic ionization potential (IP) and adiabatic electron affinity (EA)

of the oligomer, the geometries of the radical cation and radical anion forms of the representative conformer were likewise optimized using DFT. The excitation spectrum of the charge-neutral form of the representative conformer was calculated using time-dependent DFT (TD-DFT). For each polymer, the excited-state IP and EA values (denoted IP* and EA*, respectively) were calculated basing on of the vertical energy of the lowest singlet excited state (S_1).

The DFT and TDDFT calculations were performed with the program Turbomole, version 6.5. The B3LYP exchange-correlation functional[49, 50] was used in combination with the DZP basis set.[51, 52] The effects of aqueous solvation were included via the conductor-like screening model[53, 54] (COSMO). At all times, the energies and gradients were corrected for dispersion effects with the D3 semiempirical dispersion correction scheme of Grimme and coworkers.[55]

2.7 References

1. Wang, X.; Chen, L.; Chong, S. Y.; Little, M. A.; Wu, Y.; Zhu, W.-H.; Clowes, R.; Yan, Y.; Zwijnenburg, M. A.; Sprick, R. S.; Cooper, A. I., Sulfone-containing covalent organic frameworks for photocatalytic hydrogen evolution from water. *Nat. Chem.* **2018,** *10* (12), 1180-1189.
2. Bai, Y.; Wilbraham, L.; Slater, B. J.; Zwijnenburg, M. A.; Sprick, R. S.; Cooper, A. I., Accelerated Discovery of Organic Polymer Photocatalysts for Hydrogen Evolution from Water through the Integration of Experiment and Theory. *J. Am. Chem. Soc.* **2019,** *141* (22), 9063-9071.
3. Sprick, R. S.; Bai, Y.; Guilbert, A. A. Y.; Zbiri, M.; Aitchison, C. M.; Wilbraham, L.; Yan, Y.; Woods, D. J.; Zwijnenburg, M. A.; Cooper, A. I., Photocatalytic Hydrogen Evolution from Water Using Fluorene and Dibenzothiophene Sulfone-Conjugated Microporous and Linear Polymers. *Chem. Mater.* **2019,** *31* (2), 305-313.
4. Woods, D. J.; Hillman, S. A. J.; Pearce, D.; Wilbraham, L.; Flagg, L. Q.; Duffy, W.; McCulloch, I.; Durrant, J. R.; Guilbert, A. A. Y.; Zwijnenburg, M. A.; Sprick, R. S.; Nelson, J.; Cooper, A. I., Side-chain tuning in conjugated polymer photocatalysts for improved hydrogen production from water. *Energy & Environmental Science* **2020,** *13* (6), 1843-1855.
5. Sun, H. J.; Oner, I. H.; Wang, T.; Zhang, T.; Selyshchev, O.; Neumann, C.; Fu, Y. B.; Liao, Z. Q.; Xu, S. Q.; Hou, Y.; Turchanin, A.; Zahn, D. R. T.; Zschech, E.; Weidinger, I. M.; Zhang, J.; Feng, X. L., Molecular Engineering of Conjugated Acetylenic Polymers for Efficient Cocatalyst-free Photoelectrochemical Water Reduction. *Angew. Chem. Int. Ed.* **2019,** *58* (30), 10368-10374.
6. Zhang, X.-H.; Wang, X.-P.; Xiao, J.; Wang, S.-Y.; Huang, D.-K.; Ding, X.; Xiang, Y.-G.; Chen, H., Synthesis of 1,4-diethynylbenzene-based conjugated polymer photocatalysts and their enhanced visible/near-infrared-light-driven hydrogen production activity. *J. Catal.* **2017,** *350*, 64-71.
7. Zhang, T.; Hou, Y.; Dzhagan, V.; Liao, Z. Q.; Chai, G. L.; Loffler, M.; Olianas, D.; Milani, A.; Xu, S. Q.; Tommasini, M.; Zahn, D. R. T.; Zheng, Z. K.; Zschech, E.; Jordan, R.; Feng, X. L., Copper-surface-mediated synthesis of acetylenic carbon-rich nanofibers for active metal-free photocathodes. *Nat. Commun.* **2018,** *9*, 1140.
8. Pachfule, P.; Acharjya, A.; Roeser, J.; Langenhahn, T.; Schwarze, M.; Schomäcker, R.; Thomas, A.; Schmidt, J., Diacetylene Functionalized Covalent Organic Framework (COF) for Photocatalytic Hydrogen Generation. *J. Am. Chem. Soc.* **2018,** *140* (4), 1423-1427.
9. Ghosh, S.; Kouamé, N. A.; Ramos, L.; Remita, S.; Dazzi, A.; Deniset-Besseau, A.; Beaunier, P.; Goubard, F.; Aubert, P.-H.; Remita, H., Conducting polymer nanostructures for photocatalysis under visible light. *Nat. Mater.* **2015,** *14* (5), 505-511.
10. Lan, X.; Liu, X.; Zhang, Y.; Li, Q.; Wang, J.; Zhang, Q.; Bai, G., Unveiling Charge Dynamics in Acetylene-Bridged Donor−π–Acceptor Covalent Triazine Framework for Enhanced Photoredox Catalysis. *ACS Catal.* **2021**, 7429-7441.
11. Chen, L.; Wang, L.; Wan, Y.; Zhang, Y.; Qi, Z.; Wu, X.; Xu, H., Acetylene and Diacetylene Functionalized Covalent Triazine Frameworks as Metal-Free Photocatalysts for Hydrogen Peroxide Production: A New Two-Electron Water Oxidation Pathway. *Adv. Mater.* **2020,** *32* (2), 1904433.
12. Sindhu, K. S.; Anilkumar, G., Recent advances and applications of Glaser coupling employing greener protocols. *RSC Adv.* **2014,** *4* (53), 27867-27887.
13. Wang, D.; Gao, S., Sonogashira coupling in natural product synthesis. *Org. Chem. Front.* **2014,** *1* (5), 556-566.

14. Feng, J.; Dong, H.; Pang, B.; Shao, F.; Zhang, C.; Yu, L.; Dong, L., Theoretical study on the optical and electronic properties of graphene quantum dots doped with heteroatoms. *Phys. Chem. Chem. Phys.* **2018,** *20* (22), 15244-15252.
15. Kumari, V.; Mittal, A.; Jindal, J.; Yadav, S.; Kumar, N., S-, N- and C-doped ZnO as semiconductor photocatalysts: A review. *Frontiers of Materials Science* **2019,** *13* (1), 1-22.
16. Yu, W.; Zhang, J.; Peng, T., New insight into the enhanced photocatalytic activity of N-, C- and S-doped ZnO photocatalysts. *Appl. Catal. B-Environ.* **2016,** *181*, 220-227.
17. Li, L.; Fang, W.; Zhang, P.; Bi, J.; He, Y.; Wang, J.; Su, W., Sulfur-doped covalent triazine-based frameworks for enhanced photocatalytic hydrogen evolution from water under visible light. *J. Mater. Chem. A* **2016,** *4* (32), 12402-12406.
18. Luo, L.; Gong, Z.; Ma, J.; Wang, K.; Zhu, H.; Li, K.; Xiong, L.; Guo, X.; Tang, J., Ultrathin sulfur-doped holey carbon nitride nanosheets with superior photocatalytic hydrogen production from water. *Appl. Catal. B-Environ.* **2021,** *284*, 119742.
19. Fang, J.; Fan, H.; Li, M.; Long, C., Nitrogen self-doped graphitic carbon nitride as efficient visible light photocatalyst for hydrogen evolution. *J. Mater. Chem. A* **2015,** *3* (26), 13819-13826.
20. Shi, R.; Li, Z.; Yu, H.; Shang, L.; Zhou, C.; Waterhouse, G. I. N.; Wu, L.-Z.; Zhang, T., Effect of Nitrogen Doping Level on the Performance of N-Doped Carbon Quantum Dot/TiO2 Composites for Photocatalytic Hydrogen Evolution. *ChemSusChem* **2017,** *10* (22), 4650-4656.
21. Bai, Y.; Woods, D. J.; Wilbraham, L.; Aitchison, C. M.; Zwijnenburg, M. A.; Sprick, R. S.; Cooper, A. I., Hydrogen evolution from water using heteroatom substituted fluorene conjugated co-polymers. *J. Mater. Chem. A* **2020,** *8* (17), 8700-8705.
22. Wang, L.; Wan, Y.; Ding, Y.; Wu, S.; Zhang, Y.; Zhang, X.; Zhang, G.; Xiong, Y.; Wu, X.; Yang, J.; Xu, H., Conjugated Microporous Polymer Nanosheets for Overall Water Splitting Using Visible Light. *Adv. Mater.* **2017,** *29* (38), 1702428.
23. Aitchison, C. M.; Kane, C. M.; McMahon, D. P.; Spackman, P. R.; Pulido, A.; Wang, X.; Wilbraham, L.; Chen, L.; Clowes, R.; Zwijnenburg, M. A.; Sprick, R. S.; Little, M. A.; Day, G. M.; Cooper, A. I., Photocatalytic proton reduction by a computationally identified, molecular hydrogen-bonded framework. *J. Mater. Chem. A* **2020,** *8* (15), 7158-7170.
24. Lin, L.; Yu, Z.; Wang, X., Crystalline Carbon Nitride Semiconductors for Photocatalytic Water Splitting. *Angew. Chem. Int. Ed.* **2019,** *58* (19), 6164-6175.
25. Beltrán-Suito, R.; Menezes, P. W.; Driess, M., Amorphous outperforms crystalline nanomaterials: surface modifications of molecularly derived CoP electro(pre)catalysts for efficient water-splitting. *J. Mater. Chem. A* **2019,** *7* (26), 15749-15756.
26. Cai, W.; Chen, R.; Yang, H.; Tao, H. B.; Wang, H.-Y.; Gao, J.; Liu, W.; Liu, S.; Hung, S.-F.; Liu, B., Amorphous versus Crystalline in Water Oxidation Catalysis: A Case Study of NiFe Alloy. *Nano Lett.* **2020,** *20* (6), 4278-4285.
27. Xu, C.; Zhang, W.; Tang, J.; Pan, C.; Yu, G., Porous Organic Polymers: An Emerged Platform for Photocatalytic Water Splitting. *Frontiers in Chemistry* **2018,** *6* (592).
28. Meier, C. B.; Clowes, R.; Berardo, E.; Jelfs, K. E.; Zwijnenburg, M. A.; Sprick, R. S.; Cooper, A. I., Structurally Diverse Covalent Triazine-Based Framework Materials for Photocatalytic Hydrogen Evolution from Water. *Chem. Mater.* **2019,** *31* (21), 8830-8838.
29. Guiglion, P.; Butchosa, C.; Zwijnenburg, M. A., Polymeric watersplitting photocatalysts; a computational perspective on the water oxidation conundrum. *J. Mater. Chem. A* **2014,** *2* (30), 11996-12004.
30. Wang, X.; Chen, B.; Dong, W.; Zhang, X.; Li, Z.; Xiang, Y.; Chen, H., Hydrophilicity-Controlled Conjugated Microporous Polymers for Enhanced Visible-Light-Driven Photocatalytic H2 Evolution. *Macromol. Rapid Commun.* **2019,** *40* (6), 1800494.

31. Wu, Z.; Wang, J.; Xia, K.; Lei, W.; Liu, X.; Wang, D., MoS2–MoP heterostructured nanosheets on polymer-derived carbon as an electrocatalyst for hydrogen evolution reaction. *J. Mater. Chem. A* **2018,** *6* (2), 616-622.
32. Jones, A. R., Light scattering for particle characterization. *Prog. Energy Combust. Sci.* **1999,** *25* (1), 1-53.
33. Sachs, M.; Cha, H.; Kosco, J.; Aitchison, C. M.; Francàs, L.; Corby, S.; Chiang, C.-L.; Wilson, A. A.; Godin, R.; Fahey-Williams, A.; Cooper, A. I.; Sprick, R. S.; McCulloch, I.; Durrant, J. R., Tracking Charge Transfer to Residual Metal Clusters in Conjugated Polymers for Photocatalytic Hydrogen Evolution. *J. Am. Chem. Soc.* **2020,** *142* (34), 14574-14587.
34. Meier, C. B.; Sprick, R. S.; Monti, A.; Guiglion, P.; Lee, J.-S. M.; Zwijnenburg, M. A.; Cooper, A. I., Structure-property relationships for covalent triazine-based frameworks: The effect of spacer length on photocatalytic hydrogen evolution from water. *Polymer* **2017,** *126*, 283-290.
35. Bi, S.; Lan, Z.-A.; Paasch, S.; Zhang, W.; He, Y.; Zhang, C.; Liu, F.; Wu, D.; Zhuang, X.; Brunner, E.; Wang, X.; Zhang, F., Substantial Cyano-Substituted Fully sp2-Carbon-Linked Framework: Metal-Free Approach and Visible-Light-Driven Hydrogen Evolution. *Adv. Funct. Mater.* **2017,** *27* (39), 1703146.
36. Sprick, R. S.; Bonillo, B.; Clowes, R.; Guiglion, P.; Brownbill, N. J.; Slater, B. J.; Blanc, F.; Zwijnenburg, M. A.; Adams, D. J.; Cooper, A. I., Visible-Light-Driven Hydrogen Evolution Using Planarized Conjugated Polymer Photocatalysts. *Angew. Chem. Int. Ed.* **2016,** *55* (5), 1792-1796.
37. Sachs, M.; Sprick, R. S.; Pearce, D.; Hillman, S. A. J.; Monti, A.; Guilbert, A. A. Y.; Brownbill, N. J.; Dimitrov, S.; Shi, X.; Blanc, F.; Zwijnenburg, M. A.; Nelson, J.; Durrant, J. R.; Cooper, A. I., Understanding structure-activity relationships in linear polymer photocatalysts for hydrogen evolution. *Nat. Commun.* **2018,** *9* (1), 4968.
38. Vyas, V. S.; Haase, F.; Stegbauer, L.; Savasci, G.; Podjaski, F.; Ochsenfeld, C.; Lotsch, B. V., A tunable azine covalent organic framework platform for visible light-induced hydrogen generation. *Nat. Commun.* **2015,** *6* (1), 8508.
39. Li, L.; Cai, Z.; Wu, Q.; Lo, W.-Y.; Zhang, N.; Chen, L. X.; Yu, L., Rational Design of Porous Conjugated Polymers and Roles of Residual Palladium for Photocatalytic Hydrogen Production. *J. Am. Chem. Soc.* **2016,** *138* (24), 7681-7686.
40. Zhang, L.; Ding, N.; Wu, J.; Iwasaki, K.; Lin, L.; Yamaguchi, Y.; Shibayama, Y.; Shi, J.; Wu, H.; Luo, Y.; Nakata, K.; Li, D.; Wang, X.; Fujishima, A.; Meng, Q., New two-dimensional porous graphitic carbon nitride nanosheets for highly efficient photocatalytic hydrogen evolution under visible-light irradiation. *Catal. Sci. Technol.* **2018,** *8* (15), 3846-3852.
41. Yu, K.; Bi, S.; Ming, W.; Wei, W.; Zhang, Y.; Xu, J.; Qiang, P.; Qiu, F.; Wu, D.; Zhang, F., Side-chain-tuned π-extended porous polymers for visible light-activated hydrogen evolution. *Polym. Chem.* **2019,** *10* (27), 3758-3763.
42. Elsayed, M. H.; Jayakumar, J.; Abdellah, M.; Mansoure, T. H.; Zheng, K.; Elewa, A. M.; Chang, C.-L.; Ting, L.-Y.; Lin, W.-C.; Yu, H.-h.; Wang, W.-H.; Chung, C.-C.; Chou, H.-H., Visible-light-driven hydrogen evolution using nitrogen-doped carbon quantum dot-implanted polymer dots as metal-free photocatalysts. *Appl. Catal. B-Environ.* **2021,** *283*, 119659.
43. Bai, Y.; Wilbraham, L.; Gao, H.; Clowes, R.; Yang, H.; Zwijnenburg, M. A.; Cooper, A. I.; Sprick, R. S., Photocatalytic polymers of intrinsic microporosity for hydrogen production from water. *J. Mater. Chem. A* **2021**.
44. Wang, X.; Lu, S.-m.; Li, J.; Liu, Y.; Li, C., Conjugated microporous polymers with chiral BINAP ligand built-in as efficient catalysts for asymmetric hydrogenation. *Catal. Sci. Technol.* **2015,** *5* (5), 2585-2589.

45. Schwarz, D.; Kochergin, Y. S.; Acharjya, A.; Ichangi, A.; Opanasenko, M. V.; Čejka, J.; Lappan, U.; Arki, P.; He, J.; Schmidt, J.; Nachtigall, P.; Thomas, A.; Tarábek, J.; Bojdys, M. J., Tailored Band Gaps in Sulfur- and Nitrogen-Containing Porous Donor–Acceptor Polymers. *Chem. Eur. J.* **2017,** *23* (53), 13023-13027.
46. Turcani, L.; Berardo, E.; Jelfs, K. E., stk: A python toolkit for supramolecular assembly. *J. Comput. Chem.* **2018,** *39* (23), 1931-1942.
47. Grimme, S.; Bannwarth, C.; Shushkov, P., A Robust and Accurate Tight-Binding Quantum Chemical Method for Structures, Vibrational Frequencies, and Noncovalent Interactions of Large Molecular Systems Parametrized for All spd-Block Elements (Z = 1–86). *J. Chem. Theory Comput.* **2017,** *13* (5), 1989-2009.
48. Bannwarth, C.; Ehlert, S.; Grimme, S., GFN2-xTB—An Accurate and Broadly Parametrized Self-Consistent Tight-Binding Quantum Chemical Method with Multipole Electrostatics and Density-Dependent Dispersion Contributions. *J. Chem. Theory Comput.* **2019,** *15* (3), 1652-1671.
49. Becke, A. D., Density‐functional thermochemistry. III. The role of exact exchange. *J. Chem. Phys.* **1993,** *98* (7), 5648-5652.
50. Stephens, P. J.; Devlin, F. J.; Chabalowski, C. F.; Frisch, M. J., Ab Initio Calculation of Vibrational Absorption and Circular Dichroism Spectra Using Density Functional Force Fields. *J. Phys. Chem.* **1994,** *98* (45), 11623-11627.
51. Schäfer, A.; Horn, H.; Ahlrichs, R., Fully optimized contracted Gaussian basis sets for atoms Li to Kr. *J. Chem. Phys.* **1992,** *97* (4), 2571-2577.
52. Gauss, J., Effects of electron correlation in the calculation of nuclear magnetic resonance chemical shifts. *J. Chem. Phys.* **1993,** *99* (5), 3629-3643.
53. Klamt, A.; Schüürmann, G., COSMO: a new approach to dielectric screening in solvents with explicit expressions for the screening energy and its gradient. *J. Chem. Soc., Perkin Trans. 2* **1993,** *2* (5), 799-805.
54. Schäfer, A.; Klamt, A.; Sattel, D.; Lohrenz, J. C. W.; Eckert, F., COSMO Implementation in TURBOMOLE: Extension of an efficient quantum chemical code towards liquid systems. *Phys. Chem. Chem. Phys.* **2000,** *2* (10), 2187-2193.
55. Grimme, S.; Antony, J.; Ehrlich, S.; Krieg, H., A consistent and accurate ab initio parametrization of density functional dispersion correction (DFT-D) for the 94 elements H-Pu. *J. Chem. Phys.* **2010,** *132* (15), 154104.

Chapter 3: Linear Conjugated Polymer with Alkenyl Linkers for Enhanced Photocatalytic Hydrogen Evolution

Author contributions:

All the experimental work were performed by the thesis author in this chapter, except for ICP, and element analysis, which were measured by the technical staffs in the test centre. Dr. Michał Andrzej Kochman carried out the computational work in this chapter. Professor Martijn A. Zwijnenburg supervised the computational work and reviewed the whole work. Dr. Reiner Sebastian Sprick and Professor Andrew I. Cooper supervised and reviewed the whole work.

3.1 Introduction

In the family of organic materials for photocatalytic water splitting, porous photocatalysts, such as covalent organic frameworks (COFs),[1, 2] conjugated microporous polymers (CMPs),[3-6] covalent triazine-based frameworks (CTFs),[7-9] have attracted more attention due to their intrinsic porosity and large surface area. However, based on the previous reports,[7, 10] the porosity could be beneficial for the photocatalytic reactions in some cases, but it may be not the determining factor as hydrogen evolution performance would be affected by various properties. On the other hand, non-porous linear conjugated polymers also show good potential as photocatalysts, and some of them even outperform common porous polymers.[11, 12] Therefore, it is still worth exploring more linear polymer catalysts for photocatalytic conversion.

To rationally design more candidate organic photocatalysts, it is important to understand structure-property-performance relationships. In our previous studies, we have demonstrated that introducing dibenzo[*b*,*d*]thiophene sulfone into polymers can improve the hydrophilicity of the resulting material, which enhances the photocatalytic performance.[2, 13] In addition, the photocatalytic activity of polymer catalysts could be simply optimised by modifying the linkers. For example, extending the length of linker in a CTF[8] or COF[1] results in increased photocatalytic hydrogen production performance. Besides, changing the element in the linker also results in obvious effect on the photocatalytic performance.[14, 15]

Herein, inspired by these studies, we suspected that changing the linker could be a facile and effective strategy to adjust and optimize the performance of organic photocatalysts, although some other methods have been commonly used, such as heteroatomic doping,[16-19] morphology control,[20-23] and loading cocatalysts.[24-27]. In this work, three different linkers (*i.e.*, alkyl linker (-C-C-), alkenyl linker (-C=C-) and alkyne linker (-C≡C-)) with different conjugacy were investigated for their influence on HER. Moreover, several modification strategies were also applied in an attempt to further improve the HER performance of the best material (NP2) in this chapter.

3.2 Materials design and characterization

3.2.1 Synthesis of polymers

Firstly, as shown in Figure 3.1, 3,7-bis(4,4,5,5-tetramethyl-1,3,2-dioxaborolan-2-yl) dibenzo[*b*,*d*]thiophene sulfone was reacted with three diphenyl-based dibromo-monomers (*i.e.*, 1,2-diphenylethane, (*E*)-1,2-diphenylethene and 1,2-diphenylethyne) via a Pd-catalysed Suzuki cross-coupling polymerization. The final products were named as NP1, NP2 and NP3, respectively. Then, in order to further investigate whether the effect of these linkers on HER would be widely applicable, the dibenzo[*b*,*d*]thiophene sulfone moiety was replaced with the dimethyl-fluorene moiety, after the same reaction process, three new polymers were obtained and named as NF1, NF2 and NF3.

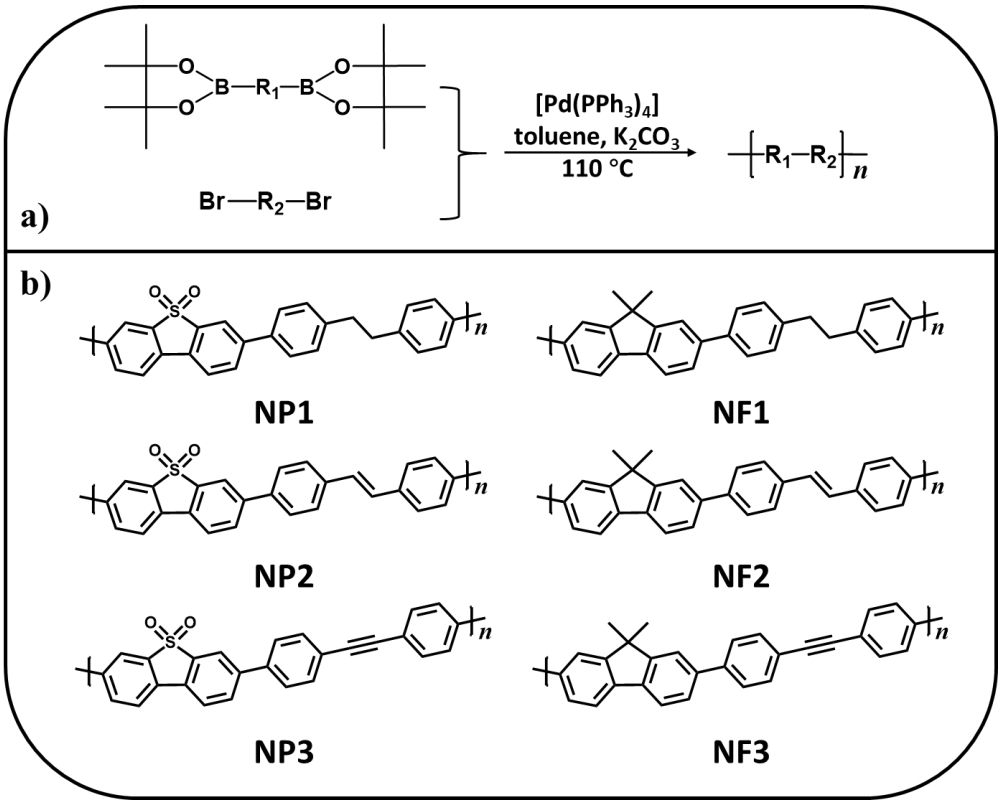

Figure 3.1 (a) Schematic diagram of Suzuki cross-coupling reaction. (b) Structures of linear conjugated polymers based on dibenzo[*b*,*d*]thiophene sulfone moiety (left, NP1-3) and dimethyl fluorene moiety (right, NF1-3).

3.2.2 Characterizations

The chemical structures of all polymers were investigated by Fourier-transform infrared spectroscopy (FT-IR) (Figure 3.2). The characteristic peak of the O=S=O stretching vibration

in NP polymers can be identified at around 1160 cm^{-1}, while in NF polymers, it is not observed. Powder X -ray diffraction (PXRD) patterns (Figure 3.3) indicated that the synthesized polymers were semi-crystalline materials as observed in previous studies.[11, 28] The NP polymers appear to have a higher degree of long-range order as evident from their sharper peak structure in their PXRD patterns compared to NF polymers. Thermogravimetric analysis showed that the NF polymers displayed the thermal stability up to around 450 ℃ in N_2, which was 50 ℃ higher than NP polymers under the same conditions (Figure 3.4). In both series alkyne linked polymers were more stable than alkenyl linked and alkyl linked polymers. The morphology images of all polymers (Figure 3.5) were studied via scanning electron microscopy (SEM). NP polymers mainly composed of flakes with varied size, while the main morphologies of NF polymers were agglomerated particles mixed with irregular blocks, which suggested that the host building blocks (the dibenzo[*b*,*d*]thiophene sulfone moiety and the dimethyl fluorene moiety) had a significant effect on the morphology of the polymers while the morphology was less affected by the linker. In addition, the Brunauer-Emmett-Teller surface area (SA_{BET}) was calculated from N_2 adsorption isotherms at 77 K, and all of these linear polymers had low BET values ranged from 26 m^2 g^{-1} to 55 m^2 g^{-1} (Figure 3.6 and 3.7), indicating that these materials are essential non-porous as expected and in line with previous publications.[11, 28, 29]

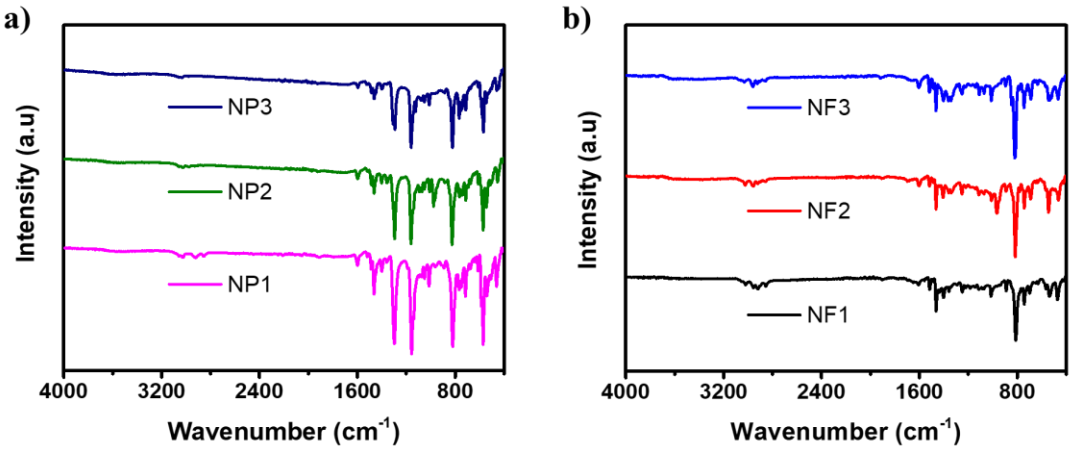

Figure 3.2 Fourier-transform infrared spectra of a) NP1-3 and b) NF1-3.

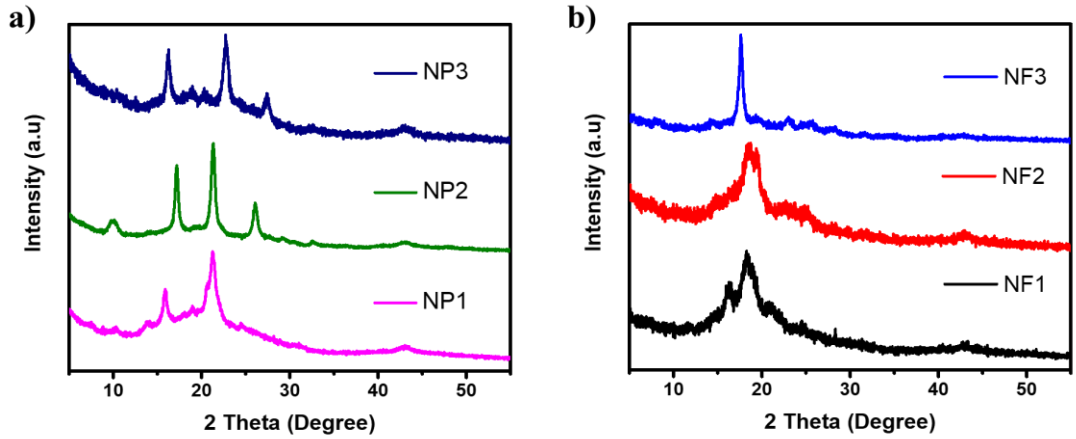

Figure 3.3 PXRD patterns of a) NP1-3 and b) NF1-3.

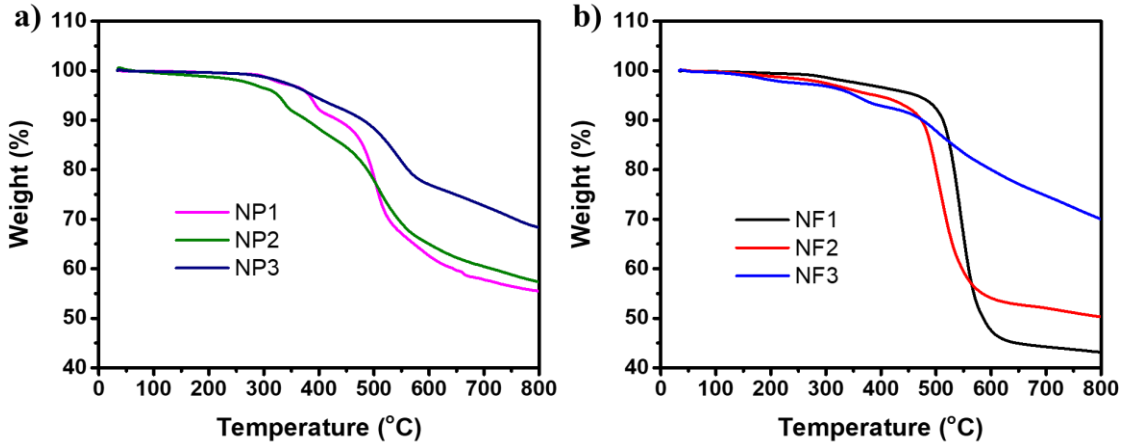

Figure 3.4 Thermogravimetric data of a) NP1-3 and b) NF1-3.

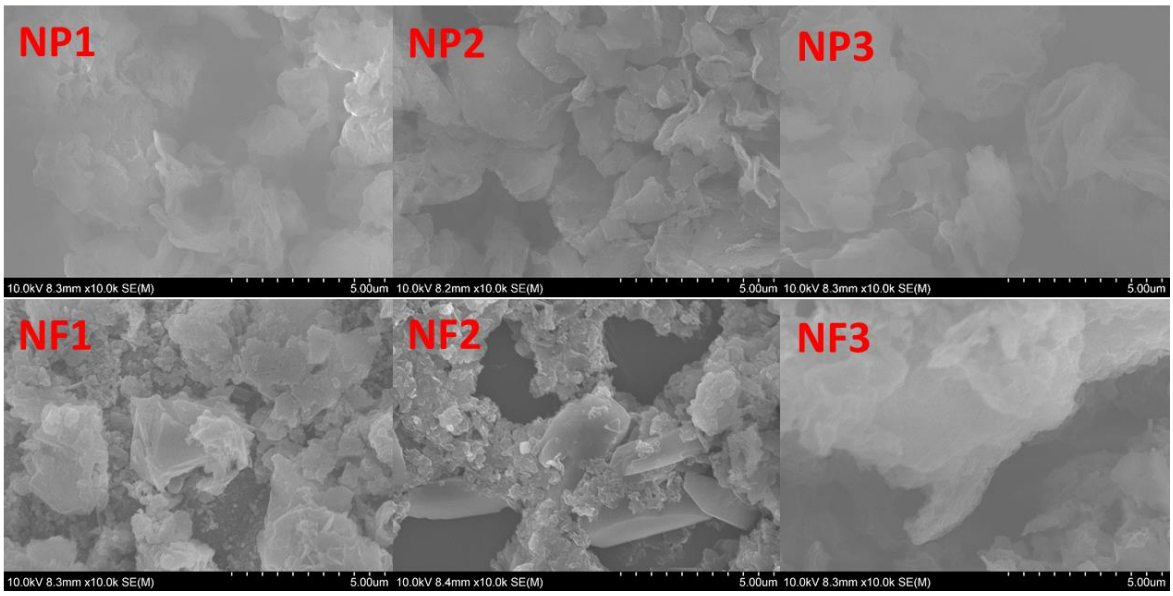

Figure 3.5 SEM images of NP1-3 and NF1-3.

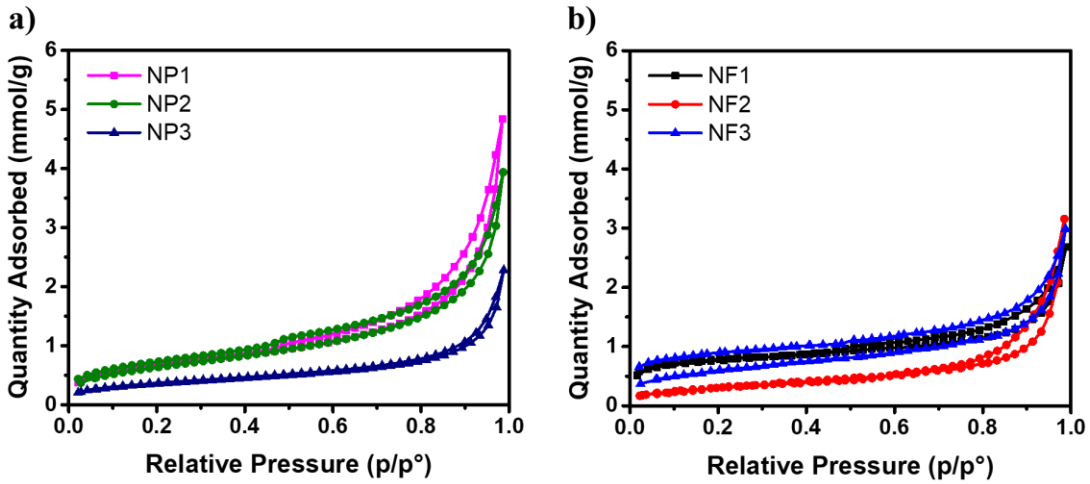

Figure 3.6 Nitrogen sorption isotherm of NP1-3 and NF1-3.

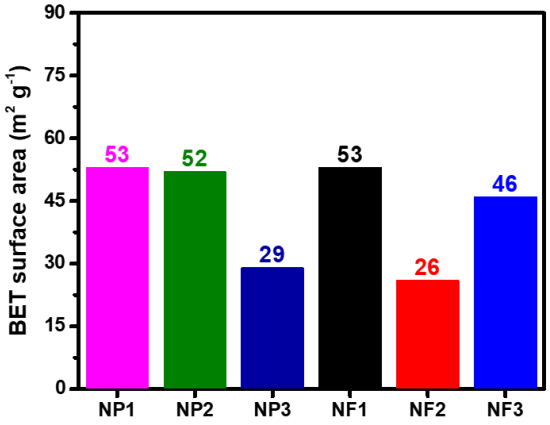

Figure 3.7 BET surface area of NP1-3 and NF1-3.

In addition, UV-vis diffuse reflectance spectra were recorded in solid state to study the optical properties of the polymers. As shown in Figure 3.8a, NP polymers have wider visible light absorption range than NF polymers with the same linker. In addition, based on UV-vis spectrum, the optical gap (E_g) was calculated via Kubelka-Munk formula. For NP1, NP2 and NP3, their optical gaps were 2.63 eV, 2.50 eV and 2.54 eV, respectively, which is a slightly narrower than their corresponding NF polymers (Table 3.1). The electron affinity (EA) and ionisation potential (IP) were predicted using DFT calculations (Figure 3.8b and Table 3.1). EA potentials indicate the driving force for water reduction while IP potentials suggest the driving force for water oxidation (or TEA oxidation in this case), which approximated in the literature by the energy of the LUMO (lowest unoccupied molecular orbital) and HOMO (highest occupied molecular orbital), respectively. It was found that the calculated fundamental

gap (E_f = IP-EA) was consistent with the experimental optical gap (Table 3.1). The predicted excited-state ionisation potentials of IP and EA are named as IP* and EA*, which evaluating the thermodynamic ability to provide electron or hole for driving the water splitting half reaction.[7, 10] All of the EA and IP* energy levels of the polymers were determined more negative than the energy level of hydrogen generation in the reaction solution containing hole sacrificial agent, indicating that all of them are thermodynamically able to reduce protons into hydrogen.

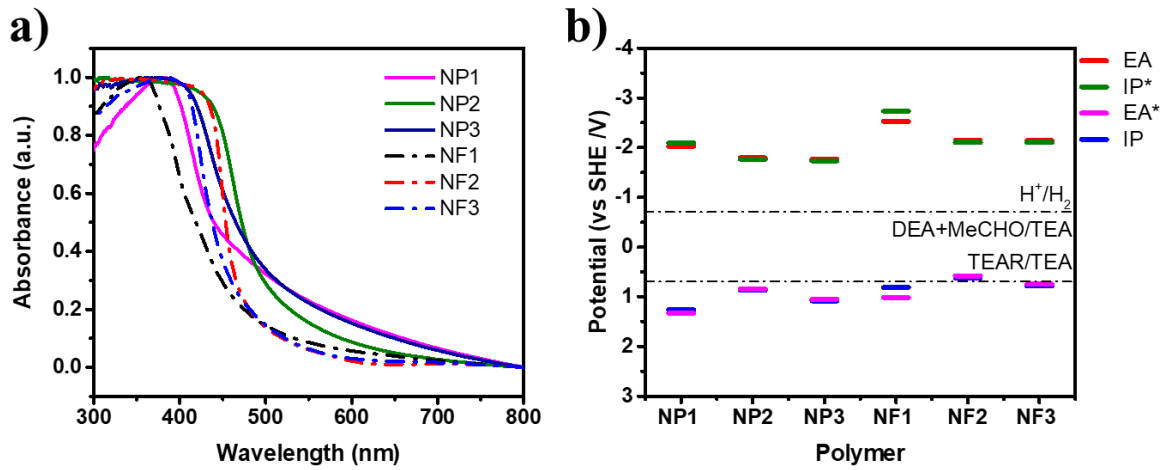

Figure 3.8 (a) Solid UV-vis spectra of NP1-3 and NF1-3. (b) Predicted EA, IP, EA*, IP* potentials of NP1-3 and NF1-3.

Table 3.1 Predicted EA, IP, fundamental gap optical gap and of NP1-3 and NF1-3.

Polymer	IP / V	EA / V	Fundamental gap[a] / V	Optical gap[b] / V
NP1	1.26	-2.03	3.29	3.29
NP2	0.87	-1.79	2.66	2.66
NP3	1.08	-1.77	2.85	2.85
NF1	0.81	-2.53	3.34	3.34
NF2	0.62	-2.15	2.77	2.77
NF3	0.78	-2.14	2.93	2.93

[a] The fundamental gap (E_f) was calculated by E_f = IP-EA

[b] The optical gap was calculated from Kubelka-Munk formula based on the spectrum of $(\alpha h\nu)^{\wedge 1/2} \propto E_g$.

3.2.3 Hydrogen evolution

The photocatalytic hydrogen production performance of the polymers was studied in H_2O/methanol (MeOH)/triethylamine (TEA) mixtures (1:1:1) under visible light irradiation ($\lambda > 420$ nm, 300 W Xe light source), without additional co-catalysts. However, it should be noted that residual palladium originating from the synthesis has been shown to act as a co-catalyst. However, when above a certain threshold concentration it only has a negligible effect on the performance as shown by others.[30, 31] As shown in Figure 3.9, the HER of NP2 was 3334 μmol g^{-1} h^{-1}, which was 1.7 times higher than NP3 and 3.3 times higher than NP1. For NF polymers, it was also found that the HER of NF2 was higher than the other two polymers, although the rate was only around one-fifth of NP2 (539 μmol g^{-1} h^{-1}). Therefore, in terms of photocatalytic performance, alkenyl linked polymers outperformed to alkyne linked and alkyl linked polymers in this study. One remarkable observation is the fact that the alkyl linked polymers showed photocatalytic activity despite their lack of extended conjugation along the backbone. Similar observations have been made for dibenzo[*b*,*d*] thiophene sulfone oligomers previously,[32] that also showed significant activity despite lacking extended backbone conjugation.

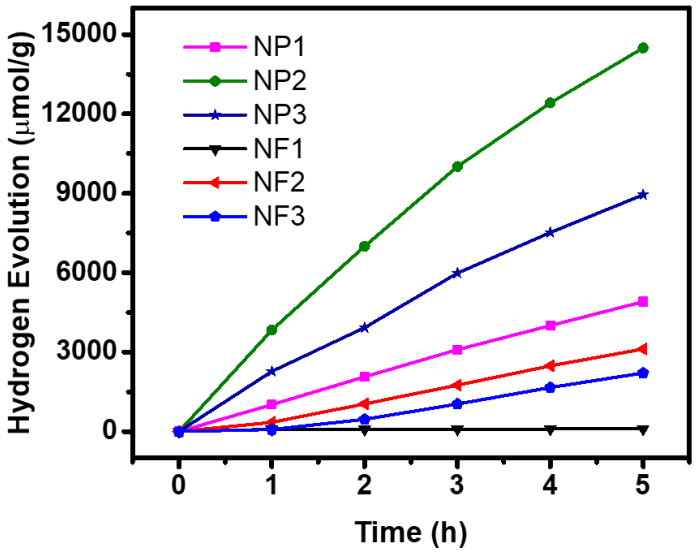

Figure 3.9 Time-course for photocatalytic H_2 evolution performance. Experimental conditions: 25 mg polymer in a solution of TEA/MeOH/H_2O (1:1:1, 25 mL) was irradiated by a 300 W Xe lamp with a filter ($\lambda > 420$ nm).

3.2.4 Stability and performance evaluation of NP2

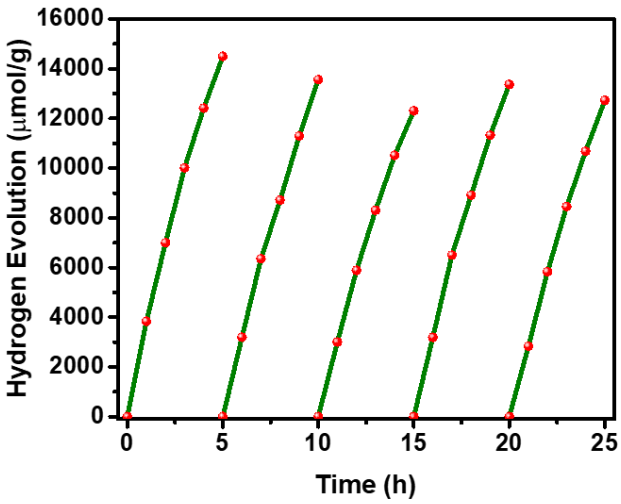

Figure 3.10 Extended photocatalysis run for NP2 in 5 cycles over total 25 hours. Experiment condition: 25 mg polymer in the mixture solution of TEA/MeOH/H_2O (1:1:1, 25 mL) was irradiated by a 300 W Xe lamp with a filter ($\lambda > 420$ nm). NP2 was recovered and the reaction solution was replaced between cycles.

To evaluate the photostability of NP2, the long term and recycling experiments were performed over 25 h under visible light illumination ($\lambda > 420$ nm). As shown in Figure 3.10, no obvious change of activity was observed over this timeframe. Furthermore, no obvious changes in the morphology, FT-IR spectra and PXRD patterns of NP2 when comparing the as made NP2 with NP2 after the photocatalytic experiment (Figure 3.11 and 3.12), indicating the good stability of NP2 photocatalyst.

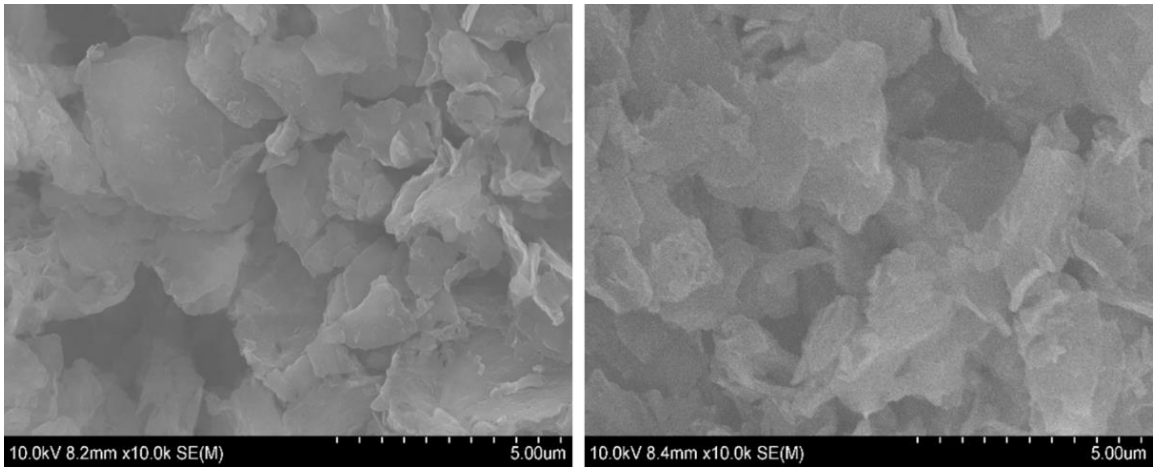

Figure 3.11 SEM images of NP2 before (Left) and after (Right) long-term photocatalytic hydrogen evolution experiment.

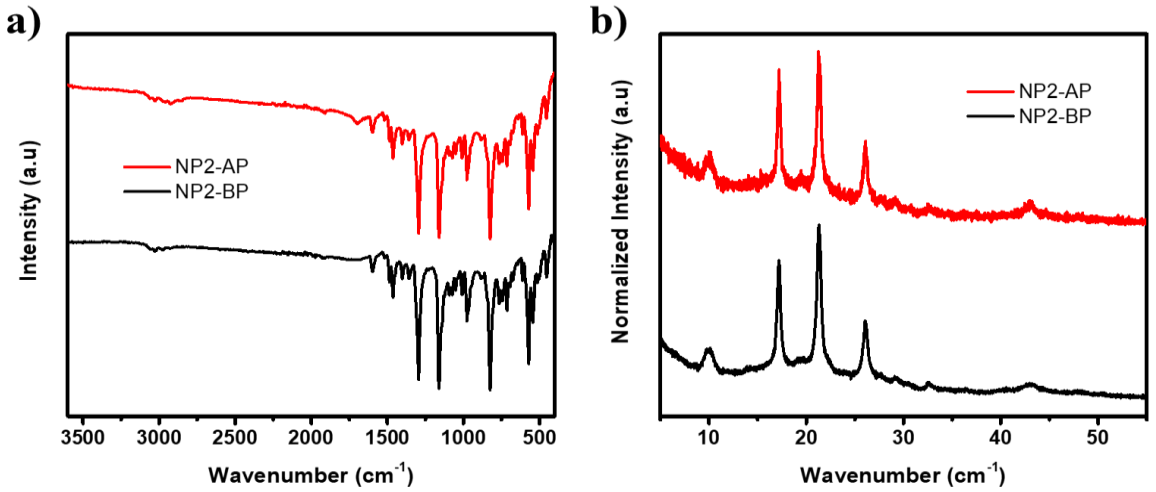

Figure 3.12 a) FT-IR spectrum and b) PXRD pattern of NP2 before (BP) and after (AP) long-term photocatalytic hydrogen evolution experiment.

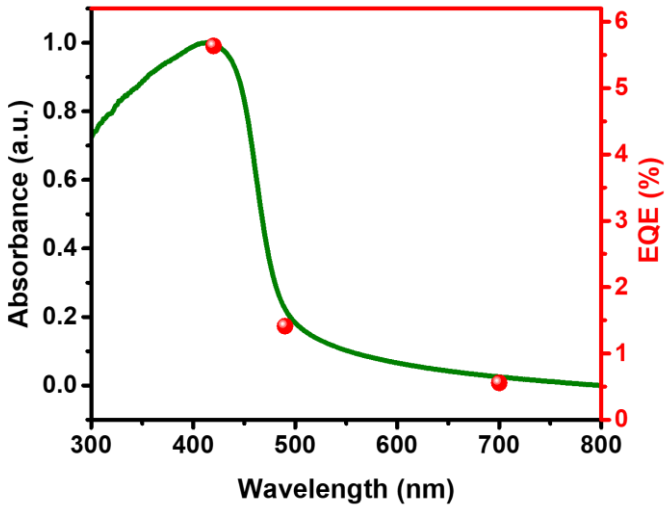

Figure 3.13 Wavelength dependent external quantum efficiency (EQE) values and solid UV-vis spectrum of NP2, λ = 420, 490, 700 nm.

External quantum efficiencies (EQE) were measured at different wavelengths to further evaluate the performance of NP2. The highest EQE value of 5.6% was obtained at 420 nm, which is comparable to some other reported organic materials, such as phenyl-benzothiadiazole copolymer (Pt/B-BT-1,4, 4.01% at 420 nm),[33] bipyridyl-based porous conjugated polymer (PCP4e, 1.8% at 350 nm),[31] although still lower than other organic polymer photocatalysts, for example, donor-π-acceptor (D-π-A) conjugated organic copolymer (PyBS-3, 29.3% at 420 nm)[34] and dibenzo[*b*,*d*]thiophene sulfone-dibenzo[*b*,*d*]thiophene co-polymer (P64, 20.7% at

420 nm)[10] (Table 3.2). In addition, the measured EQEs of NP2 also matched the UV-vis absorption spectrum well (Figure 3.13), suggesting that the hydrogen production process is indeed photocatalytic.[8]

Table 3.2 Comparation of NP1-3 with recent representative organic polymer photocatalysts for photocatalytic H_2 evolution.

Sample	Co-catalyst	Reaction solution[a]	λ / nm	EQE / %	Ref.
NP2	Pd residue	TEA/MeOH/H_2O	420	5.6	**This work**
NP3	Pd residue	TEA/MeOH/H_2O	420	4.6	**This work**
NP1	Pd residue	TEA/MeOH/H_2O	420	3.9	**This work**
P64	Pd residue	TEA/MeOH/H_2O	420	20.7	[10]
P7	Pd residue	TEA/MeOH/H_2O	420	7.2	[11]
P10	Pd residue	TEA/MeOH/H_2O	420	11.6	[28]
S-CMP3	Pd residue	TEA/MeOH/H_2O	420	13.2	[6]
CTF-2	3 wt.% Pt	TEA/MeOH/H_2O	420	1.6	[8]
Pt/B-BT-1,4	3 wt.% Pt	TEOA/H_2O	420	4.01	[33]
OB-POP-3	3 wt.% Pt	TEOA/H_2O	420	2.0	[35]
PyBS-3	~3 wt.% Pt	AA/H_2O	420	29.3	[34]
PCP_{4e}	2 wt.% Pt	TEA/H_2O	350	1.8	[31]

[a] TEA: triethylamine, MeOH: methanol, TEOA: triethanolamine, AA: ascorbic acid.

3.2.5 Discussion of performance and property relationship

The wettability of the polymers was studied via contact angle measurements of pallets of the materials against water (Figure 3.14 and Table 3.3), fitting with Young-Laplace model. It was found that alkenyl linked polymers (56.3 °for NP2 and 59.4 °for NF2) have smaller contact angles than alkyne linked polymers and alkyl linked polymers. The dispersibility of the polymer photocatalysts was studied via turbidity measurements in the H_2O/MeOH/TEA mixture reaction solution. Low transmission values indicate good dispersibility, while high values indicate that the material either floats or settles at the bottom during the measurement.

NP1-NP3 showed very similar and low transmission value (0.3-0.6%, Table 3.3), indicating that the NP polymers showed good dispersibility in the reaction mixture. The NF polymers had much higher transmission values compared to NP polymers (27.3%, 24.3% and 30.7% for NF1, NF2 and NF3, respectively). This can be attributed to the increased hydrophilicity of materials that bear sulfone groups.[13, 34] The particle sizes of all polymers were measured by static light scattering experiments (Table 3.3). The median particle sizes of NP polymers ranged from 11.4 μm to 15.1 μm and were smaller than those of the NF polymers (18.6 μm to 20.3 μm).

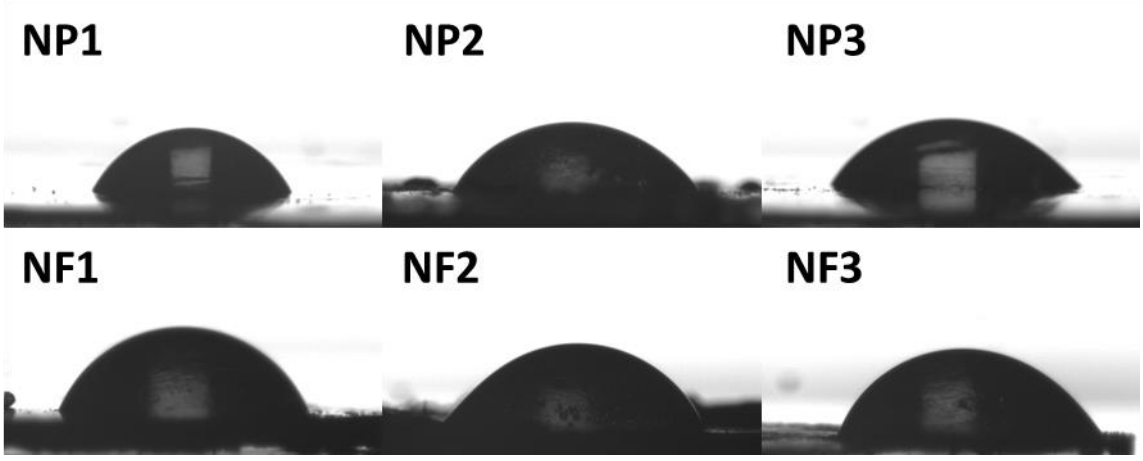

Figure 3.14 Contact angle images of NP1-3 and NF1-3 against water.

Table 3.3 Transmission, contact angle, particle size, average lifetime and of NP1-3 and NF1-3.

Polymer	Transmission[a] / %	Contact angle[b] / °	Particle size[c] / μm	τ_{avg}[d] / ns
NP1	0.5	65.4 (±0.6)	14.0	1.43
NP2	0.3	56.3 (±0.8)	11.4	1.57
NP3	0.6	59.0 (±0.6)	15.1	1.04
NF1	27.3	69.4 (±0.8)	20.1	0.30
NF2	24.3	59.4 (±0.5)	20.3	0.13
NF3	30.7	62.6 (±0.3)	18.6	0.19

[a] Measured in H_2O/MeOH/TEA; [b] Measured as pallets against water; [c] 50th percentile of particle size volume distribution; [d] Estimated fluorescence lifetimes were obtained from fitting time-correlated single photon counting decays to a sum of three exponentials in water;

Photoluminescence spectra were also measured (Figure 3.15), an obvious redshift can be observed comparing alkyl linked polymers to alkenyl and alkyne linked polymers, which can be explained by the change of optical gap induced by the variation of linkers.[3] In addition,

time-correlated single photon counting (TCSPC) showed that NP2 had the longest fluorescence lifetime of 1.57 ns among these polymers, and fluorescence lifetimes of NP polymers were longer than that of NF polymers (Table 3.4). In general, longer exciton lifetimes are considered to increase photocatalytic hydrogen evolution performance, however, NF2 showed the shortest lifetime while the HER activity the highest in the NF series. Similar observations have been made previously,[7, 10] showing limitations of the technique, as non-emissive states that could be responsible for hydrogen production are not studied with TCSPC. When correlating the HER with various material properties (Figure 3.16 and 3.17), it was found that the no single property dominated the HER performance, as reported previously.[7, 10] Having said this, it appears that the optical gap and hydrophilicity have the largest effect of the materials' activity.

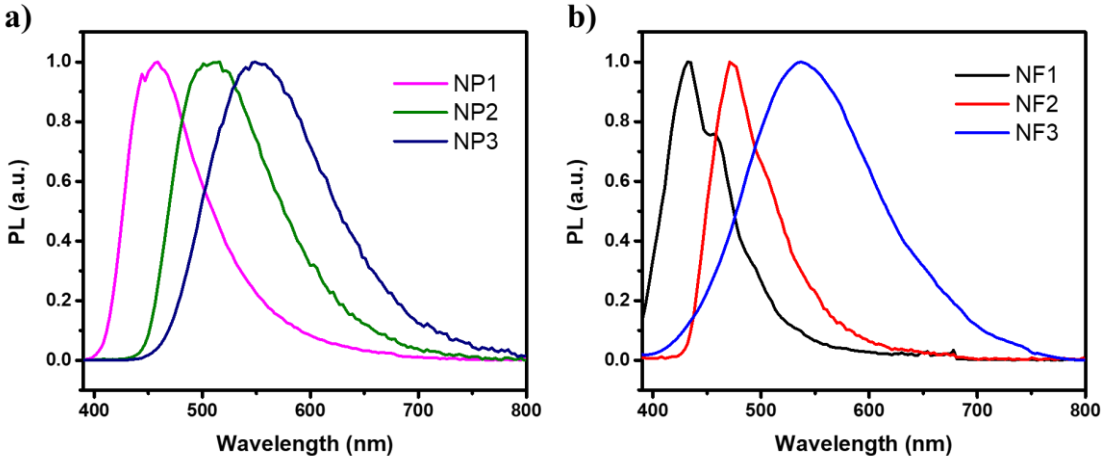

Figure 3.15 Photoluminescence emission spectra of NP1-3 and NF1-3 (λ_{exc} = 371 nm).

Table 3.4 Estimated fluorescence lifetimes of NP1-3 and NF1-3.

Polymer	$\lambda_{em\text{-}max}$ / nm	τ_1 / ns	B_1 / %	τ_2 / ns	B_2 / %	τ_3 / ns	B_3 / %	χ^2	τ_{avg} / ns
NP1	460	0.50	37.14	1.43	51.12	4.39	11.74	1.229	1.43
NP2	510	0.36	53.24	1.60	35.18	7.06	11.58	1.525	1.57
NP3	550	0.38	37.10	1.08	49.68	2.75	13.22	1.256	1.04
NF1	430	0.09	60.92	0.49	35.21	1.82	3.87	0.811	0.30
NF2	475	0.09	39.46	0.10	54.90	0.69	5.65	1.073	0.13
NF3	540	0.07	82.70	0.42	14.47	2.64	2.83	0.954	0.19

[a] Fluorescence lifetimes for all polymers obtained from fitting time-correlated single photon counting decays to a sum of three exponentials, which yield τ_1, τ_2, and τ_3 according $\sum_{i=1}^{n}(A + B_i exp(-t/\tau_i))$. τ_{avg} is the weighted average lifetime calculated as $\sum_{i=1}^{n}(B_i\tau_i)$.

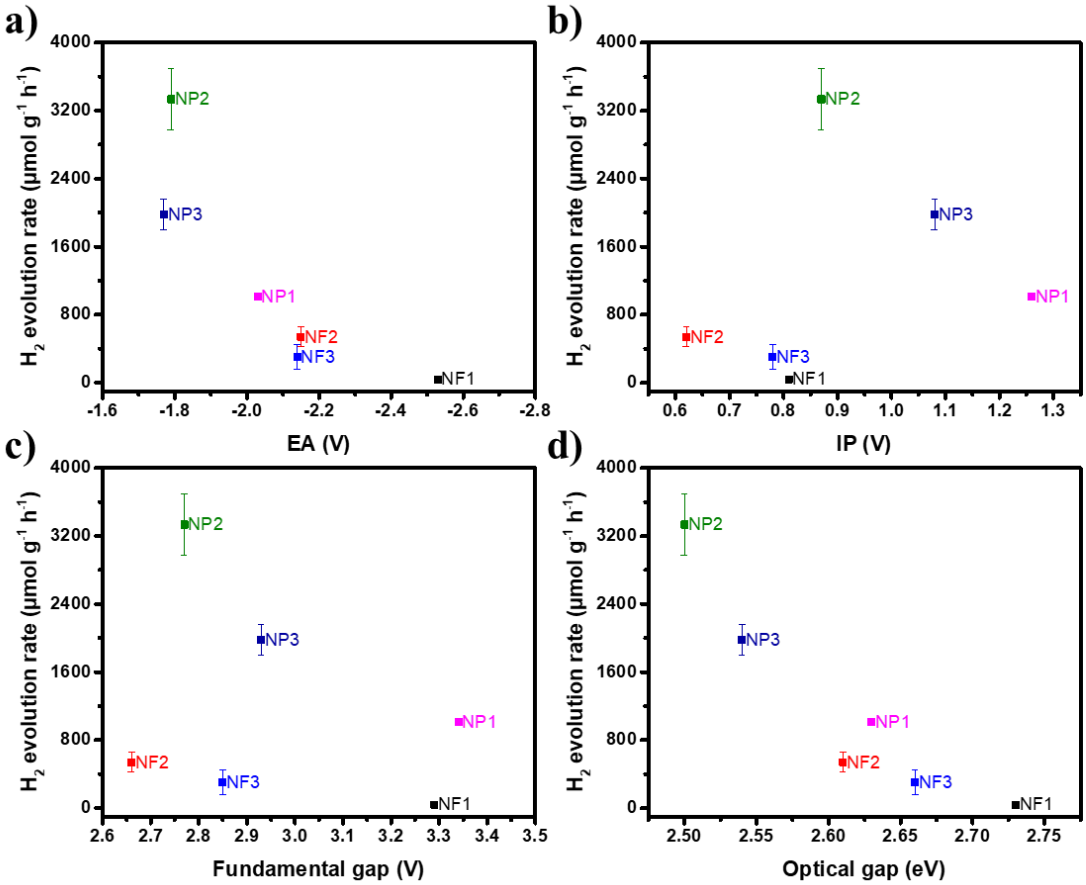

Figure 3.16 Comparison of the hydrogen evolution rates to a) EA, b) IP, c) fundamental gap (IP-EA) and d) optical gap of NP1-3 and NF1-3.

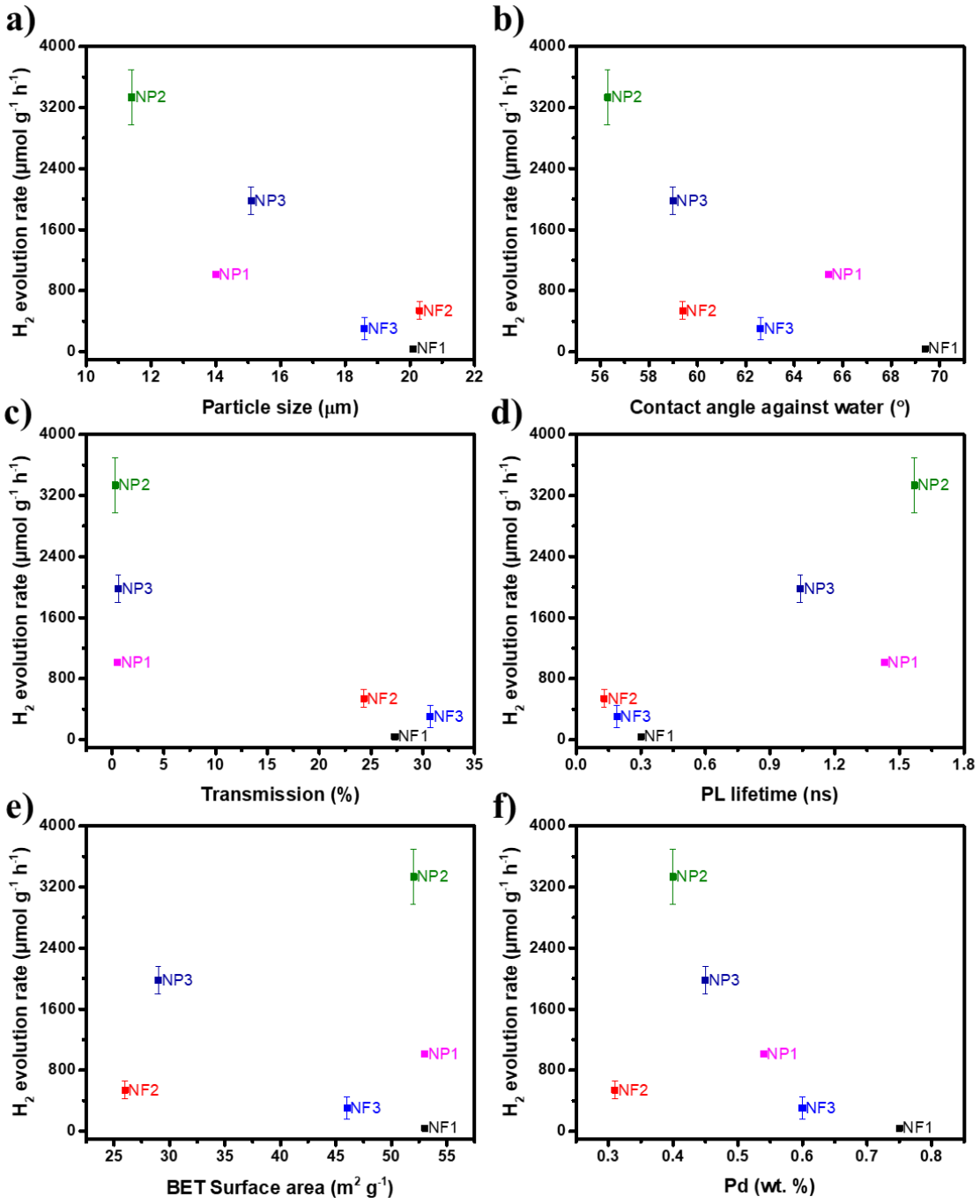

Figure 3.17 Comparison of the hydrogen evolution rates to a) particle size, b) contact angle (against water), c) transmission, d) averaged PL lifetime, e) BET surface area (SA_{BET}, N_2) and f) residue Pd content of NP1-3 and NF1-3.

3.3 Dye sensitization of NP2

3.3.1 Synthesis and characterisations

Dye sensitization is effective strategy to improve photocatalytic performance.[2, 36, 37] As an attempt to further promote the hydrogen evolution activity of NP2, three commercial dyes of perylene-3,4,9,10-tetracarboxylic dianhydride (PDI), Eosin Y (EY) and disperse red 1 (DR) with red colour were selected as the photosensitizer (Figure 3.18). Their HOMO and LUMO positions were displayed in Figure 3.19. After sensitization with a simple ultrasonic method, it was obvious that the visible light absorption of NP2 was enhanced, as shown in Figure 3.20b and the colour of NP2 also changed from green to red (Figure 3.20c). Besides, from the PXRD patterns (Figure 3.21), very weak signals of dyes could be found in the NP2/dye composites since the amount of dye was low. Besides, the SEM images of NP2/dye composites (Figure 3.22) showed the existence of similar morphology of pure dye, which indicating they have combined with NP2.

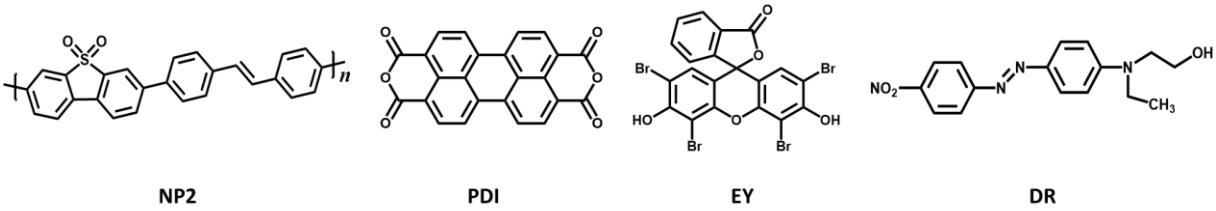

Figure 3.18 Chemical structure of commercially available dyes used for sensitizing the NP2 photocatalyst: Perylene-3,4,9,10-tetracarboxylic dianhydride (PDI), Eosin Y (EY) and Disperse Red 1 (DR).

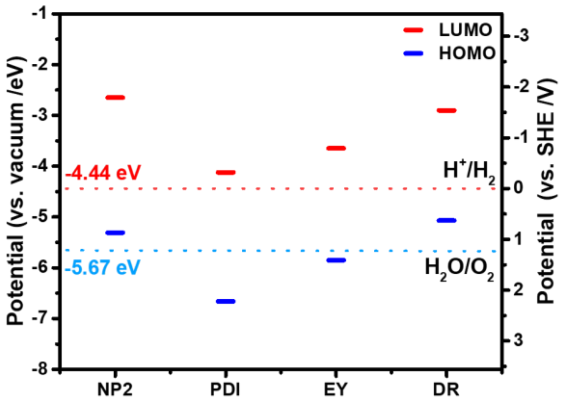

Figure 3.19 LUMO and HOMO position of NP2 at pH = 0, PDI, EY and DR calculated by DFT theory.[38-40]

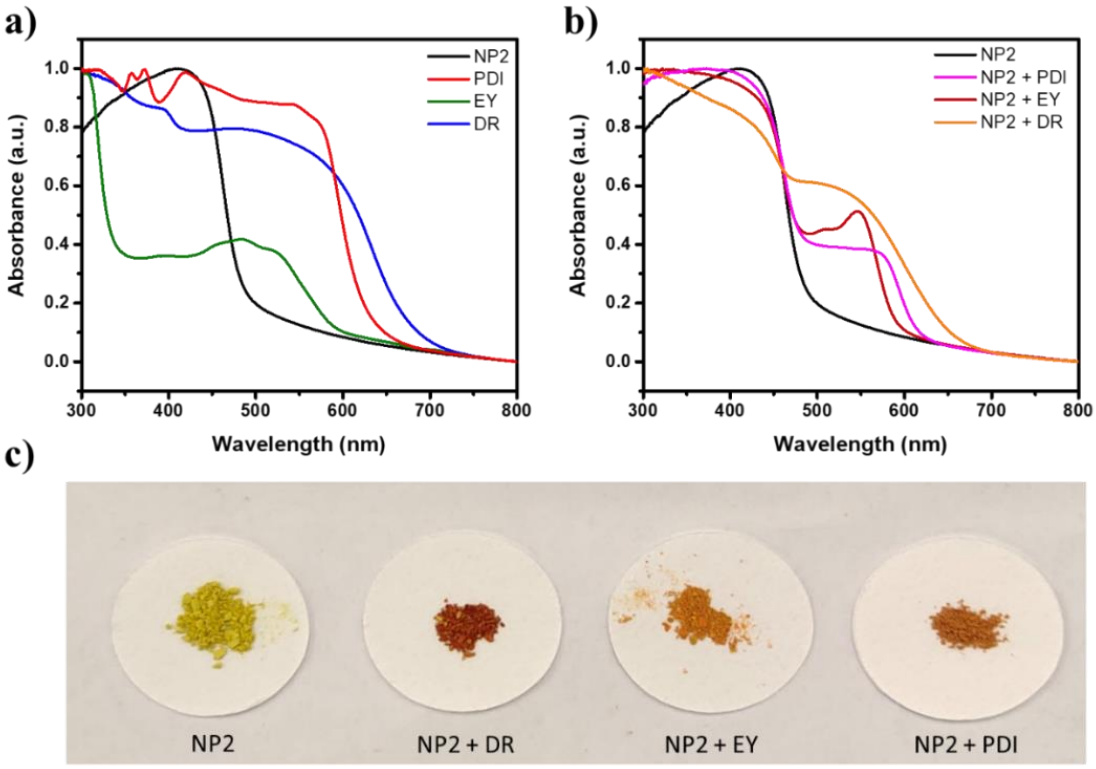

Figure 3.20 Solid UV-vis spectra of a) NP2, PDI, EY DR and b) NP2 and NP2/dye composites. c) Photographs of NP2 and NP2/dye composites.

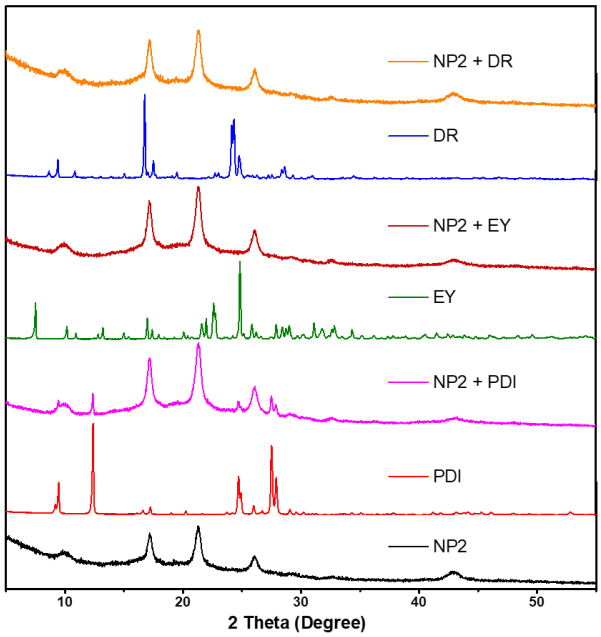

Figure 3.21 PXRD patterns of NP2, PDI, EY, DR and NP2/dye composites.

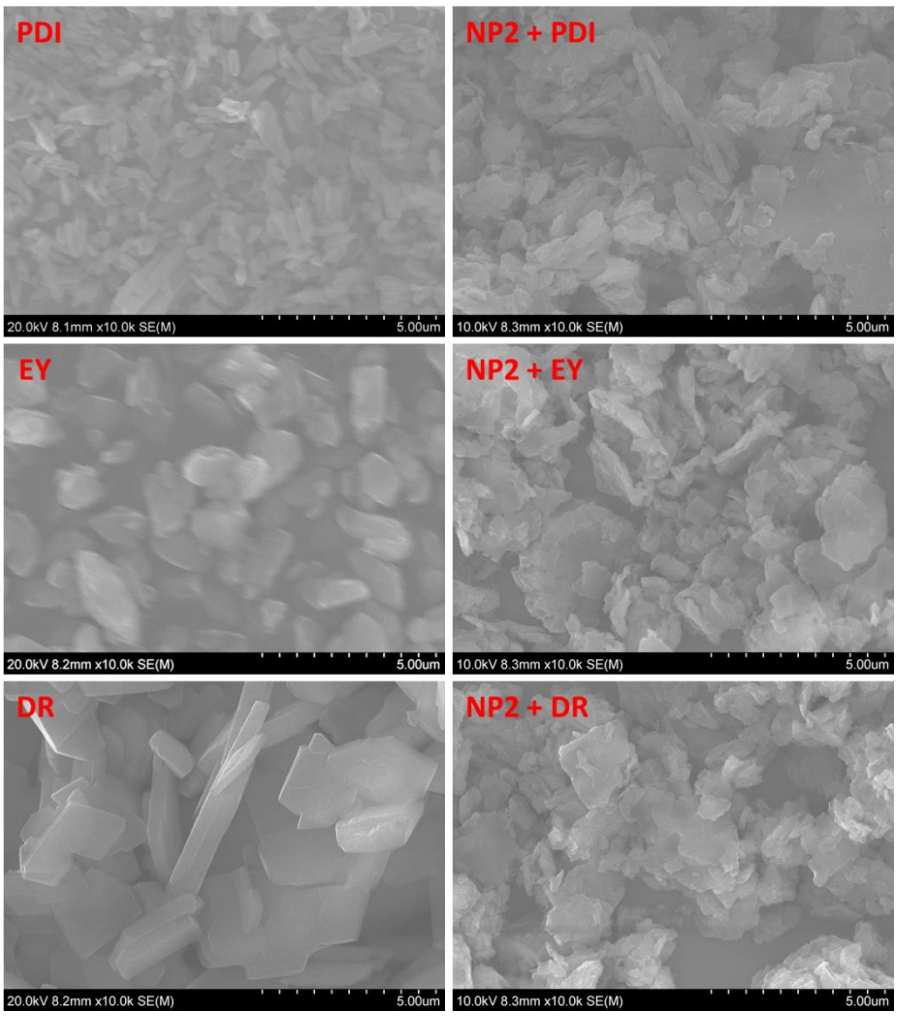

Figure 3.22 SEM images of PDI, EY, DR and NP2/dye composites.

In addition, the photoluminescence intensity of NP2 was obviously decreased or quenching after sensitizing (Figure 3.23a), indicating that there was charge transfer between dye and NP2. Moreover, the time-resolved fluorescence decay spectra of NP2 and NP2/dye composites were carried out to indirectly investigate the transfer process of photogenerated charge carriers. The average fluorescence lifetime of NP2 was 1.57 ns, while the lifetime of the NP2/dye composite was decreased to 1.28 ns, 0.50 ns, and 0.26 ns for NP/PDI, NP2/EY and NP2/DR, respectively (Figure 3.23b and Table 3.5), indicating the promoted charge transformation.

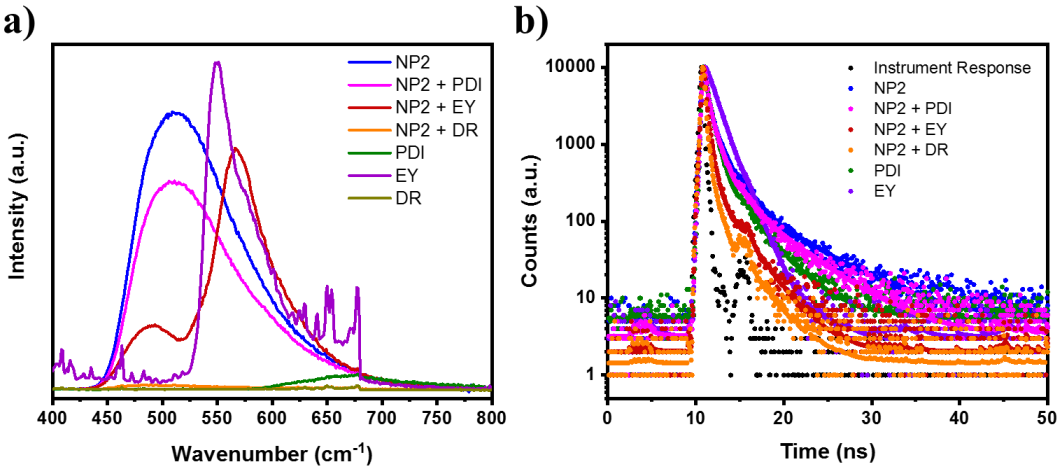

Figure 3.23 a) Photoluminescence emission spectra (λ_{exc} = 371 nm) and b) fluorescence life-time decays of NP2, dye and NP2/dye composites.

Table 3.5 Fluorescence lifetimes of NP2, dye and NP2/dye composites.

Polymer	$\lambda_{em\text{-}max}$ / nm	τ_1 / ns	B_1 / %	τ_2 / ns	B_2 / %	τ_3 / ns	B_3 / %	χ^2	τ_{avg} / ns
NP2	510	0.36	53.24	1.60	35.18	7.06	11.58	1.525	1.57
PDI	678	0.23	42.46	0.89	46.17	3.69	11.37	1.383	0.93
EY	549	1.15	6.05	1.16	77.30	1.89	16.65	1.331	1.28
DR	-	-	-	-	-	-	-	-	-
NP2 + PDI	511	0.30	53.33	1.31	36.12	6.11	10.55	1.498	1.28
NP2 + EY	492	0.16	72.27	0.75	21.47	3.52	6.26	1.265	0.50
NP2 + DR	490	0.10	87.22	0.75	10.09	3.50	2.69	1.020	0.26

[a] Fluorescence lifetimes for all polymers obtained from fitting time-correlated single photon counting decays to a sum of three exponentials, which yield τ_1, τ_2, and τ_3 according $\sum_{i=1}^{n}(A + B_i exp(-t/\tau_i))$. τ_{avg} is the weighted average lifetime calculated as $\sum_{i=1}^{n}(B_i \tau_i)$.

3.3.2 Hydrogen evolution

To evaluate the hydrogen production performance of sensitized NP2, 2 mg sample was added in the mixture of TEA/MeOH/H_2O. After 2 hours illumination under a solar simulator (1 sun), the produced hydrogen amount of NP2 was 71 µmol, while for NP2/PDI (5wt.%), NP2/EY (5wt.%) and NP2/DR (5wt.%), the amount of hydrogen increased to 91 µmol, 89 µmol and 81 µmol, respectively (Figure 3.24a). In addition, the control experiments showed that no hydrogen was detected when only dye was added into the reaction solution. For the best sample

of NP2/PDI (5wt.%), after optimizing the content of PDI (Figure 3.24b), the hydrogen production amount was only slightly increased.

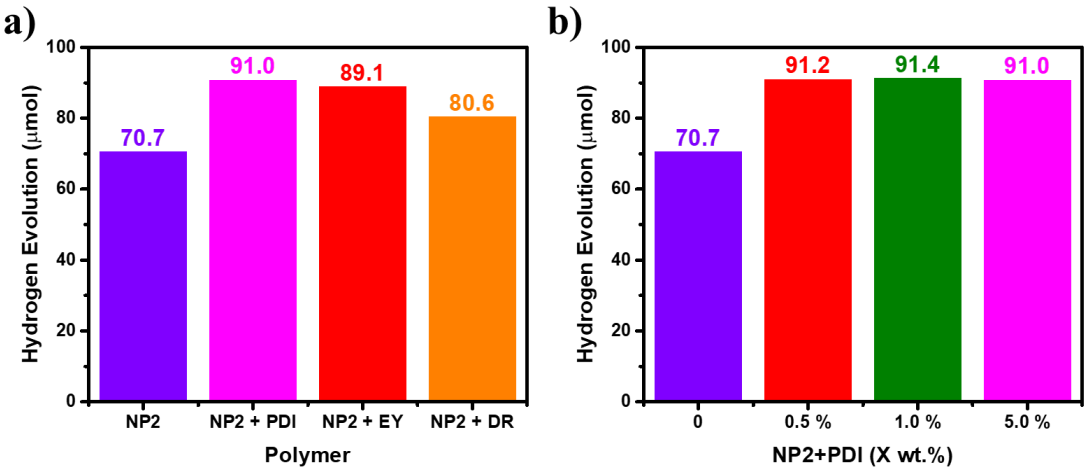

Figure 3.24 Hydrogen evolution of a) NP2 and NP2/dye (5 wt.%) composites, b) NP2/PDI composites with different PDI loading amount. Conditions: 2 mg catalyst in 5 mL TEA/MeOH/H_2O (1:1:1) mixture solution, irradiated for 2 hours by an oriel solar simulator 94123A with an output of 1.0 sun.

The improved hydrogen evolution of dye sensitized NP2 could be mainly attributed to the enhanced visible light absorption, although the performance was not obviously improved. In addition, the Z-scheme like heterojunction could also contribute to the improvement of activity, that is, the electrons generated from the dyes combined with the holes in NP2, which decreased the recombination of electrons and holes in NP2, and thus enhance the photocatalytic activity. However, the best sample of NP2/PDI only produced 0.3 times higher amount of hydrogen than NP2 even the content of PDI had been optimized, while the hydrogen evolution amount of NP2/DR was mealy increased by 14% compared with that of NP2. Therefore, other more efficient strategies should be considered.

3.4 NP2/TiO_2 heterojunction photocatalyst

3.4.1 Synthesis and characterisations

As a typical inorganic photocatalyst, TiO_2 has attracted much attention due to its merits of stability, abundance and low cost.[41] However, the main drawback of TiO_2 is large bandgap (about 3.0-3.2 eV, band positions were shown in Figure 3.25), which limits the visible light absorption and affects the photocatalytic performance.[42-44] To overcome this issue, a wide range of research work has been carried out in last decades. For example, Jiang *et al.* reported

that after modifying with soluble conjugated polymer, the photocatalytic activity of TiO_2 was enhanced significantly, which was ascribed to the wider light absorption range (to 1000 nm), and the interface enforcement between the polymer and TiO_2.[45] Ren *et al.* reported a novel covalent organic polymer (COP) modified TiO_2 catalyst. it was found that the COP not only improved the light harvesting in visible light region, but also greatly enhanced the hydrogen production rate of pure TiO_2.[46] Given that NP2 had the best photocatalytic hydrogen evolution performance in this chapter, it was also promising to modify TiO_2 and obtain a new organic-inorganic heterojunction photocatalyst, therefore, TiO_2 (P25, TiO_2 particles: a mixture of anatase and rutile) was combined with NP2 via a ultrasonic method.

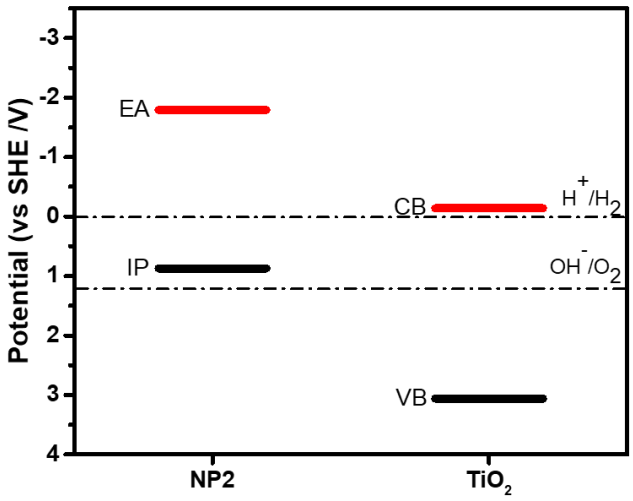

Figure 3.25 Approximate band positions of NP2 and TiO_2 at pH = 0. IP and EA of NP2 were calculated by DFT theory. The conduction band (CB) and valance band (VB) positions of TiO_2 were obtained from literature.[46]

The solid UV-vis spectra in Figure 3.26a shows that after being combined with NP2, the visible absorption of TiO_2 was obviously improved, which could be also confirmed by the sample photographs in Figure 3.26b. The PXRD patters of NP2/TiO_2 composites had no significant difference compared to the pure TiO_2 (Figure 3.27a), which could be due to the amorphous nature of NP2 and the crystalline TiO_2 dominating the patterns. However, the signals of NP2 can be found in the FT-IR spectra between 1000-1500 cm^{-1} and with the loading amount of NP2 increased, the intensity of these peaks also increased (Figure 3.27b). The morphology of TiO_2 did not change distinctly after modification, but with more loading amount of NP2 polymers, more small particles could be observed (Figure 3.28).

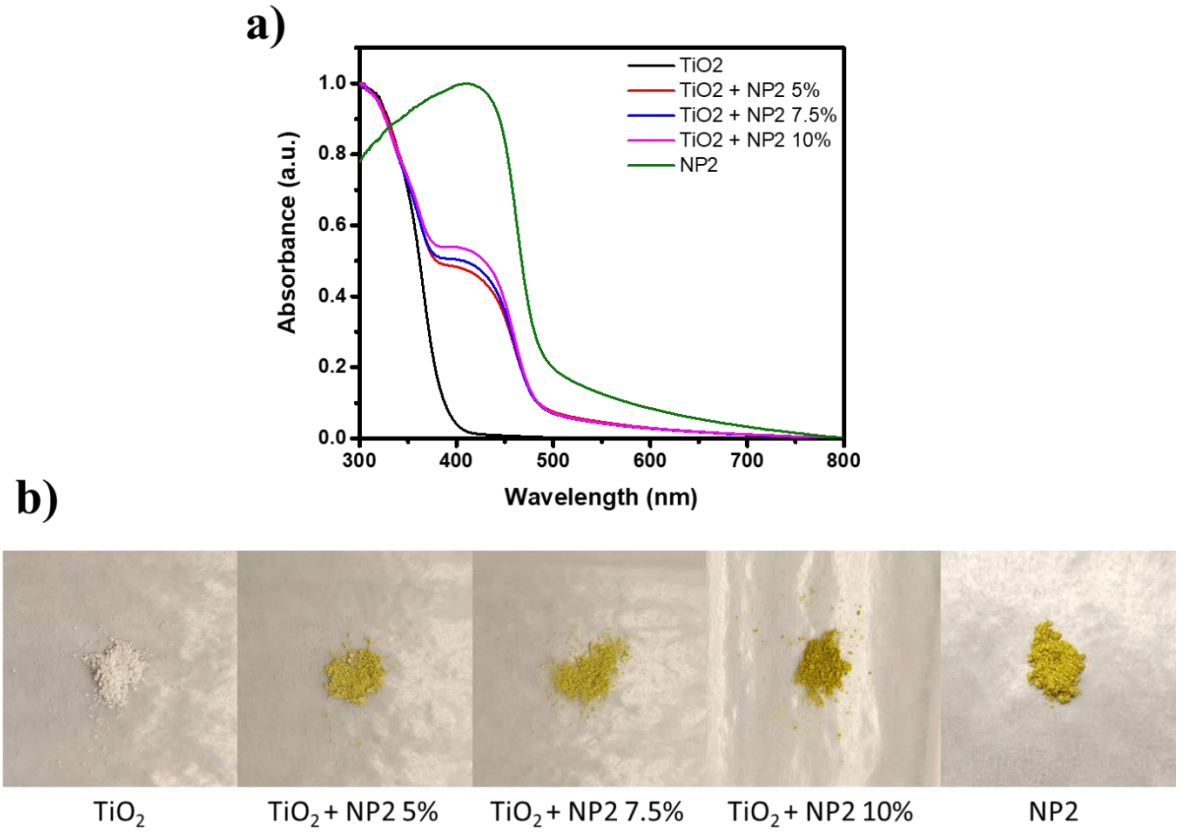

Figure 3.26 a) Solid UV-vis spectra and b) Photographs of NP2 ,TiO_2 and TiO_2/NP2 composites.

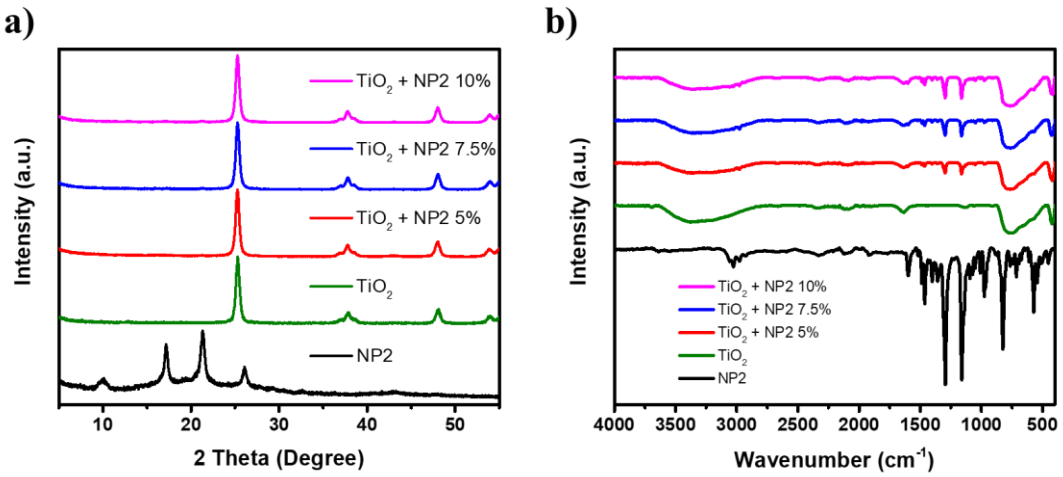

Figure 3.27 a) PXRD patterns and b) Fourier-transform infrared spectra of NP2, TiO_2 and NP2/TiO_2 composites.

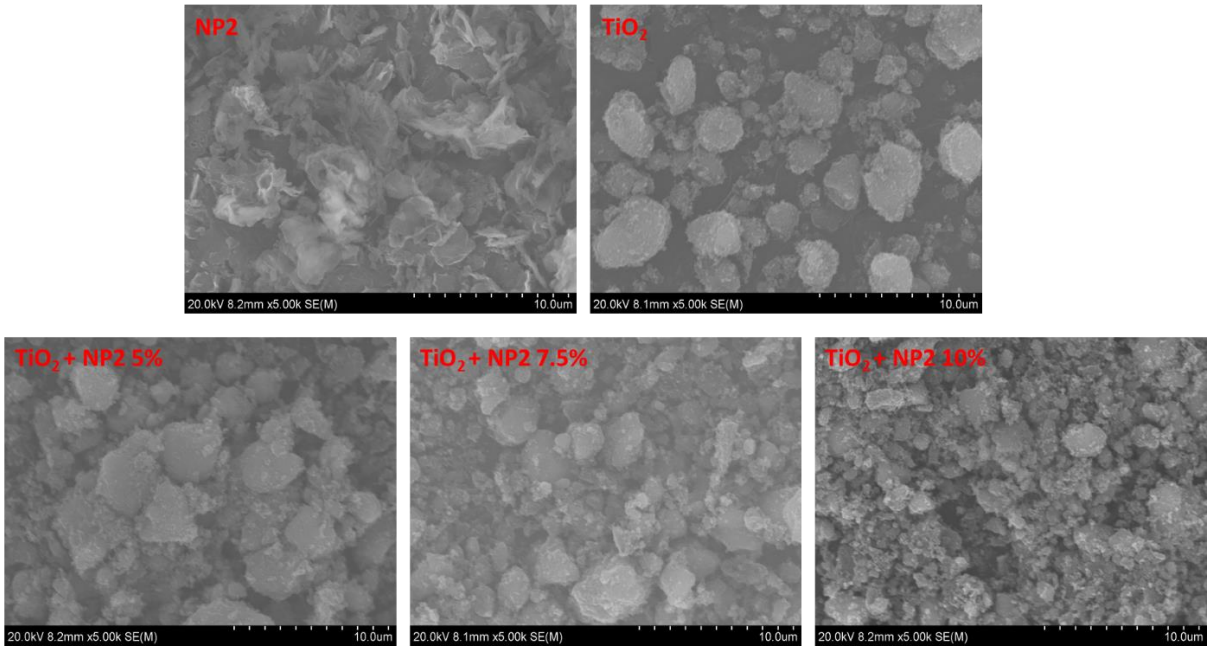

Figure 3.28 SEM images of NP2,TiO_2 and NP2/TiO_2 composites.

The PL measurements were performed to investigate the charge transfer in the heterojunction material. As shown in Figure 3.29a, there was nearly no emission from TiO_2 at this excitation wavelength (λ_{exc} = 371 nm), therefore it was not presented, while the fluorescence intensity of the NP2/TiO_2 heterojunction was decreased compared with that of NP2, which indicated the photogenerated electrons were transferred from the polymer to TiO_2.[47] In addition, the decay lifetimes of NP2/TiO_2 heterojunction were slightly decreased as demonstrated in Figure 3.29b and Table 3.6, which could be attributed to the existence of an additional pathway of interfacial electron transfer between the NP2 and TiO_2.[48, 49]

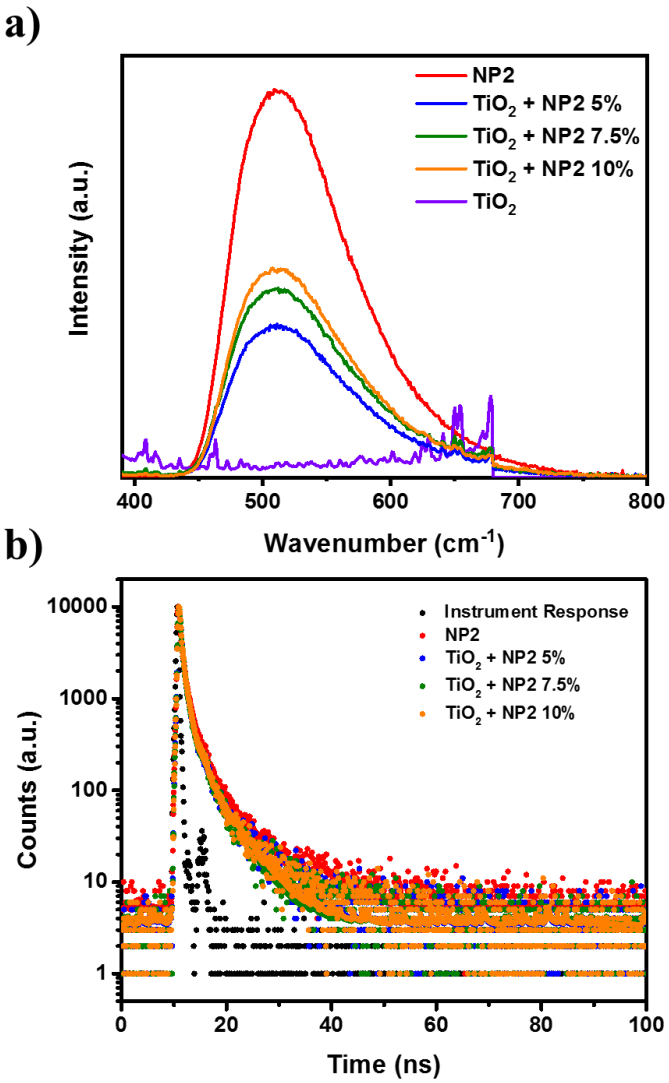

Figure 3.29 a) Photoluminescence emission spectra (λ_{exc} = 371 nm) and b) fluorescence life-time decays of NP2 and NP2/TiO_2 composites.

Table 3.6 Fluorescence lifetimes of NP2 and NP2/TiO_2 composites.

Polymer	$\lambda_{em\text{-}max}$ / nm	τ_1 / ns	B_1 / %	τ_2 / ns	B_2 / %	τ_3 / ns	B_3 / %	χ^2	τ_{avg} / ns
NP2	510	0.36	53.24	1.60	35.18	7.06	11.58	1.525	1.57
TiO_2 + NP2 5%	511	0.31	54.65	1.29	35.17	6.23	10.18	1.658	1.26
TiO_2 + NP2 7.5%	511	0.31	58.19	1.41	32.18	6.21	9.63	1.458	1.23
TiO_2 + NP2 10%	511	0.29	52.01	1.23	36.66	5.64	11.33	1.610	1.24

[a] Fluorescence lifetimes for all polymers obtained from fitting time-correlated single photon counting decays to a sum of three exponentials, which yield τ_1, τ_2 and τ_3 according $\sum_{i=1}^{n}(A + B_i exp(-t/\tau_i))$. τ_{avg} is the weighted average lifetime calculated as $\sum_{i=1}^{n}(B_i\tau_i)$.

3.4.2 Hydrogen evolution

To evaluate the photocatalytic hydrogen evolution performance, the samples were illuminated in a solution of TEA/MeOH/H_2O under a solar simulator (1 sun). As shown in Figure 3.30, the pure TiO_2 had a very low hydrogen evolution activity of 5.2 μmol for 2 hours, while after being modified with NP2, the produced hydrogen amount was increased dramatically to 53.9 μmol with 10 wt.% loading of NP2. However, unexpectedly, the NP2/TiO_2 heterojunction photocatalyst was inferior to NP2 polymer. There are two main possible reasons: 1) the HER performance of NP2 is much higher than that of TiO_2, so NP2 played a dominant role in the hybrid photocatalyst. After combination, its visible light absorption decreased because the interference of TiO_2; 2) the mechanical combination method was possibly not efficient enough, although the mutual carrier transformation happened as evidenced by the photoluminescence emission spectra and lifetime. The contact between NP2 and TiO_2 could be not very compact, which may cause the rapid recombination of photogenerated holes and electrons and thus inhibit the photocatalytic performance; 3) another possible reason is that the photogenerated electrons in NP2 transferred to TiO_2, while the driving force of TiO_2 for hydrogen evolution was not sufficient enough, which leaded to worse performance than pure NP2.

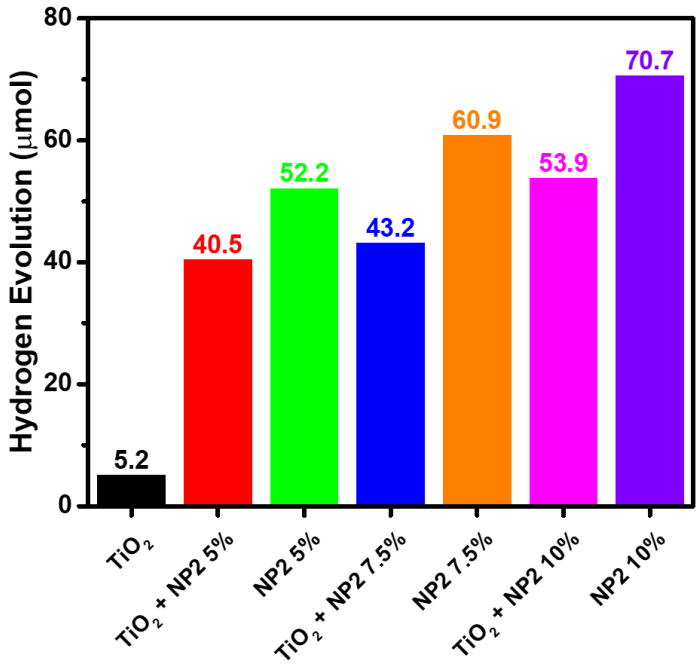

Figure 3.30 Hydrogen evolution amount of NP2, TiO_2 and NP2/TiO_2 composites. Conditions: 20 mg TiO_2 with different loading amount of NP2 in 5 mL TEA/MeOH/H_2O (1:1:1) mixture solution, irradiated for 2 hours by an oriel solar simulator 94123A with an output of 1.0 sun.

3.5 NP2/red phosphorus heterojunction photocatalyst

3.5.1 Synthesis and characterisations

Red Phosphorus (RP) is an allotrope of an inexpensive earth-abundant element with a wide range of visible light absorption.[50] It was previously used for the preparation of igniter or gunpowder.[51] Jimmy *et al.* firstly discovered that it could be also used as a photocatalyst for visible light driven H_2 evolution from water, although the activity was very low.[52] The rapid recombination of photoinduced charges under normal conditions could be a limiting factor for RP to achieve high photocatalytic efficiency.[53, 54] Therefore, it is possible to improve the performance of RP through combination with other components. For example, Xue *et al.* reported that the introduction of g-C_3N_4 onto RP surface could greatly improve the photocatalytic activity for H_2 production as well as CO_2 conversion.[55] Yang *et al.* prepared RP decorated and doped TiO_2 nanofibers and the photocatalytic hydrogen evolution performance from pure water was boosted.[56] Zhang *et al.* fabricated a highly-crystalline CdS/RP heterojunction photocatalyst with enhanced photocatalytic H_2 evolution performance.[57] In addition, the band positions of RP should be appropriate for with NP2 (Figure 3.31). Motivated by above information, RP was combined with NP2 via a simple method. Briefly, a vial was charged with NP2 polymer and a certain amount of RP ethanol solution. After ultrasonicating for 1 hour, the NP2/RP heterojunction photocatalyst was obtained by evaporating the solvent.

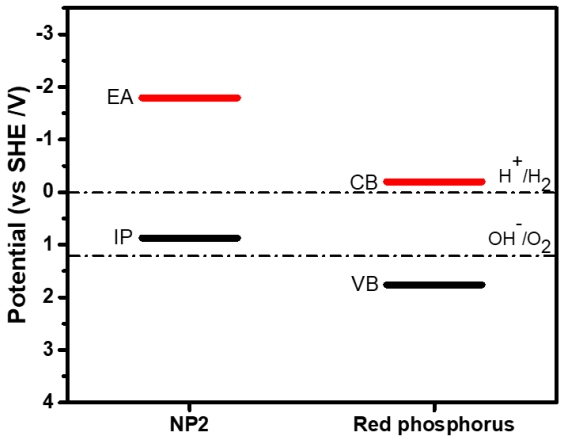

Figure 3.31 Approximate band positions of NP2 and red phosphorus at pH = 0. IP and EA of NP2 were calculated by DFT theory. The conduction band (CB) and valance band (VB) positions of red phosphorus were obtained from literature.[48]

RP is red with a low bandgap, which is beneficial for visible light absorption. After decoration with RP, the visible light absorption of NP2 was slightly increased (Figure 3.32a). The sample colour of NP2/RP was also changed but not obvious (Figure 3.32b), which could be the addition amount of RP was too low. In the PXRD patterns of NP2/RP heterojunctions, a weak signal of RP could be found at around 15 ° (Figure 3.33a). Moreover, the FT-IR spectra of NP2/RP hybrids were similar to that of NP2 (Figure 3.33b). The SEM images (Figure 3.34) revealed that the NP2 sheets aggregated to bulk after combining with RP.

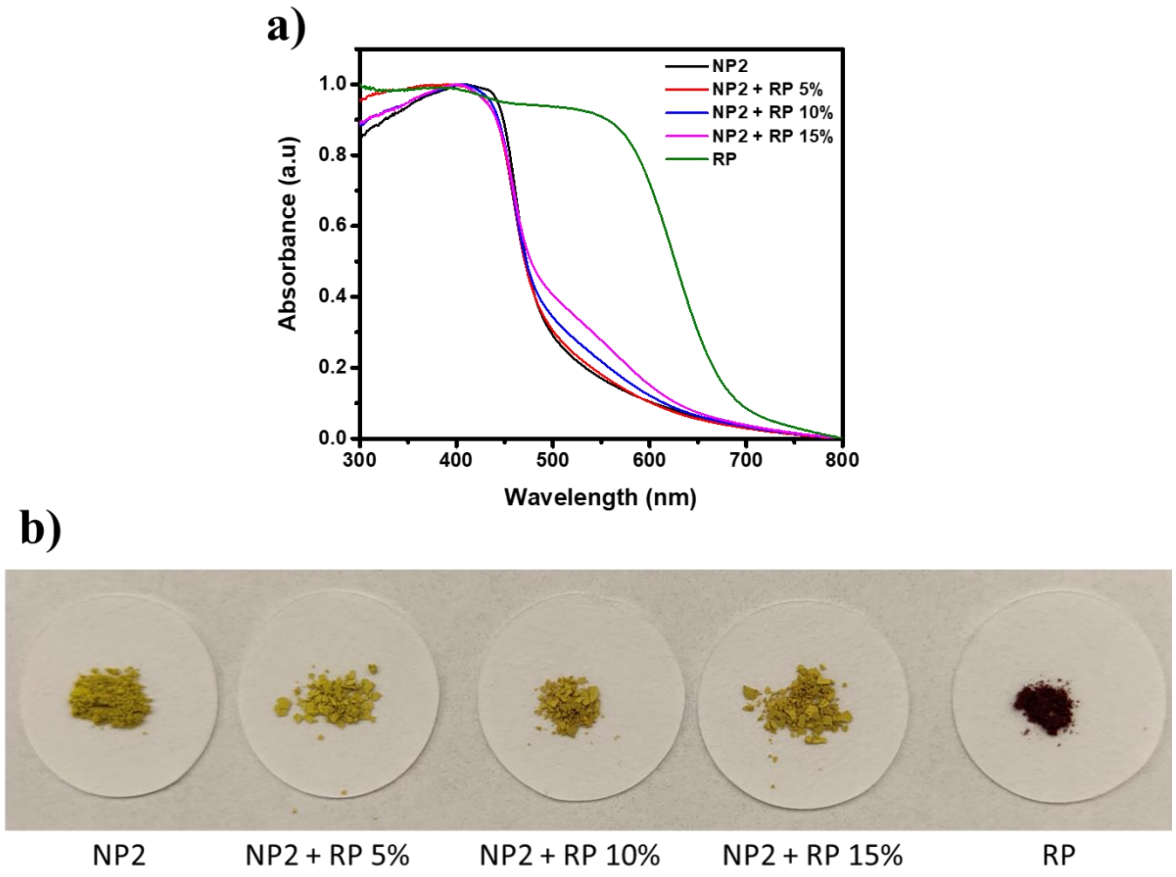

Figure 3.32 a) Solid UV-vis spectra and b) Photographs of NP2, red phosphorus (RP) and NP2/RP composites.

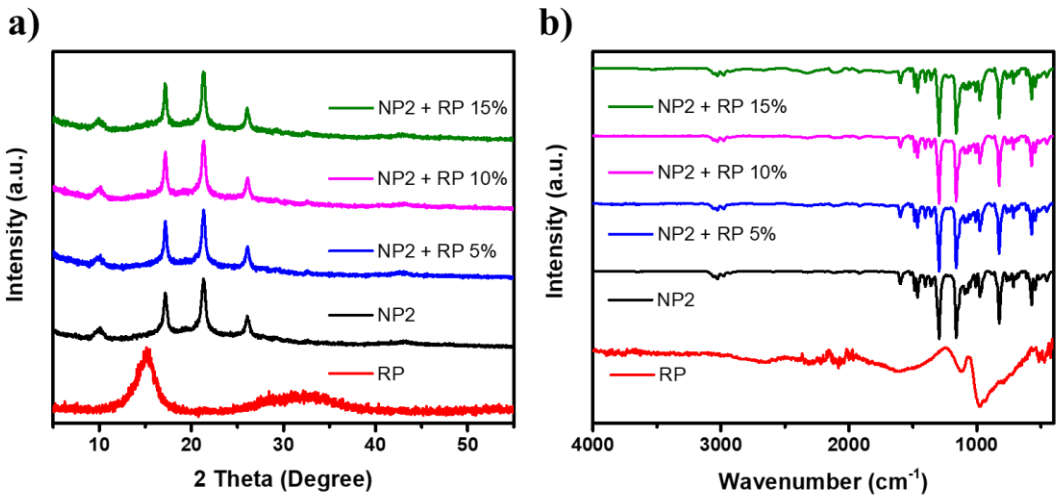

Figure 3.33 a) PXRD patterns and b) Fourier-transform infrared spectra of NP2, RP and NP2/RP composites.

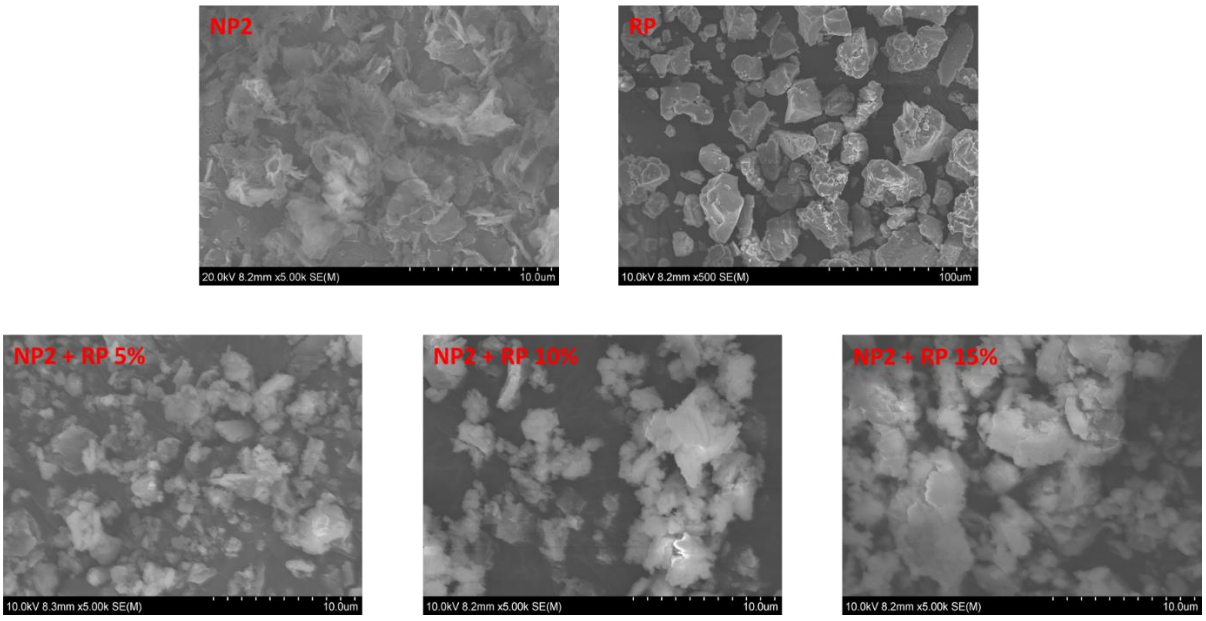

Figure 3.34 SEM images of NP2, RP and NP2/RP composites.

The PL spectra were also measured, as shown in Figure 3.35a, the emission of RP was nearly to zero at the excitation wavelength (λ_{exc} = 371 nm), while for the NP2/RP heterojunctions, an obvious red shift could be observed relative to NP2, which could be attributed to the photogenerated charges transformation between the RP and NP2.[58] The corresponding PL lifetimes were calculated by fitting the data with a triexponential decay function (Figure 3.35b

and Table 3.7), the average lifetime was prolonged for the NP2/RP hybrids, which further confirmed the interaction between these two components.[59]

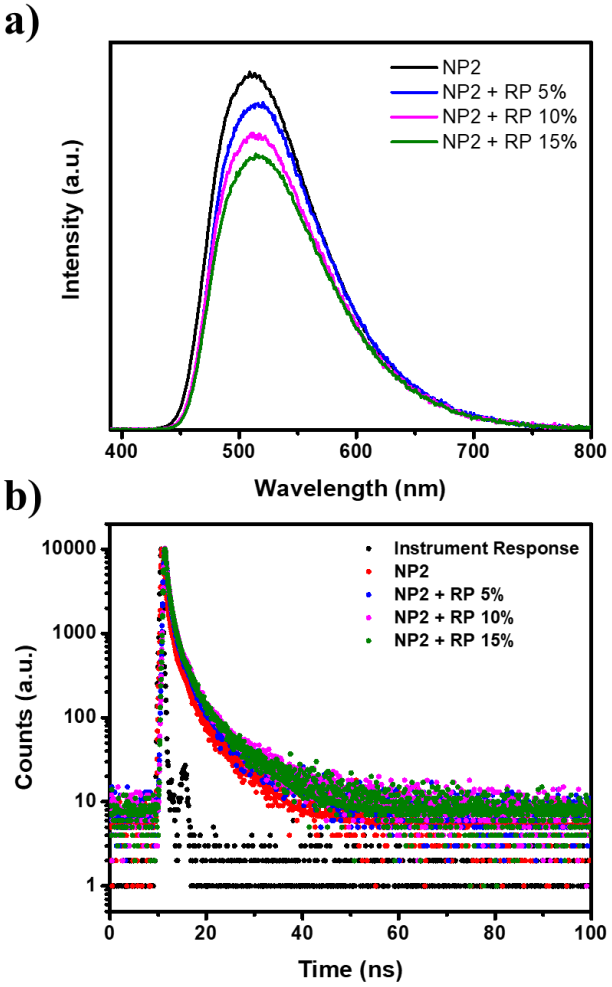

Figure 3.35 a) Photoluminescence emission spectra (λ_{exc} = 371 nm) and b) fluorescence life-time decays of NP2, RP and NP2/RP composites.

Table 3.7 Fluorescence lifetimes of NP2, RP and NP2/RP composites.

Polymer	$\lambda_{em\text{-}max}$ / nm	τ_1 / ns	B_1 / %	τ_2 / ns	B_2 / %	τ_3 / ns	B_3 / %	χ^2	τ_{avg} / ns
NP2	510	0.25	49.95	1.12	36.47	4.97	13.58	1.494	1.21
NP2 + RP 5%	516	0.48	55.52	2.05	33.60	9.10	10.88	1.170	1.94
NP2 + RP 10%	516	0.47	52.89	2.08	35.24	9.03	11.88	1.294	2.05
NP2 + RP 15%	516	0.45	51.83	1.87	35.06	8.10	13.12	1.411	1.96

[a] Fluorescence lifetimes for all polymers obtained from fitting time-correlated single photon counting decays to a sum of three exponentials, which yield τ_1, τ_2 and τ_3 according $\sum_{i=1}^{n}(A + B_i exp(-t/\tau_i))$. τ_{avg} is the weighted average lifetime calculated as $\sum_{i=1}^{n}(B_i\tau_i)$.

3.5.2 Hydrogen evolution

The hydrogen evolution experiments were carried out using TEA as a sacrificial electron donor without additional cocatalyst. The results were displayed in Figure 3.36, RP did not produce H_2 under visible light illumination. But adding 5 wt.% RP into NP2 led to a decrease amount of hydrogen from 70.7 μmol to 66.7 μmol. When the loading amount of RP increased to 15%, the hydrogen amount was further dropped to 58.2 μmol. As a result, the introduction of RP had a negative effect on the photocatalytic hydrogen evolution of NP2. The primary reason could be that after combination, the inactive RP covered the surface of NP2 as can be seen in SEM images (Figure 3.34). Although the visible light absorption of NP2 was improved, the active area of NP2 decreased. However, the combination method could be ineffective for good contact between NP2 and RP, which might be another reason. There are some typical strategies to prepare RP-based hybrids, but normally it requires high temperature (> 500 ℃) and inert atmosphere or vacuum condition.[55, 56, 60] For example, a RP/g-C_3N_4 composite with superior photocatalytic activity was prepared by mixing RP and g-C_3N_4 in the quartz tube and sealed under vacuum, then the tube was heated to 600 ℃, in this way, the RP powder can be converted to RP vapor and has better contact with g-C_3N_4, after that it crystallized in the g-C_3N_4 via cooling to room temperature.[60] Nonetheless, given that NP2 would not be stable over 300 ℃ in N_2 atmosphere as shown in the TGA result (Figure 3.4), and subjected to experimental conditions in our lab, these methods were not tried and applied.

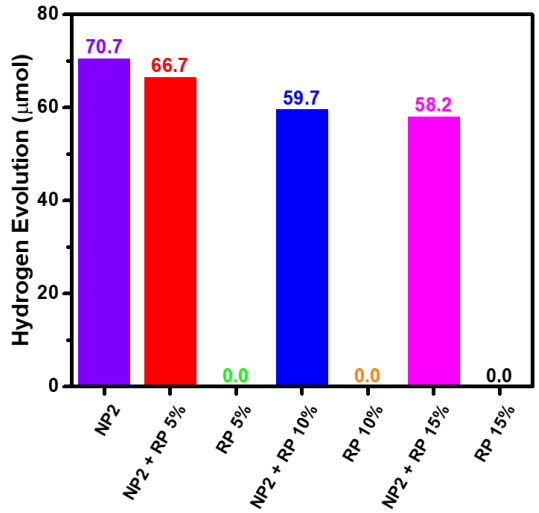

Figure 3.36 Hydrogen evolution amount of NP2, RP and NP2/RP composites. Conditions: 2 mg NP2 with different loading amount of RP in 5 mL TEA/MeOH/H_2O (1:1:1) mixture solution, irradiated for 2 hours by an oriel solar simulator 94123A with an output of 1.0 sun.

3.6 Summary

In summary, we synthesized two series of linear conjugated polymers and compared the effect of the linker on the photocatalytic activity for sacrificial hydrogen evolution from water. It was found that alkenyl linked polymers were more active compared to alkyne linked polymers with alkyl linked polymers, being the least active. The activities can be mainly attributed to the changes in the visible light absorption and hydrophilicity of the materials. Polymer NP2, the best material in this study showed a high HER of 3334 μmol g^{-1} h^{-1} with an EQE of 5.6% at 420 nm. Remarkably, even though the activity of alkyl linked polymers is low, they nevertheless show significant activity despite the lack of extended conjugation.

In addition, the hydrogen evolution performance of the best sample of NP2 can be further promoted by dye-sensitization, although there was no significant improvement. Moreover, the attempts to prepare NP2 heterojunction photocatalysts via combining with TiO_2 or RP did not achieve better result as expected, the performance of heterojunction photocatalysts were even lower than that of NP2, the main reason could be the poor contact between NP2 and TiO_2 or RP because of ineffective combination methods. But it still provides a reference for designing and exploring more organic or organic/inorganic photocatalysts in the future.

3.7 Experimental Parts

3.7.1 Materials and methods

3.7.1.1 Materials

All reagents were obtained from Sigma-Aldrich, Fluorochem, TCI or Alfa Aesar and used as received without further purification**.**

3.7.1.2 Characterization Methods

The absorption spectra of the polymers were measured on a Cary 5000 UV-visible-NIR spectrophotometer in solid powder state. Transmission FT-IR spectra were collected with an attenuated total reflectance (ATR) method on a Bruker Tensor-27 spectrometer for 16 scans with a resolution of 4 cm^{-1} at room temperature. Photoluminescence spectra were performed on a Shimadzu RF-5301PC fluorescence spectrometer. Time-correlated single photon counting (TCSPC) experiments were measured on an Edinburgh Instruments LS980-D2S2-STM spectrometer (EPL-375 diode, λ = 371 nm) equipped with picosecond pulsed LED excitation sources and a R928 detector, with a stop count rate below 5%. The instrument response of the TCSPC spectrometer was measured with colloidal silica (LUDOX® HS-40, Sigma-Aldrich) at the excitation wavelength. Decay times were fitted in the FAST software using three decay exponents. Samples were prepared by ultrasonicating the polymer in water. Thermogravimetric analysis was performed by heating samples under N_2 in open platinum pans from 25 ℃ to 800 ℃ at 10 ℃ min^{-1} on an EXSTAR6000 instrument. PXRD measurements were performed on a Panalytical Empyrean diffractometer with a Cu X-ray source (λ = 1.5418 Å, Cu Kα), polymers were placed on an aluminium well plate and screened in high throughput transmission mode with PIXCEL 3D detector and X-ray focusing mirror. Static light scattering measurements were performed on a Malvern Mastersizer 3000 Particle Sizer at a laser obscuration of 5-10%. Particle sizes were fitted according to the Mie theory with the Malvern 'General Purpose' analysis model. Transmittance of high-throughput samples was measured on a Formulaction S.A.S. Turbiscan AGS system with an 880 nm NIR diode and a detector at 180 ° (relative to the light source) in a cylindrical glass cell. Surface areas were tested on Micromeritics 2420 instrument at a temperature of 77 K. Before analysis, polymer samples were degassed offline at 110 ℃ for 15 hours under dynamic vacuum (10^{-5} bar). CHNS-O Analyzer was measured using standard microanalytical procedures. Palladium contents were determined using ICP-OES Agilent 5110 equipped with a collision/reaction cell after a microwave digestion of the materials in nitric acid (67-69%, trace metal analysis grade) in the

instrument of Perkin Elmer Microwave Titan. Water contact angles were measured using pressed pellets and a drop-shape analysis apparatus (Krüss DSA100) with the Young-Laplace fitting method. The morphology of the polymer was studied on a Hitachi S4800 scanning electron microscope (SEM).

3.7.2 Synthetic procedures

3.7.2.1 Synthesis of polymers

General procedure for Suzuki-Miyaura polycondensation: A flask was charged with the monomers, toluene and an aqueous solution of K_2CO_3 (2.0 M) and after degassed by bubbling with N_2 for 30 min, [$Pd(PPh_3)_4$] was added and degassed additional 15 minutes. The reaction mixture was heated to 110 °C and kept at this temperature for 3 days. After cooled to room temperature, the mixture was poured into methanol, and filtered off. The precipitate was further purified by Soxhlet extraction with methanol and chloroform. The final product was dried in the vacuum oven at 80 °C overnight.

NP1: 3,7-Bis(4,4,5,5-tetramethyl-1,3,2-dioxaborolan-2-yl)dibenzo[*b*,*d*]thiophene sulfone (468 mg, 1 mmol), 1,2-bis(4-bromophenyl)ethane (340 mg, 1 mmol), [$Pd(PPh_3)_4$] (18 mg), 18 mL toluene and 8 mL K_2CO_3 aqueous solution (2.0 M) were used in this polymerization. After work-up and Soxhlet the product was obtained as a grey powder (229.8 mg, 58%). Anal. Calcd for $(C_{12}H_4S)_n$: C, 79.16; H, 4.60; S, 8.13%; Found C, 73.13; H, 4.52; S, 7.56%. Pd content: 0.54%.

NP2: 3,7-Bis(4,4,5,5-tetramethyl-1,3,2-dioxaborolan-2-yl)dibenzo[*b*,*d*]thiophene sulfone (468 mg, 1 mmol), 4,4'-dibromo-*trans*-stilbene (338 mg, 1 mmol), [$Pd(PPh_3)_4$] (18 mg), 18 mL toluene and 8 mL K_2CO_3 aqueous solution (2.0 M) were used in this polymerization. After work-up and Soxhlet the product was obtained as a green powder (262.7 mg, 67%). Anal. Calcd for $(C_{12}H_4S)_n$: C, 79.57; H, 4.11; S, 8.17%; Found C, 71.16; H, 4.11; S, 6.85%. Pd content: 0.40%.

NP3: 3,7-Bis(4,4,5,5-tetramethyl-1,3,2-dioxaborolan-2-yl)dibenzo[*b*,*d*]thiophene sulfone (468 mg, 1 mmol), bis(4-bromophenyl)acetylene (336 mg, 1 mmol), [$Pd(PPh_3)_4$] (18 mg), 18 mL toluene and 8 mL K_2CO_3 aqueous solution (2.0 M) were used in this polymerization. After work-up and Soxhlet the product was obtained as a yellow powder (335.9 mg, 86%). Anal.

Calcd for $(C_{12}H_4S)_n$: C, 79.98; H, 3.61; S, 8.21%; Found C, 71.23; H, 3.58; S, 8.13%. Pd content: 0.45%.

NF1: 9,9-Dimethyl-9*H*-fluorene-2,7-diboronic acid bis(pinacol) ester (446 mg, 1 mmol), 1,2-bis(4-bromophenyl)ethane (340 mg, 1 mmol), $[Pd(PPh_3)_4]$ (18 mg), 18 mL toluene and 8 mL K_2CO_3 aqueous solution (2.0 M) were used in this polymerization. After work-up and Soxhlet the product was obtained as a grey powder (245.6 mg, 66%). Anal. Calcd for $(C_{12}H_4S)_n$: C, 93.51; H, 6.49%; Found C, 87.14; H, 6.14%. Pd content: 0.75%.

NF2: 9,9-Dimethyl-9*H*-fluorene-2,7-diboronic acid bis(pinacol) ester (446 mg, 1 mmol), 4,4'-dibromo-*trans*-stilbene (338 mg, 1 mmol), $[Pd(PPh_3)_4]$ (18 mg), 18 mL toluene and 8 mL K_2CO_3 aqueous solution (2.0 M) were used in this polymerization. After work-up and Soxhlet the product was obtained as a green powder (229.6 mg, 62%). Anal. Calcd for $(C_{12}H_4S)_n$: C, 94.01; H, 5.99%; Found C, 84.74; H, 5.57%. Pd content: 0.31%.

NF3: 9,9-Dimethy-9*H*-lfluorene-2,7-diboronic acid bis(pinacol) ester (446 mg, 1 mmol), bis(4-bromophenyl)acetylene (336 mg, 1 mmol), $[Pd(PPh_3)_4]$ (18 mg), 18 mL toluene and 8 mL K_2CO_3 aqueous solution (2.0 M) were used in this polymerization. After work-up and Soxhlet the product was obtained as a green powder (193.6 mg, 53%). Anal. Calcd for $(C_{12}H_4S)_n$: C, 94.53; H, 5.47%; Found C, 82.19; H, 4.97%. Pd content: 0.60%.

3.7.2.2 Synthesis of dye sensitized NP2 photocatalyst

The NP2/dye composites photocatalysts were prepared using the following procedure: 10 mg NP2 polymer and 1 mL DI water were charged in a vial, and then 5 wt. % dye (perylene-3,4,9,10-tetracarboxylic dianhydride, Eosin Y and Disperse Red 1) was added by injecting 500 µL 1 mg mL^{-1} dye ethanol solution. The mixture was subsequently ultrasonicated for 2 hours and stirred at room temperature for 24 hours, the final products were obtained via solvent evaporation at 80 ℃ on a hot palate.

3.7.2.3 Synthesis of NP2/TiO_2 heterojunction photocatalyst

The NP2/TiO_2 heterojunction photocatalyst was prepared via a simple mixing method. Typically, 20 mg TiO_2 and a certain amount X (X= 5 wt.%, 7.5 wt.% and 10 wt. %) of NP2 polymer were added in a vial consists of 1 mL ethanol, then the vial was sealed and transferred

to an ultrasonic bath. After ultrasonicated for 1 hour, the cap was removed, and the vial was placed in a hot plate until the solvent was evaporated. The obtained heterojunction photocatalysts were named as TiO_2 + NP2 5%, TiO_2 + NP2 7.5% and TiO_2 + NP2 10%, respectively.

3.7.2.4 Synthesis of NP2/red phosphorus heterojunction photocatalyst

First, the commercial red phosphorus was purified to remove the oxide layer on the chemical surface by a typical reported method.[48] Briefly, 1 g red phosphorus and 40 mL DI water were added in a 125 mL Telflon-lined stainless autoclave, the autoclave reactor was subsequently transferred to a oven heated to 200 ℃ for 24 h.

To prepare the NP2/red phosphorus heterojunction photocatalyst, a certain amount X (X= 5 wt%, 10 wt.% and 15 wt.%) of 1 mg mL^{-1} purified res phosphorus ethanol solution was loading on NP2 polymer, the mixture was ultrasonicated for 1 hour followed by heating on a hot plate to evaporate the solvent. The obtained heterojunction photocatalysts were named as NP2 + RP 5%, NP2 + RP 10% and NP2 + RP 15%, respectively.

3.7.3 Photocatalytic experiments

3.7.3.1 General photocatalytic hydrogen production procedure

A quartz reaction flask was charge with 25 mg polymer and 25 mL mixtures of TEA/MeOH/H_2O (1:1:1), the flask was sealed with a rubber septum. After ultrasonication for 10 minutes, the well-dispersed suspension was degassed by bubbling with N_2 for 30 minutes before illuminating with a 300 W Newport Xe light source with a 420 nm cut-off filter. The concentration of hydrogen was determined by a Bruker 450-GC gas chromatograph equipped with TCD detector. For longer-term stability experiments, after illumination for 5 hours, the polymer was recovered through filtration, and after drying, 25 mL water/methanol/triethylamine/ mixture was added again before the next run. External quantum efficiency (EQE) was estimated using the following formula:

$$\mathrm{EQE\%} = \frac{2 \times \text{Number of evolved } H_2 \text{ molecules}}{\text{Number of incident photons}} \times 100\%$$

Experiments were performed under a light-emitting diode irradiation (λ = 420, 490, 700 nm).

3.7.3.2 High-throughput photocatalytic hydrogen production procedure

Photocatalytic hydrogen evolution experiments of NP2/dye composites were performed with same process on a high-throughput automatic platform, the amount of catalyst was 2 mg, and 5 mL reaction mixture of TEA/MeOH/H_2O (1:1:1), an Oriel Solar Simulator 94123A with an output of 1.0 Sun (Class AAA, 1440 W Xe light source, 12 × 12 in.) was used as the light source. After 2 hours, the amount of hydrogen evolved was determined on an Agilent HS-GC (7890B).

3.7.4 Computational details

3.7.4.1 Conformation search

The structures of the oligomers were constructed with the program STK.[61] Afterwards, for each oligomer, we generated a set of 500 trial structures to serve as the starting points for the conformation search. These were sampled from molecular dynamics (MD) trajectories in which the electronic structure of the oligomer was treated with the use of the extended semiempirical tight-binding[62] (xTB) model. In order to allow the oligomer to sample a broad volume of the conformation space, during the MD simulations the temperature of the system was maintained at 600 K. Afterwards, the trial structures were optimized at the xTB level of theory.

The resulting equilibrium geometries were ranked according to energy. It was assumed that the lowest-energy conformer of each oligomer is representative of the properties of the given polymer. Accordingly, this conformer was selected for the calculation of the electronic and optical properties.

In the case of oligomers NF1 and NP1, it was found that the low-energy conformers are those where the oligomer chain adopts a coiled, globule-like conformation. In order to gauge the effect of conformation on the optical and electronic properties of these oligomers, we additionally took into account some representative linear conformers.

The xTB calculations were performed with the Semiempirical Extended Tight-Binding Program Package (xtb2019), version 5.6.4SE, and used the GFN_2 parameterization of the xTB model.[63] Aqueous solvation was represented via the generalized Born model augmented with

the hydrophobic solvent accessible surface area term (GBSA). At the stage of the conformation search, all oligomers were considered to exist in the charge-neutral forms.

3.7.4.2 Calculation of optical and electronic properties

Having identified the representative conformer of each oligomer, we proceeded to optimize its geometry at the density functional theory (DFT) level. In order to calculate the adiabatic ionization potential (IP) and adiabatic electron affinity (EA) of the oligomer, the geometries of the radical cation and radical anion forms of the representative conformer were likewise optimized at the DFT level. Lastly, the excitation spectrum of the charge-neutral form of the representative conformer was calculated at the time-dependent DFT (TDDFT) level of theory. For each polymer, the excited-state IP and EA values (denoted IP* and EA*, respectively) were calculated basing on of the vertical energy of the lowest singlet excited state (S_1).

The DFT and TDDFT calculations were performed with the program Turbomole, version 6.5. The B3LYP exchange-correlation functional[64, 65] was used in combination with the DZP basis set.[66, 67] The effects of aqueous solvation were included via the conductor-like screening model[68, 69] (COSMO). At all times, the energies and gradients were corrected for dispersion effects with the D3 semiempirical dispersion correction scheme of Grimme and coworkers.[70]

3.8 References

1. Pachfule, P.; Acharjya, A.; Roeser, J.; Langenhahn, T.; Schwarze, M.; Schomäcker, R.; Thomas, A.; Schmidt, J., Diacetylene Functionalized Covalent Organic Framework (COF) for Photocatalytic Hydrogen Generation. *J. Am. Chem. Soc.* **2018,** *140* (4), 1423-1427.
2. Wang, X.; Chen, L.; Chong, S. Y.; Little, M. A.; Wu, Y.; Zhu, W.-H.; Clowes, R.; Yan, Y.; Zwijnenburg, M. A.; Sprick, R. S.; Cooper, A. I., Sulfone-containing covalent organic frameworks for photocatalytic hydrogen evolution from water. *Nat. Chem.* **2018,** *10* (12), 1180-1189.
3. Sprick, R. S.; Jiang, J.-X.; Bonillo, B.; Ren, S.; Ratvijitvech, T.; Guiglion, P.; Zwijnenburg, M. A.; Adams, D. J.; Cooper, A. I., Tunable Organic Photocatalysts for Visible-Light-Driven Hydrogen Evolution. *J. Am. Chem. Soc.* **2015,** *137* (9), 3265-3270.
4. Wang, Z.; Yang, X.; Yang, T.; Zhao, Y.; Wang, F.; Chen, Y.; Zeng, J. H.; Yan, C.; Huang, F.; Jiang, J.-X., Dibenzothiophene Dioxide Based Conjugated Microporous Polymers for Visible-Light-Driven Hydrogen Production. *ACS Catal.* **2018,** *8* (9), 8590-8596.
5. Zhang, G.; Ou, W.; Wang, J.; Xu, Y.; Xu, D.; Sun, T.; Xiao, S.; Wang, M.; Li, H.; Chen, W.; Su, C., Stable, carrier separation tailorable conjugated microporous polymers as a platform for highly efficient photocatalytic H2 evolution. *Appl. Catal. B-Environ.* **2019,** *245*, 114-121.
6. Sprick, R. S.; Bai, Y.; Guilbert, A. A. Y.; Zbiri, M.; Aitchison, C. M.; Wilbraham, L.; Yan, Y.; Woods, D. J.; Zwijnenburg, M. A.; Cooper, A. I., Photocatalytic Hydrogen Evolution from Water Using Fluorene and Dibenzothiophene Sulfone-Conjugated Microporous and Linear Polymers. *Chem. Mater.* **2019,** *31* (2), 305-313.
7. Meier, C. B.; Clowes, R.; Berardo, E.; Jelfs, K. E.; Zwijnenburg, M. A.; Sprick, R. S.; Cooper, A. I., Structurally Diverse Covalent Triazine-Based Framework Materials for Photocatalytic Hydrogen Evolution from Water. *Chem. Mater.* **2019,** *31* (21), 8830-8838.
8. Meier, C. B.; Sprick, R. S.; Monti, A.; Guiglion, P.; Lee, J.-S. M.; Zwijnenburg, M. A.; Cooper, A. I., Structure-property relationships for covalent triazine-based frameworks: The effect of spacer length on photocatalytic hydrogen evolution from water. *Polymer* **2017,** *126*, 283-290.
9. Xie, J.; Shevlin, S. A.; Ruan, Q.; Moniz, S. J. A.; Liu, Y.; Liu, X.; Li, Y.; Lau, C. C.; Guo, Z. X.; Tang, J., Efficient visible light-driven water oxidation and proton reduction by an ordered covalent triazine-based framework. *Energy & Environmental Science* **2018,** *11* (6), 1617-1624.
10. Bai, Y.; Wilbraham, L.; Slater, B. J.; Zwijnenburg, M. A.; Sprick, R. S.; Cooper, A. I., Accelerated Discovery of Organic Polymer Photocatalysts for Hydrogen Evolution from Water through the Integration of Experiment and Theory. *J. Am. Chem. Soc.* **2019,** *141* (22), 9063-9071.
11. Sprick, R. S.; Bonillo, B.; Clowes, R.; Guiglion, P.; Brownbill, N. J.; Slater, B. J.; Blanc, F.; Zwijnenburg, M. A.; Adams, D. J.; Cooper, A. I., Visible-Light-Driven Hydrogen Evolution Using Planarized Conjugated Polymer Photocatalysts. *Angew. Chem. Int. Ed.* **2016,** *55* (5), 1792-1796.
12. Zhang, X.-H.; Wang, X.-P.; Xiao, J.; Wang, S.-Y.; Huang, D.-K.; Ding, X.; Xiang, Y.-G.; Chen, H., Synthesis of 1,4-diethynylbenzene-based conjugated polymer photocatalysts and their enhanced visible/near-infrared-light-driven hydrogen production activity. *J. Catal.* **2017,** *350*, 64-71.
13. Sprick, R. S.; Cheetham, K. J.; Bai, Y.; Alves Fernandes, J.; Barnes, M.; Bradley, J. W.; Cooper, A. I., Polymer photocatalysts with plasma-enhanced activity. *J. Mater. Chem. A* **2020,** *8* (15), 7125-7129.

14. Vyas, V. S.; Haase, F.; Stegbauer, L.; Savasci, G.; Podjaski, F.; Ochsenfeld, C.; Lotsch, B. V., A tunable azine covalent organic framework platform for visible light-induced hydrogen generation. *Nat. Commun.* **2015,** *6* (1), 8508.
15. Xiang, Y.; Wang, X.; Rao, L.; Wang, P.; Huang, D.; Ding, X.; Zhang, X.; Wang, S.; Chen, H.; Zhu, Y., Conjugated Polymers with Sequential Fluorination for Enhanced Photocatalytic H2 Evolution via Proton-Coupled Electron Transfer. *ACS Energy Lett.* **2018,** *3* (10), 2544-2549.
16. Cui, Y.; Wang, H.; Yang, C.; Li, M.; Zhao, Y.; Chen, F., Post-activation of in situ BF codoped g-C3N4 for enhanced photocatalytic H2 evolution. *Appl. Surf. Sci.* **2018,** *441*, 621-630.
17. Guo, L.; Niu, Y.; Xu, H.; Li, Q.; Razzaque, S.; Huang, Q.; Jin, S.; Tan, B., Engineering heteroatoms with atomic precision in donor–acceptor covalent triazine frameworks to boost photocatalytic hydrogen production. *J. Mater. Chem. A* **2018,** *6* (40), 19775-19781.
18. Liu, Q.; Shen, J.; Yu, X.; Yang, X.; Liu, W.; Yang, J.; Tang, H.; Xu, H.; Li, H.; Li, Y.; Xu, J., Unveiling the origin of boosted photocatalytic hydrogen evolution in simultaneously (S, P, O)-Codoped and exfoliated ultrathin g-C3N4 nanosheets. *Appl. Catal. B-Environ.* **2019,** *248*, 84-94.
19. Wang, H.; Bian, Y.; Hu, J.; Dai, L., Highly crystalline sulfur-doped carbon nitride as photocatalyst for efficient visible-light hydrogen generation. *Appl. Catal. B-Environ.* **2018,** *238*, 592-598.
20. Zhang, Y.-H.; Jiu, B.-B.; Gong, F.-L.; Chen, J.-L.; Zhang, H.-L., Morphology-controllable Cu2O supercrystals: Facile synthesis, facet etching mechanism and comparative photocatalytic H2 production. *J. Alloys Compd.* **2017,** *729*, 563-570.
21. Dong, H.; Hong, S.; Zuo, Y.; Zhang, X.; Lu, Z.; Han, J.; Wang, L.; Ni, L.; Li, C.; Wang, Y., Fabrication of 2D/0D Heterojunction Based on the Dual Controls of Micro/Nano-Morphology and Structure Towards High-Efficiency Photocatalytic H2 Production. *ChemCatChem* **2019,** *11* (24), 6263-6269.
22. Jiang, R.; Lu, G.; Zhou, R.; Yang, H.; Yan, Z.; Wu, D.; Liu, J.; Nkoom, M., Switching g-C3N4 morphology from double-walled to single-walled microtubes induced high photocatalytic H2-production performance. *J. Alloys Compd.* **2020,** *820*, 153166.
23. Tahir, B.; Tahir, M., Morphological effect of 1D/1D In2O3/TiO2 NRs/NWs heterojunction photo-embedded with Cu-NPs for enhanced photocatalytic H2 evolution under visible light. *Appl. Surf. Sci.* **2020,** *506*, 145034.
24. Zhao, G.; Sun, Y.; Zhou, W.; Wang, X.; Chang, K.; Liu, G.; Liu, H.; Kako, T.; Ye, J., Superior Photocatalytic H2 Production with Cocatalytic Co/Ni Species Anchored on Sulfide Semiconductor. *Adv. Mater.* **2017,** *29* (40), 1703258.
25. Liu, M.; Xia, P.; Zhang, L.; Cheng, B.; Yu, J., Enhanced Photocatalytic H2-Production Activity of g-C3N4 Nanosheets via Optimal Photodeposition of Pt as Cocatalyst. *ACS Sustainable Chem. Eng.* **2018,** *6* (8), 10472-10480.
26. Li, Z.; Ma, Y.; Hu, X.; Liu, E.; Fan, J., Enhanced photocatalytic H2 production over dual-cocatalyst-modified g-C3N4 heterojunctions. *Chinese Journal of Catalysis* **2019,** *40* (3), 434-445.
27. Xiang, X.; Zhu, B.; Cheng, B.; Yu, J.; Lv, H., Enhanced Photocatalytic H2-Production Activity of CdS Quantum Dots Using Sn2+ as Cocatalyst under Visible Light Irradiation. *Small* **2020,** *16* (26), 2001024.
28. Sachs, M.; Sprick, R. S.; Pearce, D.; Hillman, S. A. J.; Monti, A.; Guilbert, A. A. Y.; Brownbill, N. J.; Dimitrov, S.; Shi, X.; Blanc, F.; Zwijnenburg, M. A.; Nelson, J.; Durrant, J. R.; Cooper, A. I., Understanding structure-activity relationships in linear polymer photocatalysts for hydrogen evolution. *Nat. Commun.* **2018,** *9* (1), 4968.

29. Woods, D. J.; Hillman, S. A. J.; Pearce, D.; Wilbraham, L.; Flagg, L. Q.; Duffy, W.; McCulloch, I.; Durrant, J. R.; Guilbert, A. A. Y.; Zwijnenburg, M. A.; Sprick, R. S.; Nelson, J.; Cooper, A. I., Side-chain tuning in conjugated polymer photocatalysts for improved hydrogen production from water. *Energy & Environmental Science* **2020,** *13* (6), 1843-1855.
30. Kosco, J.; Sachs, M.; Godin, R.; Kirkus, M.; Francas, L.; Bidwell, M.; Qureshi, M.; Anjum, D.; Durrant, J. R.; McCulloch, I., The Effect of Residual Palladium Catalyst Contamination on the Photocatalytic Hydrogen Evolution Activity of Conjugated Polymers. *Adv. Energy Mater.* **2018,** *8* (34), 1802181.
31. Li, L.; Cai, Z.; Wu, Q.; Lo, W.-Y.; Zhang, N.; Chen, L. X.; Yu, L., Rational Design of Porous Conjugated Polymers and Roles of Residual Palladium for Photocatalytic Hydrogen Production. *J. Am. Chem. Soc.* **2016,** *138* (24), 7681-7686.
32. Aitchison, C. M.; Sachs, M.; Little, M. A.; Wilbraham, L.; Brownbill, N. J.; Kane, C. M.; Blanc, F.; Zwijnenburg, M. A.; Durrant, J. R.; Sprick, R. S.; Cooper, A. I., Structure–activity relationships in well-defined conjugated oligomer photocatalysts for hydrogen production from water. *Chem. Sci.* **2020,** *11* (33), 8744-8756.
33. Yang, C.; Ma, B. C.; Zhang, L.; Lin, S.; Ghasimi, S.; Landfester, K.; Zhang, K. A. I.; Wang, X., Molecular Engineering of Conjugated Polybenzothiadiazoles for Enhanced Hydrogen Production by Photosynthesis. *Angew. Chem. Int. Ed.* **2016,** *55* (32), 9202-9206.
34. Shu, C.; Han, C.; Yang, X.; Zhang, C.; Chen, Y.; Ren, S.; Wang, F.; Huang, F.; Jiang, J.-X., Boosting the Photocatalytic Hydrogen Evolution Activity for D–π–A Conjugated Microporous Polymers by Statistical Copolymerization. *Adv. Mater.* **2021,** *33* (26), 2008498.
35. Bi, S.; Lan, Z.-A.; Paasch, S.; Zhang, W.; He, Y.; Zhang, C.; Liu, F.; Wu, D.; Zhuang, X.; Brunner, E.; Wang, X.; Zhang, F., Substantial Cyano-Substituted Fully sp2-Carbon-Linked Framework: Metal-Free Approach and Visible-Light-Driven Hydrogen Evolution. *Adv. Funct. Mater.* **2017,** *27* (39), 1703146.
36. Peng, S.; Cao, Y.; Zhou, F.; Xu, Z.; Li, Y., CoP decorated with Co3O4 as a cocatalyst for enhanced photocatalytic hydrogen evolution via dye sensitization. *Appl. Surf. Sci.* **2019,** *487*, 315-321.
37. Wang, Y.; Hong, J.; Zhang, W.; Xu, R., Carbon nitride nanosheets for photocatalytic hydrogen evolution: remarkably enhanced activity by dye sensitization. *Catal. Sci. Technol.* **2013,** *3* (7), 1703-1711.
38. Young-Sung Kim, S.-H. K., Tae-Kyung Kim, Young-A Son, Characteristics of HOMO and LUMO Potentials by Altering Substituents: Computational and Electrochemical Determination. *Journal of the Korean Society of Dyers and Finishers* **2008,** *20* (5), 41-46.
39. Sang, L.; Lei, L.; Lin, J.; Ge, H., Co-sensitization of TiO2 electrode with Eosin Y dye and carbon dots for photoelectrochemical water splitting: The enhanced dye adsorption and the charge transfer route. *Int. J. Hydrogen Energy* **2017,** *42* (50), 29686-29693.
40. Wang, Y.; Zhou, J.; Hao, X.; Wang, Y.; Zou, Z., Fabricating direct Z-scheme PTCDA/g-C3N4 photocatalyst based on interfacial strong interaction for efficient photooxidation of benzylamine. *Appl. Surf. Sci.* **2018,** *456*, 861-870.
41. Eidsvåg, H.; Bentouba, S.; Vajeeston, P.; Yohi, S.; Velauthapillai, D., TiO2 as a Photocatalyst for Water Splitting—An Experimental and Theoretical Review. *Molecules* **2021,** *26* (6), 1687.
42. Cai, J.; Shen, J.; Zhang, X.; Ng, Y. H.; Huang, J.; Guo, W.; Lin, C.; Lai, Y., Light-Driven Sustainable Hydrogen Production Utilizing TiO2 Nanostructures: A Review. *Small Methods* **2019,** *3* (1), 1800184.
43. Kumaravel, V.; Mathew, S.; Bartlett, J.; Pillai, S. C., Photocatalytic hydrogen production using metal doped TiO2: A review of recent advances. *Appl. Catal. B-Environ.* **2019,** *244*, 1021-1064.

44. Ni, M.; Leung, M. K. H.; Leung, D. Y. C.; Sumathy, K., A review and recent developments in photocatalytic water-splitting using TiO2 for hydrogen production. *Renew. Sustain. Energy Rev.* **2007,** *11* (3), 401-425.
45. Yang, L.; Yu, Y.; Zhang, J.; Chen, F.; Meng, X.; Qiu, Y.; Dan, Y.; Jiang, L., In-situ fabrication of diketopyrrolopyrrole-carbazole-based conjugated polymer/TiO2 heterojunction for enhanced visible light photocatalysis. *Appl. Surf. Sci.* **2018,** *434*, 796-805.
46. Yang, Q.; Peng, P.; Xiang, Z., Covalent organic polymer modified TiO2 nanosheets as highly efficient photocatalysts for hydrogen generation. *Chem. Eng. Sci.* **2017,** *162*, 33-40.
47. Qu, A.; Xu, X.; Xie, H.; Zhang, Y.; Li, Y.; Wang, J., Effects of calcining temperature on photocatalysis of g-C3N4/TiO2 composites for hydrogen evolution from water. *Mater. Res. Bull.* **2016,** *80*, 167-176.
48. Liu, F.; Shi, R.; Wang, Z.; Weng, Y.; Che, C.-M.; Chen, Y., Direct Z-Scheme Hetero-phase Junction of Black/Red Phosphorus for Photocatalytic Water Splitting. *Angew. Chem. Int. Ed.* **2019,** *58* (34), 11791-11795.
49. Zhu, M.; Sun, Z.; Fujitsuka, M.; Majima, T., Z-Scheme Photocatalytic Water Splitting on a 2D Heterostructure of Black Phosphorus/Bismuth Vanadate Using Visible Light. *Angew. Chem. Int. Ed.* **2018,** *57* (8), 2160-2164.
50. Zhu, Y.; Ren, J.; Zhang, X.; Yang, D., Elemental red phosphorus-based materials for photocatalytic water purification and hydrogen production. *Nanoscale* **2020,** *12* (25), 13297-13310.
51. Scheer, M.; Balázs, G.; Seitz, A., P4 Activation by Main Group Elements and Compounds. *Chem. Rev.* **2010,** *110* (7), 4236-4256.
52. Wang, F.; Ng, W. K. H.; Yu, J. C.; Zhu, H.; Li, C.; Zhang, L.; Liu, Z.; Li, Q., Red phosphorus: An elemental photocatalyst for hydrogen formation from water. *Appl. Catal. B-Environ.* **2012,** *111-112*, 409-414.
53. Ansari, S. A.; Ansari, M. S.; Cho, M. H., Metal free earth abundant elemental red phosphorus: a new class of visible light photocatalyst and photoelectrode materials. *Phys. Chem. Chem. Phys.* **2016,** *18* (5), 3921-3928.
54. Hu, Z.; Yuan, L.; Liu, Z.; Shen, Z.; Yu, J. C., An Elemental Phosphorus Photocatalyst with a Record High Hydrogen Evolution Efficiency. *Angew. Chem. Int. Ed.* **2016,** *55* (33), 9580-9585.
55. Yuan, Y.-P.; Cao, S.-W.; Liao, Y.-S.; Yin, L.-S.; Xue, C., Red phosphor/g-C3N4 heterojunction with enhanced photocatalytic activities for solar fuels production. *Appl. Catal. B-Environ.* **2013,** *140-141*, 164-168.
56. Zhu, Y.; Li, J.; Dong, C.-L.; Ren, J.; Huang, Y.-C.; Zhao, D.; Cai, R.; Wei, D.; Yang, X.; Lv, C.; Theis, W.; Bu, Y.; Han, W.; Shen, S.; Yang, D., Red phosphorus decorated and doped TiO2 nanofibers for efficient photocatalytic hydrogen evolution from pure water. *Appl. Catal. B-Environ.* **2019,** *255*, 117764.
57. Xu, M.; Jiang, L.; Wang, J.; Feng, S.; Tremblay, P.-L.; Zhang, T., Efficient photocatalytic hydrogen evolution with high-crystallinity and noble metal-free red phosphorus-CdS nanorods. *Int. J. Hydrogen Energy* **2020,** *45* (35), 17354-17366.
58. Bai, Z.; Chang, M.; Peng, M.; Liu, P.; Lu, A.; Zhang, Z.; Qin, S., Controlling fluorescence of a nano-Al2O3 film enabled by CdSe quantum dots on CdSe/Al2O3 heterojunctions. *J. Lumin.* **2019,** *215*, 116614.
59. Gao, C.; Wei, T.; Zhang, Y.; Song, X.; Huan, Y.; Liu, H.; Zhao, M.; Yu, J.; Chen, X., A Photoresponsive Rutile TiO2 Heterojunction with Enhanced Electron–Hole Separation for High-Performance Hydrogen Evolution. *Adv. Mater.* **2019,** *31* (8), 1806596.
60. Jing, L.; Zhu, R.; Phillips, D. L.; Yu, J. C., Effective Prevention of Charge Trapping in Graphitic Carbon Nitride with Nanosized Red Phosphorus Modification for Superior Photo(electro)catalysis. *Adv. Funct. Mater.* **2017,** *27* (46), 1703484.

61. Turcani, L.; Berardo, E.; Jelfs, K. E., stk: A python toolkit for supramolecular assembly. *J. Comput. Chem.* **2018,** *39* (23), 1931-1942.
62. Grimme, S.; Bannwarth, C.; Shushkov, P., A Robust and Accurate Tight-Binding Quantum Chemical Method for Structures, Vibrational Frequencies, and Noncovalent Interactions of Large Molecular Systems Parametrized for All spd-Block Elements (Z = 1–86). *J. Chem. Theory Comput.* **2017,** *13* (5), 1989-2009.
63. Bannwarth, C.; Ehlert, S.; Grimme, S., GFN2-xTB—An Accurate and Broadly Parametrized Self-Consistent Tight-Binding Quantum Chemical Method with Multipole Electrostatics and Density-Dependent Dispersion Contributions. *J. Chem. Theory Comput.* **2019,** *15* (3), 1652-1671.
64. Becke, A. D., Density‐functional thermochemistry. III. The role of exact exchange. *J. Chem. Phys.* **1993,** *98* (7), 5648-5652.
65. Stephens, P. J.; Devlin, F. J.; Chabalowski, C. F.; Frisch, M. J., Ab Initio Calculation of Vibrational Absorption and Circular Dichroism Spectra Using Density Functional Force Fields. *J. Phys. Chem.* **1994,** *98* (45), 11623-11627.
66. Schäfer, A.; Horn, H.; Ahlrichs, R., Fully optimized contracted Gaussian basis sets for atoms Li to Kr. *J. Chem. Phys.* **1992,** *97* (4), 2571-2577.
67. Gauss, J., Effects of electron correlation in the calculation of nuclear magnetic resonance chemical shifts. *J. Chem. Phys.* **1993,** *99* (5), 3629-3643.
68. Klamt, A.; Schüürmann, G., COSMO: a new approach to dielectric screening in solvents with explicit expressions for the screening energy and its gradient. *J. Chem. Soc., Perkin Trans. 2* **1993,** *2* (5), 799-805.
69. Schäfer, A.; Klamt, A.; Sattel, D.; Lohrenz, J. C. W.; Eckert, F., COSMO Implementation in TURBOMOLE: Extension of an efficient quantum chemical code towards liquid systems. *Phys. Chem. Chem. Phys.* **2000,** *2* (10), 2187-2193.
70. Grimme, S.; Antony, J.; Ehrlich, S.; Krieg, H., A consistent and accurate ab initio parametrization of density functional dispersion correction (DFT-D) for the 94 elements H-Pu. *J. Chem. Phys.* **2010,** *132* (15), 154104.

Chapter 4: Organic Materials for Photocatalytic Hydrogen Peroxide Production

Author contributions:

ICP, element analysis and solid state NMR were measured by the technical staffs in the test centre. Meiyan Gao did the EPR measurements, Rob Clowes carried out the TGA measurements, and Alex James performed the BET measurements. All other experimental work were performed by the thesis author in this chapter. Dr. Xiaobo Li supervised the experiments of cocatalyst, stability and water oxidation half reaction, and reviewed the whole work. Professor Andrew I. Cooper supervised and reviewed the whole work.

4.1 Background

Hydrogen peroxide (H_2O_2) is an important chemical with a multitude of applications, including organic synthesis, wastewater treatments, pulp and paper bleaching. It is also a storable and transportable liquid fuel for electricity generation.[1, 2] The traditional anthraquinone (AQ) process of H_2O_2 synthesis[3, 4] consumes a significant amount of energy and produces environmental waste, as such, it is desirable to develop alternative processes for large scale production of H_2O_2.

As a sustainable and green process, photocatalytic synthesis of H_2O_2 from water is gaining increasing attention.[5-7] The photocatalytic H_2O_2 synthesis typically uses inorganic materials.[8-10] Recently, organic materials, including graphitic carbon nitride (g-C_3N_4),[11-14] supramolecular coordination complexes,[15, 16] coordination polymers[17, 18] and metal-free polymers,[19-21] have been discovered as photocatalysts to produce H_2O_2 with comparable performance to their inorganic counterparts. For example, Shiraishi *et al.* reported a resorcinol-formaldehyde resin for H_2O_2 production in pure water and achieved 0.7% solar-to-chemical conversion efficiency.[19, 20] Ohno *et al.*[14] reported an apparent quantum yield of 17.6% at 420 nm using carbon nitride after single Sb atom modification. However, the concentration of H_2O_2 solution after photocatalysis is limited to tens of mM L^{-1}, much lower than the concentration of commercial 3 wt.% H_2O_2 (979 mM L^{-1}) solution used in medical applications.[22] Therefore, developing more advanced materials for highly efficient photocatalytic H_2O_2 production is urgent.

In previous projects, the high throughput workflow has been proved a powerful platform for accelerated discovery of candidate photocatalysts. In addition, we have large amount of existing organic materials in the lab. Hence, in this chapter, the high throughput workflow was applied again to roughly screen polymer photocatalysts for H_2O_2 production. Meanwhile, some new polymers were designed and synthesized based on the initial screening results and literature research. Moreover, based on the best material of DE7 in this project, several influencing factors and the mechanism of photocatalytic H_2O_2 production were also investigated.

4.2 Benchmark

4.2.1 Preparation and characterization of RF523

Resorcinol-formaldehyde resin, RF523, is one of the best reported organic materials for photocatalytic H_2O_2 synthesis under simulated sunlight irradiation so far.[20] Here, we repeated the preparation of RF523 (RF523-R) and used it as a benchmark material for evaluating the activity of selected materials.

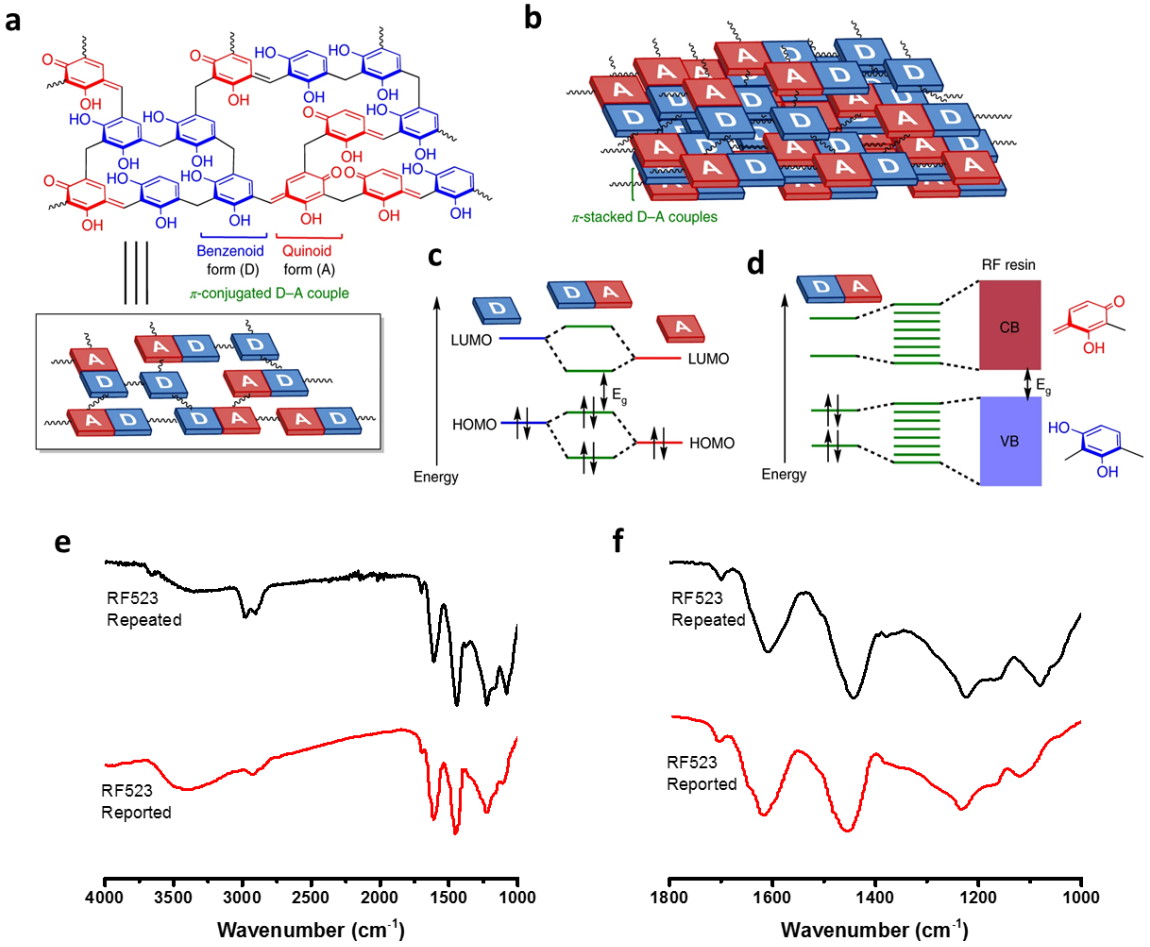

Figure 4.1 Structure of RF resins. Fundamental structure (a) and π-conjugated and π-stacked D–A structure (b) of RF resins. Electronic structures of π-conjugated D–A couples (c) and RF resins (d). [20] Fourier-transformed IR spectra (e) 4000-1000 cm^{-1} and (f) 18000-1000 cm^{-1} of RF523[20] and RF523-R.

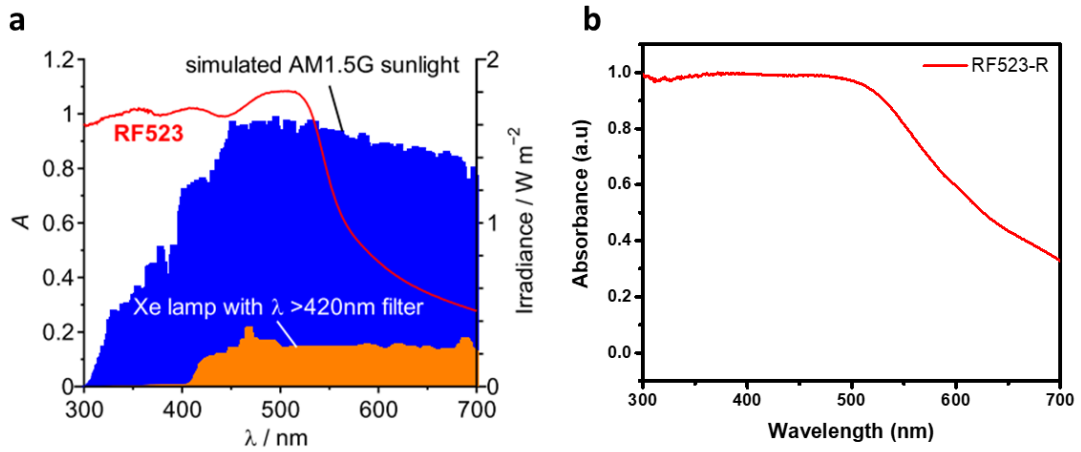

Figure 4.2 Diffuse reflectance UV–vis spectra of RF523[20] (a) and RF523-R (b).

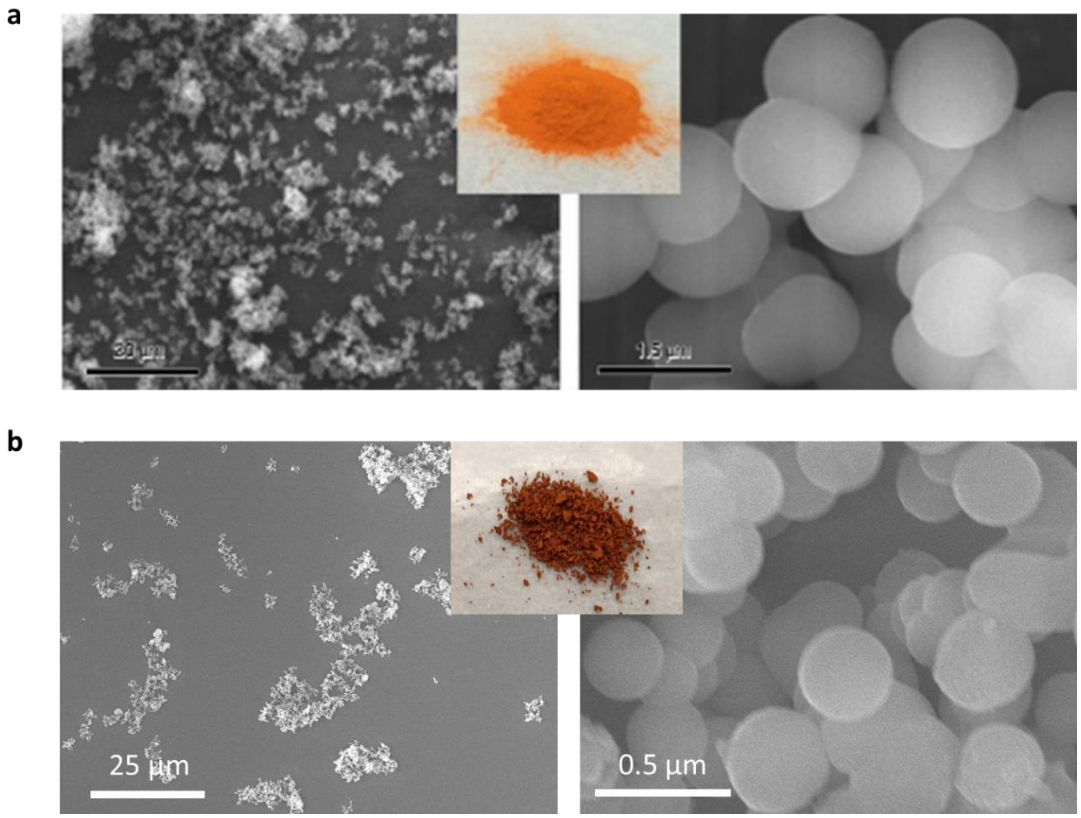

Figure 4.3 Photograph and SEM images of RF523[20] (a) and RF523-R (b).

The structure of RF523 was illustrated in Figure 4.1, and FT-IR spectrum showed that the typical peaks of RF523-R were consist with the reported RF523. But RF523-R had a slightly increased light absorption (Figure 4.2), which could be attributed to its darker red colour (Figure 4.3). Besides, SEM images showed that the morphology of them was similar (Figure 4.3). All of these results indicated the success of reproduction of RF523.

4.2.2 Comparation of H_2O_2 detection methods

4.2.2.1 UV-vis spectroscopy method-A

The amount of H_2O_2 production was carried out by UV-vis spectroscopy after iodometry.[12] The reaction is as follows:

$$H_2O_2 + 3I^- + 2H^+ = I_3^- + 2H_2O \quad (4.1)$$

in which, the product of triiodide anions (I_3^-) has a typical absorption peak at 350 nm in UV-vis spectroscopy (Figure 4.4a). The amount of produced H_2O_2 was calculated from calibration cruve using standard H_2O_2 solution with different concentrations (Figure 4.4b).

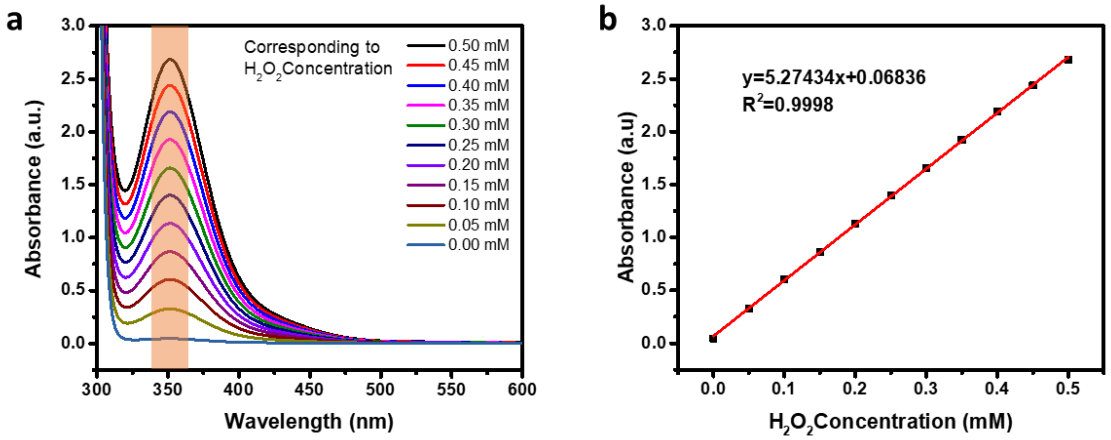

Figure 4.4 (a) UV-vis spectrum of $C_8H_5KO_4$ and KI aqueous solution after adding standard H_2O_2 solution with different concentrations. (b) Corresponding calibration curve at the absorption peak of 350 nm.

4.2.2.2 UV-vis spectroscopy method-B

The H_2O_2 concentration was also determined by cerium sulfate $Ce(SO_4)_2$ titration method.[23] The mechanism is as follows:

$$2Ce^{4+} + H_2O_2 = 2Ce^{3+} + 2H^+ + O_2 \quad (4.2)$$

In 0.5 M sulfuric acid solution, the Ce^{4+} ions have a characteristic absorption peak at 316 nm (Figure 4.5a), which is reduced by H_2O_2 to produce colourless Ce^{3+} (Eq. 4.2). From the calibration curve, the amount of H_2O_2 was calculated by calculating the amount of Ce^{4+} consumed (Figure 4.5b).

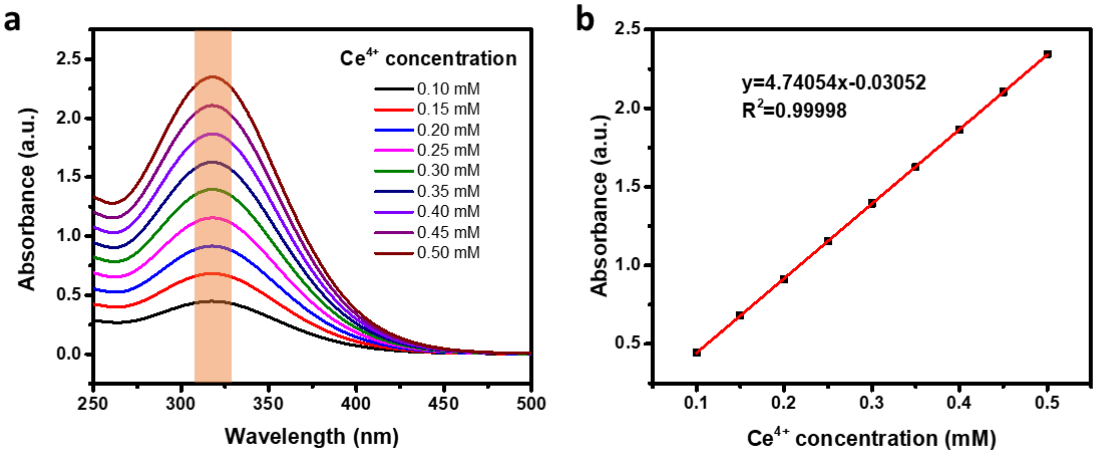

Figure 4.5 (a) UV-vis spectrum of Ce^{4+} solutions with different concentrations. (b) Corresponding calibration curve at the absorption peak of 316 nm.

4.2.2.3 $KMnO_4$ titrimetric method

The K_2MnO_4 titrimetric method for H_2O_2 detection was based on the redox reaction under acid condition:[24]

$$5H_2O_2 + 2MnO_4^- + 6H^+ = 2Mn^{2+} + 8H_2O + 5O_2 \quad (4.3)$$

The concentration of H_2O_2 was calculated according to the consumption of $KMnO_4$ solution.

4.2.2.4 Peroxide test sticks

The mechanism of this method is that the peroxidase in the test strip transfers peroxide oxygen to an organic redox indicator, which produces a blue oxidation product. Based on the visual colour comparison of the reaction zone with the fields of a colour scale, the peroxide concentration is roughly or semi-quantitatively estimated.

4.2.2.5 Results

After 24 h illumination under visible light ($\lambda > 420$ nm), the H_2O_2 amount produced using RF523-R was 74.4 μmol measured by KI titration method (UV-vis spectroscopy method-A), which was similar to the reported value of 61.6 μmol in the literature.[20] The $KMnO_4$ titration method provided a result of 78.0 μmol. The H_2O_2 production calculated from $Ce(SO_4)_2$ titration method (UV-vis spectroscopy method-B) was 103.6 μmol, which is higher than the other two methods. This is might due to the small sample volume used for the titration reaction (0.1 mL), which could introduce larger errors in measurement. From peroxide test stick, the amount of H_2O_2 production was estimated between 26.5 μmol and 88.2 μmol. Although the uncertainty

is high compared to other methods, peroxide test stick provides a fast H_2O_2 evaluation to rank the organic materials in high throughput screening approach.

Table 4.1 Comparison of different H_2O_2 detection methods using RF523-R as the test sample[a].

No.	Method	H_2O_2 / μmol
1	Reported value[b]	61.6
2	UV-vis spectroscopy method-A	74.4
3	UV-vis spectroscopy method-B	103.6
4	$KMnO_4$ titration	78.0
5	Peroxide test sticks[c]	26.5-88.2

[a] Reaction conditions: water (30 mL), catalyst (50 mg), Xe lamp with a λ > 420 nm filter, photoirradiation time (24 h). [b] H_2O_2 amount in the solution was quantified by HPLC equipped with an electrochemical analyser.[20] [c] As shown in Figure 4.6.

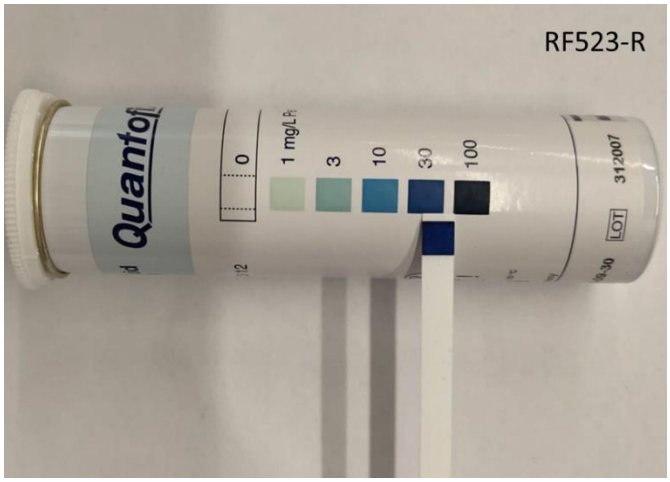

Figure 4.6 H_2O_2 production of RF523-R measured with the Peroxide test stick.

4.3 High-throughput screen candidate materials

4.3.1 Existing polymers in previous projects

Previously in Chapter 2 and Chapter 3, series of organic materials (Figure 4.7 and Figure 4.9) were synthesized and investigated for photocatalytic hydrogen production.

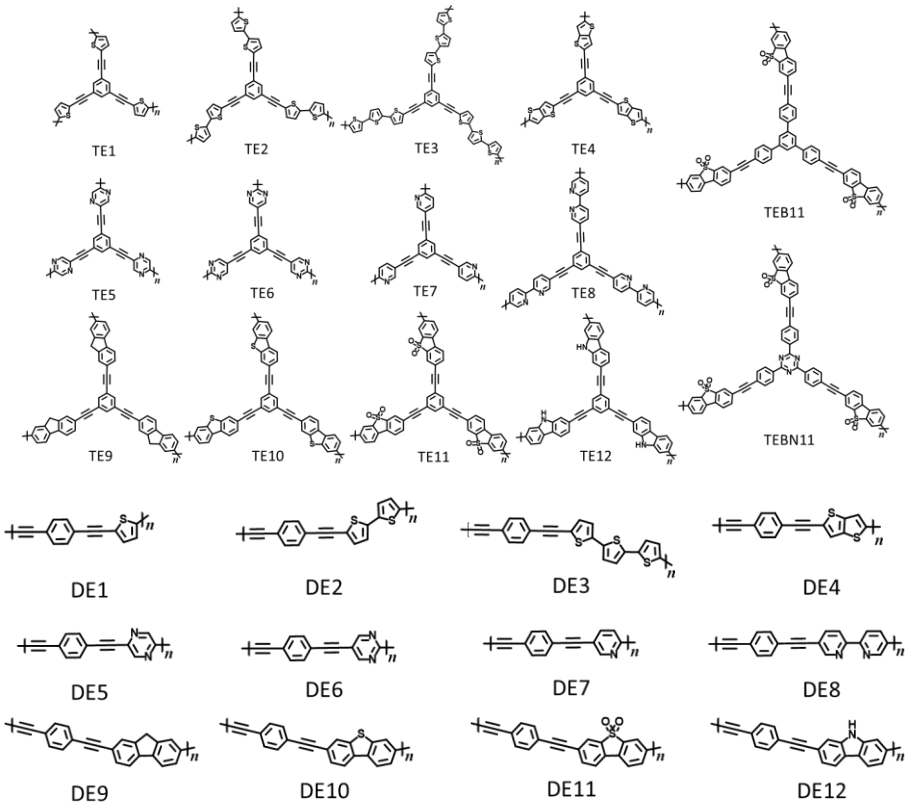

Figure 4.7 Chemical structures of the existing polymers (TE1-12 and DE1-12).

In order to test their performance for photocatalytic H_2O_2 production, they were high-throughput screened in water without or with sacrificial reagent (isopropanol, IPA) under air atmosphere, and using the peroxide test stick method to estimate the amount of H_2O_2. The results were summarised in Figure 4.8 and Figure 4.10. Among all of the materials, DE7 was found to show the darkest colour, indicating the highest H_2O_2 production. DE8, TE8, DE10 and TE12 showed white colour, indicating that no H_2O_2 or very little H_2O_2 was produced. It was further found that the addition of isopropanol, a hole scavenger, did not have significant effect on the performance of these polymers, which suggests that the photocatalytic H_2O_2 production with these polymers is not limited to water oxidation.

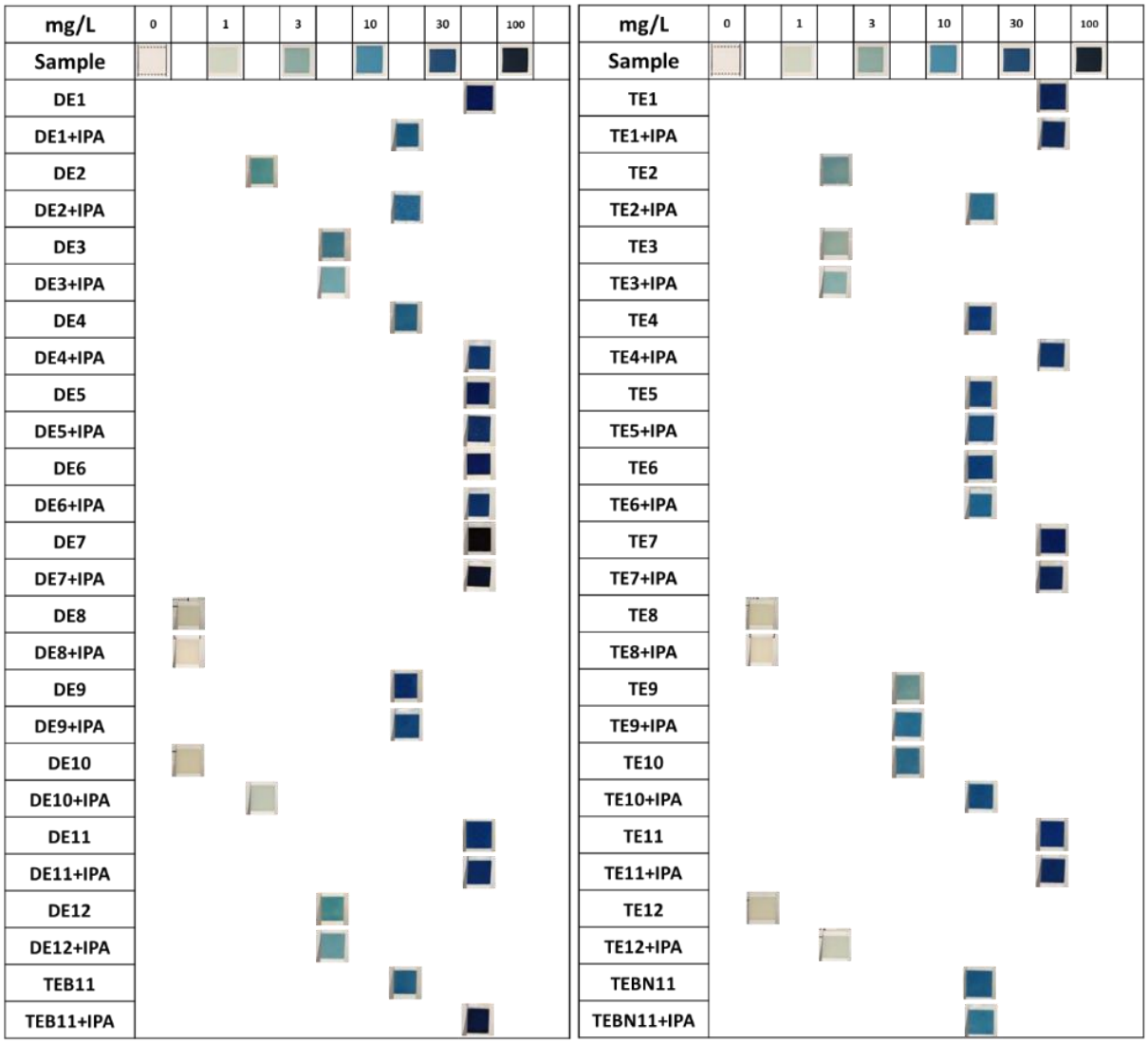

Figure 4.8 Photocatalytic H_2O_2 production of polymers with high-throughput workflow. Reaction conditions: 3 mL water and 5 mg polymer or 2.7 mL water, 0.3 mL isopropanol (IPA) and 5 mg polymer for 2.5 h illumination in air. Light source: Oriel Solar Simulator 94123A with an output of 1.0 sun.

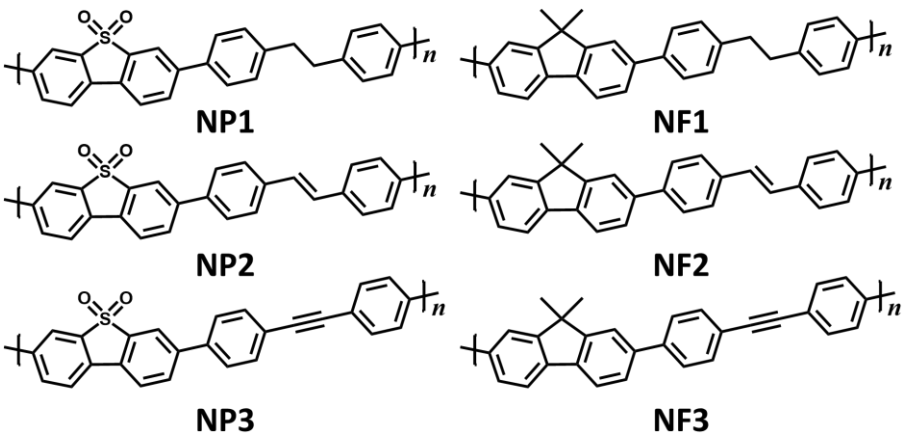

Figure 4.9 Chemical structures of the existing polymers (NF1-3 and NP1-3).

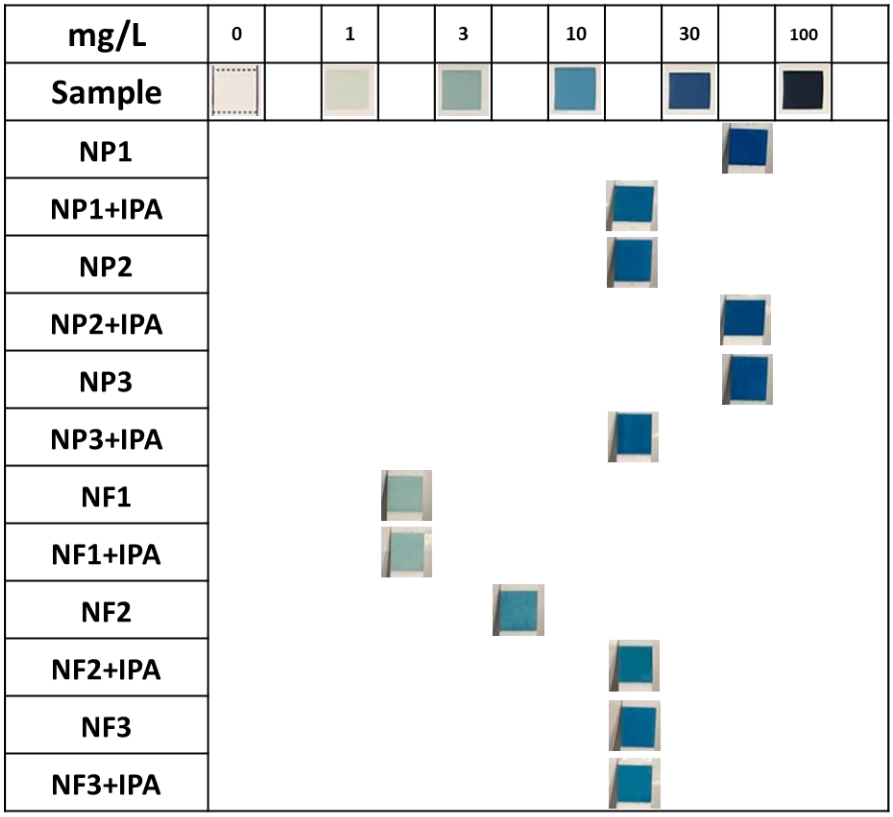

Figure 4.10 Photocatalytic H_2O_2 production of polymers with high-throughput workflow. Reaction conditions: 3 mL water and 5 mg polymer or 2.7 mL water, 0.3 mL isopropanol (IPA) and 5 mg polymer for 2.5 h illumination in air. Light source: Oriel Solar Simulator 94123A with an output of 1.0 sun.

It is interesting to investigate the performance relationship between photocatalytic H_2 production and H_2O_2 production, which could help to elucidate the insights on the photocatalytic mechanism. However, there is no correlation between them as shown in Figure 4.11. For example, DE7 had low photocatalytic H_2 production activity while it showed the highest H_2O_2 production performance. TEBN11, TEB11 and TE11 produced relatively high amount of H_2, but their H_2O_2 evolution performance were average. For NF1, NF2 and NF3, the polymer with higher H_2 production also showed higher H_2O_2 production. However, for NP1, NP2 and NP3, the results were the opposite. The above results indicate that, in addition to their common requirements on light absorption, good charge generation and separation, efficient surface redox reactions, these two photocatalytic reactions could be affected by different factors.

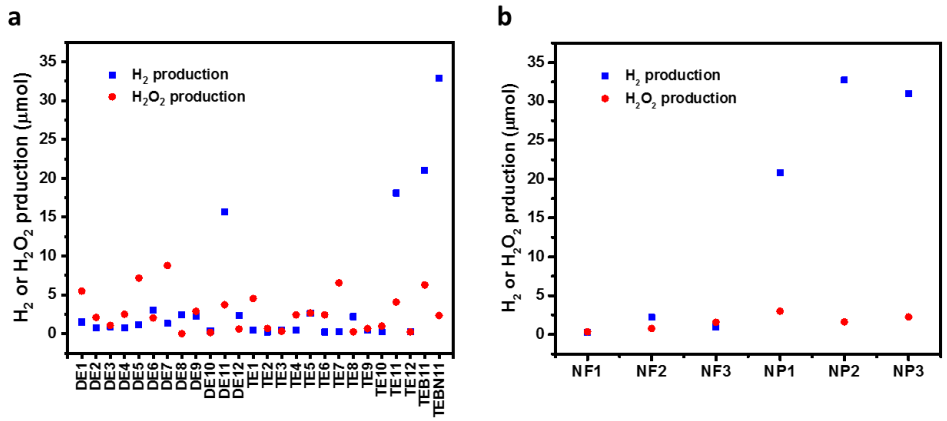

Figure 4.11 Comparation of photocatalytic H_2 and H_2O_2 production of (a) DE-n and TE-n polymers and (b) NF-n and NP-n polymers with high-throughput workflow. H_2 production: 5 mL H_2O/methanol/triethylamine mixture solution and 5 mg polymer for 2 h illumination. H_2O_2 production: 3 mL water and 5 mg polymer for 1.5 h illumination. Light source: Oriel Solar Simulator 94123A with an output of 1.0 sun, measured by KI titration method.

Then, the activity of DE7 was compared with the benchmark material of RF523-R. As shown in Figure 4.12, in the small scale experiment under a solar simulator (1 sun) illumination, the produced H_2O_2 amount of DE7 was 11.4 μmol after 2.5 h, which was nearly 3 times higher than that of RF523-R. The control experiment and the sample solutions before photoreaction both showed no H_2O_2 produced. Meanwhile, under visible light illumination (Xe light with a $\lambda >$ 420 nm filter), it displayed that DE7 produced 170.7 μmol under 24 h, while RF523-R only produced 74.4 μmol. These results demonstrated that DE7 had superior photocatalytic H_2O_2 performance than RF523-R irrespective of the light source used.

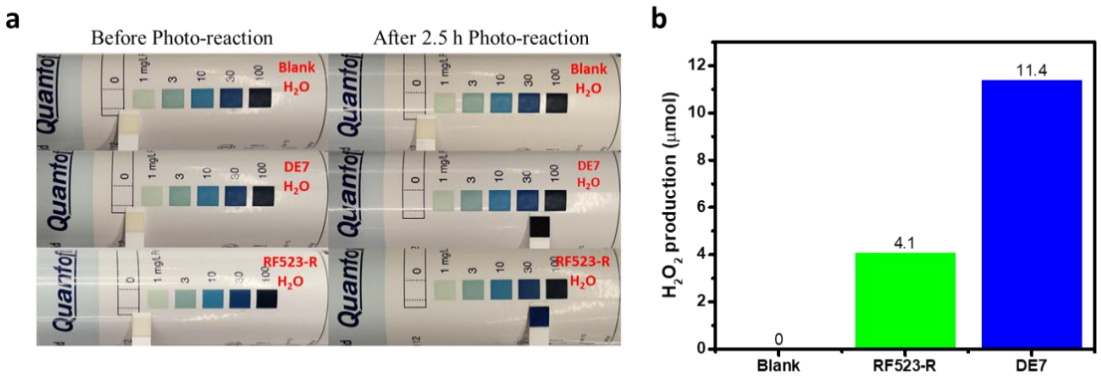

Figure 4.12 Photocatalytic H_2O_2 production of RF523-R and DE7: (a) measured by Peroxide test sticks method, (b) measured by UV-vis spectroscopy method-A. Reaction conditions: 3 mL water and 5 mg polymer for 2.5 h illumination. Light source: Oriel Solar Simulator 94123A with an output of 1.0 sun.

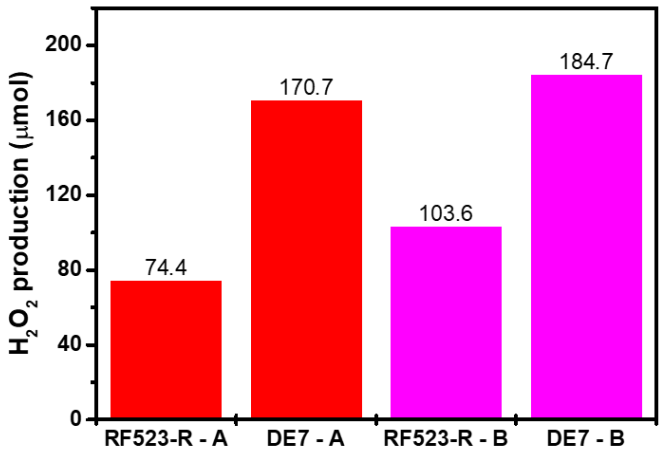

Figure 4.13 Photocatalytic H_2O_2 production of RF523-R and DE7. Reaction conditions: 30 mL water and 50 mg polymer for 24 h illumination. Light source: 300 W Xe lamp with a $\lambda > 420$ nm filter. Red column: measured by UV-vis spectroscopy method-A. Purple column: measured by UV-vis spectroscopy method-B.

4.3.2 Design and synthesise candidate polymers

4.3.2.1 Pyrene-based polymers with different oxygen-functional groups

Due to their unique optical and electric properties, pyrene-based materials have been widely used in fundamental and applied photochemical research.[25-27] In our group, a series of robust and effective pyrene-based photocatalysts have been reported for photocatalytic hydrogen evolution from water.[27] In addition, Zhu *et al.* synthesized oxygen-enriched graphitic carbon nitride polymers that have a high selectivity for photocatalytic H_2O_2 production.[12] Cui *et al.* also demonstrated that the carbon atoms adjacent to several oxygen functional groups (-COOH and C-O-C) are the active sites for oxygen reduction to hydrogen peroxide.[21] Hence, to find more promising materials, four pyrene-based polymers with different oxygen-functional groups were designed and synthesised as shown in Figure 4.14.

From the UV-vis spectra in Figure 4.15a, all of the polymers had a good visible light absorption ability up to around 700 nm. In Figure 4.15b, the typical peaks at around 1700 cm^{-1} and 1200 cm^{-1} of oxygen-groups can be confirmed in the FI-IR spectra,[21] and the PXRD patterns in Figure 4.15c showed that they were all amorphous. Finally, the photocatalytic H_2O_2 production experiment was performed in pure DI water under simulated solar light illumination. However, it was discovered that their H_2O_2 production performance were significantly lower than DE7.

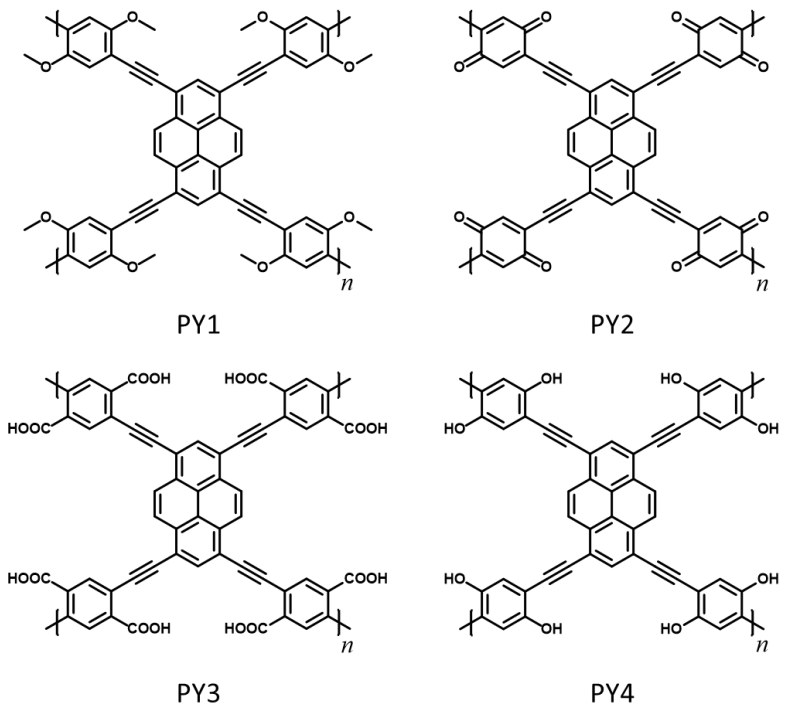

Figure 4.14 Chemical structures of pyrene-based polymers.

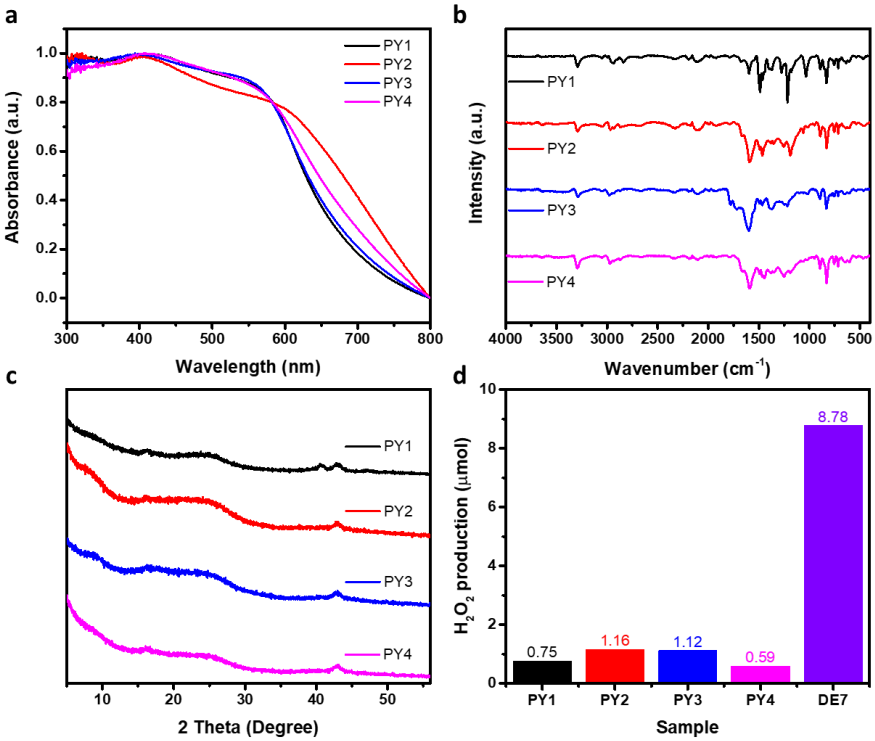

Figure 4.15 (a) UV−vis spectra (b) FT-IR spectra (c) PXRD patterns (d) Photocatalytic H_2O_2 production of pyrene-based polymers. Reaction conditions: 3 mL water and 5 mg polymer for 1.5 h illumination under Oriel Solar Simulator 94123A with an output of 1.0 sun.

4.3.2.2 CTF-based COFs materials

Covalent organic frameworks (COFs) are an emerging metal-free crystalline porous organic material, Thomas *et al.* reported the first example of utilizing COFs for photocatalytic H_2O_2 production and the good performance was attributed to the strong reduction property of the introduced diarylamine (donor) unit.[28] In addition, covalent triazine frameworks (CTFs) are a unique class of organic photocatalysts that have attracted wide attention in the photocatalytic community in recent years, Xu *et al.* reported that introducing acetylene (-C≡C-) or diacetylene (-C≡C-C≡C-) moieties into CTFs onto polymer framework promoted photocatalytic H_2O_2 productions.[23] Led by the above results, five CTF-based COFs were designed and prepared (Figure 4.16).

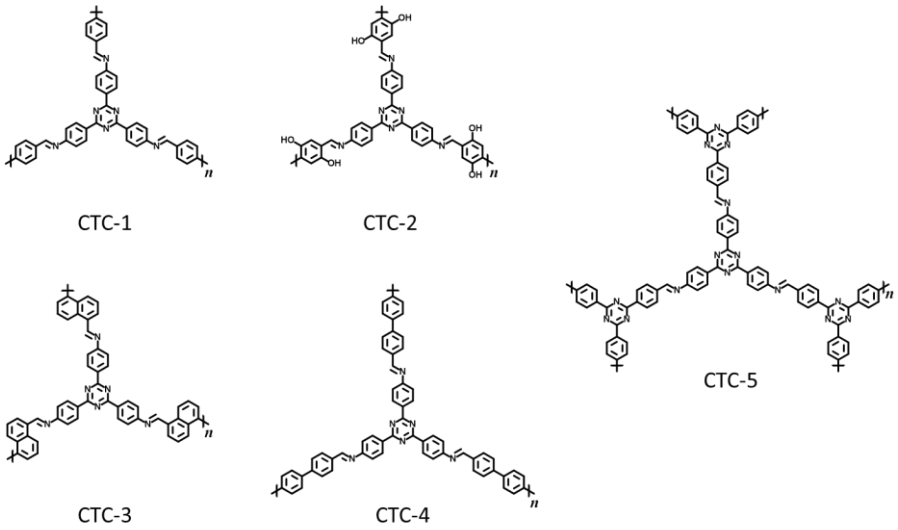

Figure 4.16 Chemical structure of CTF-based COFs.

The UV-vis spectra in Figure 4.17a of the polymers showed that CTC-2 had the best visible light absorption among the five polymers. In Figure 4.17b, the FT-IR spectra of all materials displayed two strong typical peaks of the aromatic N=C-N stretching and breathing modes at 1510 cm^{-1} and 1365 cm^{-1}.[23, 29] According to the PXRD pattens (Figure 4.17c), only CTC-5 showed a strong peak, indicating it was crystalline while others were amorphous. For photocatalytic H_2O_2 performance, as shown in Figure 4.17d, the produced H_2O_2 of CTC-1, CTC-2, CTC-3 and CTC-4 were all around 0.5 μmol, while CTC-5 produced 7 times more H_2O_2 to 3.58 μmol in 1.5 h, which could be ascribed to its crystallininity.[30] However, it was still lower than DE7. Therefore, the following work will still focus on DE7.

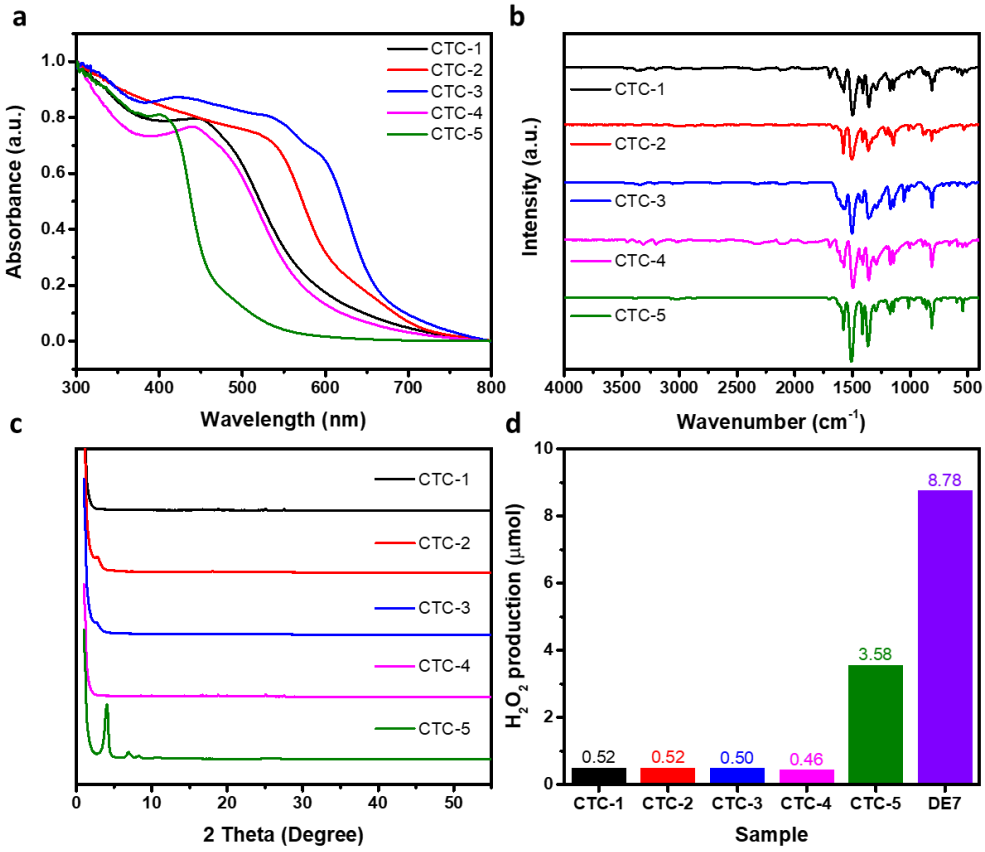

Figure 4.17 (a) UV-vis spectra (b) FT-IR spectra (c) PXRD patterns (d) Photocatalytic H_2O_2 production of CTF-based COFs. Reaction conditions: 3 mL water and 5 mg polymer for 1.5 h illumination under Oriel Solar Simulator 94123A with an output of 1.0 sun.

4.4 Optimization of H_2O_2 production

4.4.1 The effect of residual metal

We investigated the photocatalytic production of H_2O_2 with the assistance of high-throughput workflow for diverse organic polymers, including liner conjugated polymers, CMP and COF. Among them, DE7 showed the highest activity for photocatalytic H_2O_2 production.

DE7 was prepared using Sonogashira coupling reaction with $Pd(PPh_3)Cl_2$ as the main catalyst and CuI as the co-catalyst (Figure 4.18). During this process, the residual metal catalyst in the final polymer products were unavoidable, which is a common issue in metal-catalytic polymerization reaction.[31, 32] It is reported that Pd and Cu metals could lead to the decomposition of H_2O_2.[33, 34] Therefore, their presence on the photocatalytic performance need to be investigated.

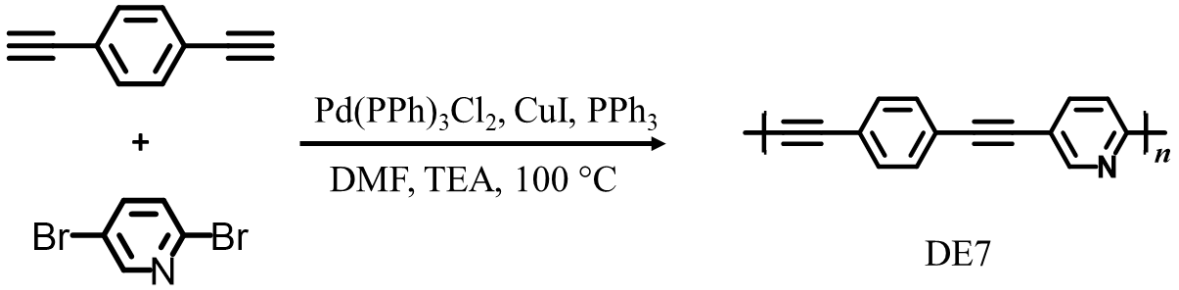

Figure 4.18 Synthesis procedure of DE7 polymer.

DE7 with different amounts of $Pd(PPh_3)Cl_2$ and CuI were prepared. As shown in Table 4.2 and Figure 4.19 and Figure 4.20, with 1% CuI, the performance of H_2O_2 was slightly increased compared with the sample prepared without CuI. However, further increasing the amount of CuI decreases the H_2O_2 production, which could be attributed to the reaction between the Cu ions and H_2O_2 leading to the decomposition of H_2O_2.[35, 36] Besides, excessive content of $Pd(PPh_3)Cl_2$ also had a negative effect on the H_2O_2 production, since too little or too much $Pd(PPh_3)Cl_2$ would decrease the yield of the product. Therefore, the optimized molar ratio of $Pd(PPh_3)Cl_2$ and CuI for synthesising DE7 was 1.5% and 1%, respectively.

Table 4.2 Optimization of residual Pd and Cu in DE7.

$Pd(PPh_3)Cl_2$[a] / %	**Pd-ICP / %**	**Cu-ICP / %**	**H_2O_2[c] / µmol**	**CuI[b] / %**	**Pd-ICP / %**	**Cu-ICP / %**	**H_2O_2[c] / µmol**
0.5	0.03	0.02	6.83	0	0.12	0.00	7.79
1.0	0.03	0.02	6.95	1	0.15	0.02	8.78
1.5	0.04	0.02	6.97	3	0.15	0.04	7.99
2.5	0.15	0.02	8.78	5	0.17	0.07	5.86
5.0	0.20	0.01	4.17	10	0.11	0.15	5.35
15	0.20	0.01	3.79	30	0.11	1.12	0.88
25	0.32	0.01	3.76	50	0.17	2.08	0.23

[a] Molar ratio of [$Pd(PPh_3)Cl_2$] / [Monomer].[b] Molar ratio of [CuI] / [Monomer].[c] Measured by UV-vis spectroscopy method-A (KI titration). Reaction conditions: 3 mL water and 5 mg polymer for 1.5 h illumination. Light source: Oriel Solar Simulator 94123A with an output of 1.0 sun.

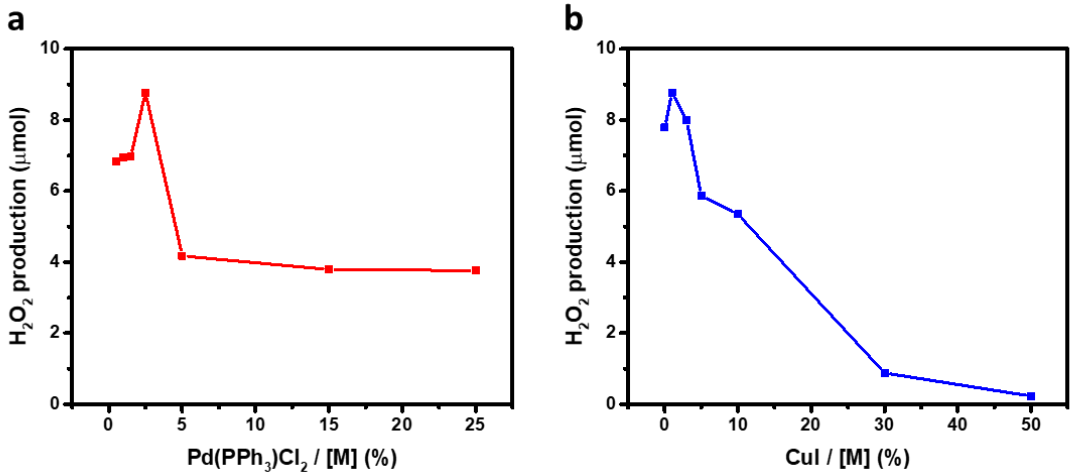

Figure 4.19 Photocatalytic H_2O_2 production of DE7 with different contents of (a) $Pd(PPh_3)Cl_2$ and (b) CuI.

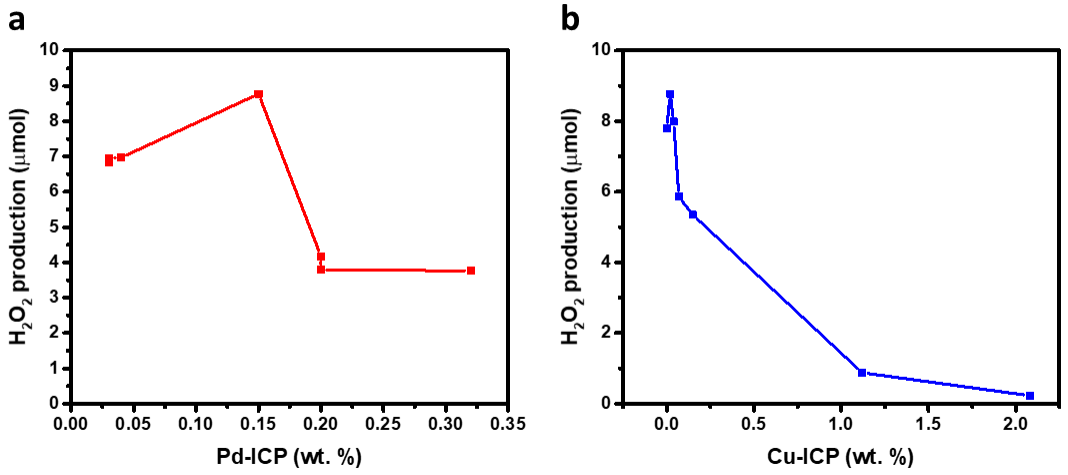

Figure 4.20 Photocatalytic H_2O_2 production of DE7 with (a) Pd residue and (b) Cu residue detected by ICP.

To further investigate the effect of CuI on photocatalytic H_2O_2 performance, DEP10 with a similar structure to DE7 was synthesized with different amount of CuI (Figure 4.21a). In the absence of residual Cu, DEP10 residual showed activity for photocatalytic H_2O_2 production. However, when the molar ratio was increased to 5% (the residual Cu was 0.64% measured by ICP), then the activity was quenched or the produced H_2O_2 was decomposed as no H_2O_2 was detected, which was consistent with the result of DE7. In another experiment, DEP10 (no CuI) coordinated with Cu or Pd was prepared by a mixing DEP10 with copper acetate or palladium acetate in methanol solution (Figure 4.21c).[37] As shown in Figure 4.21d, compared to pristine DEP10, Cu or Pd coordination to DEP10 deteriorates the activity to H_2O_2 production.

Consequently, residual Cu and Pd in a metal-catalyzed coupling reaction serve as catalytic sites, but their amounts need to be limited to photocatalytically produce H_2O_2 with high efficiency.

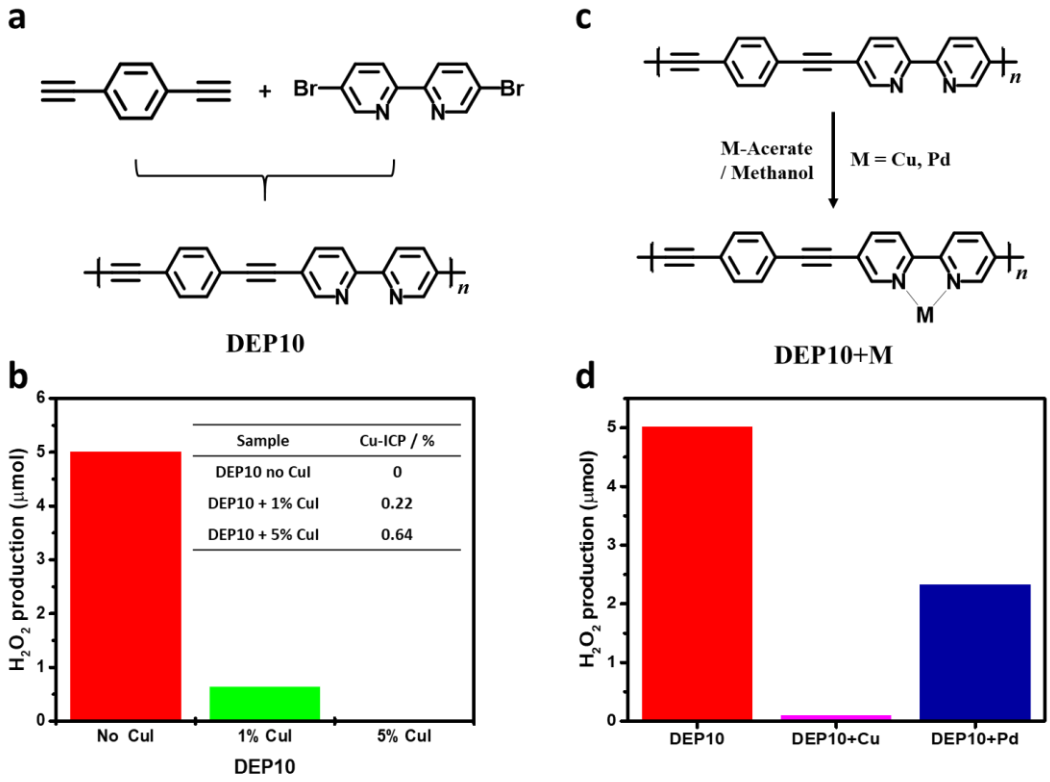

Figure 4.21 (a) Chemical structure of DEP10 and (b) H_2O_2 evolution of DEP10 with different contents of CuI (the contents of $Pd(PPh_3)Cl_2$ are all 1.5%) (c) Chemical structure of DEP10+M and (d) H_2O_2 evolution of DEP10 and DEP10+M. Reaction conditions: 3 mL water and 5 mg polymer for 1.5 h illumination. Light source: Oriel Solar Simulator 94123A with an output of 1.0 sun.

4.4.2 Design and comparison of DE7 derivatives

4.4.2.1 Synthesis

To understand the structure-activity relationship of DE7, eight DE7 derivatives (Figure 4.22) were synthesized by varying the dibromo monomers under the same condition (1.5% ($Pd(PPh_3)Cl_2$ and 1% CuI). DEP1 contains no N element in the framework, DEP2, DEP3 and DEP4 were prepared with dibromo pyridines at different positions. DE5 has the pyrimidine unit. Diazole units were introduced to obtain DEP6, DEP7 and DEP8.

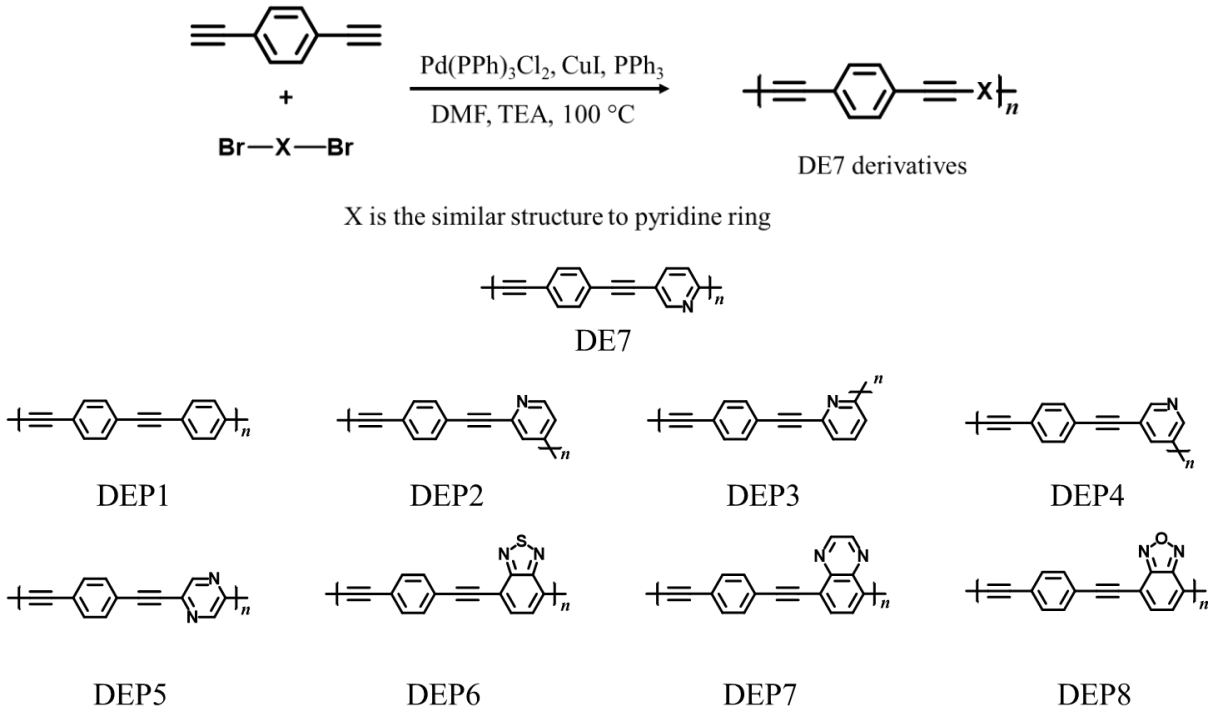

Figure 4.22 Synthetic process and chemical structures of DE7 derivatives (DEP1-8).

4.4.2.2 Characterizations

The morphologies of all polymers were characterized by SEM (Figure 4.23). DEP1 and DEP5 were similar to DE7, have morphology of wrinkled sheets. DEP2, DEP3 and DEP4 were mainly composed of irregular blocks. DEP6 showed a biscuit-like morphology, and DEP7 and DEP8 were more like crumpled spheres. The typical signal of C≡C-H at around 3300 cm^{-1} in the DE monomer was not detected in all polymers (Figure 4.24a), showing the success of the polymerization. PXRD patterns (Figure 4.24b) displayed that most polymers were semi-crystalline, except for DEP6 and DEP7, which were amorphous. The Raman spectra (Figure 4.24c) showed a peak at 2167 cm^{-1} of acetylene (C≡C) groups, indicating the formation of the conjugated polymers.[23] The peak at around 1600 cm^{-1} is attributed to the G bands of aromatic rings.[38]. The thermostability of DE7 derivatives was similar to DE7 as shown in TGA results (Figure 4.24d). DE7 and its derivatives had BET surface areas of less than 55 $m^2 g^{-1}$ (Table 4.3) as expected.

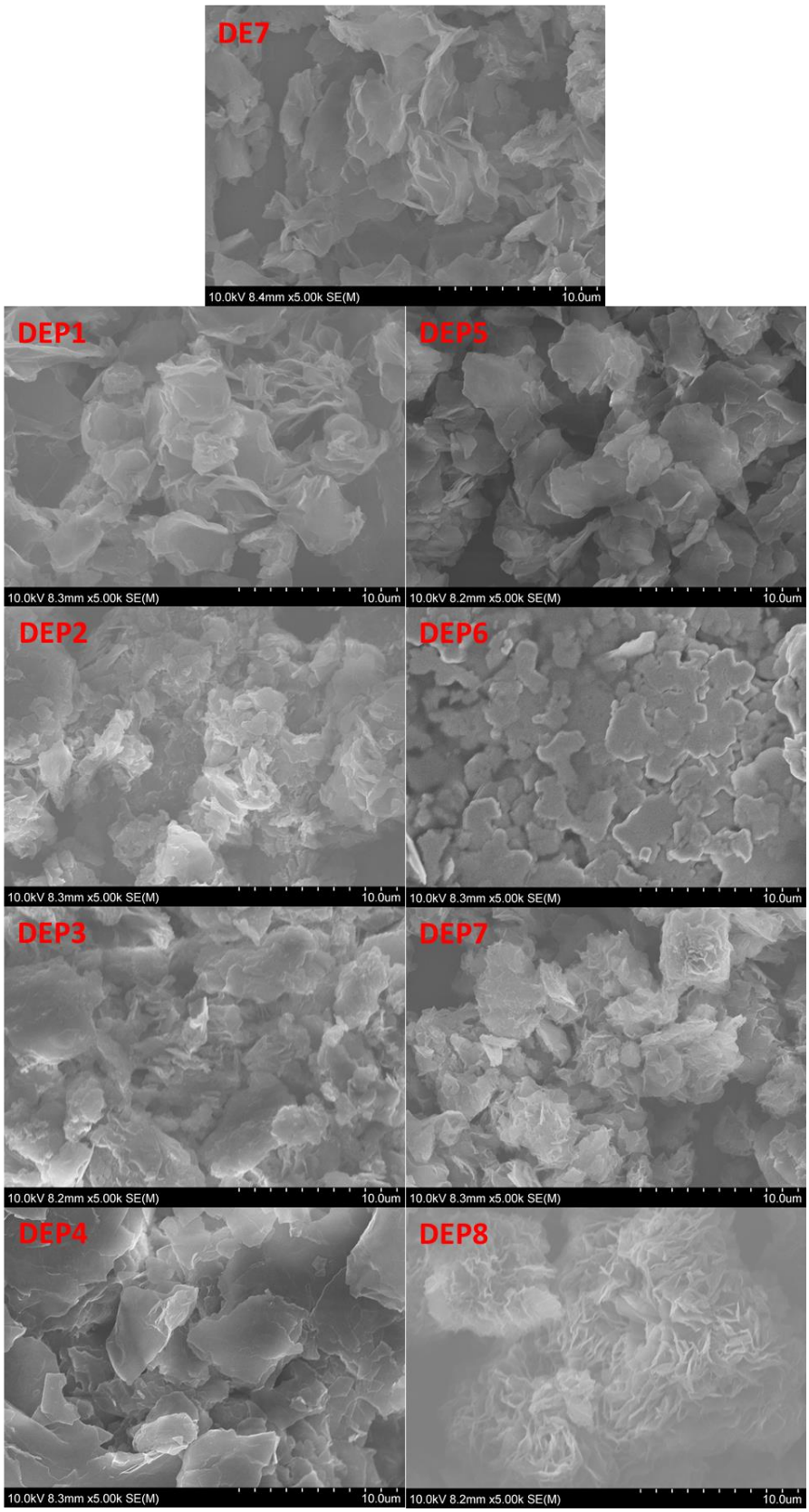

Figure 4.23 SEM images of DE7 and its derivatives (DEP1-8).

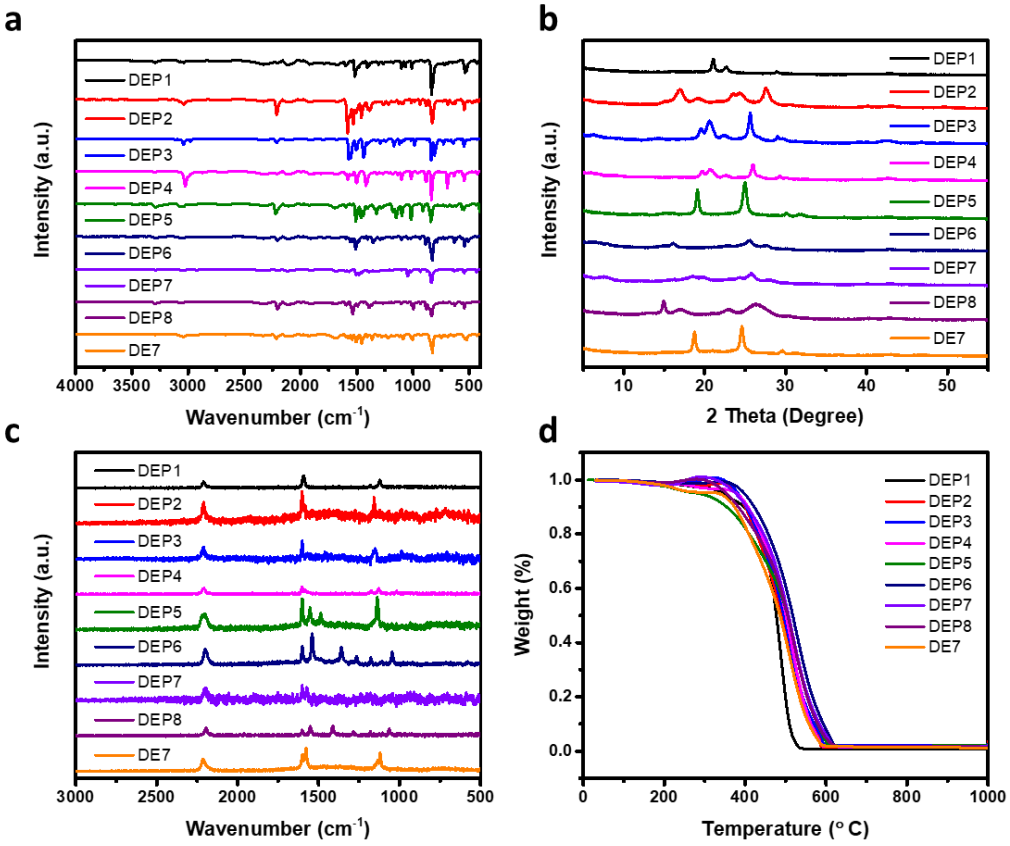

Figure 4.24 (a) FI-IR spectra (b) PXRD patterns (c) Raman spectra and (d) Thermogravimetric data of DE7 and its derivatives (DEP1-8).

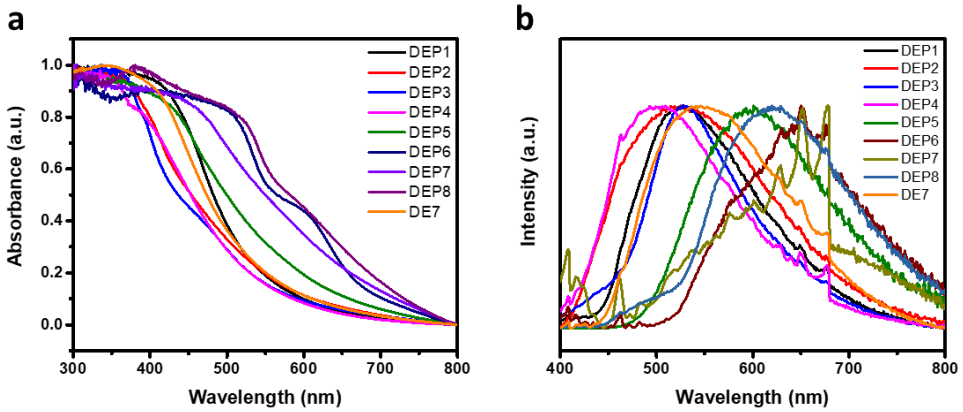

Figure 4.25 (a) Solid UV-vis spectra and (b) Photoluminescence emission spectra (λ_{exc} = 371 nm) of DE7 and its derivatives (DEP1-8).

Figure 4.25a is the UV-vis spectra of polymers, it revealed that the change in steric hindrance of DE7 lead to the decrease of visible light absorption (DEP2-4), while the introduction of

more N atom enhanced the absorbance range (DEP5-8), which was consistent with the blue shift and red shift in the corresponding FL spectra (Figure 4.25b), respectively.

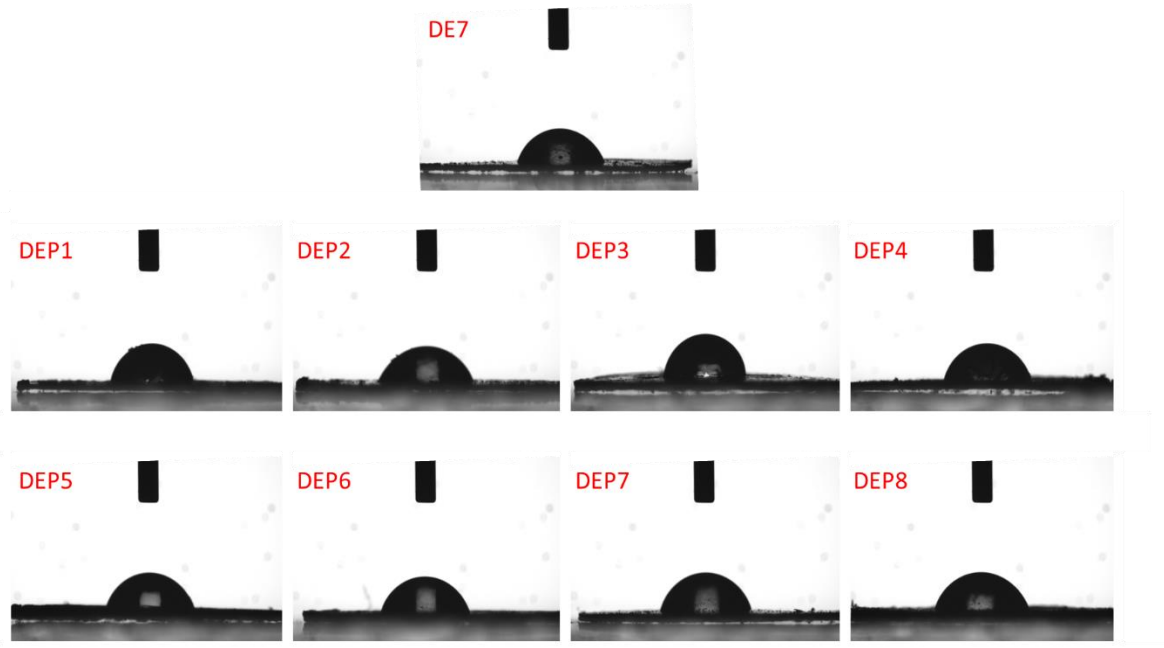

Figure 4.26 Contact angle images against water of DE7 and its derivatives (DEP1-8).

Table 4.3 Average fluorescence lifetimes, transmission values, contact angles and Brunauer-Emmett-Teller surface areas of DE7 and its derivatives (DEP1-8).

Sample	SA_{BET}[a] / m ^{2}g^{-1}	Transmission[b] / %	Contact angle[c] / °	Particle Size[d] / µm
DE7	46	0.1	69.2 (±2.9)	7.2
DEP1	31	1.7	75.2 (±0.7)	10.2
DEP2	55	0.3	66.9 (±1.6)	7.7
DEP3	14	0.1	86.5 (±0.3)	6.8
DEP4	39	0.3	72.4 (±1.4)	10.4
DEP5	37	0.3	67.1 (±0.8)	6.6
DEP6	44	0.8	68.5 (±0.6)	12.3
DEP7	42	3.2	73.8 (±0.2)	20.8
DEP8	35	2.6	66.8 (±0.4)	13.8

[a] Apparent BET surface areas (SA_{BET}) were calculated from the N_2 adsorption isotherm at 77 K. [b] Measured in water. [c] Measured as pallets against water. [d] 50th Percentile of particle size volume distribution.

Furthermore, the fluorescence lifetimes were measured in water (Table 4.4). DE7 had an average lifetime of 0.43 ns, which was longer than most of its derivatives, and DEP3 showed the longest lifetime of 1.61 ns.

Table 4.4 Estimated fluorescence lifetimes of DE7 and its derivatives (DEP1-8).

Sample	λ_{em} / nm	τ_1 / ns	B_1 / %	τ_2 / ns	B_2 / %	τ_3 / ns	B_3 / %	τ_4 / ns	B_4 / %	χ^2	τ_{avg}[a] / ns
DE7	545	0.07	49.10	0.27	29.25	0.95	17.72	3.82	3.93	1.323	0.43
DEP1	526	0.07	59.07	0.25	20.90	0.67	16.85	2.65	3.18	1.282	0.29
DEP2	525	0.11	43.53	0.60	36.44	2.11	16.74	8.18	3.29	1.391	0.89
DEP3	528	0.20	21.69	0.78	33.10	2.24	37.05	5.85	8.16	1.415	1.61
DEP4	500	0.05	58.83	0.28	24.77	0.85	14.51	3.33	1.89	0.978	0.29
DEP5	600	0.03	66.55	0.23	14.14	0.83	14.92	3.18	4.40	1.429	0.32
DEP6	650	0.04	89.01	0.26	8.04	0.65	2.44	4.26	0.51	1.334	0.09
DEP7	652	0.13	83.70	0.24	12.40	0.81	2.99	8.27	0.91	1.341	0.24
DEP8	620	0.17	57.69	0.75	2.27	0.76	27.40	2.93	12.64	1.398	0.69

[a] Fluorescence lifetimes for all polymers obtained from fitting time-correlated single photon counting decays to a sum of three exponentials, which yield τ_1, τ_2, and τ_3 according $\sum_{i=1}^{n}(A + B_i exp(-t/\tau_i))$. τ_{avg} is the weighted average lifetime calculated as $\sum_{i=1}^{n}(B_i\tau_i)$.

Next, the dispersibility of polymers in water, an important factor in photocatalytic reaction, was investigated by transmittance measurements in water (Table 4.3). The lowest transmission was 0.1% for DE7 and DEP3, which means they can disperse better in water than other polymers. It might be attributed to the pyridine unit since DEP2, DEP4 and DEP5 also show low transmission of 0.3%. DEP1 (no N atom) had a much higher transmission of 1.7%. The largest transmission value was found in DEP7 of 3.2%, indicating poor dispersibility compared with the other polymers. In addition, the particle sizes of polymers were measured by static light scattering experiments (Table 4.3). DEP5 had the smallest median particle size of 6.6 μm, while DEP7 had the largest one of 20.8 μm, which was nearly three times as much as DE7 (7.2 μm). At last, the contact angle against water experiments (Table 4.3 and Figure 4.26) was

performed to investigate the hydrophilicity of polymers. Most of the polymers had a similar contact angle to DE7 at around 70.0 °, except for DEP3 with the largest contact angle of 86.5 °.

4.4.2.3 Photocatalytic H_2O_2 production

Then, we investigated the photocatalytic H_2O_2 production performance of these polymers. DE7 was found to show the highest H_2O_2 production performance (Figure 4.27). The observed H_2O_2 production activity has no linear dependence on any individual property characterized in this study. This strongly indicates the overall activity is governed by a host of factors which interact in a complex way.

Given that DE7 is still the best photocatalyst for H_2O_2 production, following work will be focus on how to further improve its activity, and it is also important to optimize the reaction conditions to get deeper understanding of the mechanism.

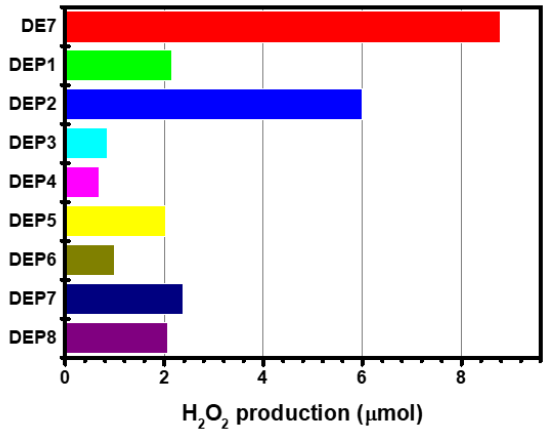

Figure 4.27 Photocatalytic H_2O_2 production of DE7 and its derivatives. Reaction conditions: 3 mL water and 5 mg polymer for 1.5 h illumination in air. Light source: Oriel Solar Simulator 94123A with an output of 1.0 sun.

4.4.3 Prepare DE7-M via microwave method

4.4.3.1 Synthesis

Due to the rapid approach and facile operation procedure, microwave-assistance method has been widely applied for synthesising organic polymers,[39, 40] therefore, DE7 was also prepared using microwave synthesis (Figure 4.28) with the reaction temperature range from 80 ℃ to 120 ℃ and named as DE7-M.

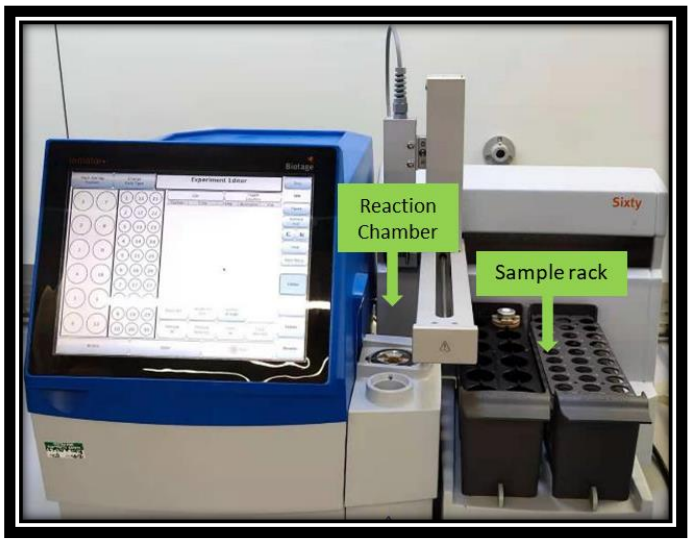

Figure 4.28 Biotage microwave: The sample was heated to a certain temperature X ℃ (X= 80, 90, 100, 110, 120) and kept for 2 hours. After filtration and purification, the final product was dried in the vacuum oven at 80 ℃ overnight.

4.4.3.2 Characterizations

Compared with DE7 synthesized in the hot sand bath, the DE7 obtained via microwave method showed a very similar morphology (Figure 4.29), even at different reaction temperature. In addition, the FI-IR spectra (Figure 4.30a), PXRD patterns (Figure 4.30b), Raman spectra (Figure 4.30c), and thermostability (Figure 4.30d) also had nearly no obvious change, which indicated that the microwave synthetic method and the variation of reaction temperature of DE7 had no or negligible effect on these intrinsic properties.

However, the visible light absorbance of DE7 was slightly enhanced using microwave method, as illustrated in Figure 4.31a, the light absorption was enhanced with higher reaction temperature. The emission peak of photoluminescence spectra shifted to long wavelength, which was consistent with the UV-vis absorption profile shift (Figure 4.31b). The average PL lifetime of DE7-M ranged from 0.56-0.83 ns, which was longer than DE7 of 0.43 ns. In addition, increasing the temperature tended to shorten the lifetime of DE7-M (Table 4.5).

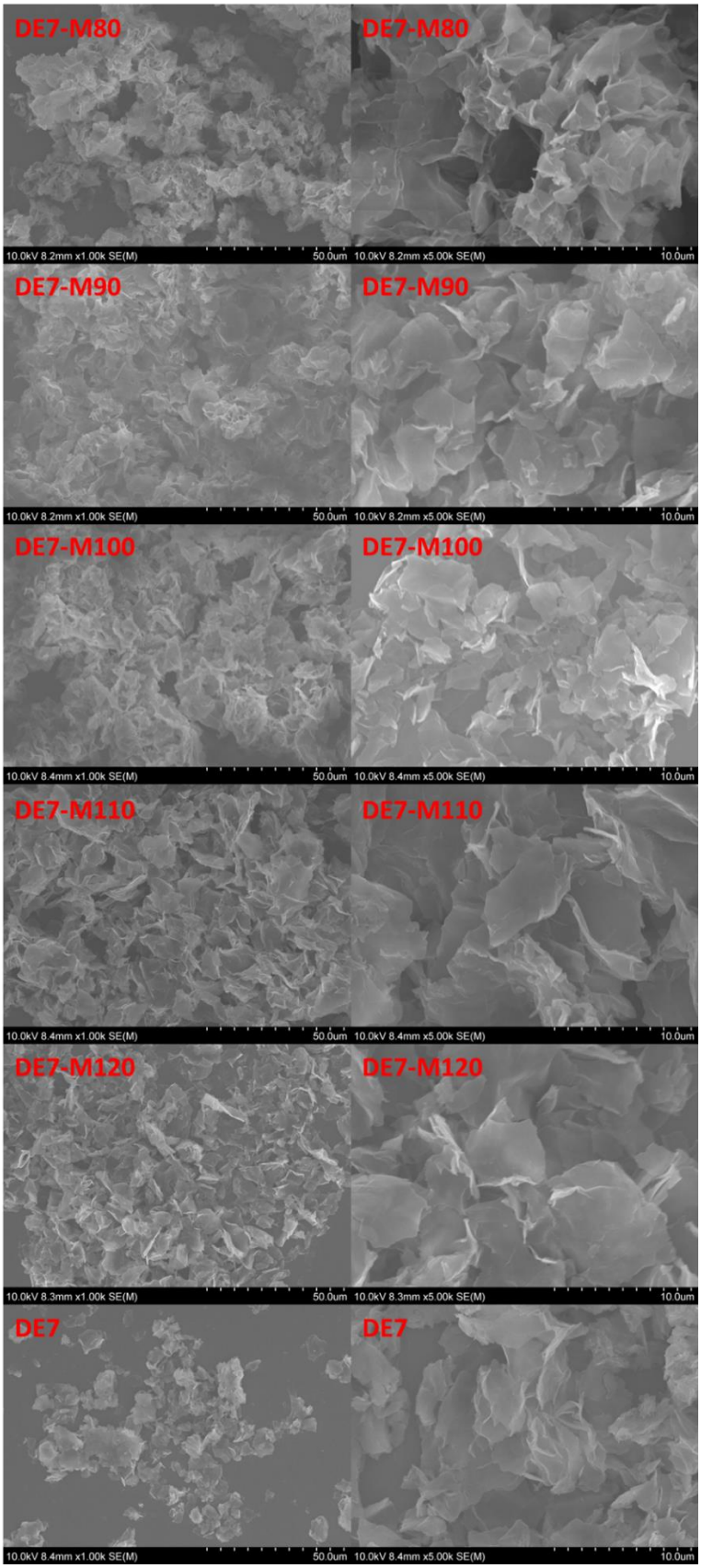

Figure 4.29 Morphology of DE7 and DE7 prepared via microwave method at different temperatures.

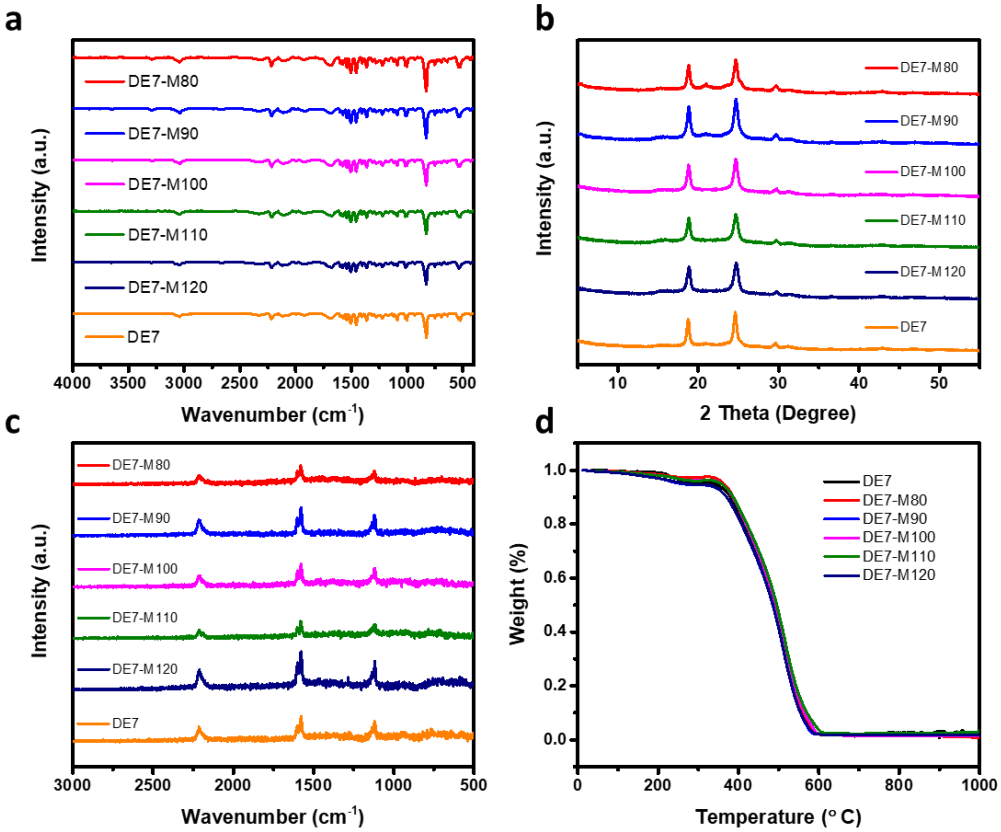

Figure 4.30 (a) FT-IR spectra and (b) PXRD patterns (c) Raman spectra and (d) Thermogravimetric data of DE7 and DE7 prepared via microwave method at different temperatures.

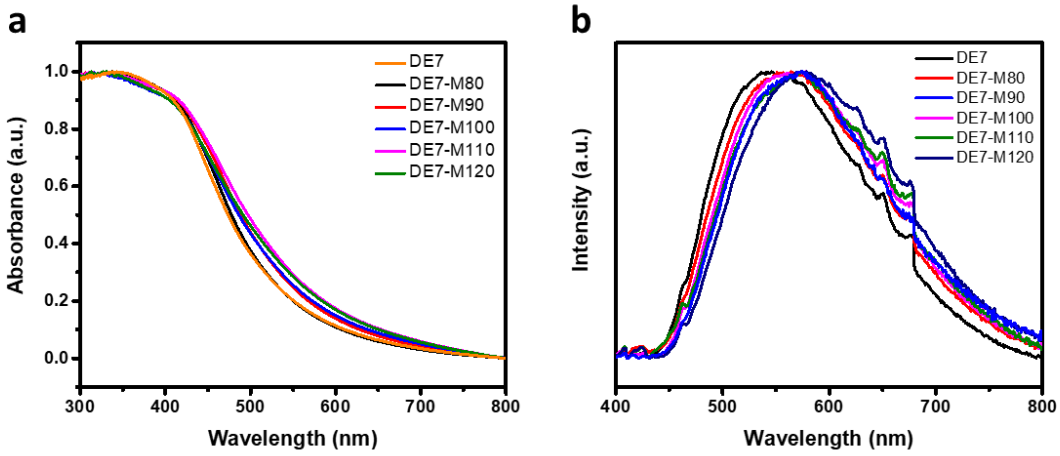

Figure 4.31 (a) UV-vis spectra (b) Photoluminescence emission spectra (λ_{exc} = 371 nm) of DE7 and DE7 prepared via microwave method at different temperatures.

Table 4.5 Estimated fluorescence lifetimes of DE7 and DE7 prepared via microwave method at different temperatures.

Sample	λ_{em} / nm	τ_1 / ns	B_1 / %	τ_2 / ns	B_2 / %	τ_3 / ns	B_3 / %	τ_4 / ns	B_4 / %	χ^2	τ_{avg}[a] / ns
DE7	545	0.07	49.10	0.27	29.25	0.95	17.72	3.82	3.93	1.323	0.43
DE7-M80	566	0.17	57.50	0.72	31.31	2.83	9.61	14.75	1.59	1.327	0.83
DE7-M90	570	0.16	62.85	0.69	28.28	2.72	7.73	13.76	1.14	1.178	0.66
DE7-M100	572	0.12	54.74	0.54	30.92	1.97	11.79	7.88	2.55	1.216	0.67
DE7-M110	575	0.11	62.06	0.55	27.07	2.18	9.57	10.64	1.30	1.271	0.56
DE7-M120	577	0.18	64.70	0.71	25.85	2.78	8.30	14.99	1.16	1.223	0.71

[a] Fluorescence lifetimes for all polymers obtained from fitting time-correlated single photon counting decays to a sum of three exponentials, which yield τ_1, τ_2, and τ_3 according $\sum_{i=1}^{n}(A + B_i exp(-t/\tau_i))$. τ_{avg} is the weighted average lifetime calculated as $\sum_{i=1}^{n}(B_i\tau_i)$.

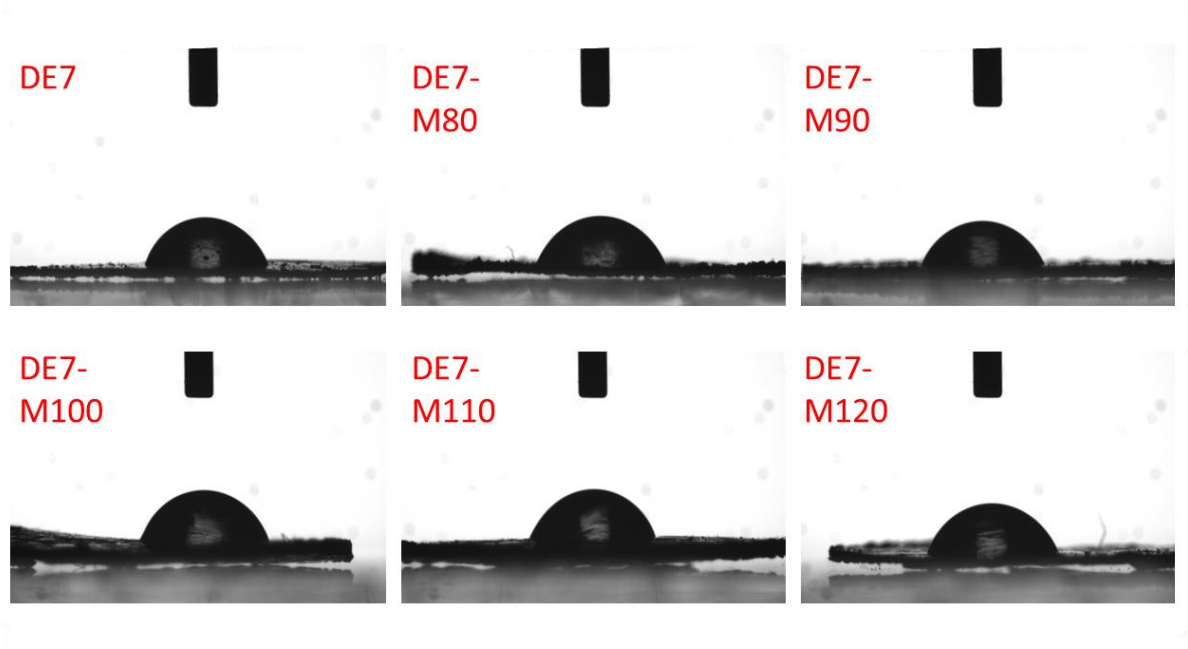

Figure 4.32 Contact angle images against water of DE7 and DE7 prepared via microwave method at different temperatures.

Table 4.6 Average fluorescence lifetimes, transmission values, contact angles and Brunauer-Emmett-Teller surface areas of DE7 and DE7 prepared via microwave method at different temperature.

Sample	τ_{avg}[a] / ns	Transmission[b] / %	Contact angle[c] / °	SA_{BET}[d] / m ^{2}g^{-1}	Particle size[e] / μm
DE7	0.43	0.1	69.2 (±2.9)	46	7.2
DE7-M80	0.83	1.7	67.0 (±2.9)	32	8.2
DE7-M90	0.66	1.1	66.8 (±2.1)	35	11.3
DE7-M100	0.67	0.9	68.2 (±1.0)	31	11.7
DE7-M110	0.56	2.3	70.6 (±1.1)	23	11.9
DE7-M120	0.71	4.5	66.3 (±1.3)	27	13.6

[a] Estimated fluorescence lifetimes were obtained from fitting time-correlated single photon counting decays to a sum of three exponentials in water. [b] Measured in water. [c] Measured as pallets against water. [d] Apparent BET surface areas (SA_{BET})were calculated from the N_2 adsorption isotherm at 77 K. [e] 50th Percentile of particle size volume distribution.

As shown in Table 4.6, DE7-M dispersed more poorly in water probably due to increased particle size (Table 4.6). And similar to DE7, DE7-M had contact angle values around 70 ° (Figure 4.32 and Table 4.6). Moreover, DE7-M had a smaller BET surface area (Table 4.6) than DE7, which could be attributed to larger particle size.

4.4.3.3 Photocatalytic H_2O_2 production

The photocatalytic H_2O_2 production experiments under solar simulated light (1 sun) were then carried out to evaluate the performance of DE7-M. It was found that DE7-M had a slightly higher H_2O_2 evolution rate compared with DE7 (Figure 4.33) in the small-scale experiment. The reaction temperature showed no profound effect on catalytic efficiency. In a larger scale experiment and under visible light illumination (Xe lamp with a $\lambda > 420$ filter), DE7-M80 produced 262.5 μmol H_2O_2 after 24 h, which was higher than DE7 with 194.6 μmol (Figure 4.34a). Under the same condition, the activity of DE7-M was found to be 3.5 times as much as RF523-R (74.4 μmol). In Figure 4.34b, the time course of H_2O_2 production experiments also showed that DE7-M80 had a higher activity than DE7.

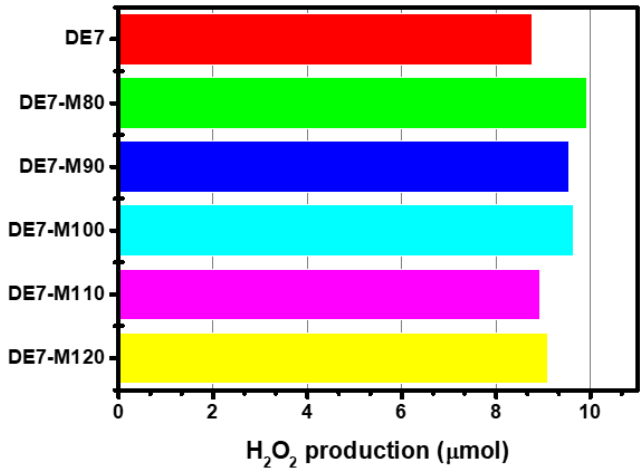

Figure 4.33 Photocatalytic H_2O_2 production of DE7 and DE7-M prepared via microwave method at different temperatures. Reaction conditions: 3 mL water and 5 mg polymer for 1.5 h illumination in air. Light source: Oriel Solar Simulator 94123A with an output of 1.0 sun.

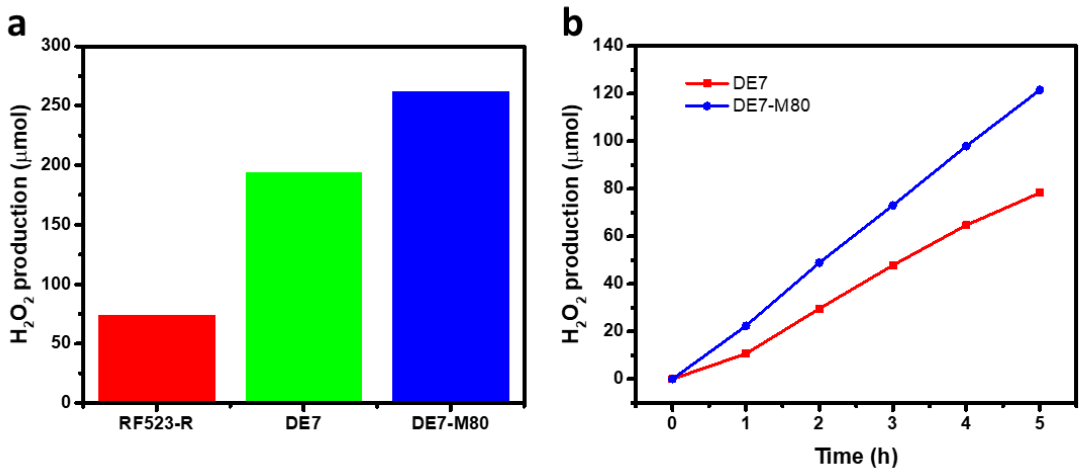

Figure 4.34 (a) Photocatalytic H_2O_2 production of RF523-R, DE7 and DE7-M80 for 24 h in O_2. (b) Time-dependent H_2O_2 production of DE7 and DE7-M80 for 5 h in O_2. Reaction conditions: 30 mL water and 50 mg polymer under a Xe lamp illumination with a filter ($\lambda > 420$ nm).

Photocurrent response experiment showed that DE7-M80 had a higher photocurrent intensity than DE7 (Figure 4.35), which indicated a higher charge transfer ability of DE7-M80.[12, 13] The above results may explain why DE7-M showed superior performance on photocatalytic H_2O_2 production than DE7.

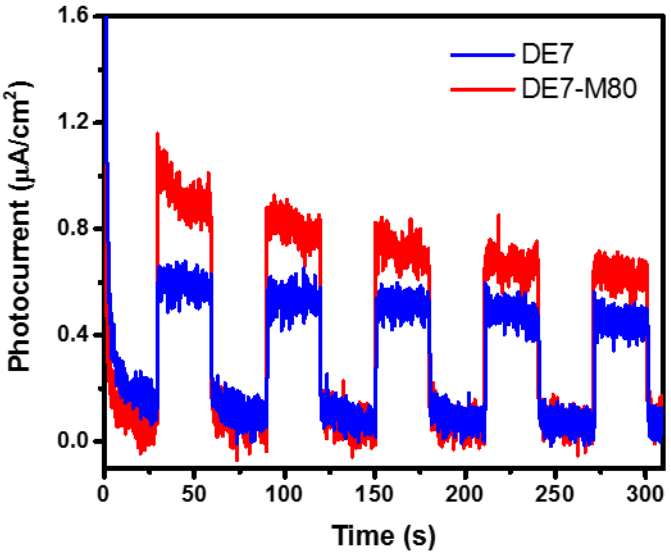

Figure 4.35 Photocurrent response of DE7 and DE7-M80.

4.4.4 Further improving H_2O_2 performance of DE7-M80

4.4.4.1 The effect of pH value

The pH of the reaction solution could have effect on the photoactivity of the studied materials.[41] Here, hydrochloric acid (HCl), sulfuric acid (H_2SO_4), nitric acid (HNO_3), phosphoric acid (H_3PO_4), trifluoroacetic acid (TFA) and acetic acid (AcOH) were used to create the acid condition of pH = 1, and sodium hydroxide (NaOH) and potassium hydroxide (KOH) were selected to prepare the base solution of pH = 13 and pH = 14, respectively. It was found that in acidic condition, the H_2O_2 production rate of DE7-M80 was increased modestly, especially in TFA aqueous solution (Figure 4.36). On the contrary, in base solution, the performance of H_2O_2 evolution dropped significantly. H_2O_2 is a kind of weak acid, and there is a dissolution equilibrium in water as follows:[34, 36]

$$H_2O_2 \rightleftharpoons H^+ + HO_2^- \quad (4.4)$$

Therefore, in acidic condition, the produced H_2O_2 would be more stable than in alkaline solution, because in base solution, the H^+ would be consumed by OH^-, leading to the accelerated decomposition of H_2O_2.

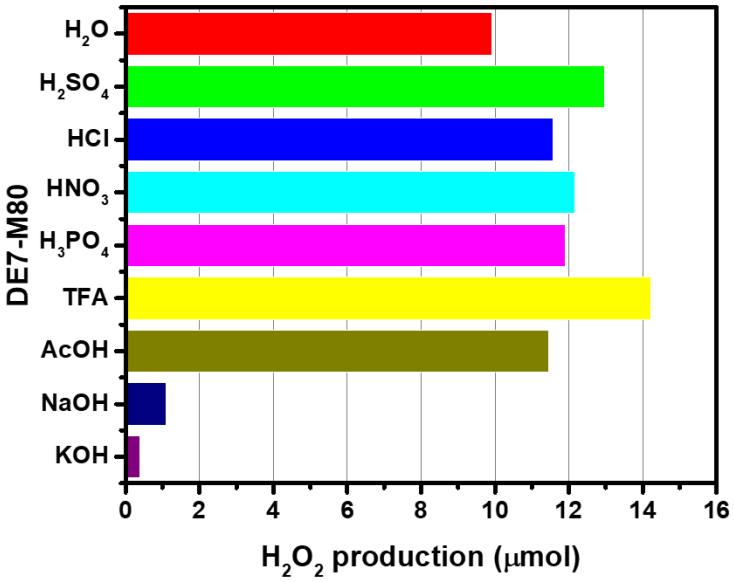

Figure 4.36 Photocatalytic H_2O_2 production in different pH aqueous solution of DE7-M80. Reaction conditions: 3 mL water and 5 mg polymer for 1.5 h illumination in air. Light source: Oriel Solar Simulator 94123A with an output of 1.0 sun.

4.4.4.2 The effect of sacrificial reagents

The ideal reaction solution should be pure water for practical application, however, adding sacrificial reagents is acceptable during the materials exploration stage for searching more candidates.[11, 13, 28, 42-44] For DE7-M80, in Figure 4.37a, it is observed that the influence of sacrificial reagent on the improving H_2O_2 production was in the order of formic acid > isopropanol > ethanol > methanol.

Expect for the above-mentioned sacrificial reagents, the other reagents listed in Figure 4.31a showed negative effect for H_2O_2 production, as no H_2O_2 was detected via both UV-vis spectrum titration method and the Peroxide test stick method. Ascorbic acid can react with H_2O_2 since it is a reducing agent. While for the amine-based reagents, due to the strong basicity of their aqueous solutions, it would decompose H_2O_2 quickly (Figure 4.37b).

When isopropanol was applied, the selectively of H_2O_2 should be considered. Because it was reported that the isopropanol could also be converted to H_2O_2 in the presence of O_2, as shown in Figure 4.37c.[2, 13]

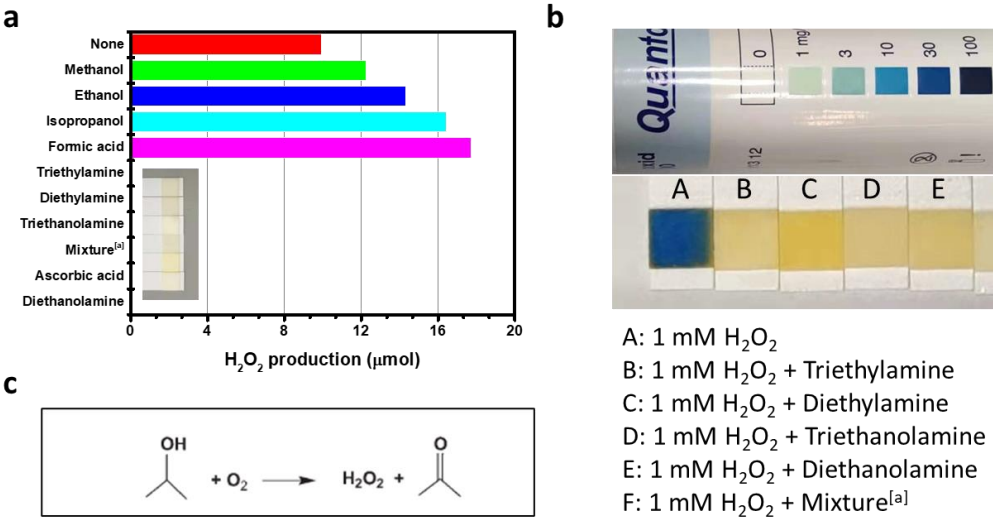

Figure 4.37 (a) Photocatalytic H_2O_2 production of DE7-M80 with adding 10 vol. % different sacrificial reagents. Reaction conditions: 2.7 mL water, 0.3 mL sacrificial reagent and 5 mg polymer for 1.5 h illumination in air. [a] The mixture is 1 mL triethylamine, 1 mL methanol and 1 mL water. Light source: Oriel Solar Simulator 94123A with an output of 1.0 sun. (b) 1mM H_2O_2 aqueous solution and after adding 10 % different sacrificial reagents, shook for seconds and measured by Peroxide test sticks. (c) H_2O_2 production by the oxidation of isopropanol.[2]

In Figure 4.38, it was found that pure isopropanol itself could not produce H_2O_2, however, when DE7-M80 was added as the catalyst, the H_2O_2 could be detected and the amount even higher than that in pure water system. It indicated that the isopropanol not only consumed the photogenerated holes thus inhibiting the combination of electrons and holes, but also providing proton sources for H_2O_2 synthesis.

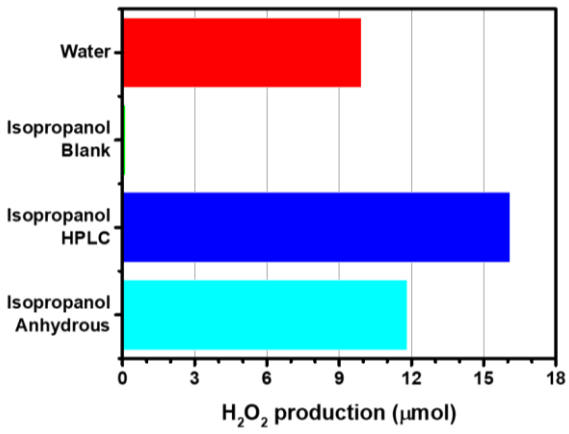

Figure 4.38 Photocatalytic H_2O_2 production of DE7-M80 in different grade of isopropanol. Reaction conditions: 3 mL water and 5 mg polymer for 1.5 h illumination in air. Light source: Oriel Solar Simulator 94123A with an output of 1.0 sun.

4.4.4.3 The effect of mass/volume ratio

Practically, it is desirable to obtain high concentration of aqueous H_2O_2 solution directly from the photocatalytic process without additional concentration step. As shown in Figure 4.39a, in 3 mL water, the concentration of produced H_2O_2 aqueous solution was firstly increased with the increase of catalyst amount. However, in Figure 4.39b, when the ratio of mass and volume was over 10, the H_2O_2 production dropped gradually. The low activity at high loading could be attributed to the poor light penetration. Interestingly, it was found that decreasing the reaction volume is a more efficient approach to achieve higher concentration (Figure 4.39b). Under the condition of 10 mg polymer in 1 mL water, a concentration of 23.8 mM L^{-1} of H_2O_2 was achieved, although was still much less than that in commercial 30 wt.% H_2O_2 aqueous solution of 9791.2 mM L^{-1}.

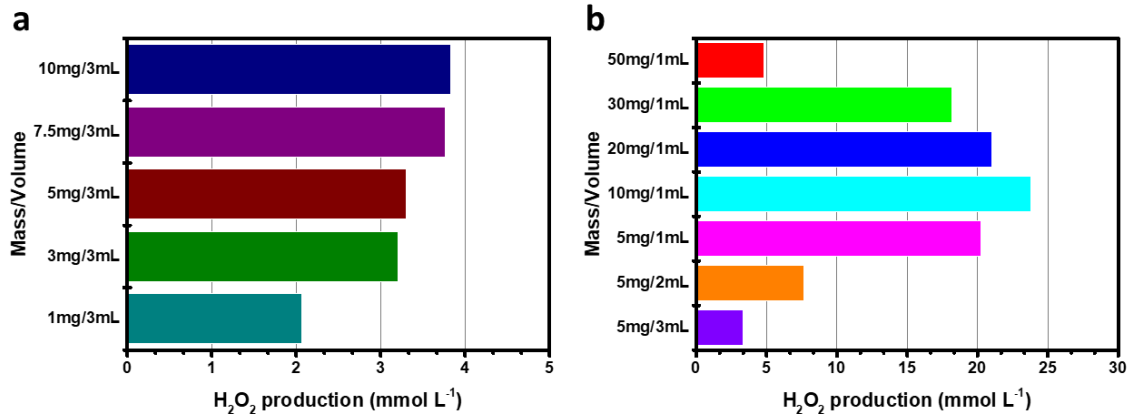

Figure 4.39 Photocatalytic H_2O_2 production of DE7-M80 in different ratios of mass and volume. Reaction conditions: X mL (X = 1, 2, 3) water and a certain amount of polymer for 1.5 h illumination in air. Light source: Oriel Solar Simulator 94123A with an output of 1.0 sun.

4.4.4.4 The effect of cocatalyst

Loading co-catalyst has been recognised as an effective strategy to improve the performance of photocatalytic reactions.[6, 45, 46] The principle of photocatalytic hydrogen peroxide is similar to that of overall photocatalytic water splitting, and both of them involve the step of water oxidation. Because it requires large activation energy barrier to form O−O bond, the kinetic of water oxidation is very slow, which is a main obstacle for high-efficient photocatalytic conversion.[47] Therefore, loading water oxidation cocatalysts onto DE7-M80 was attempted to promote the overall H_2O_2 production. As shown in Figure 4.40, after depositing Cu or Fe, the produced H_2O_2 decreased dramatically. It has been explained in section 4.4.1 that too much Cu

residual would decompose the H_2O_2. Besides, in the existence of Fe^{2+}, a Fenton reaction may happen as follows,[48, 49]

$$H_2O_2 + Fe^{2+} \rightarrow OH^{\cdot} + OH^{-} + Fe^{3+} \quad (4.5)$$

which could be attributed to the quenching of H_2O_2. However, it is interesting to mention that the introduction of Zn showed a positive effect on H_2O_2 production, which may duo to the surface complexation of Zn^{2+}.[50]

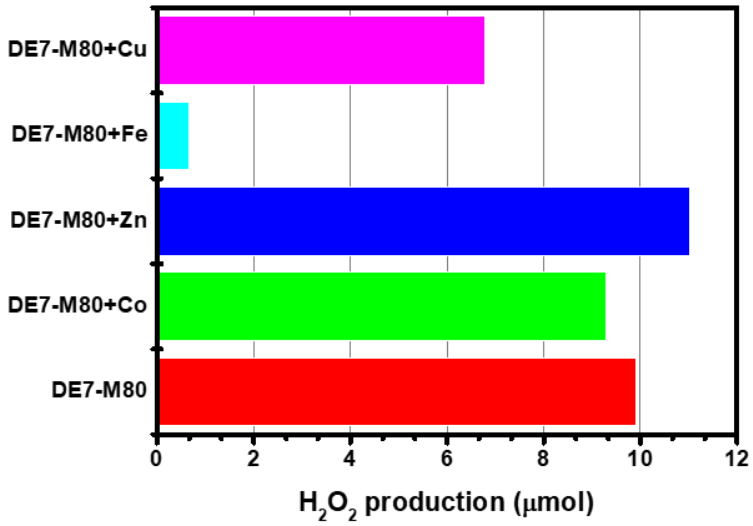

Figure 4.40 Photocatalytic H_2O_2 production of DE7-M80 in different cocatalysts. Reaction conditions: 3 mL water and 5 mg polymer and 50 μL 1 mg mL^{-1} M-acetate (M = Cu, Fe, Zn, Co) aqueous solution for 1.5 h illumination in air. Light source: Oriel Solar Simulator 94123A with an output of 1.0 sun.

It has been shown that Co-based cocatalysts are highly active for water oxidation.[45, 46, 51-54] However, it was unexpected that after loading Co, the H_2O_2 production was slightly decreased. The deposition method could be not effective, to verify the hypothesis, we further studied the effect of Co-based cocatalysts on H_2O_2 production with three different loading approaches (Figure 4.41). Again, the H_2O_2 production decreased after loading Co regardless of loading method. Cobalt oxide, such as Co_3O_4, may have catalase-like activity to decompose H_2O_2,[55-58] which might explain the decreased activity after Co cocatalysts loading. Therefore, other Co-based cocatalysts, such as CoP[45] or single Co atom[53], could be considered in the future.

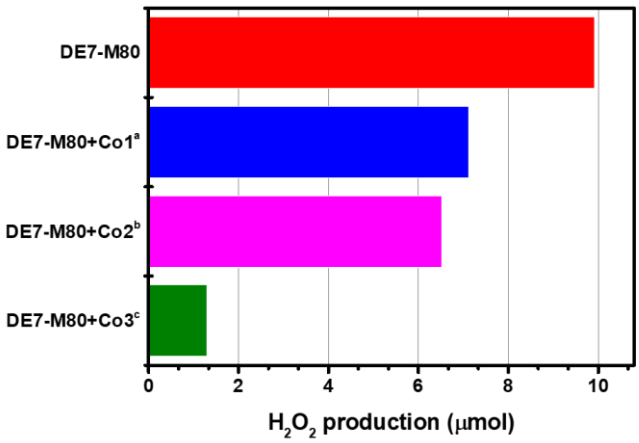

Figure 4.41 Photocatalytic H_2O_2 production of DE7-M80 loaded with Co via different methods. Reaction conditions: 3 mL water and 5 mg polymer for 1.5 h illumination in air. Light source: Oriel Solar Simulator 94123A with an output of 1.0 sun. (a) DE7-M80 was added into 2 mL Co_3O_4 quantum dot methanol dispersion (2 mg mL^{-1}), after ultrasonicating for 1 h, the solvent was evaporated, and obtained the product of DE7-M80+Co1. (b) DE7-M80 was mixed with $Co(NO_3)_2$ in the acetone/H_2O (1:1) solution, after ultrasonicated for 1 h, the solvent was evaporated, and obtained the product of DE7-M80+Co2. (c) The sample of DE7-M80+Co2 was further calcined in a muffle at 200 ℃ for 2 h in air, and the new sample was named as DE7-M80+Co3. All of the samples were loaded 3 wt. % Co by calculation.

4.4.5 Stability performance evaluation of DE7-M80

4.4.5.1 Photocatalytic decomposition of H_2O_2

The decomposition of H_2O_2 is an issue that need to be avoid during the photocatalytic conversion process and long-time storage. It could be caused by different factors, such as light wavelength range, pH, concentration, temperature and impurities.[2, 11, 13]

Figure 4.42 is the outcome of H_2O_2 decomposition in different conditions. Aqueous H_2O_2 solution was fairly stable in dark, with only 3 % decrease after 24 h. However, under visible light illumination with a 300 W Xe lamp ($\lambda > 420$ nm) for 24 h, the initial concentration of H_2O_2 was decreased by 97%. Changing the filter to larger wavelength ($\lambda > 500$ nm), it still could not avoid the decomposition after long time. It has been reported that sodium pyrophosphate could be used as a stabilizer to against the unwanted decomposition of H_2O_2, and the main principle is that it can act as a cleaning agent to complex with any existing traces of transition-metal ions that would cause the decomposition.[1, 2] However, in this case, there was no obvious effect after adding the stabilizer. But it was interesting to find that in the

presence of DE7-M80, the initial decomposition of H_2O_2 was slightly mitigated. The possible reason is that the O_2 produced from the decomposition of H_2O_2 was reduced by DE7-M80 again to generate H_2O_2.

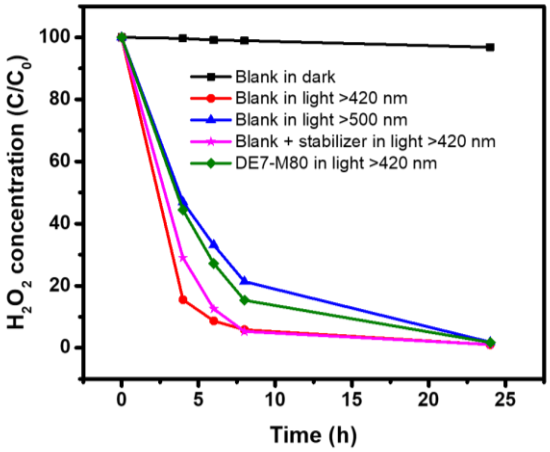

Figure 4.42 Decomposition of H_2O_2 experiments of DE7-M80.Reaction conditions: 30 mL 1 mM H_2O_2 aqueous solution, 100 mg mL^{-1} sodium pyrophosphate was used as the stabilizer, under a Xe lamp illumination with a filter ($\lambda > 420$ nm) in N_2 atmosphere.

4.4.5.2 Photostability

To evaluate the stability of DE7-M80, it was recycled after photocatalytic H_2O_2 production and then used for the next run. As shown in Figure 4.43, after 5 runs over 10 h, the activity of DE7-M80 slightly decreased while the amount of polymer was significantly reduced.

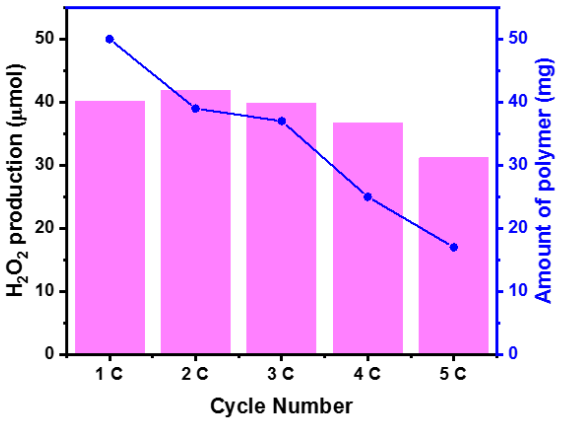

Figure 4.43 Repeat photocatalytic runs for DE7-M80. Reaction conditions: 30 mL water and 50 mg polymer under a Xe lamp illumination with a filter ($\lambda > 420$ nm) in O_2, the polymer was recovered, and the water was replaced between runs.

In addition, in the long-term experiment (Figure 4.44), after 25 h, the H_2O_2 production rate was found to decrease significantly. Bubbling O_2 into the reactor did not help to recover the production rate indicating the supply of oxygen is not the reason. After 47.5 h, the generated H_2O_2 amount was observed to decrease gradually. One possible explanation is that the H_2O_2 production rate could not catch up the decomposition rate of H_2O_2. Another possible reason is the bleaching action of H_2O_2 on DE7-M80.[2, 6]

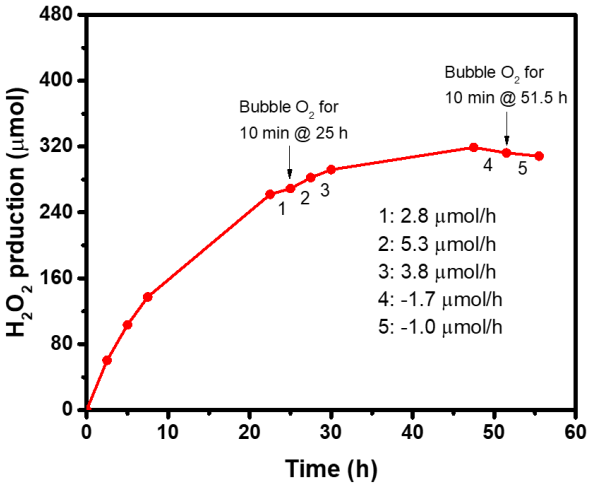

Figure 4.44 Long-term photocatalytic H_2O_2 production of DE7-M80, O_2 was bubbled before the illumination, at 25 h, and 51.5 h. Reaction conditions: 30 mL water and 50 mg polymer under a Xe lamp illumination with a filter ($\lambda > 420$ nm).

We then characterised the DE7-M80 after long-term photoreaction. Figure 4.45 is the SEM images of DE7-M80 after different hours of photocatalytic H_2O_2 reaction. After 5 h and 24 h, the morphology of DE7-M80 had no obvious change, while after 55.5 h, the wrinkled sheet disappeared, and the main morphology became to be smaller particles. Besides, the solid UV-vis spectra (Figure 4.46a) displayed that the light absorption was slightly decreased after long-term illumination. And the PXRD patterns (Figure 4.46b) showed that the semi-crystalline state of DE7-M80 could maintain for 24 h, however, after 55.5 h, the pattern was changed, indicating the change of the structural packing. In solid-state NMR spectra (Figure 4.46c), a weak peak at 167 ppm appeared after illumination, which could be assigned to C=O.[59, 60] However, no obvious change could be found in Raman spectra (Figure 4.46d).

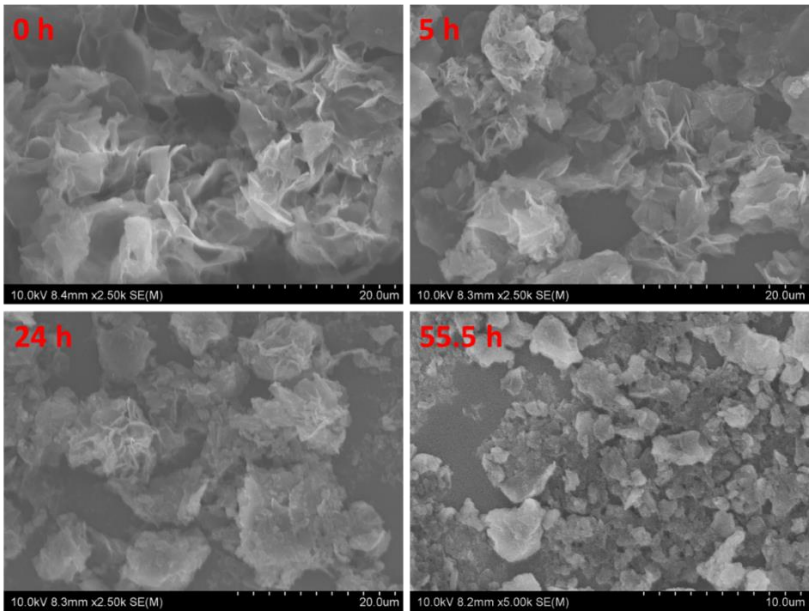

Figure 4.45 SEM images of DE7-M80 and DE7-M80 after 5 h, 24 h, and 55.5 h illumination under a Xe lamp illumination with a filter (λ > 420 nm).

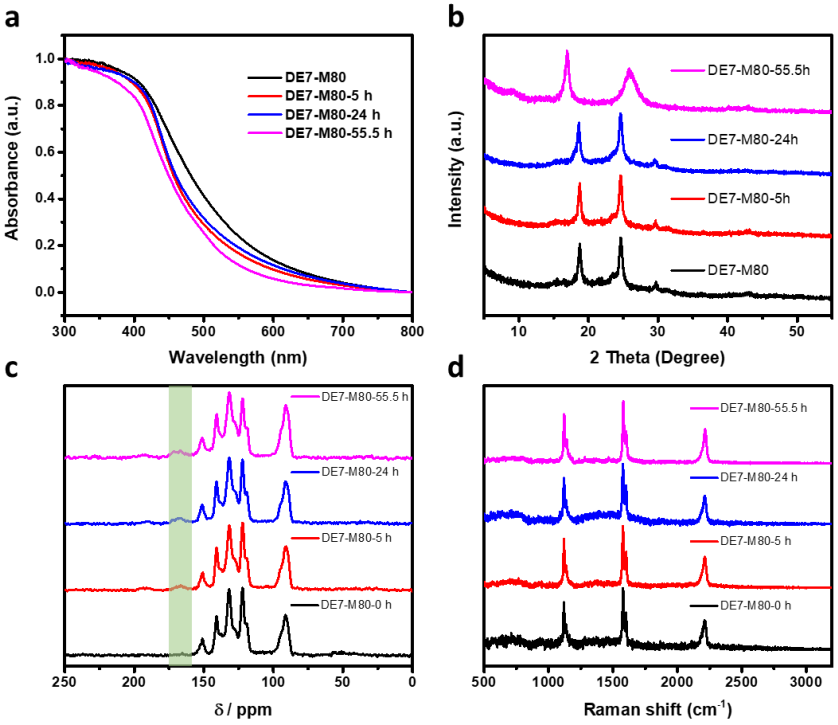

Figure 4.46 (a) Solid UV-vis spectra and (b) PXRD patterns (c) solid state NMR (d) Raman of DE7-M80 and DE7-M80 after 5 h, 24 h, and 55.5 h illumination, under a Xe lamp illumination with a filter (λ > 420 nm).

The FT-IR spectra of DE7-M80 after different hours of photocatalytic H_2O_2 production were shown in Figure 4.47a, The signals of C=N and C-N in the pyridine unit can be detected at

1502 cm^{-1} and 1366 cm^{-1}, repectivvity.[61, 62] With the increase of illumination time, the intensity of the peak at 1672 cm^{-1} gradually increased along with a shift to 1688 cm^{-1}, which could be the signal of C=O.[63] The C=O in the as made DE7-M80 might come from the impurities in the monomers (Figure 4.47b). In addition, the strongest signal of C-H peak at 828 cm^{-1} in the fresh sample, which was assigned to the substituted benzene,[63] it became very weak after 55.5 h. From the element analysis results (Table 4.7), it showed that the percentage of C, H and N all decreased, indicating new element were introduced in DE7-M80 under illumination in water, most likely element was O, as C=O signal emerged from FT-IR.

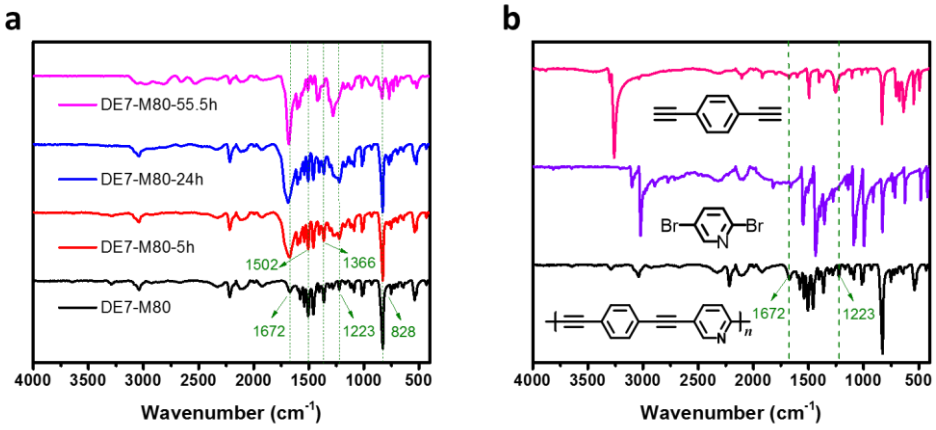

Figure 4.47 FT-IR of (a) 2,5-dibromopyridine (99%), 1,4-diethynylbenzene (96%) and as made DE7-M80; (b) DE7-M80 and DE7-M80 after 5 h, 24 h, and 55.5 h illumination under a Xe lamp illumination with a filter (λ > 420 nm).

Table 4.7 Element analysis of DE7-M80 and DE7-M80 after 5 h, 24 h, and 55.5 h illumination under a Xe lamp illumination with a filter (λ > 420 nm).

DE7-M80	%C	%H	%N
0 h	74.98	3.50	6.85
5 h	72.37	3.37	6.27
24 h	69.12	3.07	5.77
55.5 h	68.36	3.05	5.56

Therefore, based on the results mentioned above, the decomposition or oxidation of DE7-M80 occurred during photocatalytic H_2O_2 production. The possible reason is that the carbon-carbon bonds in DE7-M80 were broken, which could be caused by the photogenerated radical and O_2,[64, 65] the light energy and O_2,[66] or the produced H_2O_2[67, 68].

4.4.5.3 Conversion efficiency

To achieve higher photocatalytic H_2O_2 conversion efficiency, the reaction temperature was firstly optimized. As shown in Figure 4.48, it was found that the reaction temperature of 40 ℃ provides the highest H_2O_2 generation rate. Further increasing the temperature might cause the decomposition H_2O_2 thus decreasing the overall H_2O_2 amounts.

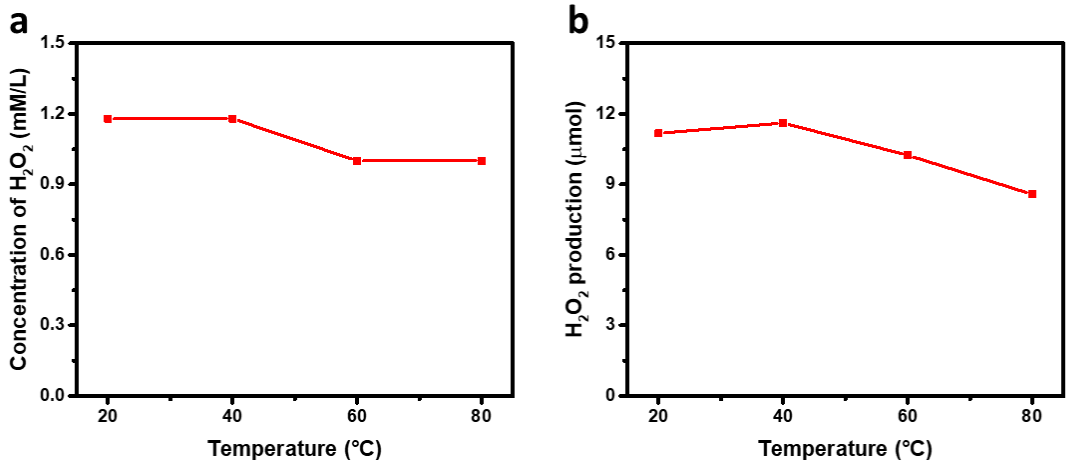

Figure 4.48 (a) Stability of H_2O_2 aqueous solution at different temperature, the initial concentration is 1.18 mM L^{-1}. (b) Photocatalytic H_2O_2 production of DE7-M80 at different temperature. Reaction conditions: 3 mL water and 5 mg polymer for 1.5 h illumination, the temperature was controlled by the hot plate. Light source: Oriel Solar Simulator 94123A with an output of 1.0 sun.

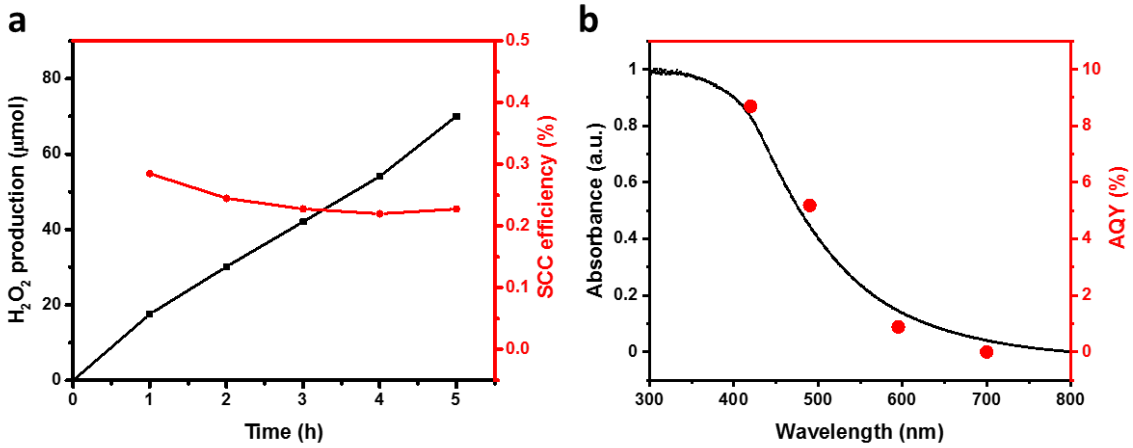

Figure 4.49 (a) Photocatalytic H_2O_2 production and the SCC efficiency of DE7-M80 in a 40 ℃ water bath under a LED simulated sunlight (1 sun) irradiation. Reaction conditions: water (50 mL), catalyst (200 mg), in O_2. (b) Wavelength dependent external quantum efficiency (AQE) values and solid UV-vis spectrum of DE7-M80. Reaction conditions: water (30 ml), catalyst (50 mg), in O_2 under a LED light (λ = 420, 490, 700 nm) illumination at room temperature.

Based on this result, the solar-to-chemical conversion (SCC) efficiency was measured (Figure 4.49a), the highest SCC value was obtained of 0.28% in the first hour, and then it slowly dropped to 0.23%. The SCC reported in this study is higher than most reported materials, such as PEI/g-C_3N_4 (0.045%),[69] C_3N_4/rGO (2.0%),[13] and CTF-BDDBN (0.14 %)[23] (Table 4.8). In addition, a high apparent quantum yield (AQY) of 8.7% was obtained at 420 nm (Figure 4.49b), indicating the excellent photocatalytic H_2O_2 production performance of DE7-M80.

Table 4.8 Comparation of the H_2O_2 yield, SCC efficiency and AQY of DE7-M80 with reported materials.

No.	Material	H_2O_2 yield / μmol	SCC / %	AQY / %	Reaction conditions	Ref.
1	DE7-M80	266 (24 h)	0.23	8.7 at 420 nm	H_2O, λ > 420 nm	**This work**
2	RF523	61.6 (24 h)	0.5	~8.0 at 420 nm	H_2O, λ > 420 nm	[20]
3	RF-acid resins	91.0 (24 h)	0.7	~9.0 at 420 nm	H_2O, λ > 420 nm	[19]
4	CTF-BDDBN	70 (24 h)	0.14	-	H_2O, λ > 420 nm	[23]
5	OCN-500	53 (10 h)	-	10.2 at 420 nm	H_2O, λ > 420 nm	[12]
6	Sb-SAPC15	18.2 (2 h)	0.61	17.6 at 420 nm	H_2O, λ > 420 nm	[14]
7	g-C_3N_4/PDI/$rGO_{0.05}$	29 (24 h)	0.20	6.1 at 420 nm	H_2O, λ > 420 nm	[13]
8	PEI/C_3N_4	4.2 (1 h)	0.045	2.21 at 420 nm	H_2O, λ > 420 nm	[69]
9	R_{370}-CN	17 (1 h)	~0.26	~4.3 at 420 nm	H_2O, λ > 420 nm	[70]
10	PCNBA0.2Co5%	~35 (12 h)	0.30	8.0 at 420 nm	H_2O, λ > 420 nm	[71]

4.5 Mechanism investigation

There are three recognized mechanisms for H_2O_2 formation in the reaction solution of water under O_2 or inert atmosphere.[2, 6] The first one is indirect sequential two-step single-electron reduction of O_2, as illustrated in Equation 4.6-4.9. The O_2 was reduced by a photogenerated electron (e^-) to superoxide radical ($O_2^{\bullet-}$), which will subsequently react with H^+ and e^- to form H_2O_2. The second one is a direct two electrons step as the O_2 reacts with H^+ and e^- to be reduced to H_2O_2 (Equation 4.10). The H_2O_2 could also be produced by two electrons oxidation of H_2O to H_2O_2 (Equation 4.11) instead of four electrons to produce O_2 (Equation 4.12).[23, 72] All of the three routes follow the overall photocatalytic process as described in Equation 4.13.

$$O_2 + e^- \rightarrow O_2^{\bullet-} \quad (4.6)$$

$$O_2^{\bullet-} + H^+ \rightarrow HO_2^{\bullet-} \quad (4.7)$$

$$HO_2^{\bullet-} + e^- \rightarrow HO_2^- \quad (4.8)$$

$$HO_2^- + H^+ \rightarrow H_2O_2 \quad (4.9)$$

$$O_2 + 2H^+ + 2e^- \rightarrow H_2O_2 \quad (4.10)$$

$$2H_2O + 2h^+ \rightarrow H_2O_2 + 2H^+ \quad (4.11)$$

$$2H_2O + 4h^+ \rightarrow O_2 + 4H^+ \quad (4.12)$$

$$O_2 + 2H_2O \rightarrow 2H_2O_2 \quad (4.13)$$

4.5.1 Gas atmosphere

In Figure 4.50a, it is observed that under N_2 atmosphere, no H_2O_2 was detected, while the produced H_2O_2 in pure O_2 (99%) was 1.6 times as much as that in air (consist of 21% O_2), indicating that the H_2O_2 was generated from the O_2. It could be further confirmed by isotopic labbing experiments (Figure 4.51). Motivated by this observation, the cap of reaction vial was removed so that the reaction solution was exposed to the ambient air, the produced H_2O_2 (18.3 μmol) more than doubled compared with that in a sealed vial (6.9 μmol, in air). Moreover, when continuing to bubble the air during the photocatalytic process, the H_2O_2 production was further improved to 26.5 μmol (Figure 4.50b).

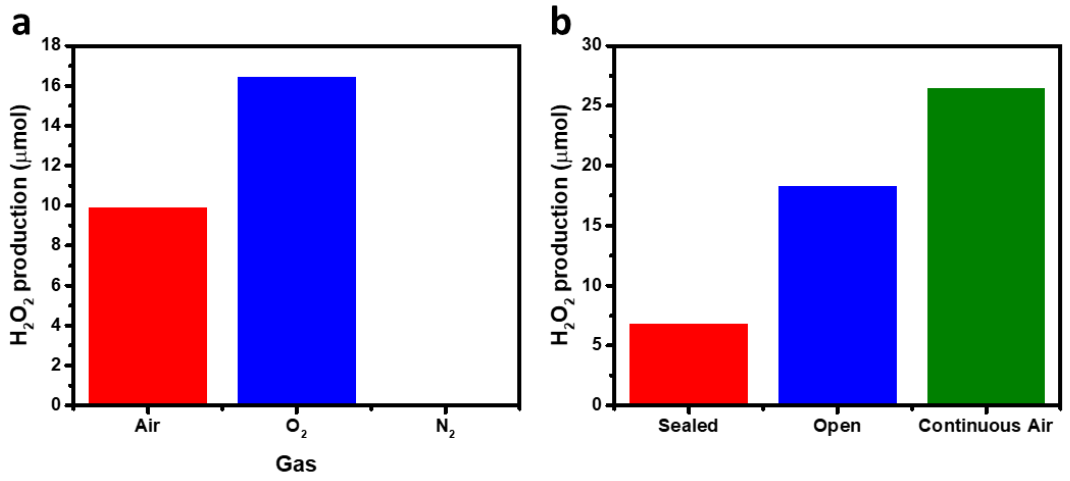

Figure 4.50 Photocatalytic H_2O_2 production of DE7-M80 (a) in different gas atmosphere. Reaction conditions: 3 mL water and 5 mg polymer for 1.5 h illumination. Light source: Oriel Solar Simulator 94123A with an output of 1.0 sun. (b) in air with different conditions. Reaction conditions: 9 mL water and 15 mg polymer for 1.5 h illumination. Light source: LED Solar Simulator with an output of 1.0 sun.

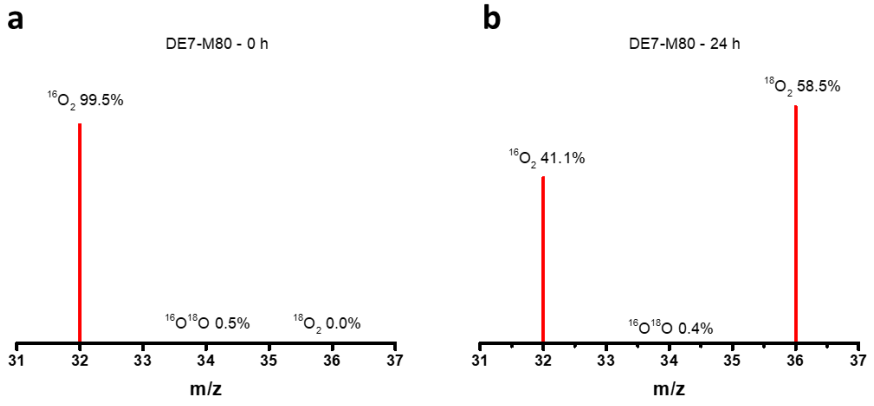

Figure 4.51 Isotopic $^{18}O_2$ labelling experiments using DE7-M with $^{18}O_2$ (a) at 0 h and (b) after 24 h. Reaction conditions: 50 mg DE7-M80 was added to 35 mL $H_2{}^{16}O$ in a flask and sealed with a rubber, 10 mL $^{18}O_2$ was injected by a syringe after bubbling with He for 10 min. Under a Xe lamp ($\lambda > 420$ nm) illumination for 24 h, the reaction solution was bubbled He again to remove residual $^{18}O_2$, then it was added in a sealed He-filled vial consisting of MnO_2. After decomposition, the gas was analysed by a Agilent 7890B GC-MS instrument.

4.5.2 Radical detection

Although the H_2O_2 was evidenced to come from the O_2, it was still unclear whether it followed the single electron two-step reduction route or the two electrons single-step reduction route.

Therefore, electron paramagnetic resonance (EPR) was performed to detect $O_2^{\bullet-}$ with 5,5-dimethyl-1-pyrroline N-oxide (DMPO) as the trapping agent. As shown in Figure 4.52, the typical signal of $O_2^{\bullet-}$ was found after illumination, suggesting that the presence of $O_2^{\bullet-}$ generated from one electron reduction of O_2. In addition, it was reported that *p*-benzoquinone (*p*-BQ) can easily react with $O_2^{\bullet-}$ to form *p*-$BQ^{\bullet-}$, thus it has been widely used as a $O_2^{\bullet-}$ scavenger.[73, 74] After adding *p*-BQ into the reaction solution, no H_2O_2 was detected in our experiment. The above results strongly suggested that the photocatalytic H_2O_2 production of DE7-M80 followed the single electron two-step reduction route.

After elucidating the H_2O_2 production route, the H_2O_2 production performance might be further improved by promoting the reduction of O_2 to $O_2^{\bullet-}$. It was reported that the electron transfer reduction of O_2 could be favoured by the strong binding or complexation of $O_2^{\bullet-}$ with metal ions that can act as Lewis acids, and the promoting effects of metal ions depend on the Lewis acidity of metal ion salts.[75, 76] Among various metal nitrates, $Sc(NO_3)_3$ showed very strong Lewis acidity.[15] In the presence of $Sc(NO_3)_3$ in reaction solution, it was found that the H_2O_2 production performance of DE7-M80 was largely enhanced, as shown in Figure 4.53, which could be attributed to the inhibition of back electron transfer from $O_2^{\bullet-}$ to O_2 after binding of Sc^{3+} to $O_2^{\bullet-}$, thus promoting the H_2O_2 evolution.

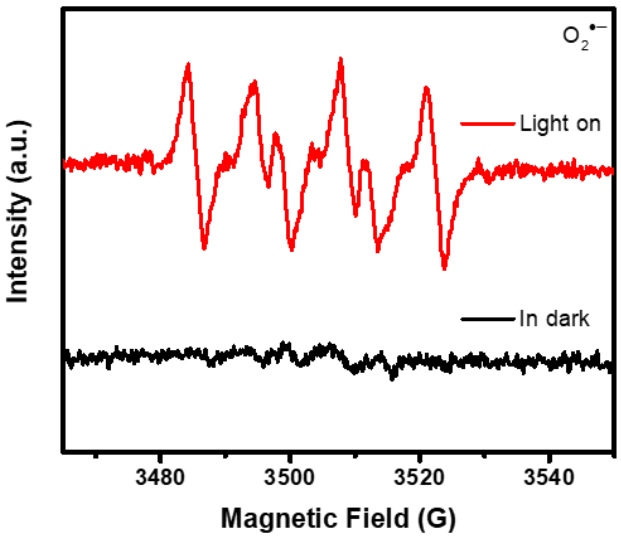

Figure 4.52 Electron paramagnetic resonance of DE7-M80 in the presence of DMPO as an electron trapping agent in H_2O/Methanol (1:9) under a Xe lamp illumination for 5 min with a filter ($\lambda > 420$ nm).

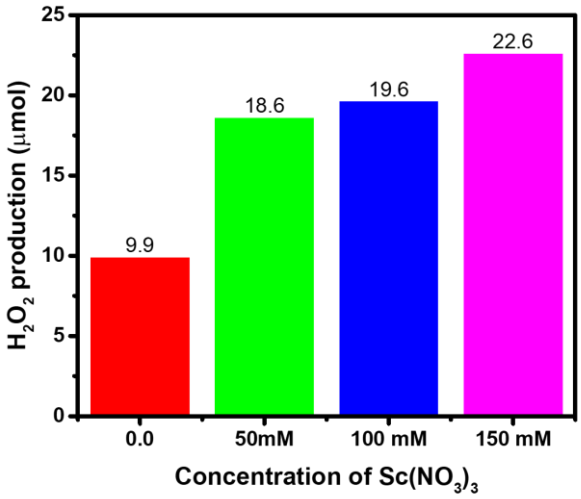

Figure 4.53 Photocatalytic H_2O_2 production of DE7-M80 in $Sc(NO_3)_3$ aqueous solution. Reaction conditions: 3 mL water and 5 mg polymer for 1.5 h illumination. Light source: Oriel Solar Simulator 94123A with an output of 1.0 sun.

4.5.3 Half photoreaction

The half reaction of H_2O_2 production was carried out in section 4.4.4.2, after adding the electron donor sacrificial agents, the production of H_2O_2 was significantly improved. In addition, in the half reaction of O_2 production, the $AgNO_3$ was used as the electron acceptor to quench the production of H_2O_2. O_2 was evolved under the visible light illumination, as shown in Figure 4.54. This result confirmed that the H_2O was oxidized to O_2 instead of H_2O_2.

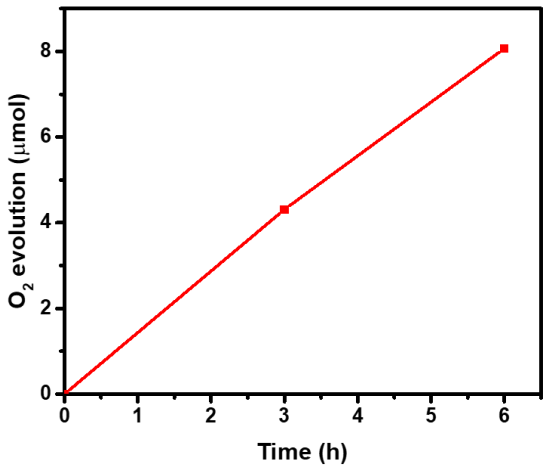

Figure 4.54 Produced O_2 in the half reaction of DE7-M80. Reaction conditions: 50 mg DE7-M80, 100 mL water, 10 mM $AgNO_3$ and 200 mg La_2O_3 in N_2 under a Xe lamp illumination with a filter (λ >420 nm).

4.5.4 Proposed mechanism path

The flat band (E_{fb}) potential of DE7-M80 was measured by the electrochemical Mott-Schottky technique in standard three-electrode system with 0.5 M Na_2SO_4 aqueous solution (pH = 7) as the electrolyte (Figure 4.55a),[77, 78] which can be further converted into -0.83 V *vs.* NHE according to the equation of $E_{NHE} = E_{Ag/AgCl} + 0.197$ V.[79, 80] In addition, the positive slope indicated that DE7-M80 was a n-type semiconductor. For many n-type semiconductors, E_{fb} is normally deemed to be more positive about 0.1 V than its conduction band potentials (E_{CB}).[79] Therefore, the E_{CB} of DE7-M80 was calculated -0.93 V *vs.* NHE. Besides, the optical gap of DE7-M80 was obtained from the UV-vis spectrum with a value of 2.34 eV (2.34 V *vs.* NHE) (Figure 4.55b), so the conductive band of DE7-M80 was calculated at1 1.41 V *vs.* NHE from the equation of $E_{vb} = E_{cb} + E_g$.

Based on the obtained results, the proposed mechanism of DE7-M80 for photocatalytic H_2O_2 evolution from water under visible light illumination ($\lambda > 420$ nm) was illustrated in Figure 4.56. The CB potential (-0.93 V *vs.* NHE, pH = 7) of DE7-M80 was more negative than the H_2O_2 production level (0.27 V *vs.* NHE, pH = 7), which provided sufficient driving force for the O_2 reduction. In detail, the O_2 was converted to the intermediate radical of $O_2^{\bullet-}$ at first by the photogenerated e^-, and then the $O_2^{\bullet-}$ reacted with H^+ and e^- to produce H_2O_2. Meanwhile, the VB level (1.41 V *vs.* NHE, pH = 7) of DE7-M80 was more positive than the energy level of water oxidation (0.82 V *vs.* NHE, pH = 7), which favoured the production of O_2.

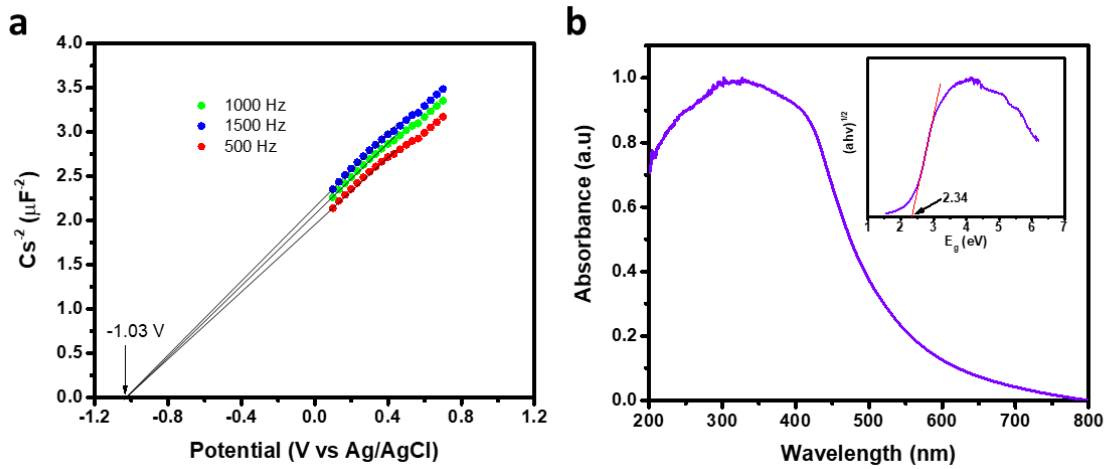

Figure 4.55 (a) Electrochemical Mott-Schottky plots of DE7-M80. (b) UV-vis spectrum with corresponding the Tauc plot (inserted figure) of DE7-M80.

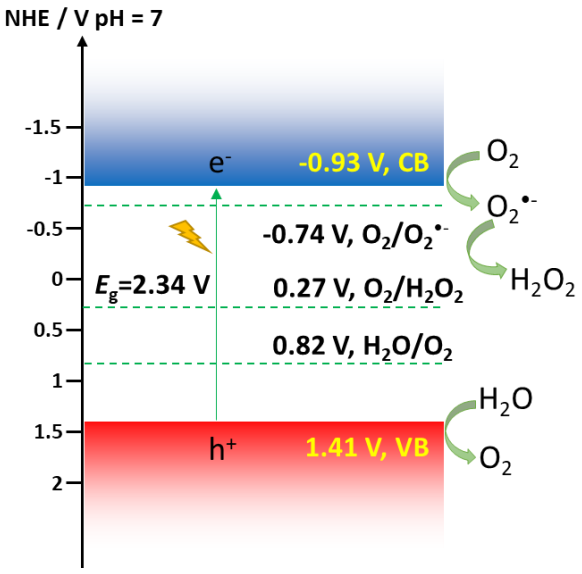

Figure 4.56 Energy band positions of DE7-M80.

4.6 Summary

Organic materials were used as photocatalysts in the photocatalytic evolution of H_2O_2. To begin with, the benchmark material of RF523 was repeated and the performance was reproduced. After that, four detection methods for H_2O_2 production were compared with each having its own advantages and disadvantages. Taken together, the Peroxide test sticks method was applied for the high-throughput preliminary screening, and the KI titration method (UV-vis spectroscopy method-A) was used for quantitative analysis. After screening a large amount of potential organic materials, DE7 showed high photocatalytic H_2O_2 production without any sacrificial reagents, even 3 times as high as RF523-R. In addition, 8 derivatives of DE7 were designed and synthesized, but all of them were inferior to DE7. However, with the assistance of a microwave instrument, the synthesis time was largely decreased from 2 days to 2 h.

Based on the best sample of DE7-M80, several important factors, such as pH, sacrificial reagents, the ratio of mass and volume and cocatalyst, were investigated. A lower pH value would be more beneficial for H_2O_2 production, while base condition will cause the decomposition of H_2O_2, similar phenomenon could be found when alkaline sacrificial reagents were added to the solution. To achieve high concentration of H_2O_2, the best ratio of mass to volume was found to be 10 mg: 1mL.

Water oxidation cocatalysts loading onto DE7 was attempted to efficiently extract the photogenerated hole from materials to catalyse water oxidation instead of self-oxidation. However, overall negative effect on the amount of generated H_2O_2 was observed here, probably due to the increased decomposition speed of H_2O_2 on these metal-based cocatalyst. In the future, more efforts need to be addressed on the choice of cocatalyst to improve the long-term photostability of organic materials in H_2O_2 production.

Finally, the DE7-M80 has high conversion efficiency, which is comparable to the most reported organic materials. And the produced H_2O_2 of DE7-M80 was mainly derived from the two-step single-electron reduction of O_2. However, after long time illumination, the DE7 decomposed, the detail mechanism is still unclear, which needs deeper investigation. This work provides new ideas for the exploration and design of more functional highly efficient organic photocatalysts for photocatalytic H_2O_2 production.

4.7 Experimental Parts

4.7.1 Materials and methods

4.7.1.1 Materials

All chemicals were obtained from Sigma-Aldrich, TCI or Fluorochem and used as received and without further purification.

4.7.1.2 Characterization method

The absorption spectra of the polymers were measured on a Cary 5000 UV-visible-NIR spectrophotometer in solid powder state. Transmission FT-IR spectra were collected with an attenuated total reflectance (ATR) method on a Bruker Tensor-27 spectrometer for 16 scans with a resolution of 4 cm^{-1} at room temperature. Photoluminescence spectra were performed on a Shimadzu RF-5301PC fluorescence spectrometer. Time-correlated single photon counting (TCSPC) experiments were measured on an Edinburgh Instruments LS980-D2S2-STM spectrometer (EPL-375 diode, λ = 371 nm) equipped with picosecond pulsed LED excitation sources and a R928 detector, with a stop count rate below 5%. The instrument response of the TCSPC spectrometer was measured with colloidal silica (LUDOX® HS-40, Sigma-Aldrich) at the excitation wavelength. Decay times were fitted in the FAST software using three decay exponents. Samples were prepared by ultrasonicating the polymer in water. Thermogravimetric analysis was performed by heating samples under N_2 in open platinum pans from 25 ℃ to 800 ℃ at 10 ℃ min^{-1} on an EXSTAR6000 instrument. PXRD measurements were performed on a Panalytical Empyrean diffractometer with a Cu X-ray source (λ = 1.5418 Å, Cu Kα), polymers were placed on an aluminium well plate and screened in high throughput transmission mode with PIXCEL 3D detector and X-ray focusing mirror. Static light scattering measurements were performed on a Malvern Mastersizer 3000 Particle Sizer at a laser obscuration of 5-10%. Particle sizes were fitted according to the Mie theory with the Malvern 'General Purpose' analysis model. Transmittance of high-throughput samples was measured on a Formulaction S.A.S. Turbiscan AGS system with an 880 nm NIR diode and a detector at 180 ° (relative to the light source) in a cylindrical glass cell. Surface areas were tested on Micromeritics 2420 instrument at a temperature of 77 K. Before analysis, polymer samples were degassed offline at 110 ℃ for 15 hours under dynamic vacuum (10^{-5} bar). CHNS-O Analyzer was measured using standard microanalytical procedures. Palladium contents were determined using ICP-OES Agilent 5110 equipped with a collision/reaction cell after a microwave digestion of the materials in nitric acid (67-69%, trace metal analysis grade) in the

instrument of Perkin Elmer Microwave Titan. Water contact angles were measured using pressed pellets and a drop-shape analysis apparatus (Krüss DSA100) with the Young-Laplace fitting method. The morphology of the polymer was studied on a Hitachi S4800 scanning electron microscope (SEM). The Raman measurements were performed on an inVia Reflex Qontor Confocal Raman microscope upon excitation of 785 nm laser. ^{13}C magic-angle spinning measurements were carried out at 100.63 MHz using a Bruker Avance III HD spectrometer and 4 mm (rotor o.d.) probe. Spectra were acquired at a spin rate of 10 kHz. Cross-polarisation (CP) spectra were recorded with TOSS spinning sideband suppression, 4 ms contact time and with a recycle delay of 4 s. Carbon spectral referencing is relative to neat tetramethylsilane, carried out by setting the high frequency signal from an external sample of adamantane to 38.5 ppm.

4.7.2 Synthetic procedures

4.7.2.1 Synthesis of RF523

The preparation method was as described in the literature[20]: the resorcinol (400 mg, 3.6 mmol), formaldehyde (37 wt.% solution, 7.2 mmol) and NH_3 (28 wt.% solution,180 μl, 3.0 mmol) were added to deionized water (40 ml) and stirred for 5 min at room temperature. The white colloidal suspension was transferred to a Teflon-lined stainless-steel autoclave and left in an oven, where the heating rate was 7 K min^{-1} and the holding time at 523 K was 24 h. The solids formed were washed thoroughly by Soxhlet extraction with acetone for 12 h and dried in vacuo at room temperature for 12 h.

4.7.2.2 Synthesis of pyrene-based polymers

General procedure for the Sonogashira polycondensation: In the glovebox, a 40 mL glass vial was charged with the monomers, $Pd(PPh_3)_4$, CuI, anhydrous *N*,*N*-dimethylformamide and triethylamine, and then sealed with a silicone septum. The sealed vessels were taken out of the glovebox, inserted in a sand bath preheated to 100 ℃ and kept at this temperature for 2 days. After cooling to room temperature, the mixture was quenched by addition of methanol, and the solids were filtered off and washed with methanol and acetone. Further purification was carried out by Soxhlet extraction with chloroform for 2 days. The final product was dried in the vacuum oven at 80 ℃ overnight.

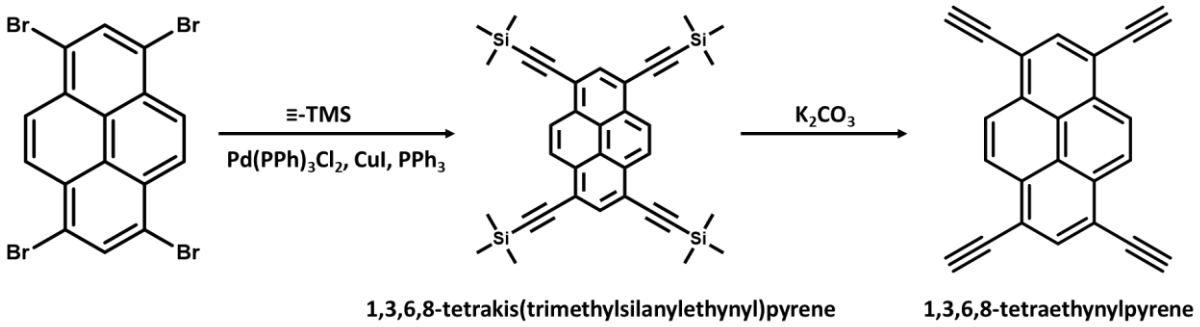

Figure 4.57 Synthesis procedure of 1,3,6,8-tetraethynylpyrene.

1,3,6,8-tetraethynylpyrene:[81] A flask was charged with 1,3,6,8-tetrabromopyrene (100 mg, 0.20 mmol), $Pd(PPh_3)_2Cl_2$ (27.0 mg, 0.04 mmol), CuI (15.0 mg, 0.08 mmol), PPh_3 (20.0 mg, 0.08 mmol), triethylamine (10 mL) and toluene (1.5 mL). Under stirring in N_2 atmosphere, the reaction solution was heated to 60 ℃, then trimethylsilylethyne (114 mg, 1.16 mmol) was injected slowly with a syringe. After that, the temperature was increased to 80 ℃ and kept for 12 h. The solvent was removed by rotary evaporation, and the solid was purified by flash column chromatography using petroleum ether as eluent to afford 1,3,6,8-tetrakis(trimethylsilanylethynyl)pyrene, after reacted with K_2CO_3 in methanol at room temperature for 24 hours, a slightly brown solid was obtained via filtration. The final product was washed with water and dried in a freeze drier.

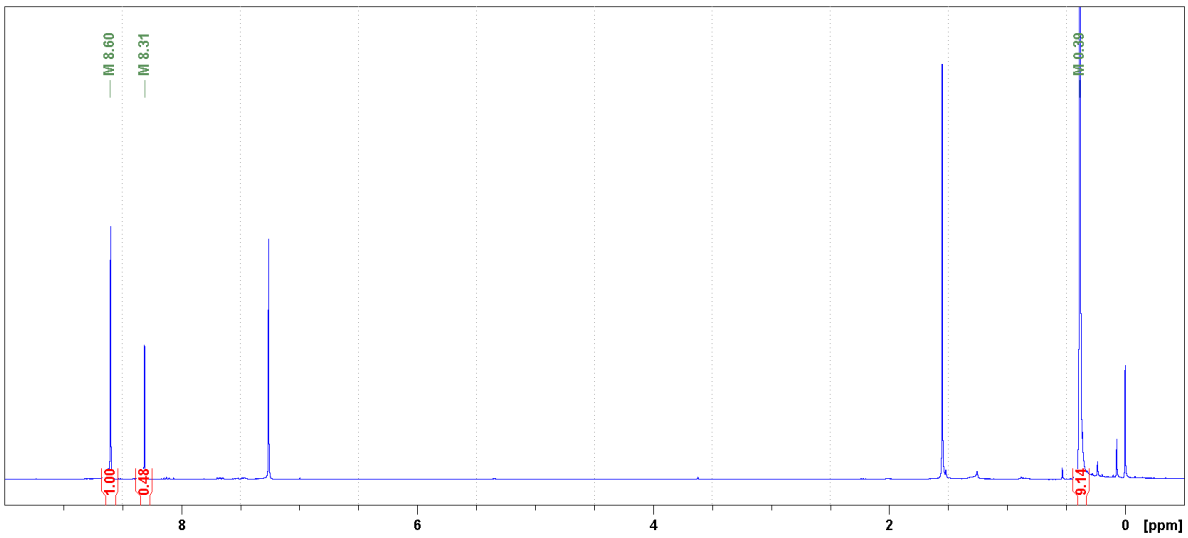

Figure 4.58 ^{1}H NMR spectrum of 1,3,6,8-tetrakis(trimethylsilanylethynyl)pyrene in chloroform. δ (ppm) : 0.39 (s, 36H), 8.31 (s, 2H), 8.60 (s, 4H).

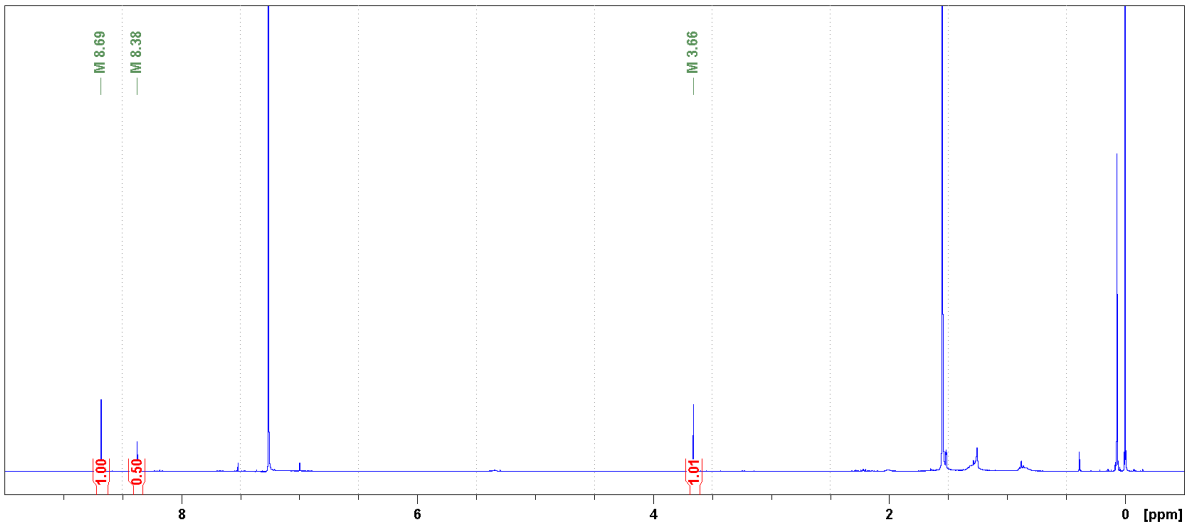

Figure 4.59 ^{1}H NMR spectrum of 1,3,6,8-tetraethynylpyrene in chloroform. δ (ppm) : 3.66 (s, 4H), 8.38 (s, 2H), 8.69 (s, 4H).

PY1: 1,4-Dibromo-2,5-dimethoxybenzene (118 mg, 0.4 mmol), 1,3,6,8-tetraethynylpyrene (60 mg, 0.2 mmol), $Pd(PPh_3)_4$ (15 mg, 0.01 mmol), CuI (10 mg, 0.05 mmol), *N*,*N*-dimethylformamide (9 mL) and triethylamine (9 mL) were used in this Sonogashira polycondensation reaction described in the general procedure. After work-up and Soxhlet, the product was obtained as a red solid (113 mg, 82%). Anal. Calcd for $(C_{40}H_{22}O_4)_n$: C, 84.79; H, 3.91; Found C, 75.78; H, 3.58. Pd content: 1.41%, Cu content: 0.47%.

PY2: 2,5-Dibromo-1,4-benzoquinone (106 mg, 0.4 mmol), 1,3,6,8-tetraethynylpyrene (60 mg, 0.2 mmol), $Pd(PPh_3)_4$ (15 mg, 0.01 mmol), CuI (10 mg, 0.05 mmol), *N*,*N*-dimethylformamide (9 mL) and triethylamine (9 mL) were used in this Sonogashira polycondensation reaction described in the general procedure. After work-up and Soxhlet, the product was obtained as a red solid (97 mg, 95%). Anal. Calcd for $(C_{36}H_{10}O_4)_n$: C, 85.37; H, 1.99; Found C, 72.03; H, 3.49. Pd content: 0.69%, Cu content: 0.28%.

PY3: 2,5-Dibromoterephthalic acid (130 mg, 0.4 mmol), 1,3,6,8-tetraethynylpyrene (60 mg, 0.2 mmol), $Pd(PPh_3)_4$ (15 mg, 0.01 mmol), CuI (10 mg, 0.05 mmol), *N*,*N*-dimethylformamide (9 mL) and triethylamine (9 mL) were used in this Sonogashira polycondensation reaction described in the general procedure. After work-up and Soxhlet, the product was obtained as a red solid (125 mg, 86%). Anal. Calcd for $(C_{40}H_{14}O_8)_n$: C, 77.17; H, 2.27; Found C, 69.30; H, 3.79. Pd content: 0.96%, Cu content: 1.24%.

PY4: 2,5-Dibromohydroquinone (107 mg, 0.4 mmol), 1,3,6,8-tetraethynylpyrene (60 mg, 0.2 mmol), $Pd(PPh_3)_4$ (15 mg, 0.01 mmol), CuI (10 mg, 0.05 mmol), *N*,*N*-dimethylformamide (9 mL) and triethylamine (9 mL) were used in this Sonogashira polycondensation reaction described in the general procedure. After work-up and Soxhlet, the product was obtained as a red solid (102 mg, 88%). Anal. Calcd for $(C_{36}H_{14}O_4)_n$: C, 84.70; H, 2.76; Found C, 75.86; H, 3.51. Pd content: 1.07%, Cu content: 1.03%.

4.7.2.3 Synthesis of CTF-based COFs

General synthesis procedure for CTF-based COFs:[82] A Pyrex tube was charged with monomers, 0.5 mL mesitylene, 0.5 mL 1,4-dioxane and 0.1 mL 6 M acetic acid, the mixture was degassed by three freeze-pump-thaw cycles. After sealed and heated at 120 ℃ for 3 days in an oven, the precipitate was collected by filtration and washed with anhydrous tetrahydrofuran and acetone. The final product was dried at 100 ℃ under vacuum overnight.

CTC-1: Terephthalaldehyde (20 mg, 0.15 mmol) and 4,4',4''-(1,3,5-triazine-2,4,6-triyl)trianiline (35 mg, 0.1 mmol) and were used in this reaction described in the general procedure. After work-up and washing, the product was obtained as an orange powder (20.5 mg, 43%). Anal. Calcd for $(C_{32}H_{20}N_5)n$: C, 80.99; H, 4.25; N, 14.76%. Found: C, 74.35; H, 4.36; N, 16.50%.

CTC-2: 2,5-Dihydroxyterephthalaldehyde (25 mg, 0.15 mmol) and 4,4',4''-(1,3,5-triazine-2,4,6-triyl)trianiline (35 mg, 0.1 mmol) and were used in this reaction described in the general procedure. After work-up and washing, the product was obtained as a red solid (44.0 mg, 84%). Anal. Calcd for $(C_{32}H_{20}N_5O_3)n$: C, 73.55; H, 3.86; N, 13.40%. Found: C, 69.58; H, 4.04, N, 13.74%.

CTC-3: 1,5-Naphthalenedicarboxaldehyde (28 mg, 0.15 mmol) and 4,4',4''-(1,3,5-triazine-2,4,6-triyl)trianiline (35 mg, 0.1 mmol) and were used in this reaction described in the general procedure. After work-up and washing, the product was obtained as a crimson solid (52.1 mg, 95%). Anal. Calcd for $(C_{38}H_{23}N_5)n$: C, 83.04; H, 4.22; N, 12.74%. Found: C, 71.14; H, 4.03, N, 12.29%.

CTC-4: 4,4'-Biphenyldicarboxaldehyde (32 mg, 0.15 mmol) and 4,4',4''-(1,3,5-triazine-2,4,6-triyl)trianiline (35 mg, 0.1 mmol) and were used in this reaction described in the general procedure. After work-up and washing, the product was obtained as an orange solid (27.1 mg, 46%). Anal. Calcd for $(C_{41}H_{26}N_5)n$: C, 83.65; H, 4.45, N, 11.90%. Found: C, 72.73; H, 4.75; N, 18.33%.

CTC-5: 4,4',4''-(1,3,5-Triazine-2,4,6-triyl)tribenzaldehyde (17 mg, 0.04 mmol) and 4,4',4''-(1,3,5-triazine-2,4,6-triyl)trianiline (15 mg, 0.04 mmol) and were used in this reaction described in the general procedure. After work-up and washing, the product was obtained as a yellow solid (23.7 mg, 81%). Anal. Calcd for $(C_{24}H_{15}N_6)_n$: C, 77.91; H, 3.92; N, 18.17%. Found: C, 76.73; H, 4.05; N, 17.53%.

4.7.2.4 Synthesis of DE7 and its derivatives

General procedure for the Sonogashira polycondensation: In the glovebox, a 40 mL glass vial was charged with the monomers, $Pd(PPh_3)_4$, CuI, anhydrous *N*,*N*-dimethylformamide and triethylamine, and then sealed with a silicone septum. The sealed vessels were taken out of the glovebox, inserted in a sand bath preheated to 100 ℃ and kept at this temperature for 2 days. After cooling to room temperature, the mixture was quenched by addition of methanol, and the solids were filtered off and washed with methanol and acetone. Further purification was carried out by Soxhlet extraction with chloroform for 2 days. The final product was dried in the vacuum oven at 80 ℃ overnight.

DE7: 2,5-Dibromopyridine (237 mg, 1 mmol), 1,4-diethynylbenzene (126 mg, 1 mmol), $Pd(PPh_3)_2Cl_2$ (18 mg, 0.025 mmol), CuI (2 mg, 0.010 mmol), triphenylphosphine (13 mg, 0.050 mmol), *N*,*N*-dimethylformamide (9 mL) and triethylamine (9 mL) were used in this Sonogashira polycondensation reaction described in the general procedure. After work-up and Soxhlet the product was obtained as a yellow solid (193.1 mg, 96%). Anal. Calcd for $(C_{15}H_7N)_n$: C, 89.53; H, 3.51; N, 6.96%. Found: C, 76.33; H, 3.28; N, 5.42%. Pd content: 0.27%, Cu content: 0.02%.

DEP1: 1,4-Dibromobenzene (236 mg, 1 mmol), 1,4-diethynylbenzene (126 mg, 1 mmol), $Pd(PPh_3)_2Cl_2$ (18 mg, 0.025 mmol), CuI (2 mg, 0.010 mmol), triphenylphosphine (13 mg,

0.050 mmol), *N*,*N*-dimethylformamide (9 mL) and triethylamine (9 mL) were used in this Sonogashira polycondensation reaction described in the general procedure. After work-up and Soxhlet the product was obtained as a yellow solid (190.7 mg, 95%). Anal. Calcd for $(C_{16}H_8)_n$: C, 95.97; H, 4.03%. Found: C, 82.44; H, 3.67%. Pd content: 0.58%, Cu content: 0.01%.

DEP2: 2,4-Dibromopyridine (237 mg, 1 mmol), 1,4-diethynylbenzene(126 mg, 1 mmol), $Pd(PPh_3)_2Cl_2$ (18 mg, 0.025 mmol), CuI (2 mg, 0.010 mmol), triphenylphosphine (13 mg, 0.050 mmol), *N*,*N*-dimethylformamide (9 mL) and triethylamine (9 mL) were used in this Sonogashira polycondensation reaction described in the general procedure. After work-up and Soxhlet the product was obtained as a yellow solid (186.0 mg, 92%). Anal. Calcd for $(C_{15}H_7N)_n$: C, 89.53; H, 3.51; N, 6.96%. Found: C, 79.95; H, 3.28; N, 5.87%. Pd content: 0.81%, Cu content: 0.01%.

DEP3: 2,6-Dibromopyridine (237 mg, 1 mmol), 1,4-diethynylbenzene(126 mg, 1 mmol), $Pd(PPh_3)_2Cl_2$ (18 mg, 0.025 mmol), CuI (2 mg, 0.010 mmol), triphenylphosphine (13 mg, 0.050 mmol), *N*,*N*-dimethylformamide (9 mL) and triethylamine (9 mL) were used in this Sonogashira polycondensation reaction described in the general procedure. After work-up and Soxhlet the product was obtained as a yellow solid (191.2 mg, 95%). Anal. Calcd for $(C_{15}H_7N)_n$: C, 89.53; H, 3.51; N, 6.96%. Found: C, 78.78; H, 3.25; N, 5.77%. Pd content: 1.02%, Cu content: 0.02%.

DEP4: 3,5-Dibromopyridine (237 mg, 1 mmol), 1,4-diethynylbenzene(126 mg, 1 mmol), $Pd(PPh_3)_2Cl_2$ (18 mg, 0.025 mmol), CuI (2 mg, 0.010 mmol), triphenylphosphine (13 mg, 0.050 mmol), *N*,*N*-dimethylformamide (9 mL) and triethylamine (9 mL) were used in this Sonogashira polycondensation reaction described in the general procedure. After work-up and Soxhlet the product was obtained as a yellow solid (194.4 mg, 97%). Anal. Calcd for $(C_{15}H_7N)_n$: C, 89.53; H, 3.51; N, 6.96%. Found: C, 76.98; H, 3.21; N, 5.63%. Pd content: 0.81%, Cu content: 0.03%.

DEP5: 2,5-Dibromopyrimidine (237 mg, 1 mmol), 1,4-diethynylbenzene(126 mg, 1 mmol), $Pd(PPh_3)_2Cl_2$ (18 mg, 0.025 mmol), CuI (2 mg, 0.010 mmol), triphenylphosphine (13 mg, 0.050 mmol), *N*,*N*-dimethylformamide (9 mL) and triethylamine (9 mL) were used in this Sonogashira polycondensation reaction described in the general procedure. After work-up and Soxhlet the product was obtained as a yellow solid (195.5 mg, 97%). Anal. Calcd for

$(C_{14}H_6N_2)_n$: C, 83.16; H, 2.99; N, 13.85%. Found: C, 72.30; H, 2.92; N, 11.29%. Pd content: 1.03%, Cu content: 0.03%.

DEP6: 4,7-Dibromobenzo[c]-1,2,5-thiadiazole (294 mg, 1 mmol), 1,4-diethynylbenzene(126 mg, 1 mmol), $Pd(PPh_3)_2Cl_2$ (18 mg, 0.025 mmol), CuI (2 mg, 0.010 mmol), triphenylphosphine (13 mg, 0.050 mmol), *N*,*N*-dimethylformamide (9 mL) and triethylamine (9 mL) were used in this Sonogashira polycondensation reaction described in the general procedure. After work-up and Soxhlet the product was obtained as a orange solid (248.5 mg, 96%). Anal. Calcd for $(C_{16}H_6N_2S)_n$: C, 74.40; H, 2.34; N, 10.85; S, 12.41%. Found: C, 68.38; H, 2.49; N, 9.61; S, 11.18%. Pd content: 0.73%, Cu content: 0.01%.

DEP7: 5,8-Dibromoquinoxaline (288 mg, 1 mmol), 1,4-diethynylbenzene(126 mg, 1 mmol), $Pd(PPh_3)_2Cl_2$ (18 mg, 0.025 mmol), CuI (2 mg, 0.010 mmol), triphenylphosphine (13 mg, 0.050 mmol), *N*,*N*-dimethylformamide (9 mL) and triethylamine (9 mL) were used in this Sonogashira polycondensation reaction described in the general procedure. After work-up and Soxhlet the product was obtained as a brown solid (243.8 mg, 97%). Anal. Calcd for $(C_{18}H_8N_2)_n$: C, 85.70; H, 3.20; N, 11.10%. Found: C, 75.44; H, 3.26; N, 9.23%. Pd content: 0.63%, Cu content: 0.03%.

DEP8: 4,7-Dibromobenzo[c][1,2,5]oxadiazole (278 mg, 1 mmol), 1,4-diethynylbenzene(126 mg, 1 mmol), $Pd(PPh_3)_2Cl_2$ (18 mg, 0.025 mmol), CuI (2 mg, 0.010 mmol), triphenylphosphine (13 mg, 0.050 mmol), *N*,*N*-dimethylformamide (9 mL) and triethylamine (9 mL) were used in this Sonogashira polycondensation reaction described in the general procedure. After work-up and Soxhlet the product was obtained as a red solid (237.8mg, 98%). Anal. Calcd for $(C_{16}H_6N_2O)_n$: C, 79.33; H, 2.50; N, 11.56%. Found: C, 73.61; H, 2.68; N, 9.72%. Pd content: 0.65%, Cu content: 0.01%.

4.7.2.5 Synthesis of DE7 via microwave assistant method

General procedure for the Sonogashira polycondensation via microwave assistant method: In the glovebox, a microwave vial was charged with the monomers, $Pd(PPh_3)_2Cl_2$, CuI, triphenylphosphine, anhydrous *N*,*N*-dimethylformamide and triethylamine, and then sealed with a silicone septum. The sealed vessels were taken out of the glovebox, and then heated to 80 ℃ in a microwave chamber and kept at this temperature for 2 hours. After cooling to room

temperature, the mixture was quenched by addition of methanol, and the solids were filtered off and washed with methanol and acetone. Further purification was carried out by Soxhlet extraction with chloroform for 2 days. The final product was dried in the vacuum oven at 80 ℃ overnight.

DE7-M80: 2,5-Dibromopyridine (237 mg, 1 mmol), 1,4-diethynylbenzene (126 mg, 1 mmol), $Pd(PPh_3)_2Cl_2$ (18 mg, 0.025 mmol), CuI (2 mg, 0.010 mmol), triphenylphosphine (13 mg, 0.050 mmol), *N*,*N*-dimethylformamide (9 mL) and triethylamine (9 mL) were used in this Sonogashira polycondensation reaction described in the general procedure. After work-up and Soxhlet the product was obtained as a yellow solid (196.0 mg, 97%). Anal. Calcd for $(C_{15}H_7N)_n$: C, 89.53; H, 3.51; N, 6.96%. Found: C, 74.98; H, 3.80; N, 6.85%. Pd content: 0.17%, Cu content: 0.02%.

DE7-M90: 2,5-Dibromopyridine (237 mg, 1 mmol), 1,4-diethynylbenzene (126 mg, 1 mmol), $Pd(PPh_3)_2Cl_2$ (18 mg, 0.025 mmol), CuI (2 mg, 0.010 mmol), triphenylphosphine (13 mg, 0.050 mmol), *N*,*N*-dimethylformamide (9 mL) and triethylamine (9 mL) were used in this Sonogashira polycondensation reaction described in the general procedure. After work-up and Soxhlet the product was obtained as a yellow solid (196.9 mg, 98%). Anal. Calcd for $(C_{15}H_7N)_n$: C, 89.53; H, 3.51; N, 6.96%. Found: C, 77.40; H, 3.21; N, 5.49%. Pd content: 0.31%, Cu content: 0.01%.

DE7-M100: 2,5-Dibromopyridine (237 mg, 1 mmol), 1,4-diethynylbenzene (126 mg, 1 mmol), $Pd(PPh_3)_2Cl_2$ (18 mg, 0.025 mmol), CuI (2 mg, 0.010 mmol), triphenylphosphine (13 mg, 0.050 mmol), *N*,*N*-dimethylformamide (9 mL) and triethylamine (9 mL) were used in this Sonogashira polycondensation reaction described in the general procedure. After work-up and Soxhlet the product was obtained as a yellow solid (198.2 mg, 99%). Anal. Calcd for $(C_{15}H_7N)_n$: C, 89.53; H, 3.51; N, 6.96%. Found: C, 77.48; H, 3.17; N, 5.45%. Pd content: 0.24%, Cu content: 0.01%.

DE7-M110: 2,5-Dibromopyridine (237 mg, 1 mmol), 1,4-diethynylbenzene (126 mg, 1 mmol), $Pd(PPh_3)_2Cl_2$ (18 mg, 0.025 mmol), CuI (2 mg, 0.010 mmol), triphenylphosphine (13 mg, 0.050 mmol), *N*,*N*-dimethylformamide (9 mL) and triethylamine (9 mL) were used in this Sonogashira polycondensation reaction described in the general procedure. After work-up and Soxhlet the product was obtained as a yellow solid (198.0 mg, 98%). Anal. Calcd for $(C_{15}H_7N)_n$:

C, 89.53; H, 3.51; N, 6.96%. Found: C, 77.33; H, 3.20; N, 5.48%. Pd content: 0.19%, Cu content: 0.02%.

DE7-M120: 2,5-Dibromopyridine (237 mg, 1 mmol), 1,4-diethynylbenzene (126 mg, 1 mmol), $Pd(PPh_3)_2Cl_2$ (18 mg, 0.025 mmol), CuI (2 mg, 0.010 mmol), triphenylphosphine (13 mg, 0.050 mmol), *N*,*N*-dimethylformamide (9 mL) and triethylamine (9 mL) were used in this Sonogashira polycondensation reaction described in the general procedure. After work-up and Soxhlet the product was obtained as a yellow solid (192.2 mg, 96%). Anal. Calcd for $(C_{15}H_7N)_n$: C, 89.53; H, 3.51; N, 6.96%. Found: C, 77.88; H, 3.27; N, 5.49%. Pd content: 0.18%, Cu content: 0.03%.

4.7.3 Photocatalytic experiments

4.7.3.1 High-throughput photocatalytic H_2O_2 production experiment

A sample vial was charged with 5 mg of polymer powders and 3 mL water or 2.7 mL water with 0.3 mL sacrificial reagent, and then ultrasonicated for 10 min after capped in air. The photocatalytic H_2O_2 evolution experiments were performed on an Oriel Solar Simulator 94123A with an output of 1.0 sun (Class AAA, 1440 W xenon, 12 × 12 in.). After 2.5 h or 1.5 h, 1 mL solution was sampled with an injection syringe after shook evenly and then filtered with a 0.2 μm Millipore filter to remove the photocatalyst. the amount of H_2O_2 was analysed with Peroxide test sticks or KI titrimetric method with UV-vis spectroscopy.

4.7.3.2 Kinetic H_2O_2 production experiment

A flask was charged with 50 mg of polymer powders and 30 mL water and sealed with a rubber septum. The suspension was ultrasonicated for 10 min to disperse well before degassing by O_2 bubbling for 10 min. The reaction solution was illuminated by A 300 W Xe lamp with a filter ($\lambda > 420$ nm). The concentration of H_2O_2 was determined by KI titrimetric method with UV-vis spectroscopy.

4.7.3.3 Photocatalytic decomposition of H_2O_2 experiment

A flask was charged with 50 mg of polymer powders and 30 mL 1.1 mM H_2O_2 aqueous solution and sealed with a rubber septum. The suspension was ultrasonicated for 10 min to disperse well before degassing by N_2 bubbling for 10 min. The reaction solution was illuminated by A 300

W Xe lamp with a filter (λ > 420 nm). The concentration of H_2O_2 was determined by KI titrimetric method with UV-vis spectroscopy.

4.7.3.4 AQY measurement

The apparent quantum yield (AQY) was determined under monochromate LED light irradiation at a certain wavelength (λ = 420 nm, 490 nm or 700 nm), and the light intensity was measured by a ThorLabs PM100D Power with a photodiode sensor.

The AQY was calculated using the following equation:

$$AQY\ \% = \frac{[\mathrm{H_2O_2}\ \text{produced (mol)}] \times\ 2}{\text{photon number entered into the reactor (mol)}} \times 100$$

$$= \frac{[\mathrm{N_a}\ \times h\ \times\ c)][\mathrm{H_2O_2}\ \text{produced (mol)}] \times\ 2}{\mathrm{I} \times \mathrm{S} \times \mathrm{t} \times \lambda} \times 100$$

Where, Na is Avogadro constant (6.022×10^{23} mol^{-1}), *h* is the Planck constant (6.626×10^{-34} J s), c is the speed of light (3×10^8 m s^{-1}), S is the irradiation area (cm^2), I is the intensity of irradiation light (W cm^{-2}), t is the photoreaction time (s), λ is the wavelength of the monochromatic light (m).

4.7.3.5 SCC Efficiency measurement

To determine the solar-to-chemical energy conversion (SCC) efficiency, an AM 1.5G solar simulator was used as the light source (100 mW cm^{-2}). 200 mg catalysts and 50 mL water were added into a flask and bubbled with O_2 for 10 minutes, the reaction was carried out at 40 ℃ in a water bath. The SCC efficiency was calculated via following equation:

$$SCC\ efficiency\ (\%) =$$

$$\frac{[\ \Delta\mathrm{G}\ \text{for}\ \mathrm{H_2O_2}\ \text{generation (J mol}^{-1})]\ [\mathrm{H_2O_2}\ \text{produced (mol)}]}{[\text{total input energy (W)}]\ [\text{reaction time (s)}]} \times 100$$

where the free energy (ΔG) for H_2O_2 formation is 117 kJ mol^{-1}, the irradiance of the AM1.5 global spectrum is 1,000 W m^{-2} and the irradiated area is 3.14×10^{-4} m^2. The total input energy was therefore 0.314 W.

4.7.4 Electrochemical analysis

4.7.4.1 Photocurrent response and impedance

Electrochemical experiments were performed on a Bio-logic SP200 workstation. The transient photocurrent responses (*I*–t) and electrochemical impedance spectra (EIS) of samples were measured in a three-electrode system (sample on FTO as the working electrode, Pt plate as the

counter electrode and Ag/AgCl as the reference electrode) under a 300 W Xe light source (Newport). The electrolyte was 0.5 M Na_2SO_4 aqueous solution. The working electrode was prepared as follows: 2 mg of the photocatalyst was ultrasonicated with 10 μL Nafion (5 wt.%) aqueous solution and 100 μL ethanol giving a slurry. The slurry was then coated onto FTO glass electrodes with an active area of 0.28 cm^2. The applied bias for intermittent photocurrent intensity measurement was 0.6 V vs. Ag/AgCl. The EIS spectra were determined by applying a 10 mV AC signal over the frequency range of 100 kHz to 10 mHz at a DC bias of 0.6 V vs. Ag/AgCl.

4.7.4.2 Mott-Schottky measurement

The Mott-Schottky plots were measured performed on a Bio-logic SP200 workstation in a standard three electrode system (working electrode : sample on FTO, counter electrode : Pt mesh, and reference electrode : Ag/AgCl) with 0.5 M Na_2SO_4 (pH = 7) as the electrolyte. Preparation of the working electrode: 2 mg polymer was added in 0.1 mL ethanol and 10 μL Nafion. After sonicated for 30 minutes, the slurry was deposited on the FTO substrate and dried in air.

4.7.5 Electron paramagnetic resonance measurements

Spin trapping electron paramagnetic resonance (EPR) measurements were performed using a an ESR spectrometer (Bruker-BioSpin, E 500). 5,5-dimethyl-1-pyrroline N-oxide (DMPO) were used as a spin-trapping reagent to detect $\cdot O_2^-$. The measurements were carried out in a H_2O/methanol (9:1, 500 μL): mixture with 2 mg catalyst and 0.1 mmol DMPO, a Xe lamp with a filter ($\lambda > 420$ nm) was applied as the light source.

4.7.6 Isotopic photoreaction experiments

A vial was charged with 50 mg DE7-M80 and 35 mL $H_2{}^{16}O$ and sealed with a rubber septum, then bubbled with He for 10 min, $^{18}O_2$ gas (purity : 99%, ca. 10 mL) was subsequently injected by a syringe. The vial was illuminated by a Xe lamp with a filter (λ >420 nm) for 24 h, He gas was bubbled again to remove the $^{18}O_2$ gas. The solutions were then injected into a vial containing MnO_2 and He gas, and the gas produced from the decompoaotion phase was detected by an Agilent 7890B GC-MS system.

4.8 References

1. Ciriminna, R.; Albanese, L.; Meneguzzo, F.; Pagliaro, M., Hydrogen Peroxide: A Key Chemical for Today's Sustainable Development. *ChemSusChem* **2016,** *9* (24), 3374-3381.
2. Campos-Martin, J. M.; Blanco-Brieva, G.; Fierro, J. L. G., Hydrogen Peroxide Synthesis: An Outlook beyond the Anthraquinone Process. *Angew. Chem. Int. Ed.* **2006,** *45* (42), 6962-6984.
3. Nishimi, T.; Kamachi, T.; Kato, K.; Kato, T.; Yoshizawa, K., Mechanistic Study on the Production of Hydrogen Peroxide in the Anthraquinone Process. *Eur. J. Org. Chem.* **2011,** *2011* (22), 4113-4120.
4. Santacesaria, E.; Di Serio, M.; Russo, A.; Leone, U.; Velotti, R., Kinetic and catalytic aspects in the hydrogen peroxide production via anthraquinone. *Chem. Eng. Sci.* **1999,** *54* (13), 2799-2806.
5. Zeng, X.; Liu, Y.; Hu, X.; Zhang, X., Photoredox catalysis over semiconductors for light-driven hydrogen peroxide production. *Green Chem.* **2021,** *23* (4), 1466-1494.
6. Hou, H.; Zeng, X.; Zhang, X., Production of Hydrogen Peroxide by Photocatalytic Processes. *Angew. Chem. Int. Ed.* **2020,** *59* (40), 17356-17376.
7. Liu, J.; Zou, Y.; Jin, B.; Zhang, K.; Park, J. H., Hydrogen Peroxide Production from Solar Water Oxidation. *ACS Energy Lett.* **2019,** *4* (12), 3018-3027.
8. Guo, S.; Zhang, S.; Fang, Q.; Abroshan, H.; Kim, H. J.; Haruta, M.; Li, G., Gold–Palladium Nanoalloys Supported by Graphene Oxide and Lamellar TiO2 for Direct Synthesis of Hydrogen Peroxide. *ACS Appl. Mater. Interfaces* **2018,** *10* (47), 40599-40607.
9. Wang, Y.; Wang, Y.; Zhao, J.; Chen, M.; Huang, X.; Xu, Y., Efficient production of H2O2 on Au/WO3 under visible light and the influencing factors. *Appl. Catal. B-Environ.* **2021,** *284*, 119691.
10. Meng, X.; Zong, P.; Wang, L.; Yang, F.; Hou, W.; Zhang, S.; Li, B.; Guo, Z.; Liu, S.; Zuo, G.; Du, Y.; Wang, T.; Roy, V. A. L., Au-nanoparticle-supported ZnO as highly efficient photocatalyst for H2O2 production. *Catal. Commun.* **2020,** *134*, 105860.
11. Shiraishi, Y.; Kanazawa, S.; Sugano, Y.; Tsukamoto, D.; Sakamoto, H.; Ichikawa, S.; Hirai, T., Highly Selective Production of Hydrogen Peroxide on Graphitic Carbon Nitride (g-C3N4) Photocatalyst Activated by Visible Light. *ACS Catal.* **2014,** *4* (3), 774-780.
12. Wei, Z.; Liu, M.; Zhang, Z.; Yao, W.; Tan, H.; Zhu, Y., Efficient visible-light-driven selective oxygen reduction to hydrogen peroxide by oxygen-enriched graphitic carbon nitride polymers. *Energy & Environmental Science* **2018,** *11* (9), 2581-2589.
13. Kofuji, Y.; Isobe, Y.; Shiraishi, Y.; Sakamoto, H.; Tanaka, S.; Ichikawa, S.; Hirai, T., Carbon Nitride–Aromatic Diimide–Graphene Nanohybrids: Metal-Free Photocatalysts for Solar-to-Hydrogen Peroxide Energy Conversion with 0.2% Efficiency. *J. Am. Chem. Soc.* **2016,** *138* (31), 10019-10025.
14. Teng, Z.; Zhang, Q.; Yang, H.; Kato, K.; Yang, W.; Lu, Y.-R.; Liu, S.; Wang, C.; Yamakata, A.; Su, C.; Liu, B.; Ohno, T., Atomically dispersed antimony on carbon nitride for the artificial photosynthesis of hydrogen peroxide. *Nat. Catal.* **2021,** *4* (5), 374-384.
15. Kato, S.; Jung, J.; Suenobu, T.; Fukuzumi, S., Production of hydrogen peroxide as a sustainable solar fuel from water and dioxygen. *Energy & Environmental Science* **2013,** *6* (12), 3756-3764.
16. Isaka, Y.; Kato, S.; Hong, D.; Suenobu, T.; Yamada, Y.; Fukuzumi, S., Bottom-up and top-down methods to improve catalytic reactivity for photocatalytic production of hydrogen peroxide using a Ru-complex and water oxidation catalysts. *J. Mater. Chem. A* **2015,** *3* (23), 12404-12412.

17. Jiang, X.; Yang, B.; Yang, Q.-Q.; Tung, C.-H.; Wu, L.-Z., Cu(ii) coordination polymers with nitrogen catenation ligands for efficient photocatalytic water oxidation. *Chem. Commun.* **2018,** *54* (38), 4794-4797.
18. Xu, J.; Chen, Z.; Zhang, H.; Lin, G.; Lin, H.; Wang, X.; Long, J., Cd3(C3N3S3)2 coordination polymer/graphene nanoarchitectures for enhanced photocatalytic H2O2 production under visible light. *Science Bulletin* **2017,** *62* (9), 610-618.
19. Shiraishi, Y.; Hagi, T.; Matsumoto, M.; Tanaka, S.; Ichikawa, S.; Hirai, T., Solar-to-hydrogen peroxide energy conversion on resorcinol–formaldehyde resin photocatalysts prepared by acid-catalysed polycondensation. *Commun. Chem.* **2020,** *3* (1), 169.
20. Shiraishi, Y.; Takii, T.; Hagi, T.; Mori, S.; Kofuji, Y.; Kitagawa, Y.; Tanaka, S.; Ichikawa, S.; Hirai, T., Resorcinol–formaldehyde resins as metal-free semiconductor photocatalysts for solar-to-hydrogen peroxide energy conversion. *Nat. Mater.* **2019,** *18* (9), 985-993.
21. Lu, Z.; Chen, G.; Siahrostami, S.; Chen, Z.; Liu, K.; Xie, J.; Liao, L.; Wu, T.; Lin, D.; Liu, Y.; Jaramillo, T. F.; Nørskov, J. K.; Cui, Y., High-efficiency oxygen reduction to hydrogen peroxide catalysed by oxidized carbon materials. *Nat. Catal.* **2018,** *1* (2), 156-162.
22. Urban, M. V.; Rath, T.; Radtke, C., Hydrogen peroxide (H2O2): a review of its use in surgery. *Wien. Med. Wochenschr.* **2019,** *169* (9), 222-225.
23. Chen, L.; Wang, L.; Wan, Y.; Zhang, Y.; Qi, Z.; Wu, X.; Xu, H., Acetylene and Diacetylene Functionalized Covalent Triazine Frameworks as Metal-Free Photocatalysts for Hydrogen Peroxide Production: A New Two-Electron Water Oxidation Pathway. *Adv. Mater.* **2020,** *32* (2), 1904433.
24. Zheng, Y.; Yu, Z.; Ou, H.; Asiri, A. M.; Chen, Y.; Wang, X., Black Phosphorus and Polymeric Carbon Nitride Heterostructure for Photoinduced Molecular Oxygen Activation. *Adv. Funct. Mater.* **2018,** *28* (10), 1705407.
25. Figueira-Duarte, T. M.; Müllen, K., Pyrene-Based Materials for Organic Electronics. *Chem. Rev.* **2011,** *111* (11), 7260-7314.
26. Shi, L.; Qi, Z.; Peng, P.; Guo, J.; Wan, G.; Cao, D.; Xiang, Z., Pyrene-Based Covalent Organic Polymers for Enhanced Photovoltaic Performance and Solar-Driven Hydrogen Production. *ACS Applied Energy Materials* **2018,** *1* (12), 7007-7013.
27. Sprick, R. S.; Jiang, J.-X.; Bonillo, B.; Ren, S.; Ratvijitvech, T.; Guiglion, P.; Zwijnenburg, M. A.; Adams, D. J.; Cooper, A. I., Tunable Organic Photocatalysts for Visible-Light-Driven Hydrogen Evolution. *J. Am. Chem. Soc.* **2015,** *137* (9), 3265-3270.
28. Krishnaraj, C.; Sekhar Jena, H.; Bourda, L.; Laemont, A.; Pachfule, P.; Roeser, J.; Chandran, C. V.; Borgmans, S.; Rogge, S. M. J.; Leus, K.; Stevens, C. V.; Martens, J. A.; Van Speybroeck, V.; Breynaert, E.; Thomas, A.; Van Der Voort, P., Strongly Reducing (Diarylamino)benzene-Based Covalent Organic Framework for Metal-Free Visible Light Photocatalytic H2O2 Generation. *J. Am. Chem. Soc.* **2020,** *142* (47), 20107–20116.
29. Schwinghammer, K.; Hug, S.; Mesch, M. B.; Senker, J.; Lotsch, B. V., Phenyl-triazine oligomers for light-driven hydrogen evolution. *Energy & Environmental Science* **2015,** *8* (11), 3345-3353.
30. Aitchison, C. M.; Kane, C. M.; McMahon, D. P.; Spackman, P. R.; Pulido, A.; Wang, X.; Wilbraham, L.; Chen, L.; Clowes, R.; Zwijnenburg, M. A.; Sprick, R. S.; Little, M. A.; Day, G. M.; Cooper, A. I., Photocatalytic proton reduction by a computationally identified, molecular hydrogen-bonded framework. *J. Mater. Chem. A* **2020,** *8* (15), 7158-7170.
31. Li, L.; Cai, Z.; Wu, Q.; Lo, W.-Y.; Zhang, N.; Chen, L. X.; Yu, L., Rational Design of Porous Conjugated Polymers and Roles of Residual Palladium for Photocatalytic Hydrogen Production. *J. Am. Chem. Soc.* **2016,** *138* (24), 7681-7686.
32. Sachs, M.; Cha, H.; Kosco, J.; Aitchison, C. M.; Francàs, L.; Corby, S.; Chiang, C.-L.; Wilson, A. A.; Godin, R.; Fahey-Williams, A.; Cooper, A. I.; Sprick, R. S.; McCulloch,

I.; Durrant, J. R., Tracking Charge Transfer to Residual Metal Clusters in Conjugated Polymers for Photocatalytic Hydrogen Evolution. *J. Am. Chem. Soc.* **2020,** *142* (34), 14574-14587.
33. Plauck, A.; Stangland, E. E.; Dumesic, J. A.; Mavrikakis, M., Active sites and mechanisms for H2O2 decomposition over Pd catalysts. *Proc. Natl. Acad. Sci.* **2016,** *113* (14), E1973.
34. Salem, I. A.; El-Maazawi, M.; Zaki, A. B., Kinetics and mechanisms of decomposition reaction of hydrogen peroxide in presence of metal complexes. *Int. J. Chem. Kinet.* **2000,** *32* (11), 643-666.
35. Pires, M. d. S.; Nogueira, F. G. E.; Torres, J. A.; Lacerda, L. C. T.; Corrêa, S.; Pereira, M. C.; Ramalho, T. C., Experimental and theoretical study on the reactivity of maghemite doped with Cu2+ in oxidation reactions: structural and thermodynamic properties towards a Fenton catalyst. *RSC Adv.* **2016,** *6* (84), 80830-80839.
36. Salem, M. A.; Salem, I. A.; Gemeay, A. H., Kinetics and mechanism of H2O2 decomposition by Cu(II)-, Co(II)-, and Fe(III)-Amine complexes on the surface of Silica-Alumina (25% Al2O3). *Int. J. Chem. Kinet.* **1994,** *26* (11), 1055-1061.
37. Aiyappa, H. B.; Thote, J.; Shinde, D. B.; Banerjee, R.; Kurungot, S., Cobalt-Modified Covalent Organic Framework as a Robust Water Oxidation Electrocatalyst. *Chem. Mater.* **2016,** *28* (12), 4375-4379.
38. Wang, L.; Wan, Y.; Ding, Y.; Wu, S.; Zhang, Y.; Zhang, X.; Zhang, G.; Xiong, Y.; Wu, X.; Yang, J.; Xu, H., Conjugated Microporous Polymer Nanosheets for Overall Water Splitting Using Visible Light. *Adv. Mater.* **2017,** *29* (38).
39. Bai, Y.; Wilbraham, L.; Slater, B. J.; Zwijnenburg, M. A.; Sprick, R. S.; Cooper, A. I., Accelerated Discovery of Organic Polymer Photocatalysts for Hydrogen Evolution from Water through the Integration of Experiment and Theory. *J. Am. Chem. Soc.* **2019,** *141* (22), 9063-9071.
40. Chen, P.; Xing, P.; Chen, Z.; Hu, X.; Lin, H.; Zhao, L.; He, Y., In-situ synthesis of AgNbO3/g-C3N4 photocatalyst via microwave heating method for efficiently photocatalytic H2 generation. *J. Colloid Interface Sci.* **2019,** *534*, 163-171.
41. Zhao, X.; You, Y.; Huang, S.; Wu, Y.; Ma, Y.; Zhang, G.; Zhang, Z., Z‐scheme photocatalytic production of hydrogen peroxide over Bi4O5Br2/g-C3N4 heterostructure under visible light. *Appl. Catal. B-Environ.* **2020,** *278*, 119251.
42. Wu, S.; Yu, H.; Chen, S.; Quan, X., Enhanced Photocatalytic H2O2 Production over Carbon Nitride by Doping and Defect Engineering. *ACS Catal.* **2020,** *10* (24), 14380-14389.
43. Zhang, P.; Tong, Y.; Liu, Y.; Vequizo, J. J. M.; Sun, H.; Yang, C.; Yamakata, A.; Fan, F.; Lin, W.; Wang, X.; Choi, W., Heteroatom Dopants Promote Two-Electron O2 Reduction for Photocatalytic Production of H2O2 on Polymeric Carbon Nitride. *Angew. Chem. Int. Ed.* **2020,** *59* (37), 16209-16217.
44. Kim, H.-i.; Choi, Y.; Hu, S.; Choi, W.; Kim, J.-H., Photocatalytic hydrogen peroxide production by anthraquinone-augmented polymeric carbon nitride. *Appl. Catal. B-Environ.* **2018,** *229*, 121-129.
45. Peng, Y.; Wang, L.; Liu, Y.; Chen, H.; Lei, J.; Zhang, J., Visible-Light-Driven Photocatalytic H2O2 Production on g-C3N4 Loaded with CoP as a Noble Metal Free Cocatalyst. *Eur. J. Inorg. Chem.* **2017,** *2017* (40), 4797-4802.
46. Zuo, G.; Zhang, Y.; Liu, S.; Guo, Z.; Zhao, Q.; Saianand, G.; Feng, L.; Li, L.; Li, W.; Zhang, N.; Meng, X.; Roy, V. A. L., A β-cyclodextrin Modified Graphitic Carbon Nitride with Au Co-Catalyst for Efficient Photocatalytic Hydrogen Peroxide Production. *Nanomaterials* **2020,** *10* (10).
47. Zhang, G.; Zang, S.; Wang, X., Layered Co(OH)2 Deposited Polymeric Carbon Nitrides for Photocatalytic Water Oxidation. *ACS Catal.* **2015,** *5* (2), 941-947.
48. Walling, C., Fenton's reagent revisited. *Acc. Chem. Res.* **1975,** *8* (4), 125-131.

49. Winterbourn, C. C., Toxicity of iron and hydrogen peroxide: the Fenton reaction. *Toxicol. Lett.* **1995,** *82-83*, 969-974.
50. Maurino, V.; Minero, C.; Pelizzetti, E.; Mariella, G.; Arbezzano, A.; Rubertelli, F., Influence of Zn(II) adsorption on the photocatalytic activity and the production of H2O2 over irradiated TiO2. *Res. Chem. Intermed.* **2007,** *33* (3), 319-332.
51. Moon, G.-h.; Kim, W.; Bokare, A. D.; Sung, N.-e.; Choi, W., Solar production of H2O2 on reduced graphene oxide–TiO2 hybrid photocatalysts consisting of earth-abundant elements only. *Energy & Environmental Science* **2014,** *7* (12), 4023-4028.
52. Zhang, J.; Chang, X.; Luo, Z.; Wang, T.; Gong, J., A highly efficient photoelectrochemical H2O2 production reaction with Co3O4 as a co-catalyst. *Chem. Commun.* **2018,** *54* (51), 7026-7029.
53. Chu, C.; Zhu, Q.; Pan, Z.; Gupta, S.; Huang, D.; Du, Y.; Weon, S.; Wu, Y.; Muhich, C.; Stavitski, E.; Domen, K.; Kim, J.-H., Spatially separating redox centers on 2D carbon nitride with cobalt single atom for photocatalytic H2O2 production. *Proc. Natl. Acad. Sci.* **2020,** *117* (12), 6376.
54. Zhang, Q.; Tan, X.; Bedford, N. M.; Han, Z.; Thomsen, L.; Smith, S.; Amal, R.; Lu, X., Direct insights into the role of epoxy groups on cobalt sites for acidic H2O2 production. *Nat. Commun.* **2020,** *11* (1), 4181.
55. Deraz, N.-A. M., Catalytic decomposition of H2O2 on promoted cobaltic oxide catalysts. *Mater. Lett.* **2002,** *57* (4), 914-920.
56. Mu, J.; Wang, Y.; Zhao, M.; Zhang, L., Intrinsic peroxidase-like activity and catalase-like activity of Co3O4 nanoparticles. *Chem. Commun.* **2012,** *48* (19), 2540-2542.
57. Makhlouf, M. T.; Abu-Zied, B. M.; Mansoure, T. H., Effect of calcination temperature on the H2O2 decomposition activity of nano-crystalline Co3O4 prepared by combustion method. *Appl. Surf. Sci.* **2013,** *274*, 45-52.
58. Wang, Q.; Chen, J.; Zhang, H.; Wu, W.; Zhang, Z.; Dong, S., Porous Co3O4 nanoplates with pH-switchable peroxidase- and catalase-like activity. *Nanoscale* **2018,** *10* (40), 19140-19146.
59. Jiang, Y.; Li, J.; Jiang, P.; Li, Y.; Leng, Y., Amino acid-paired dipyridine polymer as efficient metal- and halogen-free heterogeneous catalysts for cycloaddition of CO2 and epoxides into cyclic carbonates. *Catal. Commun.* **2018,** *111*, 1-5.
60. Cai, W.; Piner, R. D.; Stadermann, F. J.; Park, S.; Shaibat, M. A.; Ishii, Y.; Yang, D.; Velamakanni, A.; An, S. J.; Stoller, M.; An, J.; Chen, D.; Ruoff, R. S., Synthesis and Solid-State NMR Structural Characterization of 13C-Labeled Graphite Oxide. *Science* **2008,** *321* (5897), 1815.
61. Xie, J.; Shevlin, S. A.; Ruan, Q.; Moniz, S. J. A.; Liu, Y.; Liu, X.; Li, Y.; Lau, C. C.; Guo, Z. X.; Tang, J., Efficient visible light-driven water oxidation and proton reduction by an ordered covalent triazine-based framework. *Energy & Environmental Science* **2018,** *11* (6), 1617-1624.
62. Kong, D.; Han, X.; Xie, J.; Ruan, Q.; Windle, C. D.; Gadipelli, S.; Shen, K.; Bai, Z.; Guo, Z.; Tang, J., Tunable Covalent Triazine-Based Frameworks (CTF-0) for Visible-Light-Driven Hydrogen and Oxygen Generation from Water Splitting. *ACS Catal.* **2019,** *9* (9), 7697-7707.
63. Zhang, S.; Cheng, G.; Guo, L.; Wang, N.; Tan, B.; Jin, S., Strong-Base-Assisted Synthesis of a Crystalline Covalent Triazine Framework with High Hydrophilicity via Benzylamine Monomer for Photocatalytic Water Splitting. *Angew. Chem. Int. Ed.* **2020,** *59* (15), 6007-6014.
64. Meng, X.; Peng, X.; Xue, J.; Wei, Y.; Sun, Y.; Dai, Y., A biomass-derived, all-day-round solar evaporation platform for harvesting clean water from microplastic pollution. *J. Mater. Chem. A* **2021,** *9* (17), 11013-11024.

65. Yu, X.-Y.; Chen, J.-R.; Xiao, W.-J., Visible Light-Driven Radical-Mediated C–C Bond Cleavage/Functionalization in Organic Synthesis. *Chem. Rev.* **2021,** *121* (1), 506-561.
66. Tian, S.; Yue, Q.; Liu, C.; Li, M.; Yin, M.; Gao, Y.; Meng, F.; Tang, B. Z.; Luo, L., Complete Degradation of a Conjugated Polymer into Green Upcycling Products by Sunlight in Air. *J. Am. Chem. Soc.* **2021**.
67. Shimizu, M.; Orita, H.; Suzuki, K.; Hayakawa, T.; Hamakawa, S.; Takehira, K., Oxidative C-C bond cleavage of vic-diols with H2O2 catalyzed by heteropolyacids. *J. Mol. Catal. A: Chem.* **1996,** *114* (1), 217-220.
68. Lu, A.-H.; Li, W.-C.; Muratova, N.; Spliethoff, B.; Schüth, F., Evidence for C–C bond cleavage by H2O2 in a mesoporous CMK-5 type carbon at room temperature. *Chem. Commun.* **2005,** (41), 5184-5186.
69. Zeng, X.; Liu, Y.; Kang, Y.; Li, Q.; Xia, Y.; Zhu, Y.; Hou, H.; Uddin, M. H.; Gengenbach, T. R.; Xia, D.; Sun, C.; McCarthy, D. T.; Deletic, A.; Yu, J.; Zhang, X., Simultaneously Tuning Charge Separation and Oxygen Reduction Pathway on Graphitic Carbon Nitride by Polyethylenimine for Boosted Photocatalytic Hydrogen Peroxide Production. *ACS Catal.* **2020,** *10* (6), 3697-3706.
70. Zhu, Z.; Pan, H.; Murugananthan, M.; Gong, J.; Zhang, Y., Visible light-driven photocatalytically active g-C3N4 material for enhanced generation of H2O2. *Appl. Catal. B-Environ.* **2018,** *232*, 19-25.
71. Teng, Z.; Cai, W.; Liu, S.; Wang, C.; Zhang, Q.; Chenliang, S.; Ohno, T., Bandgap engineering of polymetric carbon nitride copolymerized by 2,5,8-triamino-tri-s-triazine (melem) and barbituric acid for efficient nonsacrificial photocatalytic H2O2 production. *Appl. Catal. B-Environ.* **2020,** *271*, 118917.
72. Liu, J.; Liu, Y.; Liu, N.; Han, Y.; Zhang, X.; Huang, H.; Lifshitz, Y.; Lee, S.-T.; Zhong, J.; Kang, Z., Metal-free efficient photocatalyst for stable visible water splitting via a two-electron pathway. *Science* **2015,** *347* (6225), 970.
73. Zhu, M.; Lu, J.; Hu, Y.; Liu, Y.; Hu, S.; Zhu, C., Photochemical reactions between 1,4-benzoquinone and O2•−. *Environ. Sci. Pollut. Res.* **2020,** *27* (25), 31289-31299.
74. Schneider, J. T.; Firak, D. S.; Ribeiro, R. R.; Peralta-Zamora, P., Use of scavenger agents in heterogeneous photocatalysis: truths, half-truths, and misinterpretations. *Phys. Chem. Chem. Phys.* **2020,** *22* (27), 15723-15733.
75. Fukuzumi, S.; Ohkubo, K., Fluorescence Maxima of 10-Methylacridone−Metal Ion Salt Complexes: A Convenient and Quantitative Measure of Lewis Acidity of Metal Ion Salts. *J. Am. Chem. Soc.* **2002,** *124* (35), 10270-10271.
76. Fukuzumi, S.; Ohkubo, K., Quantitative Evaluation of Lewis Acidity of Metal Ions Derived from the g Values of ESR Spectra of Superoxide: Metal Ion Complexes in Relation to the Promoting Effects in Electron Transfer Reactions. *Chem. Eur. J.* **2000,** *6* (24), 4532-4535.
77. Zhang, G.; Lan, Z.-A.; Lin, L.; Lin, S.; Wang, X., Overall water splitting by Pt/g-C3N4 photocatalysts without using sacrificial agents. *Chem. Sci.* **2016,** *7* (5), 3062-3066.
78. Gelderman, K.; Lee, L.; Donne, S. W., Flat-Band Potential of a Semiconductor: Using the Mott–Schottky Equation. *J. Chem. Educ.* **2007,** *84* (4), 685.
79. Wan, C.; Zhou, L.; Sun, L.; Xu, L.; Cheng, D.-g.; Chen, F.; Zhan, X.; Yang, Y., Boosting visible-light-driven hydrogen evolution from formic acid over AgPd/2D g-C3N4 nanosheets Mott-Schottky photocatalyst. *Chem. Eng. J.* **2020,** *396*, 125229.
80. Zhang, M.; Lu, M.; Lang, Z.-L.; Liu, J.; Liu, M.; Chang, J.-N.; Li, L.-Y.; Shang, L.-J.; Wang, M.; Li, S.-L.; Lan, Y.-Q., Semiconductor/Covalent-Organic-Framework Z-Scheme Heterojunctions for Artificial Photosynthesis. *Angew. Chem. Int. Ed.* **2020,** *59* (16), 6500-6506.

81. Liang, Z.-Q.; Chu, Z.-Z.; Yang, J.-X.; Yuan, C.-X.; Tao, X.-T.; Zou, D.-C., X-shaped tetra-substituted pyrenes: Synthesis, photophysics, and electroluminescence. *Synth. Met.* **2011,** *161* (15), 1691-1698.
82. Wang, P.; Xu, Q.; Li, Z.; Jiang, W.; Jiang, Q.; Jiang, D., Exceptional Iodine Capture in 2D Covalent Organic Frameworks. *Adv. Mater.* **2018,** *30* (29), 1801991.

Chapter 5: Summary & Outlook

In this thesis, the main aims are to develop more promising organic materials for photocatalytic H_2 evolution or H_2O_2 production, and to establish reliable structure-property relationships for guiding future exploration. Because often only a small number of samples are made and studied for their photocatalytic activity, which could result in misinterpretation of underlying factors and their importance. Therefore, a new library of organic polymer photocatalysts were synthesized and their basic properties were fully characterized with standard techniques. Moreover, their performance for photocatalytic H_2 or H_2O_2 production was also investigated with the assistance of a high throughput workflow. Based on the systematic analysis of structure-property-performance relationships, it was found that no single property dominated the photocatalytic activity, but it was rather a result of the interaction of multiple properties, which is similar to the previous study in our group.[1-2]

In **Chapter 2**, it is reported that the acetylene-based materials have good performance for photocatalytic reactions.[3-5] Hence, we focused on making two acetylene-linked polymer libraries via Sonogashira polycondensation based on the building blocks of 1,3,5-triethynylbenzene and 1,4-diethynylbenzene. They were coupled with 12 different dibromo monomers giving a diverse set of materials that we then studied for photocatalytic H_2 evolution performance in a high-throughput screening. We furthermore used a range of measurements to determine the material properties, such as thermodynamic driving-force, particle size, dispersibility under photocatalytic conditions, and light absorption. Except for the dibenzo[*b,d*]thiophene sulfone polymer of TE11 and DE11, the optical gap and dispersibility of the polymers in the suspension used for the photocatalytic experiments had larger overall effects. We then went on to modify the best-performing material, TE11, by changing the linker unit. This resulted in a triethynylbenzene-dibenzo[*b,d*]thiophene sulfone/triazine copolymer, TEBN11, with a sacrificial hydrogen evolution rate of 1894 μmol g^{-1} h^{-1} under visible light and an external quantum efficiency of 2.7% at 420 nm, which was also relatively high compared to some organic polymer catalysts reported (CTF-2, 1.6% at 420 nm[6] and OB-POP-3, 2.0% at 420 nm[7]), although lower than some dibenzo[*b,d*]thiophene sulfone co-polymers (P10, 11.6% at 420 nm[8] and P64, 20.7% at 420 nm[2]). This study shows that the high throughput screening is a powerful tool for identifying new photocatalysts. The size and diversity of the data set helps to showcase the importance of considering multiple factors in explaining the activity, which is something that might otherwise be missed in a study of only a handful of polymer photocatalysts. In future work, it would be promising to combine with machine learning for discovering candidate materials more effectively. Moreover, it is also important to get deeper

understanding of the mechanism of hydrogen evolution in sacrificial system, and the possible effect factors, such as residue metals and sacrificial reagents, need further investigation.

In **Chapter 3**, we studied the effect of linkage with different conjugacy on photocatalytic H_2 evolution. Another two series of organic linear polymers with dibenzo[*b,d*]thiophene sulfone and dimethyl fluorene as the building blocks were synthesized. Three different kinds of linkers, alkyl linker (-C-C-), alkenyl linker (-C=C-) and alkyne linker (-C≡C-), were systematically investigated. It was found that alkenyl linker (-C=C-)-based polymers outperformed both alkyl (-C-C-) and alkyne (-C≡C-) linker-base polymers. The main reason could be that the alkenyl linker (-C=C-)-based polymers have better visible light absorption and hydrophilicity. However, once again, the activity does not depend on single property. In addition, the dibenzo[*b,d*]thiophene sulfone-series of polymers showed much higher performance than dimethyl fluorene-series of polymers, which further confirmed that the dibenzo[*b,d*]thiophene sulfone is an active group for efficient H_2 evolution, as reported before.[9-11] The best material obtained in this trial was NP2, which showed a high hydrogen evolution of 3334 μmol g^{-1} h^{-1} without additional Pt cocatalyst, and achieved an EQE value of 5.6% at 420 nm, which was higher than the best material TEBN11(with 3 wt.% cocatalyst) found in **Chapter 2**. Moreover, as an attempt to further improve the performance of NP2, several strategies were applied, such as combining with TiO_2 or red phosphorus to make heterojunction photocatalysts, and dye sensitization. However, performance was not improved, which could be mainly attributed to the ineffective combination methods. Therefore, it is important to consider other methods or strategies to prepare hybrid heterojunction catalysts for efficient photocatalytic conversion.

Finally, the photocatalytic H_2O_2 production project was introduced in **Chapter 4**. We used the peroxide test sticks method for the high-throughput preliminary screening. For more accurate quantitative determination of produced H_2O_2, KI titration with UV-vis spectroscopy was applied. After testing a large number of samples, DE7 was found to have the highest activity for H_2O_2 production in pure water under visible light illumination, which was also comparable with the benchmark material of RF523.[12] However, we did not find strong relationship between H_2 production and H_2O_2 production using the same polymers as photocatalysts. We further shortened the reaction time for synthesizing DE7 via microwave heating method. The H_2O_2 production

performance was further improved, and the optimized reaction temperature was 80 ℃ (DE7-M80). In addition, based on the best sample of DE7-M80 in this study, we systematically investigated several influencing factors, such as temperature, pH, sacrificial reagents, the ratio of mass and volume. It was found that the H_2O_2 production performance could be varied by these factors. Moreover, to get a deeper understanding the mechanism of the high activity of DE7-M80, a series of experiments were carried out. The main cause of high activity is still unknown, because we did not find clear correlation between the performance and the structure or property. But we can confirm that the produced H_2O_2 came from the reduction of O_2, and it followed the two-step single electron reduction route. Although DE7 showed high active for photocatalytic H_2O_2 production, it suffered from the problem of long-term stability. It would be more significant if this drawback could be overcome. And for new catalyst, more attention must be paid to catalyst stability and to improving this, as well as increasing photocatalytic rates.

Overall, it is still desirable to discover more candidate organic photocatalysts for highly efficient solar energy conversion. Fully taking advantage of high throughput workflows, computation, mobile robots, and convenient detection methods of target products, will be very powerful to accelerate the research process. It is also important to deeply investigate the limiting steps and mechanism of the photocatalytic reactions, which is essential for rational design and synthesis of new materials for practical applications.

References

1. Meier, C. B.; Clowes, R.; Berardo, E.; Jelfs, K. E.; Zwijnenburg, M. A.; Sprick, R. S.; Cooper, A. I., Structurally Diverse Covalent Triazine-Based Framework Materials for Photocatalytic Hydrogen Evolution from Water. *Chem. Mater.* **2019,** *31* (21), 8830-8838.
2. Bai, Y.; Wilbraham, L.; Slater, B. J.; Zwijnenburg, M. A.; Sprick, R. S.; Cooper, A. I., Accelerated Discovery of Organic Polymer Photocatalysts for Hydrogen Evolution from Water through the Integration of Experiment and Theory. *J. Am. Chem. Soc.* **2019,** *141* (22), 9063-9071.
3. Chen, L.; Wang, L.; Wan, Y.; Zhang, Y.; Qi, Z.; Wu, X.; Xu, H., Acetylene and Diacetylene Functionalized Covalent Triazine Frameworks as Metal-Free Photocatalysts for Hydrogen Peroxide Production: A New Two-Electron Water Oxidation Pathway. *Adv. Mater.* **2020,** *32* (2), 1904433.
4. Pachfule, P.; Acharjya, A.; Roeser, J.; Langenhahn, T.; Schwarze, M.; Schomäcker, R.; Thomas, A.; Schmidt, J., Diacetylene Functionalized Covalent Organic Framework (COF) for Photocatalytic Hydrogen Generation. *J. Am. Chem. Soc.* **2018,** *140* (4), 1423-1427.
5. Wang, L.; Wan, Y.; Ding, Y.; Wu, S.; Zhang, Y.; Zhang, X.; Zhang, G.; Xiong, Y.; Wu, X.; Yang, J.; Xu, H., Conjugated Microporous Polymer Nanosheets for Overall Water Splitting Using Visible Light. *Adv. Mater.* **2017,** *29* (38), 1702428.
6. Meier, C. B.; Sprick, R. S.; Monti, A.; Guiglion, P.; Lee, J.-S. M.; Zwijnenburg, M. A.; Cooper, A. I., Structure-property relationships for covalent triazine-based frameworks: The effect of spacer length on photocatalytic hydrogen evolution from water. *Polymer* **2017,** *126*, 283-290.
7. Bi, S.; Lan, Z.-A.; Paasch, S.; Zhang, W.; He, Y.; Zhang, C.; Liu, F.; Wu, D.; Zhuang, X.; Brunner, E.; Wang, X.; Zhang, F., Substantial Cyano-Substituted Fully sp2-Carbon-Linked Framework: Metal-Free Approach and Visible-Light-Driven Hydrogen Evolution. *Adv. Funct. Mater.* **2017,** *27* (39), 1703146.
8. Sachs, M.; Sprick, R. S.; Pearce, D.; Hillman, S. A. J.; Monti, A.; Guilbert, A. A. Y.; Brownbill, N. J.; Dimitrov, S.; Shi, X.; Blanc, F.; Zwijnenburg, M. A.; Nelson, J.; Durrant, J. R.; Cooper, A. I., Understanding structure-activity relationships in linear polymer photocatalysts for hydrogen evolution. *Nat. Commun.* **2018,** *9* (1), 4968.
9. Sprick, R. S.; Bai, Y.; Guilbert, A. A. Y.; Zbiri, M.; Aitchison, C. M.; Wilbraham, L.; Yan, Y.; Woods, D. J.; Zwijnenburg, M. A.; Cooper, A. I., Photocatalytic Hydrogen Evolution from Water Using Fluorene and Dibenzothiophene Sulfone-Conjugated Microporous and Linear Polymers. *Chem. Mater.* **2019,** *31* (2), 305-313.
10. Wang, X.; Chen, L.; Chong, S. Y.; Little, M. A.; Wu, Y.; Zhu, W.-H.; Clowes, R.; Yan, Y.; Zwijnenburg, M. A.; Sprick, R. S.; Cooper, A. I., Sulfone-containing covalent organic frameworks for photocatalytic hydrogen evolution from water. *Nat. Chem.* **2018,** *10* (12), 1180-1189.
11. Woods, D. J.; Hillman, S. A. J.; Pearce, D.; Wilbraham, L.; Flagg, L. Q.; Duffy, W.; McCulloch, I.; Durrant, J. R.; Guilbert, A. A. Y.; Zwijnenburg, M. A.; Sprick, R. S.; Nelson, J.; Cooper, A. I., Side-chain tuning in conjugated polymer photocatalysts for improved hydrogen production from water. *Energy Environ. Sci.* **2020,** *13* (6), 1843-1855.
12. Shiraishi, Y.; Takii, T.; Hagi, T.; Mori, S.; Kofuji, Y.; Kitagawa, Y.; Tanaka, S.; Ichikawa, S.; Hirai, T., Resorcinol–formaldehyde resins as metal-free semiconductor photocatalysts for solar-to-hydrogen peroxide energy conversion. *Nat. Mater.* **2019,** *18* (9), 985-993.